Dileptons and photons as probes of the quark-gluon plasma

Habilitationsschrift

vorgelegt beim Fachbereich 07
– Mathematik und Informatik, Physik, Geographie –
der Justus-Liebig-Universität Gießen

von

Dr. Olena Linnyk

geboren in
Vinnytsya, Ukraine

· Gießen 2015 ·

In the beginning, God said, the four dimensional divergence of an anti-symmetric second rank tensor equals zero, and there was light.

— Michio Kaku

Contents

1 Introduction **1**

2 Parton-Hadron-String Dynamics **9**

2.1 Dynamical quasiparticle model for hot QCD 10

2.2 Hadronization 15

2.3 Initial conditions 16

2.4 Relativistic off-shell transport 17

2.4.1 Kadanoff-Baym equations 20

2.4.2 Derivation of the off-shell relativistic transport theory 23

2.4.3 Test-particle representation 28

2.5 Transport properties of the hot QCD matter 31

2.5.1 Shear and bulk viscosities 31

2.5.2 Electric conductivity 34

3 Some of the evidence for the QGP production **37**

3.1 Transverse momentum and rapidity spectra of hadrons 37

3.2 Collective flow of hadrons 43

3.3 Energy-density evolution in heavy-ion collisions 45

3.4 Open and hidden charm production 49

3.4.1 Cold nuclear absorption of charmonia 51

3.4.2 'Comover' suppression (and recombination) 54

3.4.3 'Threshold melting' 56

3.4.4 Interaction with pre-hadrons . . . 57
3.4.5 Discriminating hadronic and partonic phases . . . 59

4 Photon and dilepton production in the PHSD 69

4.1 Photon sources in heavy-ion collisions . . . 69
4.2 Dilepton sources in relativistic heavy-ion collisions . . . 71
4.3 Electromagnetic emission from the QGP . . . 73
4.3.1 Dilepton and photon production by perturbative partons . . . 78
4.3.2 Cross sections for dilepton production by off-shell quasiparticles. 81
4.3.3 Dilepton rates from the sQGP . . . 88
4.3.4 Photon production by dynamical quasiparticles . . . 95
4.3.5 Thermal photon rates and the LPM effect . . . 97
4.4 Emission from the interacting hadron gas . . . 100
4.4.1 Bremsstrahlung beyond the SPA . . . 100
4.4.2 Binary meson+meson and meson+nucleon reactions . . . 110
4.4.3 Vector-meson spectral functions . . . 112
4.5 Off-shell propagation . . . 115
4.6 Time integration method . . . 116

5 Comparison to dilepton measurements 117

5.1 SPS energies . . . 117
5.2 RHIC energies . . . 119
5.3 LHC energies . . . 122

6 Comparison to photon measurements 123

6.1 Direct photon spectra from SPS to LHC energies . . . 124
6.2 Elliptic flow of direct photons . . . 131
6.3 Triangular flow of direct photons . . . 138

7 Summary 141

Bibliography **142**

Acknowledgements **157**

Chapter 1

Introduction

Recent progress in elementary particle and high-energy nuclear physics is closely linked to the successes of the PHENIX and STAR experiments at the Relativistic Heavy-Ion Collider (RHIC) and the ALICE experiment at the Large Hadron Collider (LHC). Some fundamental discoveries were made in the experiment already: a new deconfined state of matter of highest ever reached energy-densities has being created. The current investigations at RHIC and LHC are devoted to the properties of deconfined QCD matter at very high temperatures and almost zero net baryon densities. On the other hand the CBM and PANDA at the Facility for Antiproton and Ion Research (FAIR); NA61 at the SPS Heavy-Ion and Neutrino Experiment (SHINE); MPD at the Nuclotron-based Ion Collider Facility (NICA) and the Beam-Energy Scan program at RHIC will study matter at high net baryon density and moderate temperature. The LHC is now providing collisions to all of its experiments at the unprecedented energy of 13 TeV, opening the way to new discoveries.

The Nuclear Physics European Collaboration Committee (NuPECC) have stated in their Long Range Plan for nuclear physics research in Europe:

> "The focus of the research in the ultra-relativistic energy regime is to study and understand how collective phenomena and macroscopic properties, involving many degrees of freedom, emerge from the microscopic laws of elementary particle-physics. ... The most striking case of a collective bulk phenomenon predicted by QCD is the occurrence of a phase transition to a deconfined chirally symmetric state, the quark gluon plasma (QGP)."

A joint effort of the experimental Collaborations and theoretical groups have uncovered some surprising properties of the produced QGP: a low viscosity, high opacity to energetic jets and apparently a fast (local) equilibration.

Some of the observables that indicated that the deconfinement transition has been reached in nuclear collisions at CERN and at RHIC were the jet suppression, strong elliptic flow v_2 and the suppression and regeneration pattern of the charmonia. Within the Hadron-String Dynamics (HSD) transport approach [1], we studied the suppression pattern of charmonia at RHIC with respect to centrality and rapidity employing various model concepts such as variants of the "comover absorption" model or the "charmonium melting" scenario. We find that especially the ratio of the forward to mid-rapidity nuclear modification factors of J/Ψ ($R_{AA}^{forward}(J/\Psi)/R_{AA}^{mid}(J/\Psi)$) cannot

be explained by the interactions with formed comoving mesons or by the color screening mechanism alone. Only when incorporating interactions of the c or $\bar{c}$ quark with a pre-hadronic medium is satisfactory agreement with the measurements are obtained.

While the last years have been devoted to explore the collective and transport properties of this partonic medium, the present focus lies on the electromagnetic emissivity of the new type of matter, i.e. its emission of *direct* photons or dilepton pairs. Consequently, our current goal has been to examine the dynamics of the QGP production and hadronization by investigating the emitted real and virtual photons, where the latter decay into dilepton pairs. This is done by modelling the equilibrating and hadronizing QCD matter and simultaneously calculating the characteristic photon radiation from it. This subject area is of high relevance, because understanding the matter in the early stage of the collision has the potential to access such novel phenomena as gluon condensation, influence of the strong electromagnetic fields, emergence of the dressed quarks and gluons from the perturbative ones.

The measurements of real and virtual photons constitute essential parts of the physics programs of most of the listed experiments. The photons interact only electromagnetically and thus escape to the detector undistorted through the dense and strongly-interacting matter, thus the information on the properties of the initially produced medium survives and can be observed.

The real and virtual photon spectra and elliptic flow v_2 reflect the properties of the hot QCD matter produced. Analyzing the slope of the direct photons transverse momentum spectrum (at $p_T < 3$ GeV), it was deduced that the temperature of the produced matter at RHIC is the highest man-made temperature ever[1]. In nature, such extreme conditions existed only for a short time approximately 6-10 milliseconds after the Big Bang.

The low-p_T direct photons probe not only the temperature [2–4] of the produced QCD-matter, but also its (transport) properties, for instance, the shear viscosity η, bulk viscosity ζ and electric conductivity σ_0. Using the direct photon elliptic flow v_2 (a measure of the azimuthal asymmetry in the photon distribution) as a viscometer was first suggested in Refs. [2, 5–8]. The photon spectra and v_2 are also sensitive to the equation of state of the produced matter [9, 10], to the possible production of a Glasma [11–13], to the rate of chemical equilibration in the QGP [14–16] and to the asymmetry induced by the strong magnetic field (flash) in the very early stage of the collision [17–19].

On the other hand, the measured photons provide a time-integrated picture of the the heavy-ion collision dynamics and are emitted by every moving charge – partons and hadrons. Therefore, a multitude of photon sources has to be differentiated in order to access the signal of interest. The dominant contributions to the inclusive photon production are the decays of mesons, mainly pions, η- and ω-mesons. The PHENIX, STAR and ALICE Collaborations subtracted the *decay* photons from the inclusive photon spectrum using cocktail calculations to obtain the *direct* photons.

However, theoretical understanding of the measured direct photon elliptic flow has been challenging. The PHENIX Collaboration [3] observed large elliptic flow

[1]Note however that the slope parameter extracted from the photon transverse momentum spectrum is not in direct proportionality to the initially reached temperature and is subject to the blue shift due to the Doppler effect.

$v_2(p_T)$ of direct photons at $p_T < 3$ GeV produced in minimal bias Au+Au collisions at $\sqrt{s_{NN}} = 200$ GeV, almost as large as the v_2 of the produced pions, which was in contrast to the theoretical expectations and predictions. Indeed, the photons produced by partonic interactions in the quark-gluon plasma phase are not expected to show considerable flow, because they are dominated by the emission in the initial phase before the elliptic flow fully develops. The PHENIX measurement initiated broad theoretical efforts to understand the origins of the large direct photon v_2.

We contributed to clarifying this question in the present works. Using the derived non-perturbative cross sections for photon (and dilepton) production in the strongly-interacting QGP, we calculated the direct photon production in heavy-ion collisions. We have studied the transverse momentum spectrum and the elliptic flow v_2 of photons from hadronic and partonic production channels in Au+Au collisions at $\sqrt{s_{NN}} =$ 200 GeV in Refs. [20–22].

In this respect, the preliminary data of the ALICE Collaboration [23] are of great interest, since they also indicate a significant direct photon signal at low p_T with a large elliptic flow. This implies an agreement with the findings at the about 14 times lower collision energy by PHENIX at RHIC. We addressed the spectra and elliptic flow of direct photon produced in the Pb+Pb collisions at $\sqrt{s_{NN}} = 2.76$ TeV within the same model as applied at RHIC energy.

Microscopic description of the collision evolution was done using the covariant off-shell transport Parton-Hadron-String Dynamics (PHSD) [24]. The degrees of freedom in the partonic and hadronic phases are the strongly interacting dynamical quasi-particles and off-shell hadrons, respectively. This approach describes the evolution of a relativistic heavy-ion collision from the initial hard scatterings and string formation, through the dynamical deconfinement phase transition to the quark-gluon plasma as well as hadronization, to the subsequent interactions in the hadronic phase.

The transport properties of the QCD matter in the vicinity of the phase transition temperature are not known with high precision from the first principles lattice QCD calculations yet. We have studied QCD matter in the process of its equilibration by doing the calculations in the box using the PHSD transport model. Thus we have calculated the electric conductivity, sheer and bulk viscosities, and the rate of chemical and thermal equilibration of the hot QCD matter. We have calculated the transport coefficients of the QCD matter at temperatures $0.7T_c$ – 3 T_c by performing the simulations within the PHSD approach in the box with periodic boundary conditions.

It was shown that the PHSD approach describes the various hadron abundances, their longitudinal rapidity distributions, as well as transverse momentum distributions from lower SPS to LHC energies. Also, the elliptic flow $v_2(p_T)$ is in accordance with the experimental observations. This allowed us to explore the dynamics of rare probes by implementing their production into the environment of the PHSD, which provides the time evolution of a relativistic heavy-ion collision.

As sources for photon production, we have incorporated the interactions of off-shell quarks and gluons in the strongly interacting quark-gluon plasma (sQGP) ($q + \bar{q} \to g + \gamma$ and $q(\bar{q}) + g \to q(\bar{q}) + \gamma$), the decays of hadrons ($\pi \to \gamma + \gamma$, $\eta \to \gamma + \gamma$, $\omega \to \pi + \gamma$, $\eta' \to \rho + \gamma$, $\phi \to \eta + \gamma$, $a_1 \to \pi + \gamma$) as well as their interactions $\pi + \pi \to \rho + \gamma$, $\rho + \pi \to \pi + \gamma$, meson-meson bremsstrahlung $m + m \to m + m + \gamma$ from all elastic meson-meson and meson-baryon scatterings $m_1 + m_2$ that occur during the

heavy-ion collisions (including $m_i = \pi, \eta, K, \bar{K}, K^0, K^*, \bar{K}^*, K^{*0}, \eta', \omega, \rho, \phi, a_1$), meson-baryon bremsstrahlung ($m + B \to m + B + \gamma$), the two-to-two vector meson+nucleon interactions ($V + p \to \gamma + p/n$ and $V + n \to \gamma + p/n$) and the decay of the Δ-resonance $\Delta \to N\gamma$.

Dilepton radiation by the constituents of the strongly interacting QGP proceeds mainly via following elementary processes: the Born $q + \bar{q} \to \gamma^*$. annihilation mechanism, gluon Compton scattering ($q + g \to \gamma^* + q$ and $\bar{q} + g \to \gamma^* + \bar{q}$), and quark-antiquark annihilation with the gluon bremsstrahlung in the final state ($q+\bar{q} \to g+\gamma^*$). The real photon radiation proceeds via the diagrams $q+g \to \gamma+q$, $\bar{q}+g \to \gamma+\bar{q}$) and $q + \bar{q} \to g + \gamma$. In the on-shell approximation, one would use well-known perturbative QCD cross sections for the processes listed above. However, in the strongly interacting QGP the gluon and quark propagators differ significantly from the non-interacting propagators. Early concepts of the QGP were guided by the idea of a system of partons which interact weakly and relied on perturbative formulae for their interaction cross sections. But the experimental observations at RHIC have shown that the new medium created in ultra-relativistic Au+Au collisions was interacting stronger than hadronic matter. Moreover, the medium showed phenomena of an almost perfect liquid of partons as extracted from the strong radial expansion and elliptic flow of final hadrons. Consequently, the concept of perturbatively interacting quarks and gluons with almost vanishing masses as constituents of the QGP had to be given up. Rather, the non-perturbative, dressed particle states with massive poles in the propagator and a finite lifetime are probably the relevant degrees-of-freedom in the strongly interacting QGP (sQGP).

In order to account for the non-perturbative effects in the photon and dilepton production from the QGP, we calculated cross sections for dilepton production by off-shell partons using phenomenological parametrizations for the quark and gluon propagators as extracted from the lattice QCD (lQCD) calculation within the dynamical quasiparticle model (DQPM). We have shown that the finite quark and gluon masses modify the magnitude as well as the mass M and transverse momentum p_T dependence of the cross sections compared to the perturbative results for massless partons.

The modifications to the dilepton production are larger at lower M^2 and at the edges of the phase space. It was shown that the most prominent effect of the quark masses on the dimuon production cross sections in the Born mechanism ($q + \bar{q} \to \gamma^*$) was a sharp threshold value for the invariant mass of the dilepton pair $M_{min} = m_{q1} + m_{q2}$. We took into account the finite width of the quasiparticles by convoluting the off-shell cross sections with phenomenological spectral functions $A(m_q)$ and $A(m_g)$ for the quarks and gluons in the quark-gluon plasma, respectively. A finite parton width parametrizes their interactions through multiple scatterings and decays. Of course, the threshold was smeared out after the integration over the quark mass distributions (spectra functions). But the suppression at $M \to 0$ (in comparison to the leading order pQCD result) remained.

In addition, the finite masses of the quark and antiquark produce additional *higher-twist* corrections to the cross section, which decrease with increasing M^2, so that the off-shell cross sections approach the on-shell result in the limit of high dilepton masses. We performed an analogous comparison to the leading twist results for the $2 \to 2$ processes $q + \bar{q} \to \gamma + g$ and $q + g \to \gamma + q$. We found that for these processes the

maximum dilepton mass shifts to a lower value as a result of producing a massive gluon or quark in the final state. For the rest of the M values, the effect of the quark and gluon masses was approx. 50%. For $m_{q/g} \to 0$, the cross section approaches the leading twist perturbative QCD result. We have applied the method to calculate dilepton and photon production by dynamical quasi-particles in equilibrated QGP to obtain the emission rates at fixed temperatures. On the other hand, we have implemented these cross sections into the PHSD transport code, which can be applied also out of equilibrium, in particular, to the evolution of the heavy-ion collision.

Our calculations reproduced the transverse momentum spectrum of direct photons. We have shown that the partonic channels constitute about a half of the observed direct photon spectrum. Other theoretical calculations also identified a significant contribution of the photons produced in the QGP to the direct photon spectrum [2, 6, 7, 25–27]. In our work, the photons produced by partonic interactions in the quark-gluon plasma phase were found to show small elliptic flow v_2, because they are dominated by the emission in the initial phase before the spacial asymmetry of the non-central collision geometry fully transforms into the momentum anisotropy. On the other hand, our calculations [20–22] reproduced the recent measurement of the PHENIX Collaboration on elliptic flow $v_2(p_T)$ of direct photons. We attribute the strong v_2 of direct photons to hadronic channels, i.e. to mesonic and baryonic reactions. The strong v_2 of the parent hadrons, in turn, stems from the interactions in the QGP. Accordingly, the presence of the QGP shows up indirectly in the direct photon elliptic flow.

The photon production via bremsstrahlung in meson-meson and meson-baryon elastic collisions was found to be a very important source to interpret the data on the direct photon spectra and elliptic flow simultaneously [20, 21]. In view of the importance of questions that can be answered by direct photon measurements, we have further improved the implementation of the photon production in the meson+meson bremsstrahlung channels in Ref. [22]. We departed from the assumption of the soft photon approximation. Instead, we derived and implemented the "exact" bremsstrahlung cross sections within a covariant one-boson-exchange (OBE) chiral model. Additionally, we investigated in Ref. [22] the suppression of the low-energy photons due to the coherence of the photon emission with long wavelength (LPM effect).

Next, we investigated the centrality dependence of the thermal photon yield and suggested that it scales with the number of participating nucleons as N_{part} in the power $\alpha = 1.5$. This turned out to be in a good agreement with the most recent estimate of $\alpha = 1.48 \pm 0.08 \pm 0.04$ by the PHENIX Collaboration.

We have also investigated the virtual photon production in relativistic $A + A$ collisions. Measuring virtual photons decaying into the dilepton pairs is a direct way compliment the real photon measurements. The invariant mass spectrum of the dileptons dN/dM is invariant with respect to the observer's frame of reference; it is free from the Doppler-corrections. Another advantage of the virtual photons (measured through the dileptons) in comparison to the real γ is the possibility to separate the different production mechanisms by the additional degree-of-freedom: the photon virtuality, i.e. the dilepton invariant mass squared M^2. Investigating the yield of dileptons differentially in the transverse momentum p_T and M^2 allows to dial particular production sources and times. The early production (the Drell-Yan process) dominates spectra

at high-M $M > 4$ GeV; low-M emission is dominated by hadron decays; the dilepton yield in the vicinity of $M = 770$ MeV gives information on the properties of the rho meson in medium; and the peaks at the masses of the charmonia can be used to study their broadening, melting and reproduction in the produced matter (for a review of the open and hidden charm production see our review). Short-lived neutral vector mesons are promising probes of in-medium effects. The modification of the meson spectral functions might be related to the expected dramatic changes of the QCD vacuum properties at high temperature and density, leading to the restoration of chiral symmetry. The radiation from the QGP is present in the wide range of masses M, but it is most prominent between the hadronic peaks, with the main competing source being the semi-leptonic decays of the heavy D and B mesons.

We have calculated the spectra of di-muons produced in In + In collisions at the incident energy 158 A GeV and compared to the NA60 data. We recall that the earlier works of Bratkovskaya et al., Dusling et al. and Rapp et al. have shown that the NA60 dilepton data signalled the in-medium modification of the ρ meson according to the "melting" scenario. We confirmed the result that the spectrum at invariant masses in the vicinity of the ρ peak was better reproduced, if a broadening of its spectral function in the medium was taken into account.

On the other hand, the spectrum at $M > 1$ GeV was shown to be dominated by partonic sources. By incorporating additional multi-meson reaction channels into the PHSD [24, 28], we have clarified the question of whether the dilepton yield at masses above 1 GeV can be accounted for by the dilepton emission in the hadronic interactions, dubbed "4π"-channels. Our conclusions within the non-equilibrium relativistic transport approach is that the dilepton spectra at $M > 1$ GeV is clearly dominated by the radiation from the QGP.

The inclusion of the partonic dilepton sources also made it possible to reproduce in the PHSD the effective temperature or the inverse slope parameter of the transverse momentum spectrum of dileptons in the intermediate-mass region.

Furthermore, we were among the first to point out that dileptons of low masses ($M < 0.6$ GeV) have a sizable contribution from partonic processes particularly, the quark annihilation with gluon bremsstrahlung in the final state. This provides another possible window for probing the properties of the sQGP. This conclusion was later shared by Rapp and collaborators.

In extension of our original study of the heavy-ion collisions at the SPS energy Elab=158 A GeV, we addressed dilepton production in the Au+Au collisions at $\sqrt{s_{NN}} = 200$ GeV and in the Pb+Pb collisions at the LHC energy of $\sqrt{s_{NN}} = 2.76$ TeV within the same approach. Similar to our findings at lower energy, we found that at the RHIC and LHC the partonic dilepton production channels are visible for the intermediate dilepton massed between the ρ and J/Ψ peaks. Their contribution is about as large as that of the correlated D-meson decays. Surprisingly, the dilepton yield from the dynamical – equilibrating and expanding – QGP appears to be exponential in mass from 1 to 2.5 GeV so that a tempting interpretation might appear to be the *thermal* radiation. On the other hand, our studies of the infinite QCD matter equilibration using the PHSD approach have shown that kinetic and chemical equilibrium might not be achieved on the partonic level in heavy-ion collisions at the top RHIC energies.

Finally, we provided predictions for the dilepton measurements in the conditions

of the STAR experiment, which happen to be in a good agreement with the recently released data from the STAR Collaboration. The recently released PHENIX data obtained with the Hadron-Blind-Detector are also in agreement with our dilepton calculations at all M.

Chosen publications

The present thesis includes some of the results, figures and text from the journal articles listed below.

1. O. Linnyk,
   J. Phys. G 38, 025105 (2011), arXiv:1004.2591,
   "Dilepton production by dynamical quasiparticles in the strongly interacting quark gluon plasma"

2. O. Linnyk, E. L. Bratkovskaya, W. Cassing,
   Int. J. Mod. Phys. E 17, 1367 (2008), arXiv:0808.1504,
   "Open and hidden charm in proton-nucleus and heavy-ion collisions"
   Invited review

3. O. Linnyk, V. Konchakovski, T. Steinert, W. Cassing, E. Bratkovskaya,
   arXiv:1504.05699, accepted for publication in Phys. Rev. C,
   "Hadronic and partonic sources of direct photons in relativistic heavy-ion collisions"

4. O. Linnyk, E. L. Bratkovskaya, W. Cassing,
   Progress in Particle and Nuclear Physics (in preparation),
   "Effective QCD and transport description of dilepton and photon production in heavy ion and elementary collisions"
   Invited review

5. O. Linnyk, W. Cassing, E. Bratkovskaya,
   Phys. Rev. C89 (2014) 034908, arXiv:1311.0279,
   "Centrality dependence of the direct photon yield and elliptic flow in heavy-ion collisions at $\sqrt{s} = 200$ GeV"

6. O. Linnyk, V.P. Konchakovski, W. Cassing, E.L. Bratkovskaya,
   Phys. Rev. C88 (2013) 034904, arXiv:1304.7030,
   "Photon elliptic flow in relativistic heavy-ion collisions: hadronic versus partonic sources"

7. V. Ozvenchuk, O. Linnyk, M.I. Gorenstein, E.L. Bratkovskaya, W. Cassing,
   Phys. Rev. C 87, 064903 (2013), e-Print: arXiv:1212.5393,
   "Shear and bulk viscosities of strongly-interacting 'infinite' parton-hadron matter within the Parton-Hadron-String (PHSD) transport approach"

8. W. Cassing, O. Linnyk, T. Steinert, V. Ozvenchuk,
   Phys. Rev. Lett. 110, 182301 (2013), arXiv:1302.0906,
   "On the electric conductivity of hot QCD matter"

9. O. Linnyk, W. Cassing, J. Manninen, E.L. Bratkovskaya, P.B. Gossiaux, J. Aichelin, T. Song, C.M. Ko,
Phys. Rev. C87 (2013) 014905, arXiv:1208.1279,
"Dilepton production in proton-proton and Pb+Pb collisions at $\sqrt{s_{NN}}$ = 2.76 TeV"

10. V. Ozvenchuk, O. Linnyk, M.I. Gorenstein, E.L. Bratkovskaya, W. Cassing,
Phys. Rev. C87 (2013) 024901, arXiv:1203.4734,
"Dynamical equilibration of strongly-interacting 'infinite' parton matter within the Parton-Hadron-String Dynamics (PHSD) transport approach."

11. O. Linnyk, W. Cassing, J. Manninen, E.L. Bratkovskaya, C.M. Ko,
Phys. Rev. C85, 024910 (2012), arXiv:1111.2975,
"Analysis of dilepton production in Au+Au collisions at $\sqrt{s_{NN}}$ = 200 GeV within the Parton-Hadron-String Dynamics (PHSD) transport approach."

12. O. Linnyk, E.L. Bratkovskaya, V. Ozvenchuk, W. Cassing, C.M. Ko,
Phys. Rev. C 84, 054917 (2011), arXiv:1107.3402,
"Dilepton production in nucleus-nucleus collisions at top SPS energy within the Parton-Hadron- String Dynamics (PHSD) transport approach"

13. E.L. Bratkovskaya, W. Cassing, V.P. Konchakovski, O. Linnyk,
Nucl. Phys. A 856, 162 (2011), arXiv:1101.5793,
"Parton-Hadron-String Dynamics at Relativistic Collider Energies"

14. J. Manninen, E. L. Bratkovskaya, W. Cassing, O. Linnyk,
Eur. Phys. J. C 71, 1615 (2011), arXiv:1005.0500,
"Dilepton production in p+p, Cu+Cu and Au+Au collisions at 200 AGeV"

15. E. L. Bratkovskaya, W. Cassing, O. Linnyk,
Phys. Lett. B 670, 428 (2009), arXiv:0805.3177,
"Low mass dilepton production at ultra-relativistic energies"

16. O. Linnyk, E. L. Bratkovskaya, W. Cassing,
Nucl. Phys. A 807, 79 (2008), arXiv:0801.4282,
"Evidence for non-hadronic interactions of charm degrees of freedom in heavy-ion collisions at relativistic energies"

17. O. Linnyk, E. L. Bratkovskaya, W. Cassing, H. Stöcker,
Phys. Rev. C 76, 041901 (2007), arXiv:0705.4443,
"Charmonium dynamics in Au+Au collisions at $\sqrt{s}$ = 200 GeV"

18. O. Linnyk, E. L. Bratkovskaya, W. Cassing, H. Stöcker,
Nucl. Phys. A 786, 183 (2007), nucl-th/0612049,
"Charmonium dynamics in nucleus-nucleus collisions at SPS and FAIR energies"

Chapter 2

Transport description of the heavy-ion collisions: Parton-Hadron-String Dynamics

The Parton-Hadron-String-Dynamics approach is a microscopic covariant transport model that incorporates effective partonic as well as hadronic degrees-of-freedom and involves a dynamical description of the hadronization process from partonic to hadronic matter. Whereas the hadronic part is essentially equivalent to the conventional HSD approach [1, 29] the partonic dynamics is based on the Dynamical Quasiparticle Model [30–33] which describes QCD properties in terms of single-particle Green's functions. With the (essentially three) DQPM parameters for the temperature-dependent effective coupling (2.2) fixed by lattice QCD results – as described later in this Chapter – the approach is fully defined in the partonic phase.

PHSD in the partonic phase gives approximately the same dynamics as the DQPM for partonic systems in equilibrium but also contains interacting hadrons and a dynamical transition between hadronic and partonic degrees-of-freedom. This approach that can also be employed for systems out of equilibrium – such as heavy-ion collisions.

One might ask whether the quasiparticle properties – fixed in thermal equilibrium – should be appropriate also for the nonequilibrium configurations. This question is nontrivial and can only be answered by detailed investigations e.g. on the basis of Kadanoff-Baym equations. We recall that such studies have been summarized in Ref. [34] for strongly interacting scalar fields that initially are far off-equilibrium and simulate momentum distributions of colliding systems at high relative momentum. The results for the effective parameters M and γ, which correspond to the time-dependent pole mass and width of the propagator, indicate that the quasiparticle properties - except for the very early off-equilibrium configuration - are close to the equilibrium mass and width even though the phase-space distribution of the particles is far from equilibrium (cf. Figs. 8 to 10 in Ref. [34]). Accordingly, we will adopt the equilibrium quasiparticle properties also for phase-space configurations out of equilibrium as appearing in relativistic heavy-ion collisions. The reader has to keep in mind that this approximation is well motivated, however, not fully equivalent to the exact solution.

On the hadronic side PHSD includes explicitly the baryon octet and decouplet, the 0^-- and 1^--meson nonets as well as selected higher resonances as in HSD [1, 29].

Hadrons of higher masses (> 1.5 GeV in case of baryons and > 1.3 GeV in case of mesons) are treated as 'strings' (color-dipoles) that decay to the known (low-mass) hadrons according to the JETSET algorithm [35]. We discard an explicit recapitulation of the string formation and decay and refer the reader to the original work [35].

2.1 Dynamical quasiparticle model for hot QCD

Early concepts of the Quark-Gluon-Plasma (QGP) were guided by the idea of a weakly interacting system of massless partons which might be described by perturbative QCD (pQCD). However, experimental observations at RHIC indicated that the new medium created in ultra-relativistic Au+Au collisions is interacting more strongly than hadronic matter. It is presently widely accepted that this medium is an almost perfect liquid of partons as extracted experimentally from the strong radial expansion and the scaling of the elliptic flow $v_2(p_T)$ of mesons and baryons with the number of constituent quarks and antiquarks. At vanishing quark chemical potential μ_q the QCD problem can be addressed at zero and finite temperature by lattice QCD calculations on a 3+1 dimensional torus with a suitable discretization of the QCD action on the euclidian lattice. These calculations so far have provided valuable information on the QCD equation of state, chiral symmetry restoration and various correlators that can be attributed/related to transport coefficients. Due to the Fermion 'sign'-problem lQCD calculations at finite μ_q are presently not robust and one has to rely on non-perturbative - but effective - models to obtain information in the (T, μ_q) plane or for systems out-off equilibrium.

A consistent dynamical approach for the description of strongly interacting systems - also out of equilibrium - can be formulated on the basis of Kadanoff-Baym (KB) equations or off-shell transport equations in phase-space representation, respectively. In the KB theory the field quanta are described in terms of dressed propagators with complex selfenergies [34]. Whereas the real part of the selfenergies can be related to mean-field potentials (of Lorentz scalar, vector or tensor type), the imaginary parts provide information about the lifetime and/or reaction rates of time-like 'particles'. Once the proper (complex) selfenergies of the degrees-of-freedom are known, the time evolution of the system is fully governed by off-shell transport equations (cf. Chapter 2). The determination/extraction of complex selfenergies for the partonic degrees-of-freedom can be performed within the Dynamical QuasiParticle Model (DQPM) by fitting lattice QCD calculations in thermal equilibrium. The DQPM postulates retarded propagators of the quark and gluon degrees-of-freedom in the form

$$G^R(\omega, \mathbf{p}) = \frac{1}{\omega^2 - \mathbf{p}^2 - M^2 + 2i\gamma\omega} \tag{2.1}$$

using $\omega = p_0$. In the scope of the DQPM the running coupling (squared) is approximated by

$$g^2(T/T_c) = \frac{48\pi^2}{(11N_c - 2N_f)\ln[\lambda^2(T/T_c - T_s/T_c)^2]}, \tag{2.2}$$

where the parameters $\lambda \approx 2.42$ and $T_s/T_c \approx 0.56$ have to be extracted from a fit

to the lattice data. In Eq. (2.2), $N_c = 3$ stands for the number of colors, T_c is the critical temperature (≈ 158 MeV), while $N_f(= 3)$ denotes the number of flavors. The parameter T_s is essentially important for the infrared enhancement of the coupling at low temperature T. It has been demonstrated in Ref. [30] that this functional form for the strong coupling $\alpha_s = g^2/(4\pi)$ is in accordance with the lQCD calculations of the Bielefeld group for the long range part of the $q - \bar{q}$ potential. Furthermore, it matches the hard-thermal-loop (HTL) limit for high temperatures T.

The dynamical quasiparticle mass (for gluons and quarks) is assumed to be given by the HTL thermal mass in the asymptotic high-momentum regime, i.e. for gluons

$$M_g^2(T) = \frac{g^2}{6}\left(\left(N_c + \frac{1}{2}N_f\right)T^2 + \frac{N_c}{2}\sum_q \frac{\mu_q^2}{\pi^2}\right) \ , \tag{2.3}$$

and for quarks (antiquarks)

$$M_{q(\bar{q})}^2(T) = \frac{N_c^2 - 1}{8N_c}g^2\left(T^2 + \frac{\mu_q^2}{\pi^2}\right) \ , \tag{2.4}$$

but with the coupling given in Eq. (2.2). The effective quarks, antiquarks and gluons in the DQPM have finite widths, which for $\mu_q = 0$ are adopted in the form

$$\gamma_g(T) \ = \ \frac{1}{3}N_c\frac{g^2T}{8\pi}\ln\left(\frac{2c}{g^2}+1\right), \quad \gamma_{q(\bar{q})}(T) = \frac{1}{3}\frac{N_c^2-1}{2N_c}\frac{g^2T}{8\pi}\ln\left(\frac{2c}{g^2}+1\right), \tag{2.5}$$

where $c = 14.4$ is related to a magnetic cut-off, which is one of the parameters of the DQPM.

The physical processes contributing to the width γ_g are both $gg \leftrightarrow gg$, $gq \leftrightarrow gq$ scattering as well as splitting and fusion reactions $gg \leftrightarrow g$, $gg \leftrightarrow ggg$, $ggg \leftrightarrow gggg$ or $g \leftrightarrow q\bar{q}$ etc. On the fermion side elastic fermion-fermion scattering $pp \leftrightarrow pp$, where p stands for a quark q or antiquark $\bar{q}$, fermion-gluon scattering $pg \leftrightarrow pg$, gluon bremsstrahlung $pp \leftrightarrow pp + g$ or quark-antiquark fusion $q\bar{q} \leftrightarrow g$ etc. emerge. Note, however, that the explicit form of (2.5) is derived for hard two-body scatterings only.

Spectral functions

In the DQPM the parton spectral functions are no longer δ-functions in the invariant mass squared but taken as (cf. Eq. (2.50) in Chapter 2)

$$\rho_j(\omega, \mathbf{p}) = \frac{\gamma_j}{2E_j}\left(\frac{1}{(\omega - E_j)^2 + \gamma_j^2} - \frac{1}{(\omega + E_j)^2 + \gamma_j^2}\right) \tag{2.6}$$

separately for quarks, antiquarks and gluons ($j = q, \bar{q}, g$). Here $E_j^2(\mathbf{p}^2) = \mathbf{p}^2 + M_j^2 - \gamma_j^2$, where the parameters γ_j, M_j from the DQPM have been described above. The spectral

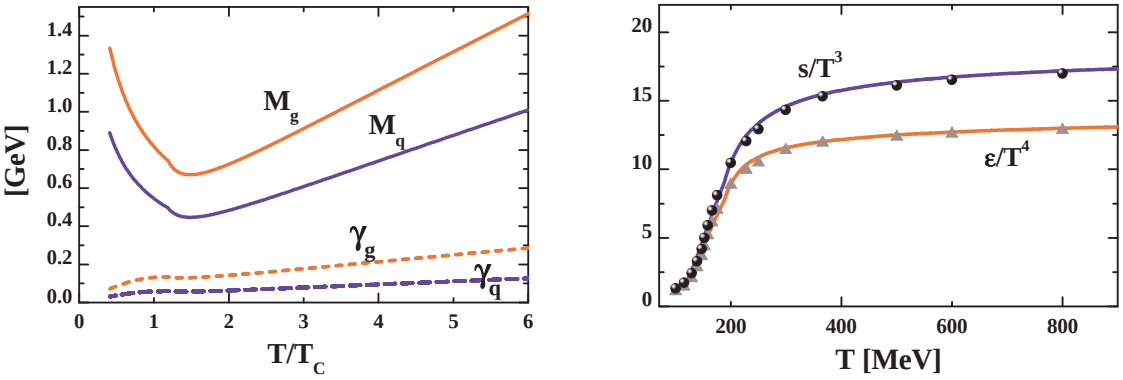

Figure 2.1: *(l.h.s.)* The effective gluon mass M_g and width γ_g as function of the scaled temperature T/T_c (upper red lines). The lower blue lines show the corresponding quantities for quarks. *(r.h.s.)* The scaled entropy density $s(T)/T^3$ (upper blue line) and scaled energy density $\epsilon(T)/T^4$ (lower red line) from the DQPM in comparison to the lQCD results from the BMW group (full dots and triangles) [36]. The figures are taken from Ref. [28].

function (2.6) is antisymmetric in ω and normalized as

$$\int_{-\infty}^{\infty} \frac{d\omega}{2\pi}\, 2\omega\, \rho_j(\omega,\mathbf{p}) = 2\int_{0}^{\infty} \frac{d\omega}{2\pi}\, 2\omega\rho_j(\omega,\mathbf{p}) = 1 \tag{2.7}$$

as mandatory for quantum field theory.

The actual gluon mass M_g and width γ_g – employed as input in the further calculations – as well as the quark mass M_q and width γ_q are depicted in Fig. 2.1 (l.h.s.) as a function of T/T_c. Note that for $\mu_q = 0$ the DQPM gives

$$M_q = \frac{2}{3} M_g, \qquad \gamma_q = \frac{4}{9}\gamma_g\ . \tag{2.8}$$

These variations of the masses with the temperature T – that appear drastic in Fig. 2.1 (l.h.s.) – become, however, rather smooth if viewed as a function of the scalar parton density ρ_s defined (in thermal equilibrium) by

$$\begin{aligned}\rho_s(T/T_c) \;=\; & d_g \int_0^\infty \frac{d\omega}{2\pi} \int \frac{d^3p}{(2\pi)^3}\, 2\sqrt{p^2}\, \rho_g(\omega,\mathbf{p})\; n_B(\omega/T)\; \Theta(p^2) \\ & + d_q \int_0^\infty \frac{d\omega}{2\pi} \int \frac{d^3p}{(2\pi)^3}\, 2\sqrt{p^2}\, \rho_q(\omega,\mathbf{p})\; n_F((\omega-\mu_q)/T)\; \Theta(p^2) \\ & + d_{\bar q} \int_0^\infty \frac{d\omega}{2\pi} \int \frac{d^3p}{(2\pi)^3}\, 2\sqrt{p^2}\, \rho_{\bar q}(\omega,\mathbf{p})\; n_F((\omega+\mu_q)/T)\; \Theta(p^2)\ , \end{aligned} \tag{2.9}$$

where n_B and n_F denote the Bose and Fermi functions, respectively, while μ_q stands for the quark chemical potential. The number of transverse gluonic degrees-of-freedom is $d_g = 16$ while the fermion degrees-of-freedom amount to $d_q = d_{\bar q} = 2N_cN_f = 18$

in case of three flavors (N_f=3). The function $\Theta(p^2)$ (with $p^2 = \omega^2 - \mathbf{p}^2$) projects on **time-like** four-momenta since only this fraction of the four-momentum distribution can be propagated within the light cone.

Thermodynamics of QCD

With the quasiparticle properties (or propagators) chosen as described above, one can evaluate the entropy density $s(T)$, the pressure $P(T)$ and energy density $\epsilon(T)$ in a straight forward manner by starting with the entropy density in the quasiparticle limit from Baym [37],

$$\begin{aligned} s^{dqp} &= -d_g \int \frac{d\omega}{2\pi} \frac{d^3p}{(2\pi)^3} \frac{\partial n_B}{\partial T} \left(\Im \ln(-\Delta^{-1}) + \Im\Pi \, \Re\Delta \right) \\ &\quad -d_q \int \frac{d\omega}{2\pi} \frac{d^3p}{(2\pi)^3} \frac{\partial n_F((\omega-\mu_q)/T)}{\partial T} \left(\Im \ln(-S_q^{-1}) + \Im\Sigma_q \, \Re S_q \right), \\ &\quad -d_{\bar{q}} \int \frac{d\omega}{2\pi} \frac{d^3p}{(2\pi)^3} \frac{\partial n_F((\omega+\mu_q)/T)}{\partial T} \left(\Im \ln(-S_{\bar{q}}^{-1}) + \Im\Sigma_{\bar{q}} \, \Re S_{\bar{q}} \right), \quad (2.10) \end{aligned}$$

where $n_B(\omega/T) = (\exp(\omega/T) - 1)^{-1}$ and $n_F((\omega - \mu_q)/T) = (\exp((\omega - \mu_q)/T) + 1)^{-1}$ denote the Bose and Fermi distribution functions, respectively, while $\Delta = (P^2 - \Pi)^{-1}$, $S_q = (P^2 - \Sigma_q)^{-1}$ and $S_{\bar{q}} = (P^2 - \Sigma_{\bar{q}})^{-1}$ stand for the full (scalar) quasiparticle propagators of gluons g, quarks q and antiquarks $\bar{q}$. In Eq. (2.10) Π and $\Sigma = \Sigma_q \approx \Sigma_{\bar{q}}$ denote the (retarded) quasiparticle selfenergies. In principle, Π as well as Δ are Lorentz tensors and should be evaluated in a nonperturbative framework. The DQPM treats these degrees-of-freedom as independent scalar fields with scalar selfenergies which are assumed to be identical for quarks and antiquarks. Note that one has to treat quarks and antiquarks separately in Eq. (2.10) as their abundance differs at finite quark chemical potential μ_q.

Since the nonperturbative evaluation of the propagators and selfenergies in QCD is a formidable task [and addressed in Dyson-Schwinger (DS) Bethe-Salpeter (BS) approaches] an alternative and practical procedure is to use physically motivated *Ansätze* with Lorentzian spectral functions for quarks[1] and gluons as in (2.6). With this choice the complex selfenergies $\Pi = M_g^2 - 2i\omega\gamma_g$ and $\Sigma_q(\mathbf{q}) = M_q(\mathbf{q})^2 - 2i\gamma_q(\mathbf{q})$ are fully defined via (2.3), (2.4), (2.5). Note that the retarded propagator (2.1),

$$G_R^{-1} = \omega^2 - \mathbf{p}^2 - M^2 + 2i\gamma\omega, \quad (2.11)$$

corresponds to the propagator of a damped harmonic oscillator (with an additional $\mathbf{p}^2$) and preserves microcausality also for $\gamma > M$ [38], i.e. in case of overdamped motion. Although the 'Ansatz' for the parton propagators is not QCD we will demonstrate that a variety of QCD observables on the lattice are compatible with this choice.

Since within the DQPM the real and imaginary parts of the propagators Δ and S now are fixed analytically the entropy density (2.10) can be evaluated numerically. As

[1] In the following the abbreviation is used that 'quarks' denote quarks and antiquarks if not specified explicitly.

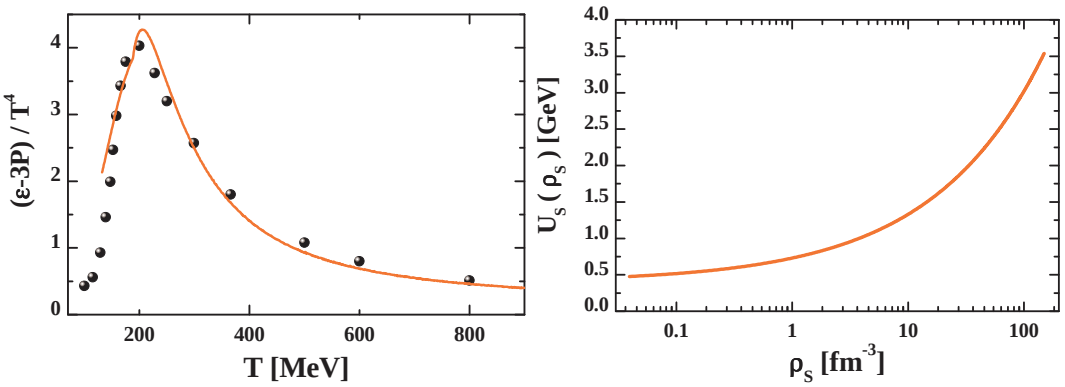

Figure 2.2: (l.h.s.) The interaction measure $(\epsilon - 3P)/T^4$ from the DQPM in comparison to the lQCD results from [36]. (r.h.s.) The scalar mean-field (2.16) for quarks and antiquarks from the DQPM as a function of the scalar parton density ρ_s for $\mu_q = 0$. The figures are taken from Ref. [28].

we deal with a grandcanonical ensemble the Maxwell relations give (at $\mu_q = 0$),

$$s = \frac{\partial P}{\partial T} \ , \tag{2.12}$$

such that the pressure can be obtained by integration of the entropy density s over T, where one tacitly identifies the 'full' entropy density s with the quasiparticle entropy density s^{dqp} (2.10). The starting point for the integration in T is chosen between 100 MeV $< T <$ 120 MeV where the entropy density is approximated by that of a noninteracting pion, η and kaon gas.

The energy density ϵ then follows from the thermodynamical relation

$$\epsilon = Ts - P \tag{2.13}$$

(for $\mu_q = 0$) and thus is also fixed by the entropy $s(T)$ as well as the interaction measure

$$W(T) := \epsilon(T) - 3P(T) = Ts - 4P \tag{2.14}$$

that vanishes for massless and noninteracting degrees-of-freedom.

A direct comparison of the resulting entropy density $s(T)$ and energy density $\epsilon(T)$ from the DQPM with lQCD results from the BMW group [36] is presented in Fig. 2.1 (r.h.s.). Both results have been divided by T^3 and T^4, respectively, to demonstrate the scaling with temperature. The agreement is sufficiently good. A satisfactory agreement also holds for the dimensionless 'interaction measure', i.e. $(\epsilon - 3P)/T^4$ (cf. Fig. 2.2, l.h.s.).

Partonic mean-field potentials

The DQPM uniquely defines a potential energy density,

$$V_p(T, \mu_q) = T^{00}_{g-}(T, \mu_q) + T^{00}_{q-}(T, \mu_q) + T^{00}_{\bar{q}-}(T, \mu_q), \tag{2.15}$$

where the different contributions T^{00}_{j-} correspond to the space-like part of the energy-momentum tensor component T^{00}_{j} of parton $j = g, q, \bar{q}$ [34]. It is found that this quantity is practically independent on the quark chemical potential (for moderate μ_q) when displayed as a function of the scalar density ρ_s instead of T and μ_q separately. Note that the field quanta involved in (2.15) are virtual and thus correspond to partons exchanged in interaction diagrams.

A scalar mean-field $U_s(\rho_s)$ for quarks and antiquarks is defined by the derivative [34],

$$U_s(\rho_s) = \frac{dV_p(\rho_s)}{d\rho_s}, \tag{2.16}$$

which is evaluated numerically within the DQPM. The result is displayed in Fig. 2.2 (r.h.s.) as a function of the parton scalar density ρ_s (2.9) and shows that the scalar mean-field is in the order of a few GeV for $\rho_s > 10$ fm^{-3}. This mean-field (2.16) is employed in the PHSD transport calculations and determines the force on a quasiparticle j, i.e. $\sim M_j/E_j \nabla U_s(x) = M_j/E_j \; dU_s/d\rho_s \; \nabla\rho_s(x)$ where the scalar density $\rho_s(x)$ is determined numerically on a space-time grid (see below).

2.2 Hadronization

Whereas the dynamics of partonic as well as hadronic systems is fixed by the DQPM or HSD, respectively, the change in the degrees-of-freedom has to be specified in line with the lattice QCD equation of state. The hadronization, i.e. the transition from partonic to hadronic degrees-of-freedom, has been introduced in Refs. [24, 39] and is repeated here for completeness. The hadronization is implemented in PHSD by local covariant transition rates e.g. for $q + \bar{q}$ fusion to a mesonic state m of four-momentum $p = (\omega, \mathbf{p})$ at space-time point $x = (t, \mathbf{x})$:

$$\frac{dN_m(x,p)}{d^4x d^4p} = Tr_q Tr_{\bar{q}} \; \delta^4(p - p_q - p_{\bar{q}}) \; \delta^4\left(\frac{x_q + x_{\bar{q}}}{2} - x\right) \omega_q \; \rho_q(p_q) \; \omega_{\bar{q}} \; \rho_{\bar{q}}(p_{\bar{q}})$$
$$\times |v_{q\bar{q}}|^2 \; W_m(x_q - x_{\bar{q}}, (p_q - p_{\bar{q}})/2) \; N_q(x_q, p_q) \; N_{\bar{q}}(x_{\bar{q}}, p_{\bar{q}}) \; \delta(\text{flavor, color}). \tag{2.17}$$

In Eq. (2.17) we have introduced the shorthand notation,

$$Tr_j = \sum_j \int d^4x_j \int \frac{d^4p_j}{(2\pi)^4} \; , \tag{2.18}$$

where $\sum_j$ denotes a summation over discrete quantum numbers (spin, flavor, color); $N_j(x,p)$ is the phase-space density of parton j at space-time position x and four-momentum p. In Eq. (2.17) δ(flavor, color) stands symbolically for the conservation of flavor quantum numbers as well as color neutrality of the formed hadronic state m which can be viewed as a color-dipole or 'pre-hadron'. Furthermore, $v_{q\bar{q}}(\rho_p)$ is the effective quark-antiquark interaction from the DQPM (displayed in Fig. 10 of Ref. [33]) as a function of the local parton $(q + \bar{q} + g)$ density ρ_p (or energy density). Furthermore, $W_m(x,p)$ is the dimensionless phase-space distribution of the formed

'pre-hadron', i.e.

$$W_m(\xi, p_\xi) = \exp\left(\frac{\xi^2}{2b^2}\right) \exp\left(2b^2(p_\xi^2 - (M_q - M_{\bar{q}})^2/4)\right) \tag{2.19}$$

with $\xi = x_1 - x_2 = x_q - x_{\bar{q}}$ and $p_\xi = (p_1 - p_2)/2 = (p_q - p_{\bar{q}})/2$ (which had been previously introduced in Eq. (2.14) of Ref. [40]). The width parameter b is fixed by $\sqrt{\langle r^2 \rangle} = b = 0.66$ fm (in the rest frame) which corresponds to an average rms radius of mesons. We note that the expression (2.19) corresponds to the limit of independent harmonic oscillator states and that the final hadron-formation rates are approximately independent of the parameter b within reasonable variations. By construction the quantity (2.19) is Lorentz invariant; in the limit of instantaneous 'hadron formation', i.e. $\xi^0 = 0$, it provides a Gaussian dropping in the relative distance squared $(\mathbf{r}_1 - \mathbf{r}_2)^2$. The four-momentum dependence reads explicitly (except for a factor 1/2)

$$(E_1 - E_2)^2 - (\mathbf{p}_1 - \mathbf{p}_2)^2 - (M_1 - M_2)^2 \leq 0 \tag{2.20}$$

and leads to a negative argument of the second exponential in Ed. (2.19) favoring the fusion of partons with low relative momenta $p_q - p_{\bar{q}} = p_1 - p_2$.

Related transition rates (2.17) are defined for the fusion of three off-shell quarks ($q_1 + q_2 + q_3 \leftrightarrow B$) to a color neutral baryonic (B or $\bar{B}$) resonances of finite width (or strings) fulfilling energy and momentum conservation as well as flavor current conservation (cf. Section 2.3 in Ref. [24]). In contrast to the familiar coalescence models this hadronization scheme solves the problem of simultaneously fulfilling all conservation laws and the constraint of entropy production. For further details we refer the reader to Refs. [24, 39].

2.3 Initial conditions

The initial conditions for the parton/hadron dynamical system have to be specified additionally. In order to describe relativistic heavy-ion reactions we start with two nuclei in their 'semi-classical' groundstate, boosted towards each other with a velocity β (in z-direction), fixed by the bombarding energy. The initial phase-space distributions of the projectile and target nuclei are determined in the local Thomas-Fermi limit as in the HSD transport approach [1, 29] or the UrQMD model [41, 42]. We recall that at relativistic energies the initial interactions of two nucleons are well described by the excitation of two color-neutral strings which decay in time to the known hadrons (mesons, baryons, antibaryons) [35]. Initial hard processes - i.e. the short-range high-momentum transfer reactions that can be well described by perturbative QCD - are treated in PHSD (as in HSD) via PYTHIA 5.7 [43]. The novel element in PHSD (relative to HSD) is the 'string melting concept' as also used in the AMPT model [44] in a similar context. However, in PHSD the strings (or possibly formed hadrons) are only allowed to 'melt' if the local energy density $\epsilon(x)$ (in the local rest frame) is above the transition energy density ϵ_c which in the present DQPM version is $\epsilon_c \approx 0.5$ GeV/fm^3. The mesonic strings then decay to quark-antiquark pairs according to an

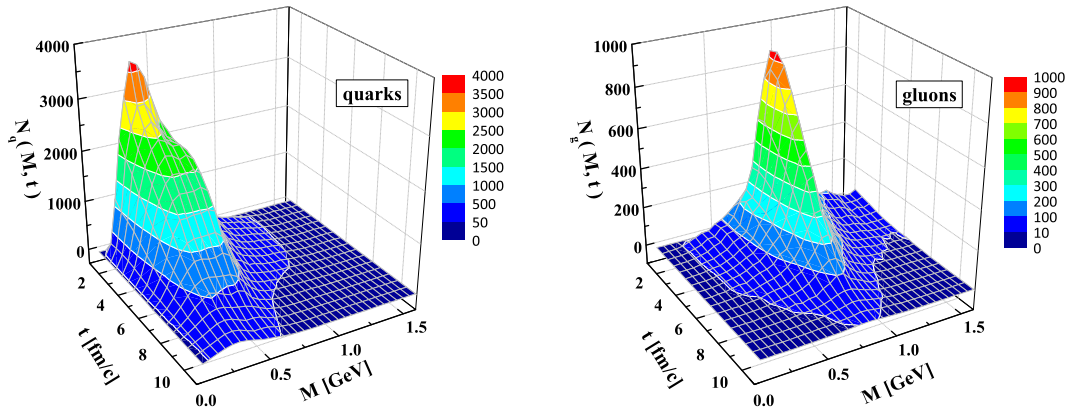

Figure 2.3: The time-dependent mass distributions for quarks (+ antiquarks) (l.h.s.) and gluons (r.h.s.) for a central Au+Au collision at $\sqrt{s}$ = 200 GeV and b=1 fm at midrapidity ($|y| \leq 1$). The figures are taken from Ref. [28].

intrinsic quark momentum distribution,

$$F(\mathbf{q}) \sim \exp(-2b^2\mathbf{q}^2) \ , \tag{2.21}$$

in the meson rest-frame (cf. Eq. (2.17) for the inverse process). The parton final four-momenta are selected randomly according to the momentum distribution (2.21) (with b= 0.66 fm), and the parton-energy distribution is fixed by the DQPM at given energy density $\epsilon(\rho_s)$ in the local cell with scalar parton density ρ_s. The flavor content of the $q\bar{q}$ pair is fully determined by the flavor content of the initial string. By construction the 'string melting' to massive partons conserves energy and momentum as well as the flavor content. In contrast to Ref. [44] the partons are of finite mass – in line with their local spectral function – and obtain a random color $c = (1, 2, 3)$ or (r, b, g) in addition. Of course, the color appointment is color neutral, i.e. when selecting a color c for the quark randomly the color for the antiquark is fixed by $-c$. The baryonic strings melt analogously into a quark and a diquark while the diquark, furthermore, decays to two quarks.

2.4 Relativistic dynamics of many-body systems and off-shell transport

The dynamical evolution of the system is entirely described by the transport dynamics in PHSD incorporating the off-shell propagation of the partonic quasiparticles according to Refs. [34, 45] as well as the transition to resonant hadronic states (or 'strings') via Eq. (2.17).

Relativistic formulations of the many-body problem are essentially described within covariant field theory. Since the fields themselves are distributions in space-time $x = (t, \mathbf{x})$ one uses the Heisenberg picture for convenience. In the Heisenberg picture the time evolution of the system is described by time-dependent operators that are evolved

with the help of the time-evolution operator $\hat{U}(t,t')$ which follows

$$i\frac{\partial \hat{U}(t,t_0)}{\partial t} = \hat{H}(t)\hat{U}(t,t_0), \tag{2.22}$$

with $\hat{H}(t)$ denoting the Hamilton operator of the system at time t. Eq. (2.22) is formally solved by

$$\hat{U}(t,t_0) = T\left(\exp\left[-i\int_{t_0}^{t} \mathrm{d}z\ \hat{H}(z)\right]\right) = \sum_{n=0}^{\infty} \frac{T[-i\int_{t_0}^{t} \mathrm{d}z\ \hat{H}(z)]^n}{n!}, \tag{2.23}$$

where T denotes the time-ordering operator, which is also denoted as Dyson series. Let's assume that the initial state is given by some density matrix $\hat{\rho}$, which may be a pure or mixed state, then the time evolution of any operator $\hat{O}$ in the Heisenberg picture from time t_0 to t is given by

$$O(t) = \langle \hat{O}_H(t) \rangle = \mathrm{Tr}\left(\hat{\rho}\,\hat{O}_H(t)\right) = \mathrm{Tr}\left(\hat{\rho}\,\hat{U}(t_0,t)\hat{O}\,\hat{U}(t,t_0)\right) = \mathrm{Tr}\left(\hat{\rho}\,\hat{U}^{\dagger}(t,t_0)\hat{O}\,\hat{U}(t,t_0)\right). \tag{2.24}$$

Eq. (2.24) implies that first the system is evolved from t_0 to t and then backward from t to t_0. This may be expressed as a time integral along the (Keldysh-)contour shown in Fig. 2.4.

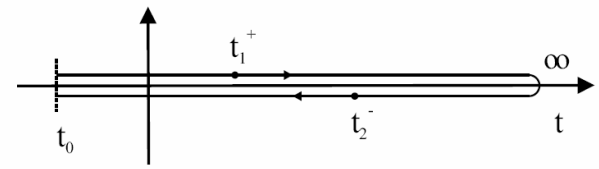

Figure 2.4: The Keldysh-contour for the time integration in the Heisenberg picture.

Two-point functions

Now Green functions on the Keldysh-contour may have time arguments on the same branch of the contour or on opposite branches. This gives four possibilities for the Green functions defined – in case of a field theory with only scalar fields $\phi(x)$ (for sake of illustration) – by

$$iG^{c}(x,y) = iG^{++}(x,y) = \langle\, \hat{T}^{c}(\phi(x)\phi(y))\, \rangle \tag{2.25}$$

$$iG^{<}(x,y) = iG^{+-}(x,y) = \langle \phi(y)\phi(x) \rangle \tag{2.26}$$

$$iG^{>}(x,y) = iG^{-+}(x,y) = \langle \phi(x)\phi(y) \rangle \tag{2.27}$$

$$iG^{a}(x,y) = iG^{--}(x,y) = \langle\, \hat{T}^{a}(\phi(x)\phi(y))\, \rangle\,, \tag{2.28}$$

which are not independent! Here $x = (x^0, \mathbf{x})$ and $y = (y^0, \mathbf{y})$. Time-ordering has to be fulfilled if both time arguments are on the same axis. The causal time-ordering operator T^c places fields at later times to the left while the anticausal operator T^a

places fields at later times to the right. The Green functions $G^>$ and $G^<$ are denoted as **Wightman functions** and will play the essential role in the dynamical description of the system. One may also write the Green function on the Keldysh-contour in terms of a 2x2 matrix

$$G(x,y) = \begin{array}{c} \\ + \\ - \end{array} \begin{array}{c} \begin{array}{cc} + & - \end{array} \\ \begin{pmatrix} G^c(x,y) & G^<(x,y) \\ G^>(x,y) & G^a(x,y) \end{pmatrix} \end{array}. \tag{2.29}$$

Note that the Green functions defined in Eqs. (2.25) to (2.28) are two-point functions, i.e. they correspond to a single-particle degree-of-freedom!

The further derivation starts with the Dyson equation for $G(x,y)$,

$$G(x,y) = G_0(x,y) + [G_0 \Sigma G](x,y), \tag{2.30}$$

with $G_0(x,y)$ denoting the bare Green function. The selfenergy $\Sigma(x,y)$ has the meaning of a one-body mean-field potential and in lowest order for fermions is given by the Hartree-Fock potential ($\times 2M$) since in the relativistic case Σ has the dimension [energy]^2.

The relation to the one-body density matrix ρ - as employed in density-matrix theory [46] - is given by

$$\rho(\mathbf{x},\mathbf{x}';t) = iG^<(\mathbf{x},\mathbf{x}';t,t), \tag{2.31}$$

since the time diagonal Green function can be identified with an integral over the energy variable ω using

$$G^<(\mathbf{x},\mathbf{x}';\omega,t) = \int_{-\infty}^{\infty} d(\tau-\tau')\ \exp(i\omega(\tau-\tau'))\ G^<(\mathbf{x},\mathbf{x}';\tau,\tau') \tag{2.32}$$

(for $t = (\tau+\tau')/2$), i.e.

$$G^<(\mathbf{x},\mathbf{x}';t) = \int_{-\infty}^{\infty} \frac{d\omega}{2\pi}\ G^<(\mathbf{x},\mathbf{x}';\omega,t). \tag{2.33}$$

Two-point functions F on the closed-time-path (CTP) generally can be expressed by retarded and advanced components as

$$F^R(x,y) = F^c(x,y) - F^<(x,y) = F^>(x,y) - F^a(x,y), \tag{2.34}$$

$$F^A(x,y) = F^c(x,y) - F^>(x,y) = F^<(x,y) - F^a(x,y)$$

giving in particular the relation

$$F^R(x,y) - F^A(x,y) = F^>(x,y) - F^<(x,y). \tag{2.35}$$

Note that the advanced and retarded components of the Green functions only contain spectral and no statistical information,

$$G^{R/A}(x,y) = G_0(x,y)\ \delta(t_1-t_2) \pm \Theta(\pm(t_1-t_2))\ [G^>(x,y) - G^<(x,y)]. \tag{2.36}$$

The Dyson-Schwinger equation

The Dyson-Schwinger equation (2.30) on the closed-time path reads in matrix form:

$$\begin{pmatrix} G^c(x,y) & G^<(x,y) \\ G^>(x,y) & G^a(x,y) \end{pmatrix} = \begin{pmatrix} G_0^c(x,y) & G_0^<(x,y) \\ G_0^>(x,y) & G_0^a(x,y) \end{pmatrix} +$$

$$\begin{pmatrix} G_0^c(x,x') & G_0^<(x,x') \\ G_0^>(x,x') & G_0^a(x,x') \end{pmatrix} \odot \begin{pmatrix} \Sigma^c(x',y') & -\Sigma^<(x',y') \\ -\Sigma^>(x',y') & \Sigma^a(x',y') \end{pmatrix} \odot \begin{pmatrix} G^c(y',y) & G^<(y',y) \\ G^>(y',y) & G^a(y',y) \end{pmatrix}, \tag{2.37}$$

where the symbol $\odot$ stands for an intermediate integration over space-time on the CTP, i.e. x' or y'. The selfenergy Σ on the CPT is defined along Eq. (2.34) and incorporates interactions of higher order. In lowest order $\Sigma/2M$ is given by the Hartree or Hartree-Fock mean-field in the non-relativistic limit (in case of fermions) but it follows a nonperturbative expansion [47].

2.4.1 Kadanoff-Baym equations

To derive the **Kadanoff-Baym equations** one multiplies Eq. (2.37) with the inverse free Green function (operator) $G_{0x}^{-1} = -(\partial_\mu^x \partial_x^\mu + m^2)$ from the left. This gives four equations which can be cast into the form:

$$-(\partial_\mu^x \partial_x^\mu + m^2) G^{R/A}(x,y) = \delta(x-y) + \Sigma^{R/A}(x,x') \odot G^{R/A}(x',y), \tag{2.38}$$

$$-(\partial_\mu^x \partial_x^\mu + m^2) G^<(x,y) = \Sigma^R(x,x') \odot G^<(x',y) + \Sigma^<(x,x') \odot G^A(x',y), \tag{2.39}$$

$$-(\partial_\mu^x \partial_x^\mu + m^2) G^>(x,y) = \Sigma^R(x,x') \odot G^>(x',y) + \Sigma^>(x,x') \odot G^A(x',y). \tag{2.40}$$

The propagation of the Green functions in the variable y is defined by the adjoint equations:

$$-(\partial_\mu^y \partial_y^\mu + m^2) G^{R/A}(x,y) = \delta(x-y) + G^{R/A}(x,x') \odot \Sigma^{R/A}(x',y), \tag{2.41}$$

$$-(\partial_\mu^y \partial_y^\mu + m^2) G^<(x,y) = G^R(x,x') \odot \Sigma^<(x',y) + G^<(x,x') \odot \Sigma^A(x',y), \tag{2.42}$$

$$-(\partial_\mu^y \partial_y^\mu + m^2) G^>(x,y) = G^R(x,x') \odot \Sigma^>(x',y) + G^>(x,x') \odot \Sigma^A(x',y). \tag{2.43}$$

Note again that the evolution of the retarded/advanced Green functions only depends on retarded/advanced quantities.

Definition of selfenergies

For the solution of the KB equations the computation/fixing of the (two-point) self-energies Σ is mandatory. In the context of field theory the latter is extracted from the effective action

$$\Gamma[G] = \Gamma^0[G_0] + \frac{i}{2}[\ln(1 - G_0\Sigma) + G\Sigma] + \Phi[G] \tag{2.44}$$

assuming a vanishing vacuum expectation value $\langle 0|\phi(x)|0\rangle$. Here $\Gamma^0[G_0]$ only depends on the free Green function G_0 and can be considered as constant in the following.

Note that all internal and external integrations in (2.44) have to be performed over the CTP. In $\Phi[G]$ all closed two-particle irreducible (2PI) diagrams are included in lowest (nontrivial) order. We recall that 2PI diagrams are those that cannot be separated in two disjunct diagrams by cutting two propagator lines; formally this implies that after second order differentiation with respect to G no separate diagrams survive.

For the derivation of selfenergies one now considers the variation of the action $\Gamma[G]$ with respect to G requiring $\delta\Gamma = 0$,

$$\delta\Gamma = 0 = \frac{i}{2}\Sigma\,\delta G - \frac{i}{2}\frac{G_0}{1 - G_0\,\Sigma}\delta\Sigma + \frac{i}{2}G\,\delta\Sigma + \delta\Phi$$
$$= \frac{i}{2}\Sigma\,\delta G - \frac{i}{2}\underbrace{\frac{1}{G_0^{-1} - \Sigma}}_{=G}\delta\Sigma + \frac{i}{2}G\,\delta\Sigma + \delta\Phi = \frac{i}{2}\Sigma\,\delta G + \delta\Phi. \tag{2.45}$$

$$\Rightarrow \Sigma = 2i\frac{\delta\Phi}{\delta G}. \tag{2.46}$$

The selfenergies thus are obtained by opening of a propagator-line in the irreducible diagrams Φ. Note that this definition of the selfenergy preserves all conservation laws of the theory (as well as causality) and does not introduce additional conserved currents. In principle the Φ-functional includes irreducible diagrams up to infinite order, but here we will consider only the contributions up to second order in the coupling (2PI). For our present purpose this approximation is sufficient since we include the leading mean-field effects as well as the leading order scattering processes that pave the way to thermalization.

Spectral function

The spectral function of the fields ϕ is of particular interest since it follows from the field commutator at unequal times and reflects the quantization of the theory. For scalar, symmetric fields ϕ it is given by

$$A(x,y) = \langle\, [\phi(x), \phi(y)]_- \,\rangle = i[G^>(x,y) - G^<(x,y)] = i[G^R(x,y) - G^A(x,y)]. \tag{2.47}$$

For homogenous systems in space we have in momentum-time representation

$$A(\mathbf{p}, t_1, t_2) = i[G^>(\mathbf{p}, t_1, t_2) - G^<(\mathbf{p}, t_1, t_2)] = i\left[-[G^<(\mathbf{p}, t_1, t_2)]^* - G^<(\mathbf{p}, t_1, t_2)\right]. \tag{2.48}$$

The quantity (2.48) was evaluated numerically as a function of $\Delta t = t_1 - t_2$ and $t = (t_1 + t_2)/2$ for a low lying momentum mode in case of the ϕ^4-theory for strong coupling λ in Ref. [45]. We observe a damped oscillation in Δt (for $\Delta t \geq 0$) in all cases with characteristic time scale $1/\gamma$ which practically does not depend on the average time t. This pattern is very similar for all momentum modes (cf. Ref. [45]).

The spectral function in energy-momentum representation is obtained by Fourier transformation with respect to the time difference $\Delta t = (t_1 - t_2)$ for each average time

t:

$$A(\mathbf{p}, p_0, t) = \int_{-\infty}^{\infty} d\Delta t \ \exp(i\Delta t\, p_0) A(\mathbf{p}, t_1 = t + \Delta t/2, t_2 = t - \Delta t/2). \tag{2.49}$$

Since the spectral function essentially shows a damped oscillation in $t_1 - t_2$, this implies that the Fourier transform (2.49) is of relativistic Breit-Wigner shape with a width γ that describes the decay in the relative time Δt. The spectral shape can be well approximated by

$$A(p_0, \mathbf{p}) \ = \frac{\gamma}{2\tilde{E}} \left(\frac{1}{(p_0 - \tilde{E})^2 + \gamma^2} - \frac{1}{(p_0 + \tilde{E})^2 + \gamma^2} \right) = \frac{2 p_0 \gamma}{(p_0^2 - \mathbf{p}^2 - M^2)^2 + 4\gamma^2 p_0^2} \tag{2.50}$$

with $\tilde{E}^2 = \mathbf{p}^2 + M^2 - \gamma^2$ where M denotes the mass of the degrees-of-freedom. We recall that this functional form is used in the DQPM model, too.

In this context it is illustrative to consider the case [38] of a massive scalar field coupled to an external fermion field ($\sim \partial_\mu \Phi(x) \bar{\Psi}(x) \gamma^\mu \Psi(x)$ with a vanishing three-current, i.e. the field equation

$$\left(\frac{\partial^2}{\partial t^2} - \triangle + M^2 + 2\gamma \frac{\partial}{\partial t} \right) \Phi(x) = 0, \tag{2.51}$$

where γ stands for the strength of the coupling (e.g. $g_s < \Psi^\dagger \Psi > /2$). (2.51) has the algebraic solution

$$\widetilde{G}(\mathbf{p}) = \frac{-1}{\omega^2 - \boldsymbol{p}^2 - M^2 + 2i\gamma\omega}, \tag{2.52}$$

which leads to the retarded Green-function $G_{\rm ret}$ obeying

$$G_{\rm ret}(x - y) = 0 \text{ for } x^0 - y^0 < 0 \tag{2.53}$$

by a 4-dimensional Fourier transformation of (2.52),

$$G_{\rm ret}(x) = \int \frac{d^4\tilde{p}}{(2\pi)^4} \ \widetilde{G}(\tilde{p}) \ \exp(-i\tilde{p}x). \tag{2.54}$$

We point out that $\Im \tilde{G}(\tilde{p})$ is given by the spectral function

$$\begin{aligned} A(\omega, \mathbf{p}) \ &= \frac{\gamma}{2\tilde{E}} \left(\frac{1}{(\omega - \tilde{E})^2 + \gamma^2} - \frac{1}{(\omega + \tilde{E})^2 + \gamma^2} \right) \\ &= \frac{2\omega\gamma}{(\omega^2 - \mathbf{p}^2 - M^2)^2 + 4\gamma^2\omega^2}. \end{aligned} \tag{2.55}$$

We recall, furthermore, that solutions of the Kadanoff-Baym equations [48] for Φ^4-theory in 2+1 dimensions [45] have lead to spectral functions that are very close to (2.55) also for strong coupling.

The equilibrium distribution

Now we introduce the energy and momentum-dependent distribution function $N(\mathbf{p}, p_0, \bar{t})$ at any system time $\bar{t}$ in case of scalar bosons by the definition

$$\begin{aligned} i\,G^{<}(\mathbf{p}, p_0, \bar{t}) &= A(\mathbf{p}, p_0, \bar{t})\;\; N(\mathbf{p}, p_0, \bar{t})\,, \\ i\,G^{>}(\mathbf{p}, p_0, \bar{t}) &= A(\mathbf{p}, p_0, \bar{t})\;[\,N(\mathbf{p}, p_0, \bar{t}) + 1\,]\,, \end{aligned} \tag{2.56}$$

since $G^{<}(\mathbf{p}, p_0, \bar{t})$ and $G^{>}(\mathbf{p}, p_0, \bar{t})$ are known from the integration of the Kadanoff-Baym equations as well as $A(\mathbf{p}, p_0, \bar{t})$. In equilibrium (at temperature T) the Green functions obey the Kubo-Martin-Schwinger relation (KMS) for all momenta $\mathbf{p}$,

$$G^{>}_{eq}(\mathbf{p}, p_0) \;=\; e^{p_0/T}\; G^{<}_{eq}(\mathbf{p}, p_0) \qquad\qquad \forall\;\; \mathbf{p}\,. \tag{2.57}$$

If there exists a conserved quantum number in the theory we have, furthermore, a contribution of the corresponding chemical potential in the exponential function which leads to a shift of arguments: $p_0/T \to (p_0 - \mu)/T$. In case of ϕ^4-theory, however, there is no conserved quantum number and thus the equilibrium state has $\mu = 0$.

From the KMS condition of the Green functions (2.57) the equilibrium form of the distribution function (2.56) at temperature T is obtained as

$$N_{eq}(\mathbf{p}, p_0) \;=\; N_{eq}(p_0) \;=\; \frac{1}{e^{p_0/T} - 1} \;=\; N_{bose}(p_0/T)\,, \tag{2.58}$$

from

$$\frac{G^{<}}{G^{>}} = e^{-p_0/T} = \frac{N_{eq}}{N_{eq}+1},$$

which is the well-known Bose distribution. As is obvious from Eq. (2.58) the equilibrium distribution can only be a function of energy p_0 and not of the momentum variable $\mathbf{p}$ in addition [45].

2.4.2 Derivation of the off-shell relativistic transport theory

Formal derivations of off-shell transport equations have been presented more than 50 years ago by Kadanoff and Baym [48] but actual solutions have barely been addressed [49, 50]. This Section is devoted to a brief derivation of generalized transport equations in first order gradient expansion including a generalized test-particle ansatz for the solution of the off-shell transport equation following Ref. [51].

The derivation of generalized transport equations starts by rewriting the Kadanoff-Baym equation for the Wightman functions in coordinate space ($x_1 = (t_1, \mathbf{x}_1), x_2 = (t_2, \mathbf{x}_2)$) (2.39) as

$$[\,\partial^{\mu}_{x_1}\partial^{x_1}_{\mu} + m^2 + \Sigma^{\delta}(x_1)\,]\;\; iG^{\lessgtr}(x_1, x_2) \;=\; i\,I_1^{\lessgtr}(x_1, x_2), \tag{2.59}$$

where the collision terms on the r.h.s. of Eq. (2.59) are given in $D = d + 1$ space-time dimensions by convolution integrals over coordinate-space selfenergies and Green

functions:

$$I_1^{\lessgtr}(x_1,x_2) = -\int_{t_0}^{t_1} d^D z \; [\Sigma^{>}(x_1,z) - \Sigma^{<}(x_1,z)]\, G^{\lessgtr}(z,x_2) + \int_{t_0}^{t_2} d^D z \Sigma^{\lessgtr}(x_1,z)\, [G^{>}(z,x_2) - G^{<}(z,x_2)]\,. \tag{2.60}$$

In the general case of an arbitrary (scalar) quantum field theory Σ^{δ} is the local (non-dissipative tadpole) part of the path self-energy while $\Sigma^{\lessgtr}$ resemble the non-local collisional self-energy contributions. In the representation (2.60) the integration boundaries are exclusively given for the time coordinates, while the integration over the spatial coordinates extends over the whole spatial volume from $-\infty$ to $+\infty$ in d dimensions.

Since transport theories are formulated in phase-space one changes to the Wigner representation via Fourier transformation with respect to the rapidly varying ('intrinsic') relative coordinate $\Delta x = x_1 - x_2$ and treats the system evolution in terms of the ('macroscopic') mean space-time coordinate $x = (x_1 + x_2)/2$ and the four-momentum $p = (p_0, \mathbf{p})$. The functions in Wigner space are obtained as

$$\bar{F}(p,x) \;=\; \int_{-\infty}^{\infty} d^D \Delta x \quad e^{+i\,\Delta x_\mu\, p^\mu} \quad F(x_1 = x + \Delta x/2,\, x_2 = x - \Delta x/2)\,. \tag{2.61}$$

For the formulation of transport theory in the Wigner representation we have to focus not only on the transformation properties of ordinary two-point functions as given in Eq. (2.61), but also of convolution integrals as appearing in Eq. (2.60). A convolution integral in D dimensions (for arbitrary functions F, G),

$$H(x_1,x_2) \;=\; \int_{-\infty}^{\infty} d^D z \; F(x_1,z)\; G(z,x_2) \tag{2.62}$$

transforms as

$$\begin{aligned} \bar{H}(p,x) \;&=\; \int_{-\infty}^{\infty} d^D \Delta x \quad e^{+i\,\Delta x_\mu\, p^\mu} \quad H(x_1,x_2) \\ &=\; \int_{-\infty}^{\infty} d^D \Delta x \quad e^{+i\,\Delta x_\mu\, p^\mu} \quad \int_{-\infty}^{\infty} d^D z \;\; F(x_1,z) \;\; G(z,x_2) \\ &=\; e^{+i\,\frac{1}{2}\,(\partial_p^\mu \cdot \partial_\mu^{x'} \,-\, \partial_x^\mu \cdot \partial_\mu^{p'})} \;\; \left[\; \bar{F}(p,x) \;\; \bar{G}(p',x')\right]\Big|_{x'=x,\, p'=p}\,. \end{aligned} \tag{2.63}$$

In accordance with the standard assumption of transport theory we assume that all functions only smoothly evolve in the mean space-time coordinates and thus restrict to first order derivatives. All terms proportional to second or higher order derivatives in the mean space-time coordinates (also mixed ones) will be dropped. Thus the Wigner transformed convolution integrals (2.62) are given in *first order gradient approximation*

by,

$$\bar{H}(p,x) \;=\; \bar{F}(p,x)\;\bar{G}(p,x) \;+\; i\,\frac{1}{2}\,\{\,\bar{F}(p,x)\,,\,\bar{G}(p,x)\,\} \;+\; \mathcal{O}(\partial_x^2)\,, \tag{2.64}$$

using the relativistic generalization of the Poisson bracket

$$\{\,\bar{F}(p,x)\,,\,\bar{G}(p,x)\,\} \;:=\; \partial_\mu^p\,\bar{F}(p,x)\cdot\partial_x^\mu\,\bar{G}(p,x) \;-\; \partial_x^\mu\,\bar{F}(p,x)\cdot\partial_\mu^p\,\bar{G}(p,x)\;. \tag{2.65}$$

In order to obtain the dynamics for the spectral functions within the approximate (first order gradient) scheme we start with the Dyson-Schwinger equations for the retarded and advanced Green functions in coordinate space (2.38). – Note that the convolution integrals in (2.38) extend over the whole space and time range in contrast to the equations of motion for the Wightman functions given in Eqs. (2.39) and (2.40)! – The further procedure consists in the following steps:

i) First we transform the above equations into the Wigner representation and apply the first order gradient approximation. In this limit the convolution integrals yield the product terms and the general Poisson bracket of the selfenergies and the Green functions $\{\,\Sigma^{R/A}, G^{R/A}\,\}$. We, further on, represent both equations in terms of real quantities by the decomposition of the retarded and advanced Green functions and selfenergies as

$$\begin{aligned} \bar{G}^{R/A} \;&=\; \Re\,\bar{G}^R \,\pm\, i\,\Im\,\bar{G}^R \;=\; \Re\,\bar{G}^R \,\mp\, i\,\bar{A}/2\,, \qquad & \bar{A} \;&=\; \mp\,2\,\Im\,\bar{G}^{R/A}\,, \\ \bar{\Sigma}^{R/A} \;&=\; \Re\,\bar{\Sigma}^R \,\pm\, i\,\Im\,\bar{\Sigma}^R \;=\; \Re\,\bar{\Sigma}^R \,\mp\, i\,\bar{\Gamma}/2\,, \qquad & \bar{\Gamma} \;&=\; \mp\,2\,\Im\,\bar{\Sigma}^{R/A}\,. \end{aligned} \tag{2.66}$$

We find that in Wigner space the real parts of the retarded and advanced Green functions and selfenergies are equal, while the imaginary parts have opposite sign and are proportional to the spectral function $\bar{A}$ and the width $\bar{\Gamma}$, respectively. The next step consists in

ii) the separation of the real part and the imaginary part of the two equations for the retarded and advanced Green functions, that have to be fulfilled independently. Thus we obtain four real-valued equations for the self-consistent retarded and advanced Green functions. In the last step

iii) we get simple relations by linear combination of these equations, i.e. by adding/subtracting the relevant equations.

This finally leads to two algebraic relations for the spectral function $\bar{A}$ and the real part of the retarded Green function $Re\,\bar{G}^R$ in terms of the width $\bar{\Gamma}$ and the real part of the retarded self-energy $Re\,\bar{\Sigma}^R$ as [51]:

$$[\,p_0^2 - \mathbf{p}^2 - m^2 - \bar{\Sigma}^\delta + \Re\,\bar{\Sigma}^R\,]\;\Re\,\bar{G}^R \;=\; 1 \;+\; \frac{1}{4}\,\bar{\Gamma}\;\bar{A}\,, \tag{2.67}$$

$$[\,p_0^2 - \mathbf{p}^2 - m^2 - \bar{\Sigma}^\delta + \Re\,\bar{\Sigma}^R\,]\;\bar{A} \;=\; \bar{\Gamma}\;\Re\,\bar{G}^R\,. \tag{2.68}$$

Note that all terms with first order gradients have disappeared in Eqs. (2.67) and (2.68). A first consequence of (2.68) is a direct relation between the real and the

imaginary parts of the retarded/advanced Green function, which reads (for $\bar{\Gamma} \neq 0$):

$$\Re\,\bar{G}^R \;=\; \frac{p_0^2 - \mathbf{p}^2 - m^2 - \bar{\Sigma}^\delta - \Re\,\bar{\Sigma}^R}{\bar{\Gamma}}\;\bar{A}\,. \tag{2.69}$$

Inserting Eq. (2.69) in Eq. (2.67) we end up with the following result for the spectral function and the real part of the retarded Green function

$$\bar{A} \;=\; \frac{\bar{\Gamma}}{[\,p_0^2 - \mathbf{p}^2 - m^2 - \bar{\Sigma}^\delta - \Re\,\bar{\Sigma}^R\,]^2 + \bar{\Gamma}^2/4} \;=\; \frac{\bar{\Gamma}}{\bar{M}^2 + \bar{\Gamma}^2/4}\,, \tag{2.70}$$

$$\Re\,\bar{G}^R \;=\; \frac{[\,p_0^2 - \mathbf{p}^2 - m^2 - \bar{\Sigma}^\delta - \Re\,\bar{\Sigma}^R\,]}{[\,p_0^2 - \mathbf{p}^2 - m^2 - \bar{\Sigma}^\delta - \Re\,\bar{\Sigma}^R\,]^2 + \bar{\Gamma}^2/4} \;=\; \frac{\bar{M}}{\bar{M}^2 + \bar{\Gamma}^2/4}\,, \tag{2.71}$$

where we have introduced the mass-function $\bar{M}(p,x)$ in Wigner space:

$$\bar{M}(p,x) \;=\; p_0^2 - \mathbf{p}^2 - m^2 - \bar{\Sigma}^\delta(x) - \Re\,\bar{\Sigma}^R(p,x)\,. \tag{2.72}$$

The spectral function (2.70) shows a typical Breit-Wigner shape with energy- and momentum-dependent self-energy terms. Although the above equations are purely algebraic solutions and contain no derivative terms, they are valid up to the first order in the gradients!

In addition, subtraction of the real parts and adding up the imaginary parts lead to the time evolution equations

$$p^\mu\,\partial_\mu^x\,\bar{A} \;=\; \frac{1}{2}\,\{\,\bar{\Sigma}^\delta + \Re\,\bar{\Sigma}^R\,,\,\bar{A}\,\} \;+\; \frac{1}{2}\,\{\,\bar{\Gamma}\,,\,\Re\,\bar{G}^R\,\}\,, \tag{2.73}$$

$$p^\mu\,\partial_\mu^x\,\Re\,\bar{G}^R \;=\; \frac{1}{2}\,\{\,\bar{\Sigma}^\delta + \Re\,\bar{\Sigma}^R\,,\,\Re\,\bar{G}^R\,\} \;-\; \frac{1}{8}\,\{\,\bar{\Gamma}\,,\,\bar{A}\,\}\,. \tag{2.74}$$

The Poisson bracket containing the mass-function $\bar{M}$ leads to the well-known drift operator $p^\mu\,\partial_\mu^x\,\bar{F}$ (for an arbitrary function $\bar{F}$), i.e.

$$\begin{aligned}\{\,\bar{M}\,,\,\bar{F}\,\} \;&=\; \{\,p_0^2 - \mathbf{p}^2 - m^2 - \bar{\Sigma}^\delta - \Re\,\bar{\Sigma}^R\,,\,\bar{F}\,\} \\ &=\; 2\,p^\mu\,\partial_\mu^x\,\bar{F} \;-\; \{\,\bar{\Sigma}^\delta + \Re\,\bar{\Sigma}^R\,,\,\bar{F}\,\}\,,\end{aligned} \tag{2.75}$$

such that the first order equations (2.73) and (2.74) can be written in a more comprehensive form as

$$\{\,\bar{M}\,,\,\bar{A}\,\} \;=\; \{\,\bar{\Gamma}\,,\,\Re\,\bar{G}^R\,\}\,, \tag{2.76}$$

$$\{\,\bar{M}\,,\,\Re\,\bar{G}^R\,\} \;=\; -\,\frac{1}{4}\,\{\,\bar{\Gamma}\,,\,\bar{A}\,\}\,. \tag{2.77}$$

When inserting (2.70) and (2.71) we find that these first order time evolution equations

are *solved* by the algebraic expressions. In this case the following relations hold [51]:

$$\{\,\bar{M}\,,\,\bar{A}\,\} \;=\; \{\,\bar{\Gamma}\,,\,\Re\,\bar{G}^R\,\} \;=\; \{\,\bar{M}\,,\,\bar{\Gamma}\,\}\;\frac{\bar{M}^2-\bar{\Gamma}^2/4}{[\,\bar{M}^2+\bar{\Gamma}^2/4\,]^2}\,, \tag{2.78}$$

$$\{\,\bar{M}\,,\,\Re\,\bar{G}^R\,\} \;=\; -\frac{1}{4}\,\{\,\bar{\Gamma}\,,\,\bar{A}\,\} \;=\; \{\,\bar{M}\,,\,\bar{\Gamma}\,\}\;\frac{\bar{M}\,\bar{\Gamma}/2}{[\,\bar{M}^2+\bar{\Gamma}^2/4\,]^2}\,. \tag{2.79}$$

Thus we have derived the proper structure of the spectral function (2.70) within the first-order gradient (or semiclassical) approximation. Together with the explicit form for the real part of the retarded Green function (2.71) we now have fixed the dynamics of the spectral properties, which is consistent up to first order in the gradients.

As a next step we rewrite the memory terms in the collision integrals (2.60) such that the time integrations extend from $-\infty$ to $+\infty$. In this respect we consider the initial time $t_0=-\infty$ whereas the upper time boundaries t_1, t_2 are taken into account by Θ-functions, i.e.

$$\begin{aligned} I_1^{\lessgtr}(x_1,x_2) \;=\;& -\int_{-\infty}^{\infty} d^Dx' \;\; \Theta(t_1-t')\;[\,\Sigma^{>}(x_1,x')-\Sigma^{<}(x_1,x')\,]\;\; G^{\lessgtr}(x',x_2) \\ & +\int_{-\infty}^{\infty} d^Dx' \;\; \Sigma^{\lessgtr}(x_1,x')\;\; \Theta(t_2-t')\;[\,G^{>}(x',x_2)-G^{<}(x',x_2)\,] \\ =\;& -\int_{-\infty}^{\infty} d^Dx' \;\; \Sigma^R(x_1,x')\,G^{\lessgtr}(x',x_2) \;+\; \Sigma^{\lessgtr}(x_1,x')\,G^A(x',x_2)\;. \end{aligned} \tag{2.80}$$

We now perform the analogous steps as invoked before for the retarded and advanced Dyson-Schwinger equations. We start with a first order gradient expansion of the Wigner transformed Kadanoff-Baym equation using (2.80) for the memory integrals. Again we separate the real and the imaginary parts in the resulting equation, which have to be satisfied independently. At the end of this procedure we obtain a generalized transport equation:

$$\begin{aligned} \underbrace{2\,p^\mu\,\partial_\mu^x\,i\bar{G}^{\lessgtr} \;-\; \{\,\bar{\Sigma}^\delta+\Re\,\bar{\Sigma}^R,\,i\bar{G}^{\lessgtr}\,\}}_{\{\,\bar{M}\,,\,i\bar{G}^{\lessgtr}\,\}} - \{\,i\bar{\Sigma}^{\lessgtr}\,,\,\Re\,\bar{G}^R\,\} \;&=\; i\bar{\Sigma}^{<}\,i\bar{G}^{>} \;-\; i\bar{\Sigma}^{>}\,i\bar{G}^{<} \\ - \{\,i\bar{\Sigma}^{\lessgtr}\,,\,\Re\,\bar{G}^R\,\} \;&=\; i\bar{\Sigma}^{<}\,i\bar{G}^{>} \;-\; i\bar{\Sigma}^{>}\,i\bar{G}^{<} \end{aligned} \tag{2.81}$$

as well as a generalized mass-shell equation

$$\underbrace{[\,p^2-m^2-\bar{\Sigma}^\delta-\Re\,\bar{\Sigma}^R\,]}_{\bar{M}}\;\; i\bar{G}^{\lessgtr} \;=\; i\bar{\Sigma}^{\lessgtr}\,\Re\,\bar{G}^R \;+\; \frac{1}{4}\,\{\,i\bar{\Sigma}^{>},\,i\bar{G}^{<}\,\} \;-\; \frac{1}{4}\,\{\,i\bar{\Sigma}^{<},\,i\bar{G}^{>}\,\} \tag{2.82}$$

with the mass-function $\bar{M}$ specified in Eq. (2.72). Since the Green function $G^{\lessgtr}(x_1,x_2)$ consists of an antisymmetric real part and a symmetric imaginary part with respect to the relative coordinate x_1-x_2, the Wigner transform of this function is purely imaginary. It is thus convenient to represent the Wightman functions in Wigner space by the real-valued quantities $i\bar{G}^{\lessgtr}(p,x)$. Since the collisional selfenergies obey the same

symmetry relations in coordinate space and in phase-space, they will be kept also as $i\bar{\Sigma}^{\lessgtr}(p,x)$ further on.

In the transport equation (2.81) one recognizes on the l.h.s. the drift term $p^\mu \partial_\mu^x i\bar{G}^{\lessgtr}$, as well as the Vlasov term with the local self-energy $\bar{\Sigma}^\delta$ and the real part of the retarded self-energy $Re\,\bar{\Sigma}^R$. On the other hand the r.h.s. represents the collision term with its typical 'gain and loss' structure. The loss term $i\bar{\Sigma}^> \; i\bar{G}^<$ (proportional to the Green function itself) describes the scattering out of a respective phase-space cell, whereas the gain term $i\bar{\Sigma}^< \; i\bar{G}^>$ takes into account scatterings into the actual cell. The last term on the l.h.s. $\{\, i\bar{\Sigma}^{\lessgtr}, \Re\bar{G}^R \,\}$ is very *peculiar* since it does not contain directly the distribution function $i\bar{G}^<$. This second Poisson bracket vanishes in the quasiparticle approximation and thus does not appear in the on-shell Boltzmann limit. As demonstrated in detail in Refs. [45, 48] the second Poisson bracket $\{\, i\bar{\Sigma}^{\lessgtr}, \Re\bar{G}^R \,\}$ governs the evolution of the off-shell dynamics for nonequilibrium systems.

Although the generalized transport equation (2.81) and the generalized mass-shell equation (2.82) have been derived from the same Kadanoff-Baym equation in a first order gradient expansion, both equations are not exactly equivalent [45, 52]. Instead, they deviate from each other by contributions of second gradient order, which are hidden in the term $\{\, i\bar{\Sigma}^{\lessgtr}, \Re\bar{G}^R \,\}$. A consistency, however, can be achieved by rewriting the self-energy $\bar{\Sigma}^<$ by $\bar{G}^< \cdot \bar{\Gamma}/\bar{A}$ in the Poisson bracket term $\{\bar{\Sigma}^<, \Re\bar{G}^R\}$. The generalized transport equation (2.81) then can be written in short-hand notation

$$\frac{1}{2}\,\bar{A}\,\bar{\Gamma}\,\left[\,\{\,\bar{M}\,,\; i\bar{G}^<\,\} \;-\; \frac{1}{\bar{\Gamma}}\,\{\,\bar{\Gamma}\,,\; \bar{M}\cdot i\bar{G}^<\,\}\right] \;=\; i\bar{\Sigma}^<\, i\bar{G}^> \;-\; i\bar{\Sigma}^>\, i\bar{G}^< \qquad (2.83)$$

with the mass-function $\bar{M}$ (2.72). The transport equation (2.83) within the Botermans-Malfliet (BM) form resolves the discrepancy between the generalized mass-shell equation (2.82) and the generalized transport equation in its original Kadanoff-Baym form (2.81).

2.4.3 Test-particle representation and numerical solution

The generalized transport equation (2.83) allows to extend the traditional on-shell transport approaches for which efficient numerical recipes have been set up. In order to obtain a practical solution to the transport equation (2.83) we use a test-particle ansatz for the Green function $G^<$, more specifically for the real and positive semi-definite quantity (using $\bar{G} = G, \bar{\Sigma} = \Sigma, \bar{\Gamma} = \Gamma$),

$$F(x,p) \;= i\,G^<(x,p) \;\sim\; \sum_{i=1}^{N} \delta^{(3)}(\mathbf{x} - \mathbf{X}_i(t)) \;\; \delta^{(3)}(\mathbf{p} - \mathbf{P}_i(t)) \;\; \delta(p_0 - \epsilon_i(t))\,, \quad (2.84)$$

where the sum over i describes the sum over all (properly normalized) testparticles. In the most general case (where the self energies depend on four-momentum P, time

t and the spatial coordinates $\mathbf{X}$) the equations of motion for the test-particles i read

$$\frac{d\vec{X}_i}{dt} = \frac{1}{1-C_{(i)}}\frac{1}{2\epsilon_i}\left[2\,\vec{P}_i + \vec{\nabla}_{P_i}\Re\Sigma^R_{(i)} + \frac{\epsilon_i^2 - \vec{P}_i^2 - M_0^2 - \Re\Sigma^R_{(i)}}{\Gamma_{(i)}}\vec{\nabla}_{P_i}\Gamma_{(i)}\right], \quad (2.85)$$

$$\frac{d\vec{P}_i}{dt} = -\frac{1}{1-C_{(i)}}\frac{1}{2\epsilon_i}\left[\vec{\nabla}_{X_i}\Re\Sigma^R_i + \frac{\epsilon_i^2 - \vec{P}_i^2 - M_0^2 - \Re\Sigma^R_{(i)}}{\Gamma_{(i)}}\vec{\nabla}_{X_i}\Gamma_{(i)}\right], \quad (2.86)$$

$$\frac{d\epsilon_i}{dt} = \frac{1}{1-C_{(i)}}\frac{1}{2\epsilon_i}\left[\frac{\partial\Re\Sigma^R_{(i)}}{\partial t} + \frac{\epsilon_i^2 - \vec{P}_i^2 - M_0^2 - Re\Sigma^R_{(i)}}{\Gamma_{(i)}}\frac{\partial\Gamma_{(i)}}{\partial t}\right], \quad (2.87)$$

where the notation $F_{(i)}$ implies that the function is taken at the coordinates of the test-particle, i.e. $F_{(i)} \equiv F(t, \mathbf{X}_i(t), \mathbf{P}_i(t), \epsilon_i(t))$.

In Eqs. (2.85-2.87), a common multiplication factor $(1 - C_{(i)})^{-1}$ appears, which contains the energy derivatives of the retarded self energy

$$C_{(i)} = \frac{1}{2\epsilon_i}\left[\frac{\partial}{\partial\epsilon_i}\Re\Sigma^R_{(i)} + \frac{\epsilon_i^2 - \vec{P}_i^2 - M_0^2 - Re\Sigma^R_{(i)}}{\Gamma_{(i)}}\frac{\partial}{\partial\epsilon_i}\Gamma_{(i)}\right]. \quad (2.88)$$

It yields a shift of the system time t to the 'eigentime' of particle i defined by $\tilde{t}_i = t/(1 - C_{(i)})$. As the reader immediately verifies, the derivatives with respect to the 'eigentime', i.e. $d\mathbf{X}_i/d\tilde{t}_i$, $d\mathbf{P}_i/d\tilde{t}_i$ and $d\epsilon_i/d\tilde{t}_i$ then emerge without this renormalization factor for each test-particle i when neglecting higher order time derivatives in line with the semiclassical approximation scheme. Note that the test-particle equations of motion (presented above) should not be applied for arbitrary selfenergies Σ^R and width Γ since the theory must obey micro-causality. This leads to severe constraints for the selfenergies [38, 53, 54].

Some limiting cases should be mentioned explicitly: In case of a momentum-independent 'width' $\Gamma(x)$ we take $M^2 = P^2 - Re\Sigma^R$ as an independent variable instead of P_0, which then fixes the energy (for given $\mathbf{P}$ and M^2) to

$$p_0^2 = \mathbf{p}^2 + M^2 + \Re\Sigma(x, \mathbf{p}, M^2)^R\,. \quad (2.89)$$

Eq. (2.87) then turns to ($\Delta M_i^2 = M_i^2 - M_0^2$)

$$\frac{d\Delta M_i^2}{dt} = \frac{\Delta M_i^2}{\Gamma_{(i)}}\frac{d\Gamma_{(i)}}{dt} \qquad \leftrightarrow \qquad \frac{d}{dt}\ln\left(\frac{\Delta M_i^2}{\Gamma_{(i)}}\right) = 0 \quad (2.90)$$

for the time evolution of the test-particle i in the invariant mass squared. In case of $\Gamma = const.$ the familiar equations of motion for test-particles in on-shell transport approaches are regained. We mention in passing that in the Parton-Hadron-String Dynamics (PHSD) transport approach [24, 28] the width of partonic degrees-of-freedom (so far) is taken as momentum independent such that the simple limit (2.90) applies (see below).

The time integration for the test-particle-equations of motion (cf. Eqs. (2.85), (2.86), (2.87)) is performed in the same way as in case of hadronic off-shell transport,

where (in view of the presently momentum-independent width γ) the simple relation (2.90) is employed. For the collisions of partons two variants are at our disposal: i) geometrical collision criteria as used in standard hadronic transport, ii) the in-cell method developed in Ref. [55]. The latter can easily be extended to describe $2 \leftrightarrow 3$ or $1 \leftrightarrow 3$ processes etc. in a covariant way [56] and is the better choice at high particle densities (cf. Refs. [57–59]). The hadronization is performed by integrating the rate equations (e.g. (2.17)) in space and time which are discretized on a four-dimensional grid by Δt and $\Delta V(t) = \Delta x(t)\Delta y(t)\Delta z(t)$. In beam direction we use an initial grid size $\Delta z = 1/\gamma_{cm}$ fm with γ_{cm} denoting the Lorentz-γ factor in the nucleon-nucleon center-of-mass system while in the transverse direction we use $\Delta x = \Delta y = 1$ fm. The grid size is increased dynamically during the transport calculation such that all particles are included on the actual grid. This practically implies that the grid boundary in beam direction approximately moves with the velocity of light. In each time step Δt and cell ΔV the integrals in (2.17) and the respective integrals for baryon (antibaryon) formation are evaluated by a sum over all (time-like) test-particles using (e.g. for the quark density)

$$\frac{1}{\Delta V}\int_{\Delta V} d^3x \int_{-\infty}^{\infty} \frac{d\omega_q}{2\pi}\, 2\omega_q \int_{-\infty}^{\infty} \frac{d^3p_q}{(2\pi)^3}\, \rho_q(\omega_q, p_q)\, \tilde{N}_q(x, p_q) = \frac{1}{\Delta V} \sum_{J_q \text{ in } \Delta V} 1 \;=\; \rho_q(\Delta V)\;, \tag{2.91}$$

where the sum over J_q implies a sum over all test-particles of type q (here quarks) in the local volume ΔV in each parallel run. In Eq. (2.91) $\tilde{N}$ denotes the occupation number in phase space which in thermal equilibrium is given by Bose- or Fermi-functions, respectively. In case of other operators like the scalar density, energy density etc. the number 1 in Eq. (2.91) has to be replaced by $\sqrt{P_J^2}/\omega_J$, ω_J etc. In order to obtain lower numerical fluctuations the integrals are averaged over the parallel runs (typically 50 at RHIC energies). For each individual test-particle (i.e. x_q and p_q fixed) the additional integrations in Eq. (2.17) give a probability for a hadronization process to happen; the actual event then is selected by a Monte Carlo algorithm. Energy-momentum conservation fixes the four-momentum p of the hadron produced and its space-time position x is determined by (2.17). The final state is either a hadron with flavor content fixed by the fusing quarks (and/or antiquarks) or by a string of invariant mass $\sqrt{s}$ (with the same flavor), if $\sqrt{s}$ is above 1.3 GeV for mesonic or above 1.5 GeV for baryonic quark content.

On the partonic side the following elastic and inelastic interactions are included in PHSD $qq \leftrightarrow qq$, $\bar{q}\bar{q} \leftrightarrow \bar{q}\bar{q}$, $gg \leftrightarrow gg$, $gg \leftrightarrow g$, $q\bar{q} \leftrightarrow g$ exploiting 'detailed-balance' with interaction rates again from the DQPM [24, 33]. Numerical tests of the parton dynamics with respect to conservation laws, interaction rates in and out-off equilibrium in a finite box with periodic boundary conditions have been presented in Ref. [15]. In fact, in Ref. [15] it was shown that the PHSD calculations 'in the box' give practically the same results in equilibrium as the DQPM.

For illustration of the parton dynamics we display the time evolution of the quark and gluon distributions in mass for a central Au + Au collision at $\sqrt{s_{NN}} = 200$ GeV in Fig. 2.3 which shows the number of 'particles' as a function of invariant mass M

and time t at midrapidity ($|y| \leq 1$). Note that by integration over M one obtains the number of quarks (+ antiquarks) $N_q(t)$ and gluons $N_g(t)$ in the rapidity interval $|y| \leq 1$ while dividing by $N_q(t)$ and $N_g(t)$, respectively, an estimate for the particle spectral functions is obtained. Note that the mass distributions displayed here are the product of the spectral functions and the occupation numbers in a restricted phase space. Due to a moderate variation of the partons pole mass and width with the scalar density ρ_s the shapes of the partonic mass distributions do not change very much in time. The average quark mass is about 0.5 GeV while the average gluon mass is only slightly less than 1 GeV. Note, however, that the width of the mass function - which reflects the actual interaction rate per parton - remains significant for all times up to hadronization.

2.5 Transport properties of the hot QCD matter

Apart from proton-proton, proton-nucleus or nucleus-nucleus collisions the PHSD approach can also be employed to study the properties of the interacting hadron/parton system in a finite box with periodic boundary conditions. To this aim the system is initialized by a homogeneous distribution of test-particles in a finite box with a momentum distribution close to a thermal one. Note that in PHSD the system cannot directly be initialized by a temperature and chemical potential since these 'Lagrange parameters' can only be determined when the system has reached a thermal and chemical equilibrium, i.e. when all forward and backward reaction rates have become equal.

The evaluation of transport coefficients can be performed in different ways and is usually performed by evaluating the temporal decay of correlators in the Kubo formalism [60, 61]. However, the results do not differ very much from those in the relaxation time approximation (RTA) which is easier to work out. We will thus focus on the latter approximation in this review for brevity.

2.5.1 Shear and bulk viscosities

The starting hypothesis of the relaxation time approximation is that the collision integral can be approximated (linearized) by

$$C[f] = -\frac{f - f^{eq}}{\tau} =: -\gamma(f - f^{eq}), \tag{2.92}$$

where τ is the relaxation time and f^{eq} the equilibrium distribution. In this approach it has been shown that the shear and bulk viscosities (without mean-field or potential effects) can be written as (e.g. in Ref. [62]):

$$\eta = \frac{1}{15T} \sum_a \int \frac{d^3p}{(2\pi)^3} \frac{|\mathbf{p}|^4}{E_a^2} \tau_a(E_a) f_a^{eq}(E_a/T), \tag{2.93}$$

$$\zeta = \frac{1}{9T} \sum_a \int \frac{d^3p}{(2\pi)^3} \frac{\tau_a(E_a)}{E_a^2} \left[(1 - 3v_s^2)E_a^2 - M_a^2\right] f_a^{eq}(E_a/T), \tag{2.94}$$

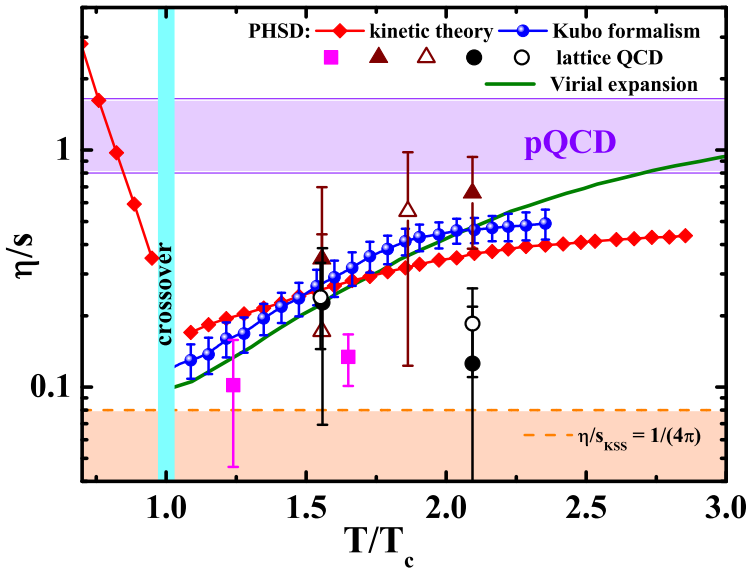

Figure 2.5: The shear viscosity to entropy density ratio η/s as a function of temperature of the system obtained by the PHSD simulations using different methods: the relaxation time approximation (red line+diamonds) and the Kubo formalism (blue line+dots). The other symbols denote lattice QCD data for pure $SU_c(3)$ gauge theory from different sources. The orange dashed line demonstrates the Kovtun-Son-Starinets bound $(\eta/s)_{KSS} = 1/(4\pi)$. For comparison, the results in the virial expansion approach (solid green line) [63] are shown as a function of temperature. The figure is taken from Ref. [16].

where the sum is over particles of different type a (in our case, $a = q, \bar{q}, g$). In the PHSD transport approach the relaxation time can be expressed in the following way:

$$\tau_a = \gamma_a^{-1}, \tag{2.95}$$

where γ_a is the width of particles of type $a = q, \bar{q}, g$, defined by Eq. (2.5). In our numerical simulation the volume V averaged shear and bulk viscosities assume the following expressions:

$$\eta = \frac{1}{15TV}\sum_{i=1}^{N}\frac{|\mathbf{p}_i|^4}{E_i^2}\gamma_i^{-1}, \quad \zeta = \frac{1}{9TV}\sum_{i=1}^{N}\frac{\gamma_i^{-1}}{E_i^2}\left[(1-3v_s^2)E_i^2 - M_i^2\right]^2, \tag{2.96}$$

where the speed of sound $v_s = v_s(T)$ is taken from the DQPM using

$$v_s^2 = \frac{\partial P}{\partial \epsilon}. \tag{2.97}$$

In Fig. 2.5 we present the shear viscosity to entropy density ratio η/s as a function of the temperature of the system extracted from the PHSD simulations in the box employing different methods: the relaxation time approximation (red line+diamonds) and the Kubo formalism (blue line+dots). For comparison, the results from the virial expansion approach (green line) [63] and lattice QCD data for pure $SU_c(3)$ gauge

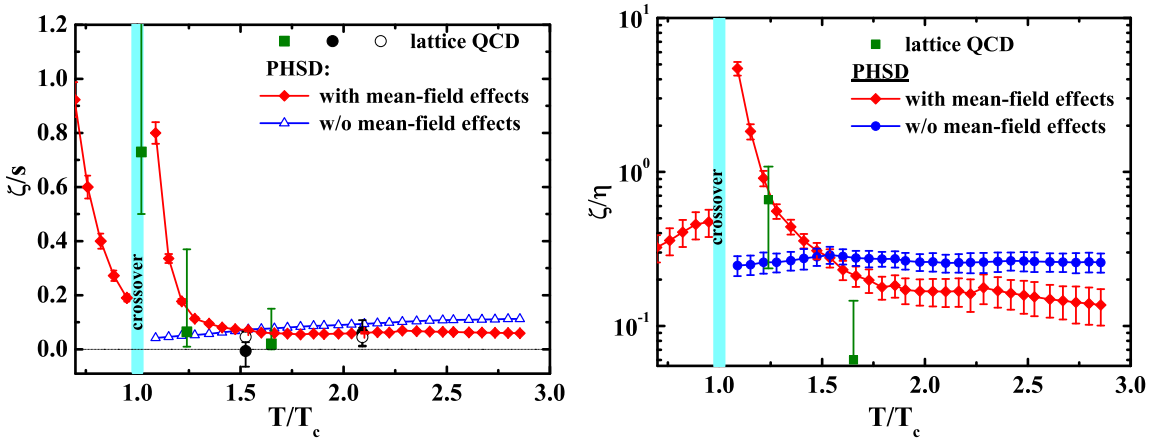

Figure 2.6: (l.h.s.) The bulk viscosity to entropy density ratio ζ/s as a function of temperature of the system extracted from the PHSD simulations in the box using the relaxation time approximation including mean-field effects (red line+diamonds) and without potential effects (blue line+open triangles). The other symbols show the available lattice QCD data from different sources (r.h.s.). The bulk to shear viscosity ratio as a function of temperature as obtained by the PHSD simulations in the box employing the relaxation time approximation including mean-field effects (red line+diamonds) and without potential effects (blue line+circles). Figures taken from Ref. [16].

theory are shown as a function of temperature, too.

In the absence of the chemical potential there should be no consideration of vector or tensor fields, only scalar fields. This affects the bulk viscosity, but not the shear viscosity. The expression for the bulk viscosity with potential effects is [62]

$$\zeta = \frac{1}{T}\sum_a \int \frac{d^3p}{(2\pi)^3}\frac{\tau_a(E_a)}{E_a^2} f_a^{eq}(E_a/T)\Big[\Big(\frac{1}{3}-v_s^2\Big)|\mathbf{p}|^2 - v_s^2\Big(M_a^2 - T^2\frac{d(M_a^2)}{d(T^2)}\Big)\Big]^2 \quad (2.98)$$

In the numerical simulation the volume averaged bulk viscosity with mean-field effects is calculated as

$$\zeta = \frac{1}{TV}\sum_{i=1}^{N}\frac{\gamma_i^{-1}}{E_i^2}\Big[\Big(\frac{1}{3}-v_s^2\Big)|\mathbf{p}|^2 - v_s^2\Big(M_i^2 - T^2\frac{d(M_i^2)}{d(T^2)}\Big)\Big]^2. \quad (2.99)$$

Using the DQPM expressions for masses of quarks and gluons (2.3) and (2.4), we can calculate the derivative $d(M^2)/d(T^2)$ as well as v_s^2 according to Eq. (2.97). For the actual results we refer the reader to Fig. 2.6 (l.h.s.), where the bulk viscosity to entropy density ratio ζ/s is presented as a function of temperature of the system extracted from the PHSD simulations in the box using the relaxation time approximation including mean-field effects (red line+diamonds) and without potential effects (blue line+open triangles). The r.h.s. of Fig. 2.6 shows the bulk to shear viscosity ratio as a function of temperature. Let us stress that contrary to η/s, the ratio ζ/s has a maximum close to T_c.

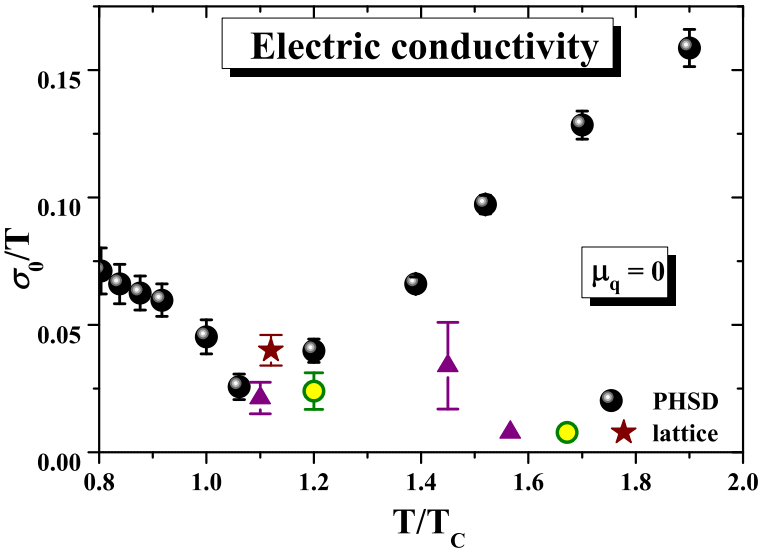

Figure 2.7: The dimensionless ratio of electric conductivity over temperature σ_0/T (2.102) as a function of the scaled temperature T/T_c for $\mu_q = 0$ in comparison to recent lattice QCD results. The figure is taken from Ref. [64].

2.5.2 Electric conductivity

Whereas shear and bulk viscosities of hot QCD matter at finite temperature T presently are roughly known, the electric conductivity $\sigma_0(T, \mu_q)$ is a further macroscopic quantity of interest since it controls the electromagnetic emissivity of the plasma. First results from lattice calculations on the electromagnetic correlator have provided results that varied by more than an order of magnitude. Furthermore, the conductivity dependence on the temperature T (for $T>T_c$) is widely unknown, too, as well as its dependence on μ_q. The electric conductivity σ_0 is also important for the creation of electromagnetic fields in ultra-relativistic nucleus-nucleus collisions from partonic degrees-of-freedom, since σ_0 specifies the imaginary part of the electromagnetic (retarded) propagator and leads to an exponential decay of the propagator in time $\sim\exp(-\sigma_0(t-t')/(\hbar c))$.

In order to include the effects from an external electric field $\mathbf{E}$ or magnetic field $\mathbf{B}$ on the charged degrees-of-freedom, the propagation of each charged test-particle j in the PHSD is performed with the additional Lorentz force in the equation of motion:

$$\frac{d}{dt}\mathbf{p}^j = q_j e(\mathbf{E} + \frac{\mathbf{p}^j}{E^j} \times \mathbf{B}), \tag{2.100}$$

where q_j denotes the fractional charge of the test-particle $(\pm 1/3, \pm 2/3)$ and E^j its energy. We recall that the external electric field will lead to an acceleration of positively and negatively charged particles in opposite directions while the particle scatterings/interactions will damp this acceleration and eventually lead to an equilibrium current if the external field is of moderate strength. The electric current density $j_z(t)$

(for an external electric field in z-direction) is calculated by

$$j_z(t) = \frac{1}{VN} \sum_{k=1}^{N} \sum_{j=1}^{N_k(t)} eq_j \frac{p_z^j(t)}{E_j(t)}. \tag{2.101}$$

The summation in (2.101) is carried out over N ensemble members $k = 1 \dots N$ while $N_k(t)$ denotes the time-dependent number of 'physical' (u, d, s) quarks and antiquarks that varies with time t due to the processes $q + \bar{q} \leftrightarrow g \leftrightarrow q' + \bar{q}'$ in a single member of the ensemble (run). The number of runs N is typically taken as a few hundred which gives a current $j_z(t)$ practically independent on the number of ensemble members N. We recall that (without external fields) each run of the ensemble is a micro-canonical simulation of the dynamics as inherent in the PHSD transport approach which strictly conserves the total four-momentum as well as all discrete conservation laws (e.g. net fermion number for each flavor etc.). A note of caution has to be given, since due to an external field we deal with an open system with increasing energy density (temperature) in time. Therefore we employ sufficiently small external fields eE_z, such that the energy increase during the computation time (in each run) stays below 2% and the increase in temperature below 1 MeV. For the details we refer the reader to Refs. [64, 65].

We find that for constant electric fields up to $eE_z = 50$ MeV/fm a stable electric current j_{eq} emerges that is $\sim E_z$. Accordingly, we obtain the conductivity $\sigma_0(T, \mu_q)$ from the ratio of the stationary current density j_{eq} and the electric field strength as

$$\frac{\sigma_0(T, \mu_q)}{T} = \frac{j_{eq}(T, \mu_q)}{E_z T} \ . \tag{2.102}$$

The results for the dimensionless ratio (2.102) at $\mu_q = 0$ are displayed in Fig. 2.7 by the full dots as a function of the scaled temperature T/T_c in comparison to recent lattice QCD results and suggest a minimum in the ratio $\sigma_0(T, \mu_q = 0)/T$ close to the critical temperature T_c followed by an approximate linear rise up to 2 T_c. The recent lQCD results are roughly compatible with the PHSD predictions.

Within PHSD (or the DQPM) also the dependence of the electrical conductivity on the quark chemical potential can be evaluated [65]. The numerical result could be fitted by a quadratic correction

$$\frac{\sigma_0(T, \mu_q)}{T} = \frac{\sigma_0(T, \mu_q = 0)}{T} \left(1 + a(T)\mu_q^2\right) \tag{2.103}$$

with $a(T) \approx 11.6$ GeV^{-2} for $T = 0.2$ GeV. This result comes about as follows: We recall that the electric conductivity of gases, liquids and solid states is described in the relaxation time approach by the Drude formula,

$$\sigma_0 = \frac{e^2 n_e \tau}{m_e^*}, \tag{2.104}$$

where n_e denotes the density of non-localized charges, τ is the relaxation time of the charge carriers in the medium and m_e^* their effective mass. This expression can be

directly computed for partonic degrees-of-freedom within the DQPM, which matches the quasiparticles properties to lattice QCD results in equilibrium. In the DQPM, the relaxation time for quarks/antiquarks is given by $\tau = 1/\gamma_q(T, \mu_q)$, where $\gamma_q(T, \mu_q)$ is the width of the quasiparticle spectral function (2.5). Furthermore, the spectral distribution for the mass of the quasiparticle has a finite pole mass $M_q(T, \mu_q)$ that is also fixed in the DQPM (2.4) as well as the density of $(u, \bar{u}, d, \bar{d}, s, \bar{s})$ quarks/antiquarks as a function of temperature T and chemical potential μ_q. The latter is given by an expression similar to the scalar density ρ_s in (2.9) but $\sqrt{p^2}$ replaced by ω. Thus, we obtain for the dimensionless ratio (2.102) the expression

$$\frac{\sigma_0(T, \mu_q)}{T} \approx \frac{2}{9} \frac{e^2 n_{q+\bar{q}}(T, \mu_q)}{M_q(T, \mu_q)\gamma_q(T, \mu_q)T}, \tag{2.105}$$

where $n_{q+\bar{q}}(T, \mu_q)$ denotes the total density of quarks and antiquarks and the pre-factor $2/9$ reflects the flavor averaged fractional quark charge squared $(\sum_f q_f^2)/3$. As found in Ref. [65] the DQPM results match well with the explicit PHSD calculations in the box also for finite μ_q since PHSD in equilibrium is a suitable transport realization of the DQPM. In the DQPM we have $\gamma_q(T, \mu_q) \approx \gamma_q(T, \mu_q = 0)$ and $M_q(T, \mu_q) \approx M_q(T, \mu_q = 0)$ for $\mu_q \leq 100$ MeV, however,

$$n_{q+\bar{q}}(T, \mu_q) \approx n_{q+\bar{q}}(T, \mu_q = 0) \left(1 + a(T)\mu_q^2\right) \tag{2.106}$$

with the same coefficient $a(T)$ as in Eq. (2.103).

The temperature dependence of the expansion coefficient $a(T)$ is found to be $\sim 1/T^2$ such that the ratio σ_0/T can be approximated by

$$\frac{\sigma_0(T, \mu_q)}{T} \approx \frac{\sigma_0(T, \mu_q = 0)}{T} \left(1 + c_{\sigma_0} \frac{\mu_q^2}{T^2}\right). \tag{2.107}$$

A fit to the coefficient c_{σ_0} in the temperature range 170 MeV$\leq T \leq$ 250 MeV gives $c_{\sigma_0} \approx 0.46$. This completes our study on the stationary electric conductivity σ_0 which can be well understood in its variation with T and μ_q within the DQPM or PHSD, respectively. We note that the conductivity σ_0 controls the electromagnetic emissivity of systems in thermal equilibrium at low photon momentum (see Section 5.3).

Chapter 3

Some of the evidence for the QGP production

3.1 Transverse momentum and rapidity spectra of hadrons

In this Section we employ the PHSD and HSD approaches to nucleus-nucleus collisions from $\sqrt{s_{NN}} = 5.5$ GeV to 2.76 TeV. Note that at RHIC or more specifically LHC energies other initial conditions (e.g. a color-glass condensate (CGC) [66, 67]) might be necessary. In the present work we discard such alternative initial conditions and explore to what extent the present initial conditions (described in Section 2.3) are compatible with differential measurements by the various collaborations at the SPS, RHIC or LHC. A more detailed comparison to results from CGC initial conditions in Pb-Pb collisions at $\sqrt{s_{NN}} = 2.76$ TeV may be found in Ref. [68].

Since PHSD is essentially fixed by lQCD data at $\mu_q = 0$ in thermal equilibrium in the partonic phase and by HSD in the hadronic phase, it is of interest how the PHSD approach compares to the HSD model (without explicit interacting partonic degrees-of-freedom) as well as to experimental data from the SPS, RHIC or LHC collaborations. We start with proton rapidity distributions at the SPS that demonstrate the amount of initial baryon stopping and thus control the energy transfer in relativistic nucleus-nucleus collisions. Since we find the HSD results for the proton rapidity distribution dN/dy to be identical with the PHSD results (within statistics) we will only compare PHSD calculations to data of the NA49 Collaboration. Accordingly, in Fig. 3.1 the proton rapidity distributions from PHSD are compared to the data from Ref. [69] for 7% central Pb+Pb collisions at 40 and 80 A·GeV (l.h.s.). The r.h.s. of Fig. 3.1 shows the net-proton dN/dy from PHSD for 158 A·GeV Pb+Pb collisions for different centrality bins (bin 0 – 0-5%; bin 1 – 5-12%; bin 2 – 12.5-23.5%; bin 3 – 23.5-33.5%; bin 4 – 33.5-43.5% and bin 5 – 43.5-78.5% central events) in comparison to the experimental data from Ref. [70]. In fact, the PHSD results demonstrate that the baryon stopping is reasonably reproduced in Pb+Pb collisions as a function of bombarding energy and centrality of the reaction at the SPS energies.

Since the energy is dominantly transferred to mesons, which asymptotically appear mostly as pions and kaons, we continue with pion and $K^{\pm}$ rapidity distributions for

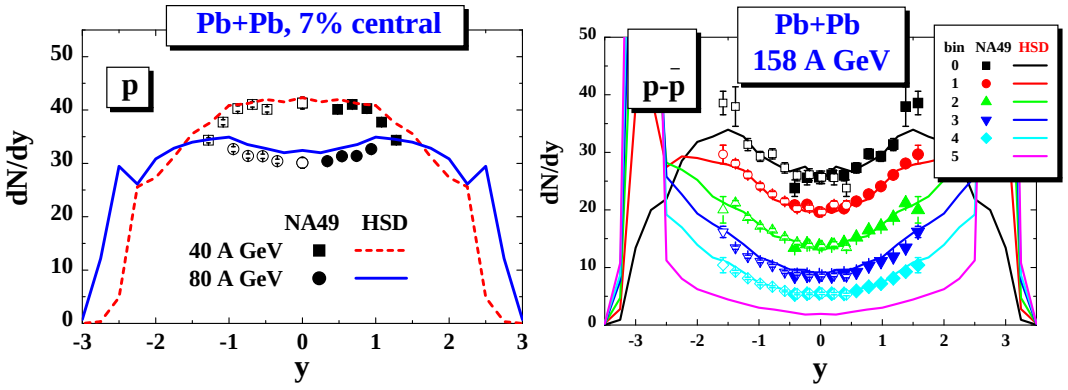

Figure 3.1: The proton rapidity distributions for central (7%) Pb+Pb collisions at 40 and 80 (l.h.s.) in comparison to the data from Ref. [69]. The r.h.s. of the figure presents the net-proton rapidity distribution at 158 A·GeV for different centrality bins (bin 0 – 0-5%; bin 1 – 5-12%; bin 2 – 12.5-23.5%; bin 3 – 23.5-33.5%; bin 4 – 33.5-43.5% and bin 5 – 43.5-78.5% central events) from PHSD (solid lines) in comparison to the experimental data from the NA49 Collaboration [70]. The figures are taken from Ref. [24].

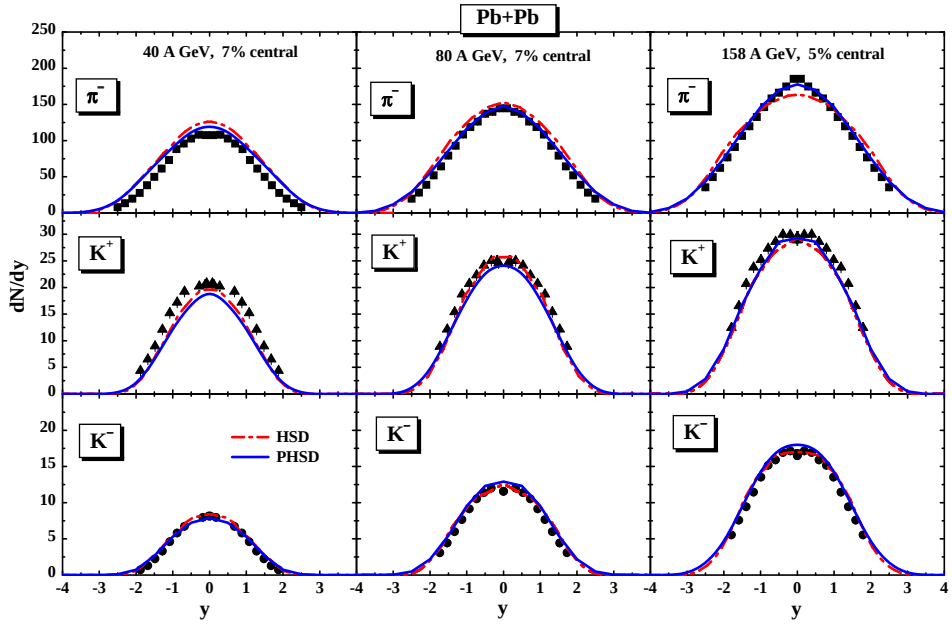

Figure 3.2: The rapidity distribution of π^- (upper part), K^+ (middle part) and K^- (lower part) for 7% or 5% central Pb+Pb collisions at 40, 80 and 158 A·GeV from PHSD (solid blue lines) in comparison to the distribution from HSD (dashed red lines) and the experimental data from the NA49 Collaboration [71, 72]. The figures are taken from Ref. [24].

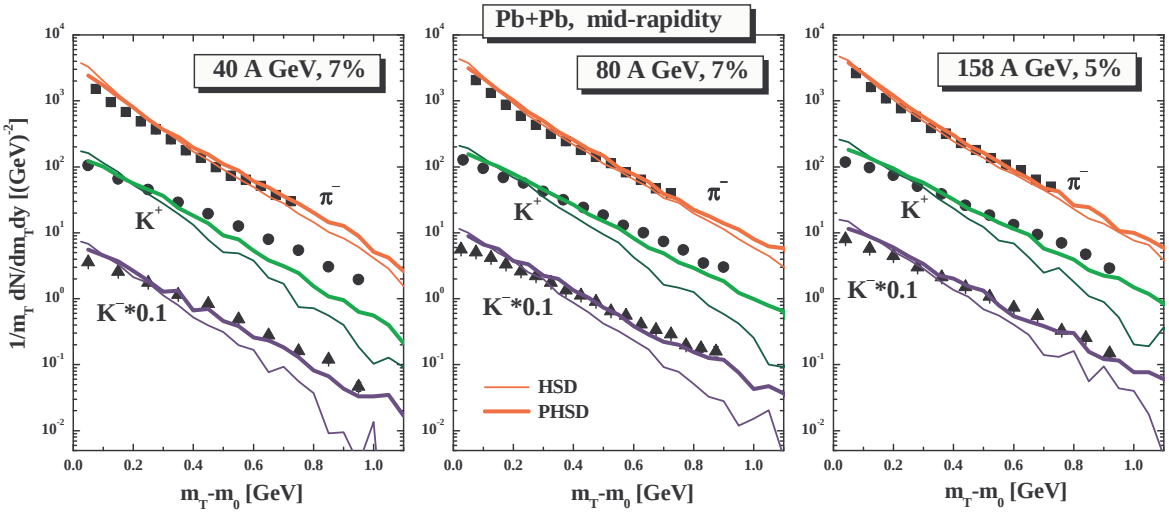

Figure 3.3: The π^-, K^+ and K^- transverse mass spectra for central Pb+Pb collisions at 40, 80 and 158 A·GeV from PHSD (thick solid lines) in comparison to the distributions from HSD (thin solid lines) and the experimental data from the NA49 Collaboration [71]. The figures are taken from Ref. [24].

7% central Pb+Pb collisions at 40 and 80 A·GeV and 5% central collisions at 158 A·GeV since here rather complete data sets are available from the experimental side [71]. The results from PHSD (solid blue lines) are compared in Fig. 3.2 with the corresponding results from HSD (dashed red lines) and the experimental data for the same centralities in comparison to the rapidity spectrum from HSD (dashed red lines) and the experimental data from the NA49 Collaboration [71]. The actual deviations between the PHSD and HSD spectra are very moderate; the π^- rapidity distribution is slightly squeezed in width (in PHSD) and shows a more pronounced peak at midrapidity (at 158 A·GeV) more in line with the data. Nevertheless, it becomes clear from Fig. 3.2 that the energy transfer - reflected in the light meson spectra - is rather well described by PHSD, which thus passes another test. Fig. 3.2 demonstrates that the longitudinal motion is rather well understood within the transport approaches and dominated by initial string formation and decay. Actually, there is no sizeable sensitivity of the rapidity spectra to an intermediate partonic phase. But what about the transverse degrees-of-freedom?

The answer to this question is offered in Fig. 3.3 where we show the transverse mass spectra of π^-, K^+ and K^- mesons for 7% central Pb+Pb collisions at 40 and 80 A·GeV and 5% central collisions at 158 A·GeV in comparison to the data of the NA49 Collaboration [71]. Here the slope of the π^- spectra is only slightly enhanced in PHSD (thick solid lines) relative to HSD (thin solid lines) which demonstrates that the pion transverse mass spectra also show no sizeable sensitivity to the partonic phase. However, the $K^\pm$ transverse mass spectra are substantially hardened with respect to the HSD calculations at all bombarding energies - i.e. PHSD is more in line with the data - and thus suggest that partonic effects are better visible in the strangeness degrees-of-freedom. The hardening of the kaon spectra can be traced back to parton-parton scattering as well as a larger collective acceleration of the partons in

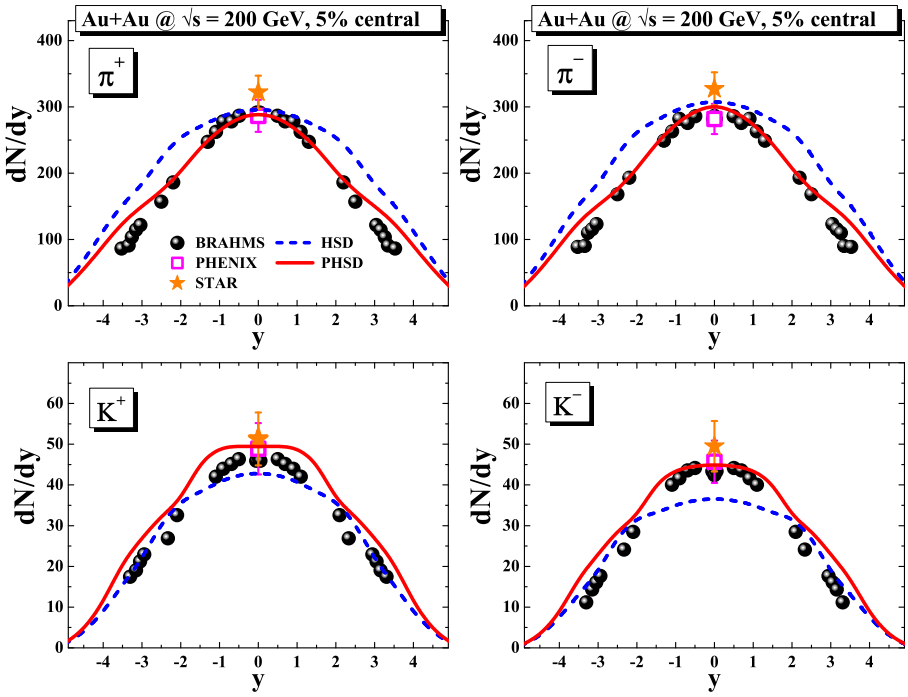

Figure 3.4: The rapidity distribution of π^+ (upper part, l.h.s.), K^+ (lower part, l.h.s.), π^- (upper part, r.h.s.) and K^- (lower part, r.h.s.) for 5% central Au+Au collisions at $\sqrt{s} = 200$ GeV from PHSD (solid lines) in comparison to the distribution from HSD (dashed lines) and the experimental data from the RHIC Collaborations [73, 74]. The figure is taken from Ref. [28].

the transverse direction due to the presence of repulsive fields for the partons. The enhancement of the spectral slope for kaons and anti-kaons in PHSD (due to collective partonic flow) shows up much clearer for the kaons due to their significantly larger mass (relative to pions). We recall that in Refs. [75, 76] the underestimation of the $K^{\pm}$ slope by HSD (and also UrQMD) had been suggested to be a signature for missing partonic degrees-of-freedom. In fact, the PHSD calculations support this early suggestion.

We continue with rapidity spectra from PHSD (solid red lines) for charged pions and kaons in 5% central Au+Au collisions at $\sqrt{s_{NN}} = 200$ GeV which are compared in Fig. 3.4 to the data from the RHIC Collaborations [73, 74] as well as to results from HSD (dashed blue lines). We find the rapidity distributions of the charged mesons to be slightly narrower than those from HSD and actually closer to the experimental data. Also note that there is slightly more production of $K^{\pm}$ mesons in PHSD than in HSD while the number of charged pions is slightly lower. The actual deviations between the PHSD and HSD spectra are not dramatic but more clearly visible than at SPS energies (cf. Figs. 8,9). Nevertheless, it becomes clear from Fig. 3.4 that the energy transfer in the nucleus-nucleus collision from initial nucleons to produced hadrons - reflected dominantly in the light meson spectra - is rather well described by PHSD also at the top RHIC energy.

Independent information on the active degrees-of-freedom is provided again by

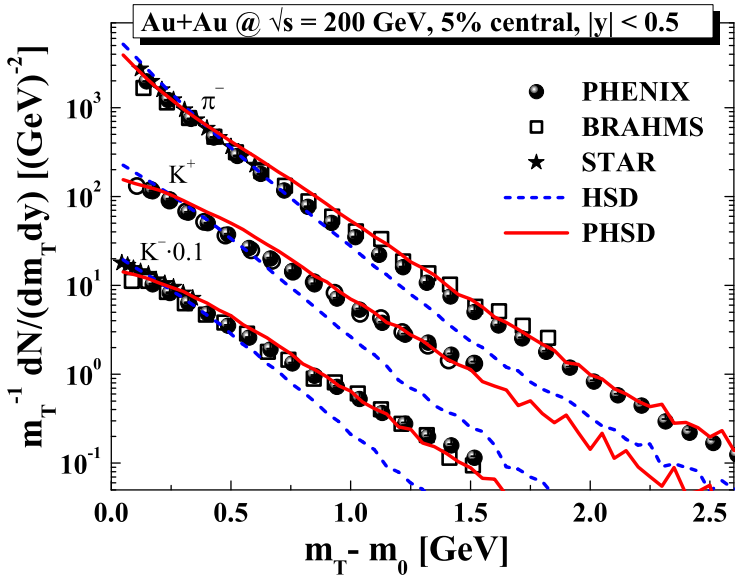

Figure 3.5: The π^-, K^+ and K^- transverse mass spectra for 5% central Au+Au collisions at $\sqrt{s} = 200$ GeV from PHSD (solid lines) in comparison to the distributions from HSD (dashed lines) and the experimental data from the BRAHMS, PHENIX and STAR Collaborations [73, 74]. The figure is taken from Ref. [28].

transverse mass spectra of the hadrons especially in central collisions. The PHSD results for the top RHIC energy are displayed in Fig. 3.5 where we show the transverse mass spectra of π^-, K^+ and K^- mesons for 5% central Au+Au collisions at $\sqrt{s} =$ 200 GeV in comparison to the data of the RHIC Collaborations [73, 74]. Here the slope of the π^- spectra is slightly enhanced in PHSD (solid red lines) relative to HSD (dashed blue lines) which demonstrates that the pion transverse mass spectra also show some sensitivity to the partonic phase (contrary to the SPS energy regime). The $K^\pm$ transverse mass spectra are substantially hardened with respect to the HSD calculations - i.e. PHSD is more in line with the data - and thus suggest that partonic effects are better visible in the strangeness degrees-of-freedom. The hardening of the kaon spectra can be traced back also to parton-parton scattering as well as a larger collective acceleration of the partons in the transverse direction due to the presence of the repulsive scalar mean-field for the partons.

We, finally, come to the presently highest laboratory energies for Pb+Pb collisions at the LHC, however, recall that the PHSD approach had to be properly upgraded to LHC energies with respect to a more recent PYTHIA 6.4 implementation [79]. The transition between the different PYTHIA regions in energy is smooth with respect to $\sqrt{s_{NN}}$ of the individual collisions such that PHSD preserves all results at lower bombarding energies where PYTHIA 6.4 does not work sufficiently well. In PYTHIA 6.4 we use the Innsbruck pp tune (390) which allows to describe reasonably the p-p collisions at $\sqrt{s_{NN}} = 7$ TeV in the framework of the PHSD transport approach (cf. Fig. 1 in Ref. [79]). The overall agreement with LHC experimental data for the distribution in the charged particle multiplicity N_{ch}, the charged particle pseudorapidity distri-

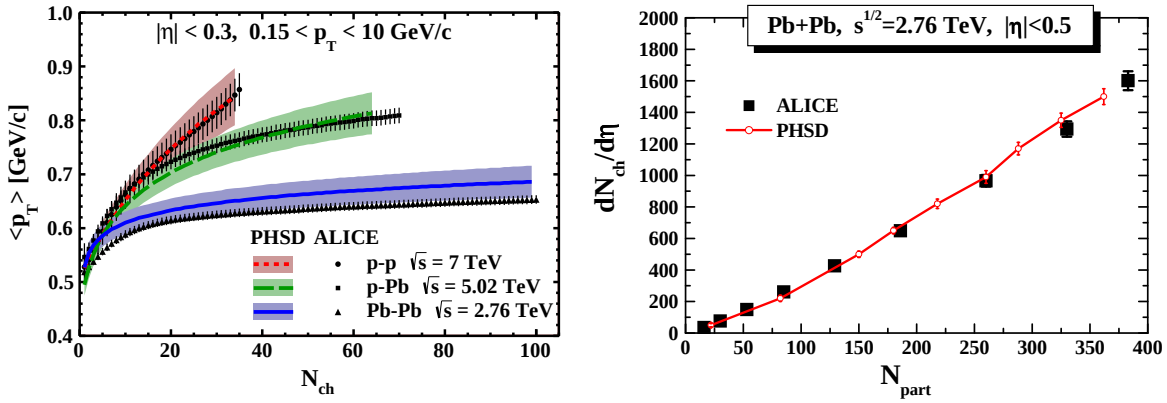

Figure 3.6: (l.h.s.) Mean p_T results for p-p, p-Pb and Pb-Pb collisions from the PHSD transport approach in comparison to the ALICE experimental data from Ref. [77] at midrapidity. Note the different invariant energies for p-p, p-Pb and Pb-Pb collisions. (r.h.s.) Pseudo-rapidity distribution of charged hadrons $dN_{ch}/d\eta$ at midrapidity as a function of the number of participants N_{part} from PHSD (solid line) in comparison to the data from the ALICE Collaboration [78] for Pb+Pb at $\sqrt{s_{NN}}$= 2.76 TeV. The figures are taken from Ref. [68].

bution, the transverse momentum p_T spectra and the correlation of the average p_T with the number of charged particles N_{ch} is satisfactory. Also a variety of observables from p-Pb collisions at $\sqrt{s_{NN}} = 5.02$ TeV compare quite well with the experimental observations [79].

One might ask whether the PHSD approach still works at LHC energies for nucleus-nucleus (Pb+Pb) collisions although the invariant energy is higher by about a factor of 13.8 compared to the top RHIC energy. In Fig. 3.6 (l.h.s.) we compare the average p_T (at midrapidity) as a function of charged multiplicity N_{ch} in p+p reactions at $\sqrt{s_{NN}} = 7$ TeV, p+Pb collisions at $\sqrt{s_{NN}} = 5.02$ TeV and Pb+Pb collisions at $\sqrt{s_{NN}} =$ 2.76 TeV from the PHSD to the experimental data from Ref. [77]. Note that for low multiplicities ($N_{ch} < 5$) the mean p_T is almost independent on energy (see also Ref. [77]) which in PHSD can be traced back to the fact that (for the acceptance $|\eta| \leq$ 0.3, $0.15 \leq p_T \leq 10$ GeV/c) only events with one or two binary collisions N_{bin} are selected for all systems. Actually, the correlation $< p_T > (N_{ch})$ only weakly depends on $\sqrt{s_{NN}}$ for pp reactions at these LHC energies, however, when plotting $p_T(N_{ch})$ on an event-by-event basis, large fluctuations in p_T or N_{ch} are obtained within PHSD. The same holds true for p+Pb and Pb+Pb reactions where a fixed N_{ch} can be obtained by reactions with a varying number of binary collisions N_{bin}. Each of these binary reactions then has a low N_{ch} and $< p_T >$, respectively. The ensemble average finally leads to the average correlation shown in Fig. 3.6 (l.h.s.). Nevertheless, the agreement between data and calculations (within the statistical accuracy) is encouraging. Note again that only very peripheral Pb+Pb collisions are probed for $N_{ch} < 100$.

In order to shed some light on the centrality dependence of charged particle production we display in Fig. 3.6 (r.h.s.) the results for the pseudo-rapidity distribution $dN_c/d\eta$ at midrapidity from the default PHSD calculations in comparison to the ALICE data as a function of the number of participants N_{part} that has been determined

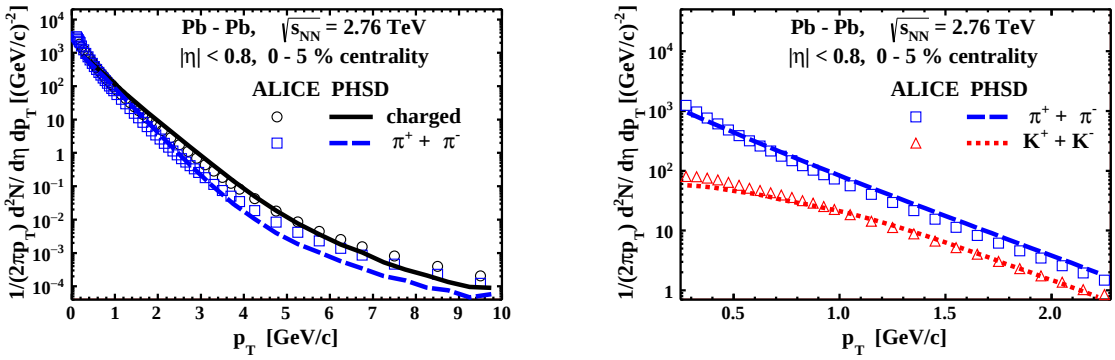

Figure 3.7: (l.h.s.) Transverse momentum spectra from PHSD in comparison to the results of the ALICE Collaboration for all charged particles [80, 81] (solid line) as well as for charged pions [82] (dashed line). (r.h.s.) Transverse momentum spectra from PHSD for $p_T \leq 2$ GeV/c in comparison to the results of the ALICE Collaboration [80–82] for pions and kaons. The figures are taken from Ref. [68].

dynamically in the PHSD calculations. A quite acceptable agreement is seen, suggesting that the bulk parton dynamics is not much different at top RHIC and LHC energies.

We continue with the transverse momentum spectra for central Pb+Pb reactions at $\sqrt{s_{NN}} = 2.76$ TeV (0-5% centrality) which are compared in Fig. 3.7 with results from the ALICE Collaboration for all charged particles [80, 81] (PHSD: black solid line) as well as for charged pions [82] (PHSD: dashed blue line). Note that except for the upgrade in the PYTHIA version no additional parameters or changes have been introduced in the PHSD. In this respect the approximate reproduction of the midrapidity p_T spectra for central collisions over 7 orders of magnitude in Fig. 3.7 (l.h.s.) is quite remarkable. A closer look at the low momentum spectra is offered in Fig. 3.7 (r.h.s.) where the PHSD spectra for pions and kaons are compared to results of the ALICE Collaboration [80–82] (symbols).

In summarizing, the partonic phase in PHSD at the top RHIC energy and at LHC leads to a narrowing of the longitudinal momentum distribution, a reduction of pion production, a slight enhancement of kaon production and to a hardening of their transverse mass spectra relative to HSD (closer to the data). These effects are clearly visible especially in the transverse degrees-of-freedom and are more pronounced than at SPS energies due to the larger space-time region of the partonic phase.

3.2 Collective flow of hadrons

Of additional interest are the collective properties of the strongly interacting system which are explored experimentally by the azimuthal momentum distribution of particles in a fixed rapidity interval. The azimuthal momentum distribution of the emitted particles is commonly expressed in the form of a Fourier series as

$$E\frac{d^3N}{d^3p} = \frac{d^2N}{2\pi p_T dp_T dy}\left(1+\sum_{n=1}^{\infty} 2v_n(p_T)\cos[n(\psi-\Psi_n)]\right), \tag{3.1}$$

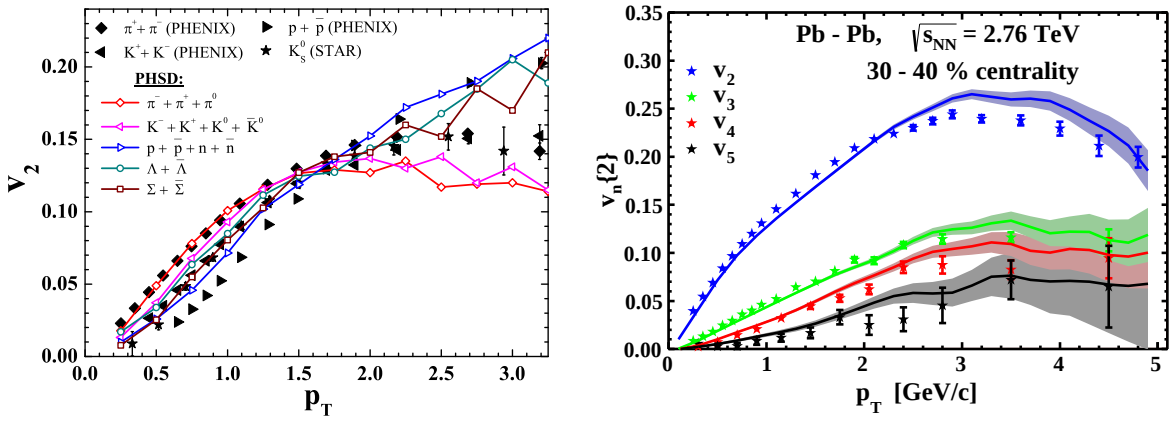

Figure 3.8: (l.h.s.) The hadron elliptic flow v_2 for inclusive Au+Au collisions as a function of the transverse momentum p_T (in GeV) for different hadrons in comparison to the data from the STAR [83, 84] and PHENIX Collaborations [85] within the same rapidity cuts. (r.h.s.) The flow coefficients v_2, v_3, v_4 and v_5 of all charged particles as a function of p_T for the centralities 30-40% in case of Pb-Pb collisions at $\sqrt{s_{NN}} =$ 2.76 TeV. The ALICE data have been adopted from Ref. [78]. The figures are taken from Refs. [28, 68].

where v_n is the magnitude of the n'th order harmonic term relative to the angle of the initial-state spatial plane of symmetry Ψ_n and $p = (E, \vec{p})$ is the four-momentum of the particle under consideration. We here focus on the coefficients v_2, v_3 and v_4 which implies that we have to perform event-by-event calculations in order to catch the initial fluctuations in the shape of the interaction zone and the event plane Ψ_{EP}; e. g., we calculate the triangular flow v_3 with respect to Ψ_3 as $v_3\{\Psi_3\} = \langle\cos(3[\psi - \Psi_3])\rangle/\mathrm{Res}(\Psi_3)$. The event plane angle Ψ_3 and its resolution $\mathrm{Res}(\Psi_3)$ are evaluated as described in Ref. [86] via the two-sub-events method [87, 88].

We here briefly summarize the main results. Fig. 3.8 (l.h.s.) shows the final hadron v_2 versus the transverse momentum p_T for different particle species at the top RHIC energy in comparison to the data from the STAR [83, 84] and PHENIX Collaborations [85]. We observe a mass separation in p_T as well as a separation in mesons and baryons for $p_T > 2$ GeV roughly in line with data. The elliptic flow of mesons is slightly underestimated for $p_T > 2$ GeV in PHSD which is opposite to ideal hydrodynamics which overestimates v_2 at high transverse momenta. On the other hand, the proton (and antiproton) elliptic flow is slightly overestimated at low $p_T <$ 1.5 GeV. We note in passing that also the momentum integrated results for v_2 as a function of the number of participating nucleons N_{part} from PHSD compare well to the data from Ref. [89]. In contrast, the HSD results clearly underestimate the elliptic flow as pointed out before [90]. The relative enhancement of v_2 in PHSD with respect to HSD can be traced back to the high interaction rate in the partonic phase and to the repulsive scalar mean-field for partons; the PHSD calculations without mean-fields only give a small enhancement for the elliptic flow relative to HSD.

Stepping up in energy of the collision to $\sqrt{s_{NN}} = 2.76$ TeV reached at the LHC, the PHSD results for the flow coefficients v_2, v_3, v_4 and v_5 of all charged particles are shown

in Fig. 3.8 as a function of p_T for the centralities 30-40% in Pb+Pb collisions (r.h.s.) in comparison to the ALICE data from Ref. [78]. The PHSD results for $v_2(p_T), v_3(p_T)$ and $v_4(p_T)$ describe the data reasonably up to about 3.5 GeV/c, whereas at higher transverse momenta the statistics of the present calculations is insufficient to draw robust conclusions. This also holds for the flow coefficient v_5 which still is in line with the data within error bars. It is quite remarkable that the collective behavior is reproduced in the PHSD approach not only for the semi-central collisions $(30-40$ %) but also for $0-5\%$ central collisions, which are sensitive to the initial state fluctuations (see Ref. [68]).

These tests indicate that the 'soft' physics at LHC in central A-A reactions is very similar to the top RHIC energy regime although the invariant energy is higher by more than an order of magnitude. Furthermore, the PHSD approach seems to work from lower SPS energies up to LHC energies for p-p, p-A as well as A-A collisions, i.e. over a range of more than two orders in $\sqrt{s_{NN}}$. Note that for even lower bombarding energies the PHSD approach merges to the HSD model which has been successfully tested from the SIS to the SPS energy regime in the past [1, 91, 92]. Since the bulk dynamics is well described in PHSD in comparison to experimental data in a wide dynamical range we may continue with the electromagnetic emissivity of the reactions which (in principle) does not employ any new parameter.

3.3 Energy-density evolution in heavy-ion collisions

The HSD approach [1] provides the space-time geometry of nucleus-nucleus reactions and a rather reliable estimate for the local energy densities achieved, since the production of secondary particles with light and a single strange quark/antiquark is described well from SIS to RHIC energies [93, 94] (see also Section 5). In the transport approach the local energy density is calculated from the energy-momentum tensor $T_{\mu\nu}(x)$ for all space-time points x in the local rest frame: $\varepsilon(x) = T^{loc}_{00}(x)$, where $T^{loc}_{00}(x)$ is calculated from $T_{\mu\nu}(x)$ by a Lorentz boost to the local rest frame. In order to exclude contributions to $T_{\mu\nu}$ from noninteracting nucleons in the initial phase all nucleons without prior interactions are discarded in the rapidity intervals $[y_{tar} - 0.4, y_{tar} + 0.4]$ and $[y_{pro} - 0.4, y_{pro} + 0.4]$ where y_{tar} and y_{pro} denote projectile and target rapidity, respectively. Note that the initial rapidity distributions of projectile and target nucleons are smeared out due to Fermi motion by about $\Delta y \approx \pm 0.4$. Some comments on the choice of the grid in space-time are in order here: In the actual calculation (for Au+Au collisions) the initial grid has a dimension of 1 fm $\times$ 1 fm $\times$ $1/\gamma_{cm}$ fm, where γ_{cm} denotes the Lorentz γ-factor in the nucleon-nucleon center-of-mass system. After the time of maximum overlap t_m of the nuclei the grid-size in beam direction $\Delta z_0 = 1/\gamma_{cm}$ [fm] is increased linearly in time as $\Delta z = \Delta z_0 + a(t - t_m)$, where the parameter a is chosen in a way to keep the particle number in the local cells of volume $\Delta V(t) = \Delta x \Delta y \Delta z(t)$ roughly constant during the longitudinal expansion of the system. In this way local fluctuations of the energy density $\varepsilon(x)$ due to fluctuations in the particle number are kept low. Furthermore, the time-step is taken as $\Delta t = 0.2\Delta z(t)$ and increases in time in analogy to $\Delta z(t)$. This choice provides a high resolution in space and time for the

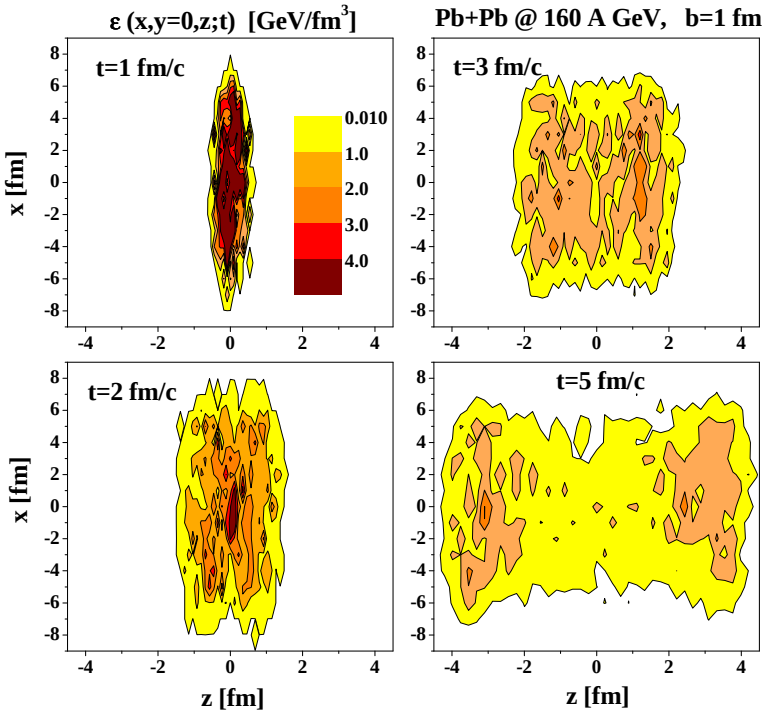

Figure 3.9: The energy density $\varepsilon(x, y = 0, z; t)$ from HSD for a Pb+Pb collision at 160 A·GeV and impact parameter $b = 1$ fm in terms of contour lines (0.01, 1, 2, 3, 4 GeV/fm^3) for times of 1, 2, 3 and 5 fm/c (from contact). Note that noninteracting nucleons have been discarded in the actual calculation of the energy-momentum tensor. The figure is taken from Ref. [95].

initial phase and keeps track of the relevant dynamics throughout the entire collision history.

SPS energies

As a first example we display in Fig. 3.9 the energy density $\varepsilon(x, y = 0, z; t)$ for a Pb+Pb collision at 160 A·GeV and impact parameter $b = 1$ fm in terms of contour lines for times of 1, 2, 3 and 5 fm/c (from contact). It is clearly seen that energy densities above 4 GeV/fm^3 are reached in the early overlap phase of the reaction and that $\varepsilon(x)$ drops within a few fm/c below 1 GeV/fm^3 in the center of the grid. On the other hand the energy density in the region of the leading particles - moving almost with the velocity of light - stays above 1 GeV/fm^3 due to Lorentz time dilatation since the time t here is measured in the nucleon-nucleon center-of-mass system. Note that in the local rest frame of the leading particles the eigentime τ is roughly given by $\tau \approx t/\gamma_{cm}$ with $\gamma_{cm} \approx 9.3$ (at 160 A·GeV).

Another view of the space time evolution of the energy density is given in Fig. 3.10 where we display $\varepsilon(x = 0, y = 0, z; t)$ for the same system as in Fig. 3.9 on a linear scale. The contact time of the two Pb nuclei here is 2 fm/c and the overlap phase of the Lorentz contracted nuclei is identified by a sharp peak in space-time which is essentially given by the diameter of the nuclei divided by γ_{cm}. As noted before, the energy density in the center of the reaction volume ($z \approx 0$) drops fast below 1 GeV/fm^3

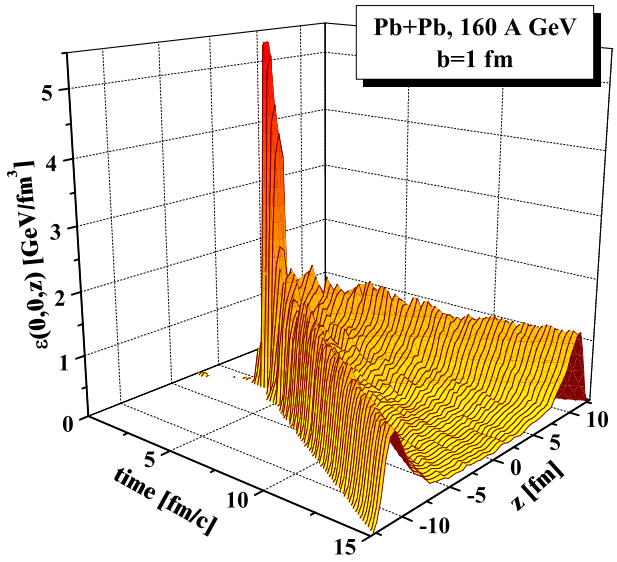

Figure 3.10: The energy density $\varepsilon(x=0, y=0, z; t)$ from HSD for a Pb+Pb collision at 160 A·GeV and impact parameter $b = 1$ fm on a linear scale. Note that noninteracting nucleons have been discarded in the actual calculation of the energy-momentum tensor such that $\varepsilon(x) \neq 0$ only after contact of the two Pb nuclei which is ~ 2 fm/c. The figure is taken from Ref. [95].

whereas the ridges close to the light-cone basically stem from the leading ends of the strings formed in the early nucleon-nucleon collisions. In these space-time regions all reaction rates are reduced by the factor $\sim 1/\gamma_{cm}$ such that the transport calculations have to be carried out to large times of several hundred fm/c in order to catch the dynamics and decays in these regions. In the central regime, however, all interaction rates vanish after about 15 fm/c. Since the $c, \bar{c}$ pairs are produced dominantly at midrapidity with a small spread in rapidity ($\sigma_y \approx 0.8$ at 160 A·GeV) it is the central region that is of primary interest for this study.

RHIC energies

The energy density $\varepsilon(\mathbf{r}; t)$ becomes very high in a central Au+Au collision at $\sqrt{s} =$ 200 GeV as shown in Fig. 3.11 (in analogy to Fig. 3.10 for the top SPS energies). Fig. 3.11 shows the space-time evolution of the energy density $\varepsilon(x=0, y=0, z; t)$ for a Au+Au collision at 21300 AGeV or $\sqrt{s} = 200$ GeV. It is clearly seen that energy densities above 16 GeV/fm^3 are reached in the early overlap phase of the reaction and that $\varepsilon(x)$ drops after about 6 fm/c (starting from contact) below 1 GeV/fm^3 in the center of the grid. On the other hand the energy density in the region of the leading particles - moving almost with the velocity of light - stays above 1 GeV/fm^3 due to

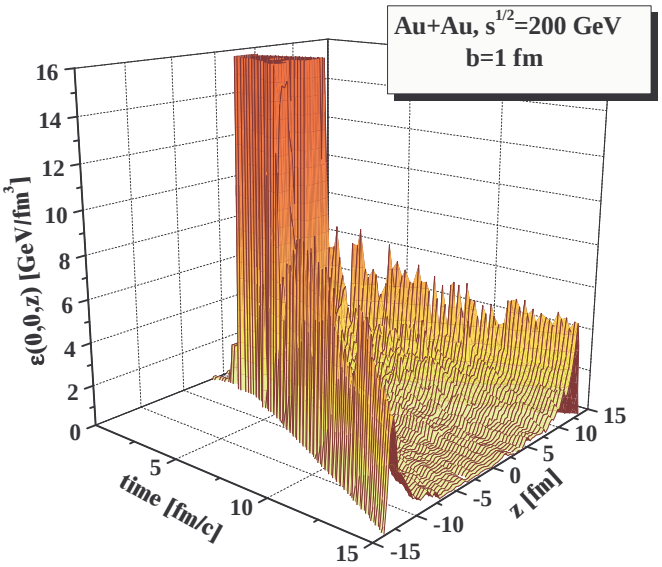

Figure 3.11: The energy density $\varepsilon(x = 0, y = 0, z; t)$ from HSD for a central Au+Au collision at $\sqrt{s} = 200$ GeV. The time t is given in the nucleon-nucleon center-of-mass system. The figure is taken from Ref. [96].

Lorentz time dilatation since the time t in the transport calculation is measured in the nucleon-nucleon center-of-mass system. As seen from Fig. 3.11, the energy density in the local rest frame is a rapidly changing function of time in nucleus-nucleus collisions. For orientation let us quote the relevant time scales (in the cms reference frame):

– The $c\bar{c}$ formation time $\tau_c \approx 1/M_\perp$ is about 0.05 fm/c for a transverse mass of 4 GeV; the transient time for a central Au+Au collision at $\sqrt{s} = 200$ GeV is $t_r \approx 2R_A/\gamma_{cm} \approx 0.13$ fm/c. According to standard assumptions, the $c\bar{c}$ pairs are produced in the initial hard NN collisions dominantly by gluon fusion in the time period t_r. In fact, the formation time τ_c is significantly smaller than t_r, which implies that the c or $\bar{c}$ quarks may interact with the impinging nucleons of the projectile or target for times $t \leq t_r$.

– Using the Bjorken estimate for the energy density and employing the time-scale $t_r = 0.13$ fm/c, the energy density – after the nuclei have punched through each other – amounts to about $5/0.13 > 30$ GeV/fm^3 (as quoted also in the HSD calculations in Refs. [96, 97]). Even when adding the $c\bar{c}$ formation time, this gives an energy density $\sim 5/0.18 \approx 28$ GeV/fm^3. So the numbers in Fig. 3.11 agree with transparent and simple estimates and illustrate the high initial densities after $c\bar{c}$ production from primary interactions.

The energy densities quoted above are considerably different from the estimate

$$\tau \cdot \epsilon_{Bj} = \frac{< E_T > \frac{dN}{d\eta}}{\pi R_T^2}, \tag{3.2}$$

where $< E_T >$ is the average transverse energy per particle, $dN/d\eta$ the number of particles per unit of pseudorapidity, and τ a formation time parameter often used

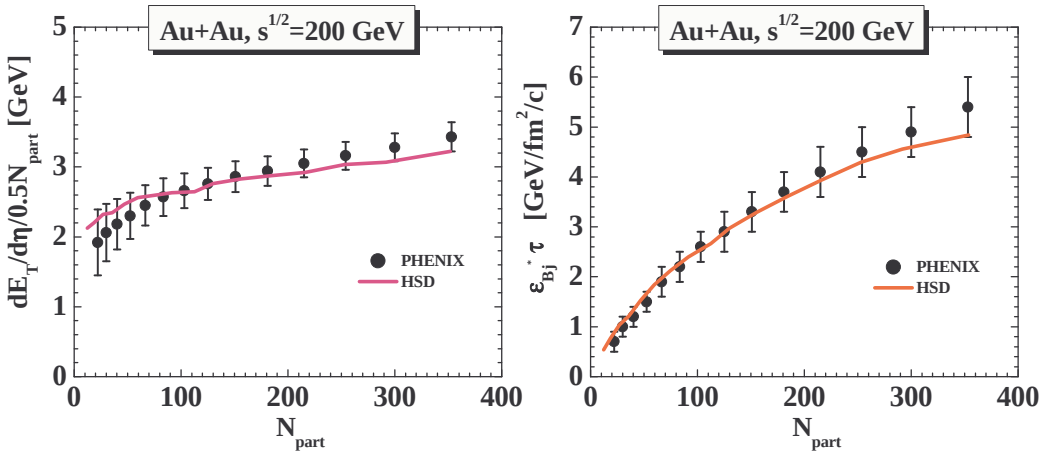

Figure 3.12: Left part: The transverse energy E_T per pseudorapidity interval $d\eta$ divided by the number of participant pairs ($0.5N_{part}$) from HSD (solid line) in comparison to the PHENIX data (dots) [98]. Right part: The Bjorken energy density $\varepsilon_{Bj} \cdot \tau$ from HSD (solid line) for Au+Au collisions at $\sqrt{s} = 200$ GeV in comparison to the PHENIX data (dots) [98]. The figure is taken from Ref. [96].

as $\tau = 1$ fm/c. Furthermore, πR_T^2 denotes the overlap area for the corresponding centrality. Is is important to point out that the estimate (3.2) is only well defined for the product $\tau \cdot \epsilon_{Bj}$! The question naturally arises, if the transport calculations follow the corresponding experimental constraints.

To this aim we show $dE_T/d\eta$ (divided by half the number of participants N_{part}) from HSD in Fig. 3.12 (l.h.s.) in comparison to the measurements by PHENIX [98]. Accordingly, the Bjorken energy density ϵ_{Bj} – multiplied by the time-scale τ (3.2)– from HSD is shown additionally in the r.h.s. of Fig. 3.12 in comparison to the PHENIX data as a function of N_{part}. The similarity between the calculated quantities and the experimental data demonstrates that the space-time evolution of the energy-momentum tensor $T_{\mu\nu}$ in HSD is sufficiently well under control also at RHIC energies.

3.4 Open and hidden charm production

An investigation of the formation and suppression dynamics of J/Ψ, χ_c and Ψ' mesons opens the possibility to address fundamental questions about the properties of the state of matter at high temperature and density. Up to date, a simultaneous description of the seemingly energy-independent suppression of J/Ψ together with its narrow rapidity distribution and a strong elliptic flow v_2 of charmed hadrons - as found at the Relativistic-Heavy-Ion-Collider (RHIC) - has presented a challenge to microscopic theories. The large discrepancies of present studies are striking in view of the success of the hadron-string transport theories in describing charmonium data at SPS energies. This has lead to the conjecture that the sizeable difference between the measured yields and transport predictions is due to a neglect of the transition from hadronic to partonic matter, e.g. a strongly-coupled Quark-Gluon-Plasma (sQGP). In the present work, we report new results on the charmonium nuclear modification factor R_{AA}, rapidity

distribution, the elliptic flow v_2 of D mesons, the ratios $\langle J/\Psi\rangle/\langle\pi\rangle$ and $\Psi'/(J/\Psi)$ for energies from about 20 A·GeV - relevant for the future Facility-for-Antiproton-and-Ion-Research (FAIR) - up to top RHIC energies.

We recall that in the early stage of the nucleus-nucleus collisions the dissociation and the regeneration of J/Ψ by fundamentally different mechanisms are possible: The $c\bar{c}$ pairs produced early in the reaction - by gluon-gluon fusion in primary nucleon-nucleon interactions - might be completely dissociated in the dense medium and not be formed as bound states due to color screening. In this model scenario charmonia have to be recreated by some mechanism to yield a finite production cross section of J/Ψ and Ψ'. The $c\bar{c}$ pairs might also be formed in some pre-hadronic resonance (color-dipole) state that will further develop to the charmonium eigenstates in vacuum. Such resonance states can be dissociated in the medium due to interactions with other degrees of freedom but also be recreated by the inverse reaction channels. Independently, charmonia might also be generated in a statistical fashion at the phase boundary between the QGP and an interacting hadron gas such that their abundance would appear in statistical (chemical) equilibrium with the light and strange hadrons [99, 100]. In the latter model the charmonium spectra carry no information on a possible preceding partonic phase. Indeed, in Ref. [101] a success of the statistical hadronization model [102, 103] has been put forward. Another alternative is the model for coalescence of charmonium in the sQGP [104]. For further variants or model concepts for charmonium suppression/enhancement we refer the reader to the reviews [105, 106]. In this work our aim is to shed some light on various model concepts by exploiting relativistic microscopic transport theory.

The Hadron-String-Dynamics (HSD) approach [1] provides the space-time geometry of nucleus-nucleus reactions and a rather reliable estimate for the local energy densities achieved, since the production of secondary particles with light and single strange quarks/antquarks is described well from SIS to RHIC energies [93]. As we have discussed in the previous section, the high energy-densities reached in $Au + Au$ collisions at RHIC clearly indicate that a strongly interacting QGP (sQGP) has been created for a couple of fm/c in the central overlap volume. Charmonia are a promising probe that is sensitive to the properties of the early stage of the collision and that can possibly differentiate between hadronic and partonic medium.

In the systematic study summarized in Ref. [107], we describe the implementation of charmonium production in $p + p$, $d + A$, and $A + A$ reactions in the HSD transport approach. We observed that the interactions of J/Ψ's with mesons in the late stages of the collision (when the energy density falls below a critical value of about 1 GeV/fm^3 corresponding roughly to the critical energy density for a parton/hadron phase transition) gives a sizable contribution to its anomalous suppression at all beam energies as demonstrated in Refs. [76, 90, 108–110]. Accordingly, this hadronic contribution has to be incorporated when comparing possible models for QGP-induced charmonium suppression to experimental data. On the other hand, as known from our studies in Refs. [108, 109] charmonium interactions with the purely hadronic medium alone (which is modeled rather precisely by HSD) are not sufficient to describe the J/Ψ suppression pattern at RHIC in detail.

Based on the microscopic HSD transport theory, we investigate in particular the following scenarios for the anomalous absorption of charmonia:

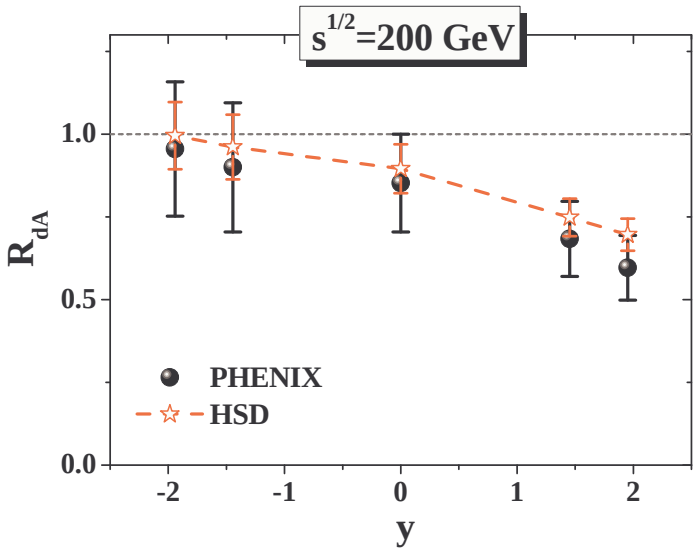

Figure 3.13: J/Ψ production cross section in $d+Au$ collisions relative to that in $p+p$ collisions (see text for the definition of R_{dA}) in HSD (red stars) as compared to the PHENIX data [116] (full dots).

(1) the 'threshold melting' mechanism;
(2) a dissociation by the scattering on hadron-like correlators, *i.e.* the 'comover' scenario;
(3) additional scattering of charm with pre-hadrons which might be considered as color neutral precursors of hadronic states (cf. Refs. [111–114]).

These scenarios will be described briefly below. We will present in particular the effect of the interactions of charm quarks in the pre-hadronic medium on $R_{AA}(y)$ of J/Ψ by comparing our calculations to RHIC data. Furthermore, by studying the J/Ψ to π ratio as a function of the number of participating nucleons N_{part}, we will test the assumption of charmonium production by statistical hadronization as advocated in Refs. [100, 101, 115].

3.4.1 Cold nuclear absorption of charmonia

The yield of J/Ψ in $p+A$ and $A+A$ reactions is modified compared to that in $p+p$ scaled with the number of initial binary scatterings N_{coll} [117, 118]. Indeed, the produced $c\bar{c}$ can be dissociated or absorbed on either the residual nucleus of the projectile or target or on light co-moving particles (usually on mesons or, at high energy, on partons) produced in the very early phase. The latter reactions are only important in nucleus-nucleus collisions and not in $p+A$ or $d+A$ as the number of 'comovers' created in proton- or deuteron-induced processes is small. In contrast, charmonium absorption on baryons is the leading suppression mechanism in $d+A$ $(p+A)$ scattering and is an important base-line for the study of the absorption in the hot and dense medium created in $A+A$ reactions.

In order to study the effect of charmonium rescattering on projectile/target nu-

cleons, we adopt in HSD the following dissociation cross sections of charmonia with baryons independent of the energy:

$$\sigma_{c\bar{c}B} = 4.18 \text{ mb}; \qquad (3.3)$$
$$\sigma_{J/\Psi B} = 4.18 \text{ mb}; \ \sigma_{\chi_c B} = 4.18 \text{ mb}; \ \sigma_{\Psi' B} = 7.6 \text{ mb}.$$

In (3.3) the cross section $\sigma_{c\bar{c}B}$ stands for a (color dipole) pre-resonance ($c\bar{c}$) - baryon cross section, since the $c\bar{c}$ pair produced initially cannot be identified with a particular charmonium due to the uncertainty relation in energy and time. For the life-time of the pre-resonance $c\bar{c}$ pair (in it's rest frame) a value of $\tau_{c\bar{c}} = 0.3$ fm/c is assumed following Ref. [119]. This time scale corresponds to the mass difference of the Ψ' and J/Ψ.

The values for the cross sections $\sigma_{J/\Psi N}, \sigma_{c\bar{c}N}$ at RHIC energies are currently debated in the literature. On one side, all the data on the J/Ψ production in $p+A$ at energies $\sqrt{s} \leq 40$ GeV were found to be consistent with an energy-independent cross section of the order of $4-7$ mb [117, 120–123]. On the other hand, the corresponding cross sections at the much higher energy of $\sqrt{s} = 200$ GeV, *e.g.* at RHIC, are expected to be smaller [124], since part of the suppression might be attributed to other (initial-state) cold-matter effects, such as gluon shadowing [125–127], radiative gluon energy loss in the initial state or multiple gluon rescattering. We recall that 'shadowing' is a depletion of low-momentum partons in a nucleon embedded in a nucleus compared to the population in a free nucleon, which leads to a lowering in the charmonium production cross section. The reasons for depletion, though, are numerous, and models of shadowing vary accordingly. There is, therefore, a considerable (about a factor of 3) uncertainty in the amount of shadowing predicted at RHIC [125–129]. In the analysis of the $d+Au$ data at $\sqrt{s} = 200$ GeV, in which the maximum estimate for the effect of the shadowing was made [124, 127], the additional absorption on baryons allowed by the data was found to lead to $\sigma_{J/\Psi N} = 1-3$ mb or higher, if some contribution of anti-shadowing is present. The authors of [127] advocate $\sigma_{J/\Psi N} = 3$ mb in order to preserve the agreement with the data of the Fermilab experiment E866. The PHENIX Collaboration [116] finds a breakup cross section of $2.8^{+1.7}_{-1.4}$ mb (using EKS shadowing) which still overlaps with the CERN value of 4.18 mb (though with large error bars). However, the theoretical uncertainty is still large, since in the works above only an approximate model for baryonic absorption was applied and not a microscopic transport approach that e.g. also includes secondary production channels of charm pairs as described in Section 3.

Within HSD we have found the baryoninc absorption cross sections (3.3) to agree with the data at SPS energies [108]. In Fig. 3.13 we compare the HSD result (employing the same cross sections (3.3) for baryonic absorption and neglecting shadowing) for the J/Ψ production in $d+Au$ collisions at $\sqrt{s} = 200$ GeV to the inclusive PHENIX data [116]. The quantity plotted is the nuclear modification factor defined as

$$R_{dA} \equiv \frac{dN^{dAu}_{J/\Psi}/dy}{\langle N_{coll} \rangle \cdot dN^{pp}_{J/\Psi}/dy}, \qquad (3.4)$$

where $dN^{dAu}_{J/\Psi}/dy$ is the J/Ψ invariant yield in $d+A$ collisions, $dN^{pp}_{J/\Psi}/dy$ is the J/Ψ

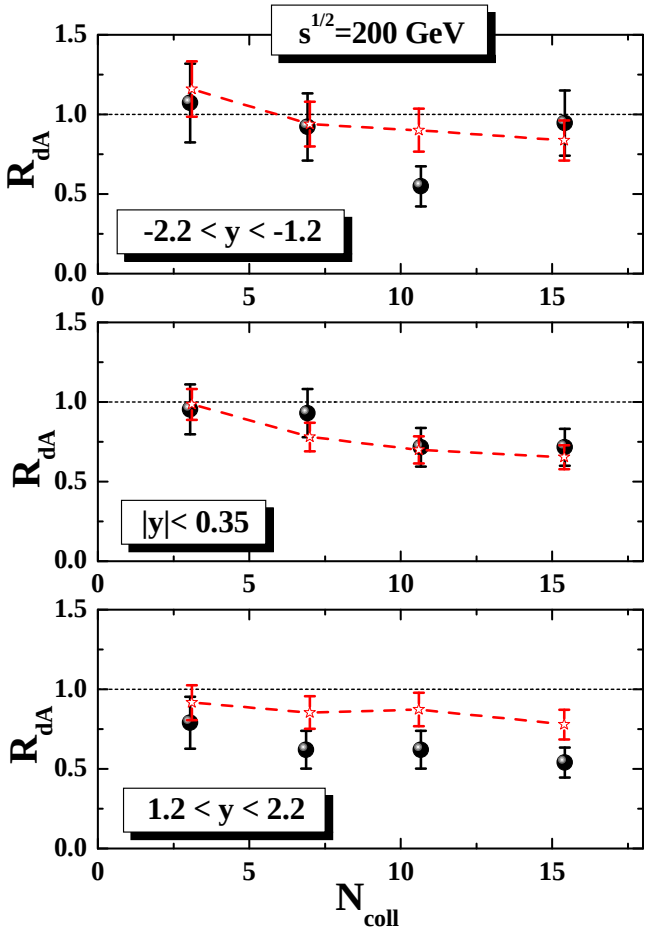

Figure 3.14: The ratio R_{dA} (3.4) for backward, central and forward rapidity bins as a function of the number of binary collisions N_{coll} for $d + Au$ at $\sqrt{s} = 200$ GeV. The experimental data have been taken from Ref. [116]. The HSD results (stars connected by red dashed lines) show calculations without including low-x gluon shadowing and slightly overestimate R_{dA} in the forward interval $1.2 < y < 2.2$. The theoretical error bars are due to the finite statistics of the calculation.

invariant yield in $p + p$ collisions; $\langle N_{coll} \rangle$ is the average number of binary collisions for the same rapidity bin. In our analysis we have used $\langle N_{coll} \rangle = 7.6 \pm 0.3$ according to the PHENIX estimate [116].

It is seen from Fig. 3.13 that the calculations follow approximately the decrease in R_{dA} with rapidity, however, with a tendency to overshoot at forward rapidity. Within error bars we find the values of $\sigma_{c\bar{c}B}$ from (3.3) to be compatible with the inclusive RHIC measurement as well as with the lower energy data [121]. This finding is also in line with the analysis of the PHENIX Collaboration in Ref. [116]

In order to shed some further light on the role of shadowing, we compare our calculations for R_{dA} in different rapidity bins as a function of the centrality of the d+Au collision, which in Fig. 3.14 is represented by the number of binary collisions N_{coll}. The latter number is directly taken from the number of binary hard NN collisions in the transport calculation while the comparison with experiment is based on a Glauber model analysis of the data similar to that performed in Ref. [130]. The actual results

displayed in Fig. 3.14 (stars connected by dashed lines) and the PHENIX data from Ref. [116] are roughly compatible for the rapidity intervals -2.2 $< y <$ -1.2 and $|y| <$ 0.35, but demonstrate that the suppression at forward rapidity (1.2 $< y <$2.2) is underestimated in the color-dipole dissociation model with a constant cross section of 4.18 mb. This clearly points to the presence of shadowing effects at least at forward rapidities which is not so pronounced in the inclusive data set in Fig. 3.13. A more serious question is a quantification of the shadowing due to the limited statistics of both the experimental data and the calculations. Here we do not attempt to attribute a fixed number for the shadowing effect but merely point out that independent high statistics data will be necessary to fix this unsatisfactory situation from the experimental side.

Nevertheless, some note of caution is appropriate for the further analysis of charmonium suppression in $Au + Au$ collisions: There are 'cold nuclear matter effects' such as 'gluon shadowing' beyond those incorporated in the transport calculations, and especially quantitative statements about any 'agreement with data' might have to be reconsidered. In case of $Au + Au$ reactions the shadowing from projectile/target will show up symmetrically around $y = 0$ and in part contribute to the stronger J/Ψ suppression at forward/backward rapidities. Nevertheless, following Granier de Cassagnac [130], an anomalous suppression of J/Ψ beyond 'cold nuclear matter effects' is clearly present in the $Au + Au$ data to be investigated below.

It is well known that the baryonic (normal) absorption alone cannot explain the suppression of charmonia in heavy-ion collisions with increasing centrality [105]. We have implemented in HSD several different mechanism for the additional (anomalous) suppression of charmonia which will be explained in the following Subsections. By comparing the results from these scenarios to each other and to the available data the mechanism of charmonium interactions with the medium can be probed.

3.4.2 'Comover' suppression (and recombination)

First of all let us stress that the interactions with 'comoving' mesons lead not only to the dissociation of charmonia, but also to their recreation via the inverse recombination process $D + \bar{D} \to c\bar{c} + m$, where $m = \{\pi, \rho, \omega, K, ...\}$. As already pointed out before, the $J/\Psi, \chi_c, \Psi'$ formation cross sections by open charm mesons or the inverse 'comover' dissociation cross sections are not well known and the significance of these channels is discussed controversely in the literature [102, 104, 131–135]. We here follow the concept of Refs. [76, 90] and introduce a simple 2-body transition model with a single parameter $|M_0|^2$, that allows to implement the backward reactions uniquely by employing detailed balance for each individual channel.

Since the charmonium-meson dissociation and backward reactions typically occur with low relative momenta ('comovers'), it is legitimate to write the cross section for the process $1 + 2 \to 3 + 4$ as

$$\sigma_{1+2\to 3+4}(s) = 2^4 \frac{E_1 E_2 E_3 E_4}{s} |\tilde{M}_i|^2 \left(\frac{m_3 + m_4}{\sqrt{s}}\right)^6 \frac{p_f}{p_i}, \tag{3.5}$$

where E_k denotes the energy of hadron k ($k = 1, 2, 3, 4$), respectively. The initial and

final momenta for fixed invariant energy $\sqrt{s}$ are given by

$$p_i^2 = \frac{(s-(m_1+m_2)^2)(s-(m_1-m_2)^2)}{4s},$$
$$p_f^2 = \frac{(s-(m_3+m_4)^2)(s-(m_3-m_4)^2)}{4s}, \tag{3.6}$$

where m_k denotes the mass of hadron k. In (3.5) $|\tilde{M}_i|^2$ ($i = \chi_c, J/\Psi, \Psi'$) stands for the effective matrix element squared, which for the different 2-body channels is taken of the form

$$\begin{aligned}
&|\tilde{M}_i|^2 = |M_i|^2 \ \text{ for } \ (\pi,\rho) + (c\bar{c})_i \to D + \bar{D} \\
&|\tilde{M}_i|^2 = 3|M_i|^2 \ \text{ for } \ (\pi,\rho) + (c\bar{c})_i \to D^* + \bar{D},\ D + \bar{D}^*,\ D^* + \bar{D}^* \\
&|\tilde{M}_i|^2 = \frac{1}{3}|M_i|^2 \ \text{ for } \ (K,K^*) + (c\bar{c})_i \to D_s + \bar{D},\ \bar{D}_s + D \\
&|\tilde{M}_i|^2 = |M_i|^2 \ \text{ for } \ (K,K^*) + (c\bar{c})_i \to D_s + \bar{D}^*,\ \bar{D}_s + D^*,\ D_s^* + \bar{D}, \\
&\qquad\qquad\qquad\qquad\qquad\qquad\qquad\qquad \bar{D}_s^* + D,\ \bar{D}_s^* + D^*
\end{aligned} \tag{3.7}$$

The relative factors of 3 in (3.7) are guided by the sum rule studies in [136] which suggest that the cross section is increased whenever a vector meson D^* or $\bar{D}^*$ appears in the final channel while another factor of 1/3 is introduced for each s or $\bar{s}$ quark involved. The factor $((m_3+m_4)/\sqrt{s})^6$ in (3.5) accounts for the suppression of binary channels with increasing $\sqrt{s}$ and has been fitted to the experimental data for the reactions $\pi + N \to \rho + N, \omega + N, \phi + N, K^+ + \Lambda$ in Ref. [137].

We use the same matrix elements for the dissociation of all charmonium states i ($i = \chi_c, J/\Psi, \Psi'$) with mesons:

$$|M_{J/\Psi}|^2 = |M_{\chi_c}|^2 = |M_{\Psi'}|^2 = |M_0|^2. \tag{3.8}$$

We note for completeness that in Ref. [90] the parameter $|M_0|^2$ was fixed by comparison to the J/Ψ suppression data from the NA38 and NA50 Collaborations for S+U and Pb+Pb collisions at 200 and 158 AGeV, respectively. In a later study [108], however, this parameter has been readjusted in accordance with the updated value of the cross section (3.3) of charmonium dissociation on baryons (following the latest NA50 and NA60 analysis [117, 120]). The best fit is obtained for $|M_0|^2 = 0.18$ fm^2/GeV^2; this value will be employed in our following studies, too.

The advantage of the model introduced in [76, 90] is that detailed balance for the binary reactions can be employed strictly for each individual channel, *i.e.*

$$\sigma_{3+4\to 1+2}(s) = \sigma_{1+2\to 3+4}(s)\frac{(2S_1+1)(2S_2+1)}{(2S_3+1)(2S_4+1)}\,\frac{p_i^2}{p_f^2}, \tag{3.9}$$

and the role of the backward reactions ($(c\bar{c})_i$+meson formation by $D + \bar{D}$ flavor exchange) can be explored without introducing any additional parameter once $|M_0|^2$ is fixed. In Eq. (3.9) the quantities S_j denote the spins of the particles, while p_i^2 and p_f^2 denote the cms momentum squared in the initial and final channels, respectively.

The uncertainty in the cross sections (3.9) is of the same order of magnitude as that in Lagrangian approaches using *e.g.* $SU(4)_{flavor}$ symmetry [138, 139], since the form factors at the vertices are essentially unknown [136]. It should be pointed out that the 'comover' dissociation channels for charmonia are described in HSD with the proper individual thresholds for each channel in contrast to the more schematic 'comover' absorption model in Refs. [129, 140].

The regeneration of charmonia by recombination of D (D^*) mesons in the hadronic phase was first studied by C.M. Ko and collaborators in [135]. The conclusion at that time was that this process is unlikely at RHIC energies [132, 135, 141]. On the other hand, it has been shown within HSD [90] that the contribution of the $D + \bar{D}$ annihilation to the produced J/Ψ at RHIC is considerable. Moreover, the equilibrium in the reaction $J/\Psi + m \leftrightarrow D\bar{D}$ is reached (i.e. the charmonium recreation is comparable with the dissociation by 'comoving' mesons). The reason for such differences is that the pioneering study [135] within the hadron gas model was confined to J/Ψ reactions with π's into two particular $D\bar{D}$ channels ($D + \bar{D}^*$ and $D^* + \bar{D}^*$). On the contrary, in Ref. [90] the interactions with all mesons into all possible combinations of $D\bar{D}$ states have been taken into account. Note that the ρ-meson density at RHIC is large such that the channel with the most abundant ρ-meson resonance is dominant. Furthermore, in Ref. [90] the feed down from χ_c and Ψ' decays has been considered. The results of [90] are in accordance with independent studies in Refs. [142–145]. Later work within the HSD approach [109] has supported the conclusions of Ref. [90] and stressed the importance for $D\bar{D}$ annihilation in the late (purely hadronic) stages of the collisions.

3.4.3 'Threshold melting'

This scenario is based on the idea of sequential dissociation of charmonia with increasing temperature [146–149], *i.e.* of charmonium melting in the QGP due to color screening as soon as the fireball temperature reaches the dissociation temperatures of ($\approx 2T_c$ for J/Ψ, $\approx T_c$ for excited states, where T_c stands for the critical temperature of the deconfinement phase transition). In the early approaches the temperature of the fireball has been estimated using e.g. the Bjorken formula (3.2). We modify the standard sequential dissociation model in two aspects: (i) the energy density is calculated locally and microscopically instead of using schematic estimates; (ii) the model incorporates a charmonium regeneration mechanism (by $D\bar{D}$ annihilation processes).

The 'threshold scenario' for charmonium dissociation now is implemented in a straight forward way: whenever the local energy density $\varepsilon(x)$ is above a threshold value ε_j, where the index j stands for $J/\Psi, \chi_c, \Psi'$, the charmonium is fully dissociated to $c + \bar{c}$. The default threshold energy densities adopted are

$$\varepsilon_{J/\Psi} = 16 \text{ GeV/fm}^3 \text{ , } \varepsilon_{\chi_c} = 2 \text{ GeV/fm}^3, \text{ and } \varepsilon_{\Psi'} = 2 \text{ GeV/fm}^3. \tag{3.10}$$

The dissociation of charmonia is widely studied using lattice QCD (lQCD) [150–154] in order to determine the dissociation temperature (or energy density) via the maximum entropy method. On the other hand one may use potential models - reproducing the charmonium excitation spectrum in vacuum - to calculate Mott transition

temperatures in a hot medium. Both approaches have their limitations and the quantitative agreement between the different groups is still unsatisfactory:

- (A) Potential models employ the static heavy quark-antiquark pair free energy - calculated on the lattice - to obtain the charmonium spectral functions. This leads to the dissociation temperatures [155]

$$T_{melt}(J/\Psi) \leq 1.2\,T_c,\ T_{melt}(\chi_c) \leq T_c,\ T_{melt}(\Psi') \leq T_c.$$

- (B) The maximum entropy method is used to relate the Euclidean thermal correlators of charmonia - calculated on the lattice - to the corresponding spectral functions and yields higher dissociation temperatures [150]

$$T_{melt}(J/\Psi) = 1.7{-}2\,T_c,\ T_{melt}(\chi_c) = 1.1{-}1.2\,T_c$$

or [151]

$$T_{melt}(J/\Psi) \geq 1.5\,T_c,\ T_{melt}(\chi_c) = 1.1\,T_c.$$

Our earlier analysis of experimental data at the SPS in the 'threshold melting' approach [108] lead us to conclude from the observation of a considerable amount of J/Ψ in the most central $Pb + Pb$ collisions that the assumption of a melting of J/Ψ close to T_c contradicts the data. Therefore, the values (3.10) are applied also in the current study.

3.4.4 Interaction with pre-hadrons

Two more scenarios are implemented in our present HSD simulations that are closely related to the 'comover suppression' and the 'threshold melting' scenarios outlined in the previous sub-sections. The essential difference is that the comoving hadrons (including the D-mesons) exist only at energy densities below some energy density ε_{cut}, which is a free parameter. We employ $\varepsilon_{cut} = \varepsilon_c \approx 1$ GeV/fm^3, which is equal to the critical energy density ε_c for the parton/hadron phase transition. This scenario clearly separates 'formed hadrons' from possible pre-hadronic states at higher energy densities. Indeed, it is currently not clear whether D- or D^*-mesons survive at energy densities above ε_c but hadronic correlators with the quantum numbers of the hadronic states are likely to persist above the phase transition [156]. One may speculate that similar correlations (pre-hadrons) survive also in the light quark sector above T_c such that 'hadronic comovers' – with modified spectral functions – might show up also at energy densities above ε_c.

We recall that the concept of (color neutral) pre-hadrons - explained in more detail in Refs. [111, 113] - has been also used in the hadron electroproduction studies off nuclei in Refs. [111, 112] as well as for high p_T hadron suppression [113] or jet suppression at RHIC energies [114]. It has been found that the pre-hadron concept works well for hadron attenuation in nuclei at HERMES energies [111, 112] but underestimates the high p_T hadron suppression [113] as well as the jet attenuation at RHIC energies [114]. Nevertheless, the amount of attenuation due to such pre-hadronic interactions emerged to be about 50% of the experimentally observed suppression at RHIC such

that their effect might not simply be discarded. It should be stressed that the concept of pre-hadrons refers to the string breaking mechanism as described in Refs. [111, 113] and is independent on the energy density. A detailed study on the space-time evolution of pre-hadrons and their formation to hadrons for *pp* collisions has been performed by Gallmeister and Falter in Ref. [157].

In line with the investigations in Refs. [113, 114] we also study J/Ψ production and absorption in $Au + Au$ collisions at $\sqrt{s} = 200$ AGeV assuming the absorption of charmonia on pre-hadrons as well as their regeneration by pre-hadrons. This adds additional interactions of the particles with charm quarks (antiquarks) in the very early phase of the nucleus-nucleus collisions as compared to the default HSD approach. Since these pre-hadronic (color-dipole) states represent some new degrees-of-freedom, the interactions of charmed states with these objects have to be specified separately.

For notation we define a pre-hadronic state consisting of a quark-antiquark pair as pre-meson $\tilde{m}$ and a state consisting of a diquark-quark pair as pre-baryon $\tilde{B}$. The dissociation cross section of a $c\bar{c}$ color dipole state with a pre-baryon is taken to be of the same order as with a formed baryon,

$$\sigma^{diss}_{c\bar{c}\tilde{B}} = 5.8 \text{ mb}, \tag{3.11}$$

whereas the cross section with a pre-meson follows from the additive quark model as [111, 112]

$$\sigma^{diss}_{c\bar{c}\tilde{m}} = \frac{2}{3}\sigma^{diss}_{c\bar{c}\tilde{B}}. \tag{3.12}$$

Elastic cross sections are taken as

$$\sigma^{el}_{c\bar{c}\tilde{B}} = 1.9 \text{ mb}, \qquad \sigma^{el}_{c\bar{c}\tilde{m}} = \frac{2}{3}\sigma^{el}_{c\bar{c}\tilde{B}}. \tag{3.13}$$

Furthermore, elastic interactions of a charm quark (antiquark) are modeled by the scattering of an unformed D or D^* meson on pre-hadrons with only light quarks as

$$\sigma^{el}_{D\tilde{B}} = 3.9 \text{ mb}, \qquad \sigma^{el}_{D\tilde{m}} = \frac{2}{3}\sigma^{el}_{D\tilde{B}}. \tag{3.14}$$

In this way we may incorporate in HSD some dynamics of quark-antiquark pairs with a medium that has not yet formed the ordinary hadrons. However, it has to be stressed that further explicit partonic degrees of freedom, i.e. gluons and their mutual interactions as well as gluon interactions with quarks and antiquarks, are not taken into account in the present HSD approach. Therefore, we do not expect to reproduce any details of the measured J/Ψ yield. The study of this particular model situation is motivated first of all by the possibility to assess the conceptual influence of charm scattering on pre-hadrons (in the early reaction phase) on the final rapidity distribution of the J/Ψ's (see below).

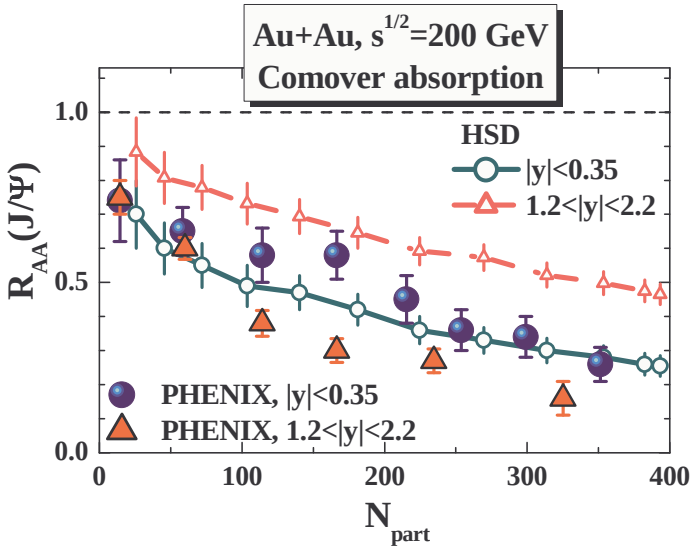

Figure 3.15: The J/Ψ nuclear modification factor R_{AA} (3.15) for Au+Au collisions at $\sqrt{s} = 200$ AGeV as a function of the number of participants N_{part} in comparison to the data from [118] for midrapidity (full circles) and forward rapidity (full triangles). The HSD results for the purely hadronic 'comover' scenario are displayed in terms of the lower (green solid) line with open circles for midrapidity $J/\Psi's$ ($|y| \leq 0.35$) and in terms of the upper (red dashed) line with open triangles for forward rapidity ($1.2 \leq |y| \leq 2.2$).

3.4.5 Discriminating hadronic and partonic phases

In the transport approach we calculate the J/Ψ survival probability $S_{J/\Psi}$ and the nuclear modification factor R_{AA} as

$$S_{J/\Psi} = \frac{N_{fin}^{J/\Psi}}{N_{BB}^{J/\Psi}}, \quad R_{AA} = \frac{dN_{AA}^{J/\Psi}/dy}{N_{coll} \cdot dN_{pp}^{J/\Psi}/dy}, \tag{3.15}$$

where $N_{fin}^{J/\Psi}$ and $N_{BB}^{J/\Psi}$ denote the final number of J/Ψ mesons and the number of J/Ψ's produced initially by BB reactions, respectively. Note that $N_{fin}^{J/\Psi}$ includes the decays from the final χ_c. In (3.15), $dN_{AA}^{J/\Psi}/dy$ denotes the final yield of J/Ψ in AA collisions, $dN_{pp}^{J/\Psi}/dy$ is the yield in elementary pp reactions while N_{coll} is the number of initial binary collisions.

The suppression of charmonia by the 'comover' dissociation channels within the model described in [108] for a matrix element squared $|M_0|^2 = 0.18$ fm^2/GeV^2 has been presented already in Ref. [109] as well as the results for the 'threshold melting scenario' employing the thresholds $\varepsilon_{J/\Psi} = 16$ GeV/fm^3, $\varepsilon_{\chi_c} = \varepsilon_{\Psi'} = 2$ GeV/fm^3. Note that the charmonium reformation channels by $D + \bar{D}$ channels had been incorporated, too (*cf.* Ref. [90]). Since the PHENIX Collaboration has released a new data set we compare our calculations with the most recent PHENIX data [118] in Fig. 3.15 for the J/Ψ nuclear modification factor R_{AA} (3.15) for Au+Au collisions at $\sqrt{s} = 200$ AGeV as a function of the number of participants N_{part} for midrapidity (full circles) and forward

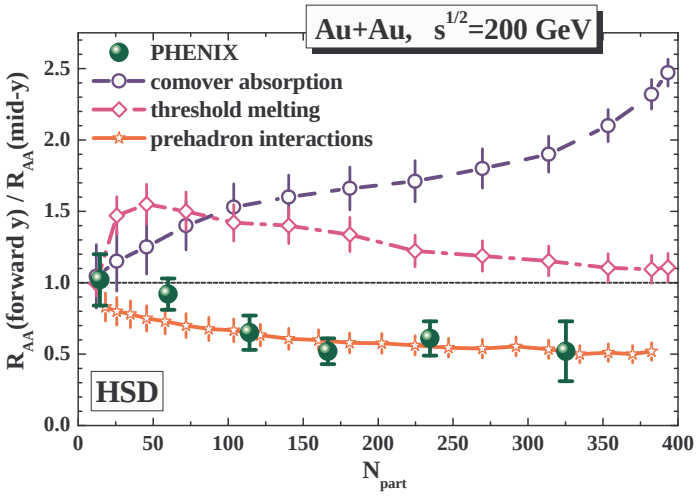

Figure 3.16: The ratio of the nuclear modification factors R_{AA} at mid-rapidity ($|y| < 0.35$) and at forward rapidity ($1.2 < |y| < 2.2$) *vs* centrality in $Au + Au$ collisions at $\sqrt{s} = 200$ GeV. The HSD results in the purely hadronic scenario ('comover absorption') are displayed in terms of the blue dashed line (with open circles) and in case of the 'threshold melting' scenario in terms of the violet dot-dashed line (with open squares). The lower full green dots represent the data of the PHENIX Collaboration [118]. The lower solid (red) line with stars gives the result for the 'comover absorption' scenario when including additional pre-hadronic interactions with charm (see text).

rapidity (full triangles). The HSD results for the purely hadronic 'comover' scenario are displayed in terms of the lower (blue solid) line with open circles for midrapidity $J/\Psi's$ ($|y| \leq 0.35$) and in terms of the upper (red dashed) line with open triangles for forward rapidity ($1.2 \leq |y| \leq 2.2$). The numerical results appear acceptable at midrapidity ($|y| \leq 0.35$) but the even larger suppression at forward rapidity (seen experimentally) is fully missed (cf. Ref. [109]).

The failure of the traditional 'comover absorption' model as well as 'threshold melting' scenario at the top RHIC energy is most clearly seen in the centrality dependence of the ratio of the nuclear modification factors R_{AA} at forward rapidity ($1.2 < |y| < 2.2$) and at mid-rapidity ($|y| < 0.35$) as shown in Fig. 3.16. The HSD results in the purely hadronic scenario ('comover absorption') are displayed in terms of the blue dashed line (with open circles) and in case of the 'threshold melting' scenario in terms of the dot-dashed violet line (with open squares). The error bars on the theoretical results indicate the statistical uncertainty due to the finite number of Monte-Carlo events in the calculations. The lower full green dots in Fig. 3.16 represent the corresponding data of the PHENIX Collaboration [118] which show a fully different pattern as a function of centrality (here given in terms of the number of participants N_{part}). The failure of these 'standard' suppression models at RHIC has lead to the conclusion in Ref. [109] that the hadronic 'comover absorption and recombination' model is falsified by the PHENIX data and that strong interactions in the pre-hadronic (or partonic) phase should be necessary to explain the large suppression at forward rapidities.

In this work we follow up the latter idea and incorporate in the 'comover scenario'

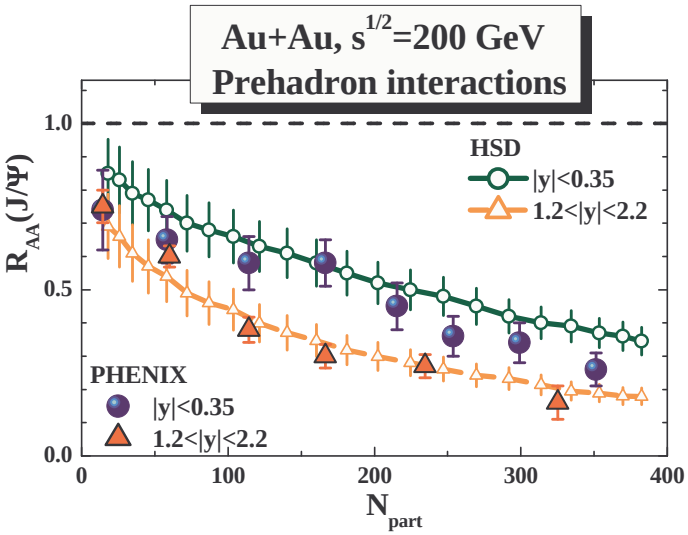

Figure 3.17: The J/Ψ nuclear modification factor R_{AA} (3.15) for Au+Au collisions at $\sqrt{s} = 200$ AGeV as a function of the number of participants N_{part} in comparison to the data from [118] for midrapidity (full circles) and forward rapidity (full triangles). The HSD results for the hadronic 'comover' scenario including additionally pre-hadronic interactions of charm are displayed in terms of the upper (green solid) line with open circles for midrapidity $J/\Psi's$ ($|y| \leq 0.35$) and in terms of the lower (orange dashed) line with open triangles for forward rapidity ($1.2 \leq |y| \leq 2.2$).

the additional pre-hadronic cross sections (3.11) - (3.14) for the early charm interactions to have a first glance at the dominant effects. The J/Ψ suppression pattern in this case is shown in Fig. 3.17 in comparison to the same data as in Fig. 3.15. Now, indeed, the suppression pattern for central and forward rapidities becomes rather similar to the data within the statistical accuracy of the calculations. Indeed, the ratio of R_{AA} at forward rapidity to midrapidity now follows closely the experimental trend as seen in Fig. 3.16 by the lower red solid line.

Some further information may be gained from the J/Ψ rapidity distributions in Au+Au collisions at RHIC. The latter distribution is shown in Fig. 3.18 in comparison to the PHENIX data for central collisions (upper l.h.s.), semi-central (upper r.h.s.), semi-peripheral (lower l.h.s.) and peripheral reactions (lower r.h.s.) for the standard 'comover' scenario (dashed blue lines) and the 'comover' model including additionally pre-hadronic interactions of charm according to (3.11) - (3.14) (solid red lines). Whereas for peripheral reactions these additional early interactions practically play no role, the latter lead to a narrowing of the J/Ψ rapidity distribution with the centrality of the collision (roughly in line with the data). In the standard 'comover' model an opposite trend is seen: here the interactions of charmonia with formed hadrons produce a dip in the rapidity distribution at $y \approx 0$ which increases with centrality since the density of formed hadrons increases accordingly around midrapidity. Since the total number of produced $c\bar{c}$ pairs is the same (for the respective centrality class) and detailed balance is incorporated in the reaction rates we find an surplus of J/Ψ at more forward rapidities. The net result is a broadening of the J/Ψ rapidity distribution

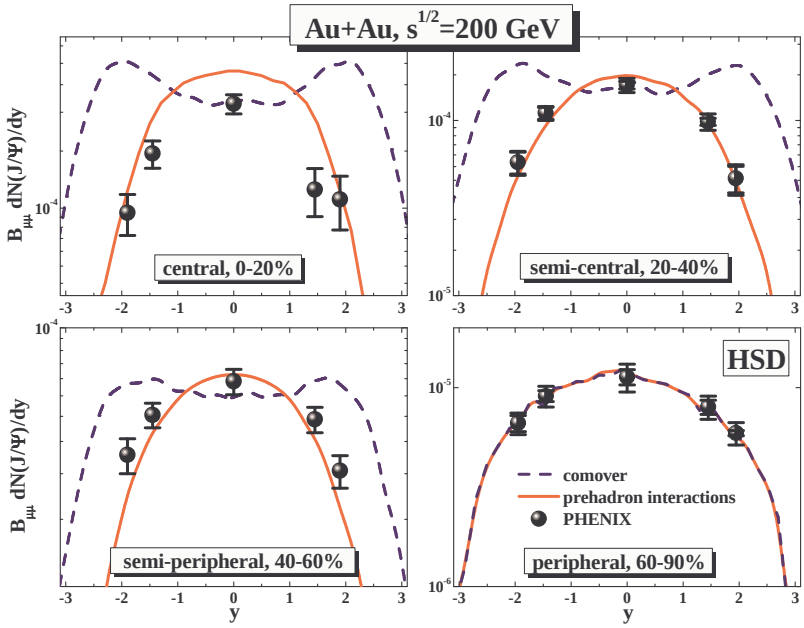

Figure 3.18: The rapidity distribution $dN_{J/\Psi}/dy$ for different centralities from the standard 'comover' model (dashed blue lines) and the 'comover' model with additional pre-hadronic interactions of charm according to (3.11) - (3.14) (solid red lines). The full dots show the respective data from the PHENIX Collaboration [118]. The calculated lines have been smoothed by a spline algorithm. The reactions are Au+Au at $\sqrt{s}$ = 200 GeV.

with centrality opposite to the trend observed in experiment.

Summarizing the results displayed in Figs. 7 - 10 we like to point out that the hadronic 'comover' dynamics for charmonium dissociation and recreation - as well as the standard charmonium 'melting' scenario - do not match the general dependences of the J/Ψ in rapidity and centrality as seen by the PHENIX Collaboration. In fact, a narrowing of the J/Ψ rapidity distribution cannot be achieved by comover interactions with formed hadrons since the latter appear too late in the collision dynamics. Only when including early pre-hadronic interactions with charm a dynamical narrowing of the charmonium rapidity distribution with centrality can be achieved as demonstrated more schematically within our pre-hadronic interaction model. Consequently, the PHENIX data on J/Ψ suppression demonstrate the presence and important impact of pre-hadronic or partonic interactions in the early charm dynamics. This finding is line with earlier studies in Refs. [90, 113, 114] demonstrating the necessity of non-hadronic degrees of freedom in the early reaction phase for the elliptic flow v_2, the suppression of hadrons at high transverse momentum p_T and far-side jet suppression in central Au+Au collisions at RHIC energies.

As pointed in Ref. [108], an independent measurement of Ψ' will provide further information on the charm reaction dynamics and final charmonium formation. For instance, a leveling off of the Ψ' to J/Ψ ratio with increasing centrality would be a signal for charm chemical equilibration in the medium [101–103]. Additionally, it provides a very clear distinction between the 'threshold melting' scenario and the

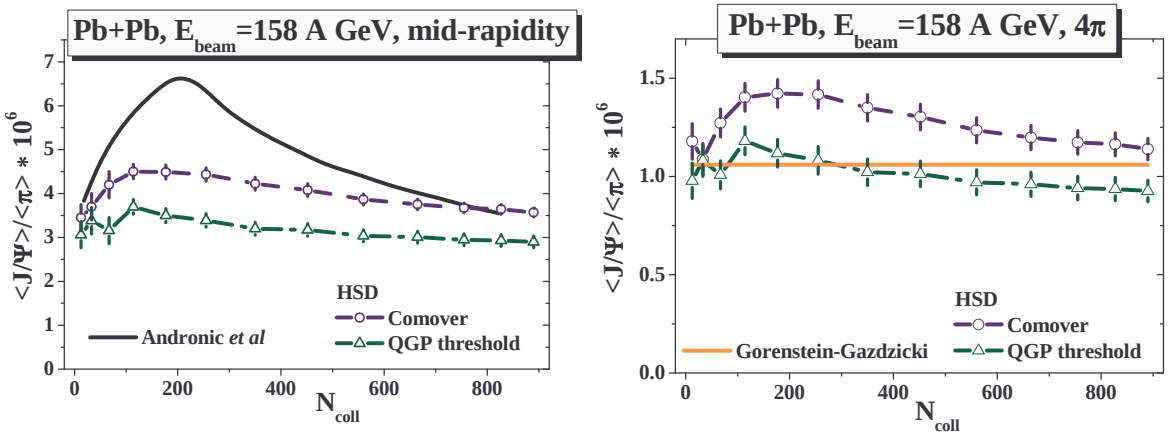

Figure 3.19: Ratio of the averaged J/Ψ to π multiplicity for $Pb+Pb$ at the SPS beam energy of 158 A·GeV at mid-rapidity (l.h.s.) and in full 4π acceptance (r.h.s.) as a function of the number of binary collisions N_{coll} for the different suppression scenarios implemented in HSD - the 'comover' model (dashed blue line with open circles) and the 'threshold melting' scenario (green dot-dashed line with open triangles) - in comparison to the statistical model by Gorenstein and Gazdzicki [100] (r.h.s.; straight orange line) and the statistical hadronization model by Andronic *et al.* [101] (l.h.s.; solid black line).

'comover' approach. Detailed predictions for the Ψ' to J/Ψ ratio as a function of centrality have already been presented in Ref. [107] for FAIR, SPS and RHIC energies.

Testing the assumption of statistical hadronization

The assumption of statistical hadronization – *i.e.* of J/Ψ's being dominantly produced at hadronization in a purely statistically fashion according to available phase space and the number of available c and $\bar{c}$ quarks – leads to a scaling of the $\langle J/\Psi\rangle/\langle h\rangle$ ratio with the system size [100], where $\langle h\rangle$ is the average hadron multiplicity. Since $\langle h\rangle \sim \langle\pi\rangle$, we calculate the ratio $\langle J/\Psi\rangle/\langle\pi\rangle$ in HSD in the different scenarios for charmonium suppression:

- 'threshold melting' + recombination via $D\bar{D} \to c\bar{c} + m$ including the backward reactions $c\bar{c} + m \to D\bar{D}$,
- hadronic ('comover') absorption: $D\bar{D} \to c\bar{c} + m$ and the backward reactions $c\bar{c} + m \to D\bar{D}$;
- 'prehadron interactions': $D\bar{D} \to c\bar{c}+m$ and the backward reactions $c\bar{c}+m \to D\bar{D}$ as well as early pre-hadronic charm interactions as described in Section 6.

The results of our calculations are shown in Fig. 3.19 together with the prediction of the statistical model of Gorenstein and Gazdzicki [100] for the full phase space (straight orange line; r.h.s.) and the statistical hadronization model by Andronic *et al.* [101, 158] for mid-rapidity (solid black line; l.h.s.) for Pb+Pb at 158 A·GeV. The centrality dependence here is given by the number of initial binary collisions N_{coll}.

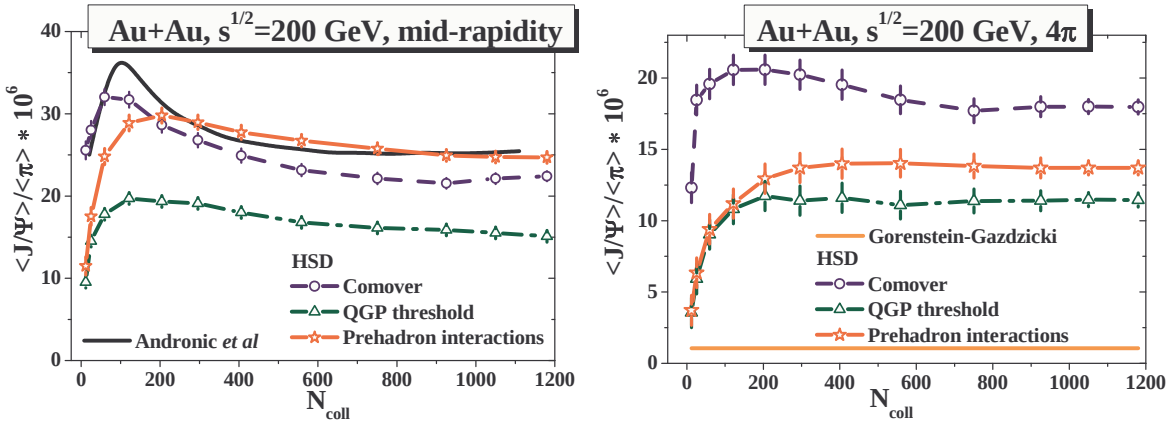

Figure 3.20: Same as Fig. 3.19 but for $Au + Au$ at the top RHIC energy of $\sqrt{s} = 200$ GeV. The red solid line shows additionally the result of the 'comover' model including the pre-hadronic charm interactions (see text).

The actual comparison in Fig. 3.20 indicates that the statistical model by Andronic *et al.* [101] predicts a sizeably larger J/Ψ to π ratio at midrapidity for peripheral and semi-peripheral reactions than the microscopic HSD results for the different scenarios. For central reactions - where an approximate equilibrium is achieved - all scenarios give roughly the same ratio. In full 4π phase space the HSD results indicate also a slightly higher J/Ψ to π ratio in the 'comover' model relative to the 'melting' scenario but both ratios only weakly depend on centrality roughly in line with the statistical model of Gorenstein and Gazdzicki [100] (orange straight line). Consequently, only peripheral reactions of heavy nuclei might be used to disentangle the different scenarios at top SPS energies at midrapidity (or in full phase space).

The situation is different for Au+Au collisions at the top RHIC energy as may be extracted from Fig. 3.20 where the J/Ψ to pion ratio (l.h.s.: at midrapidity; r.h.s.: for 4π acceptance) is shown again as a function of N_{coll}. The standard 'comover' model (dashed blue lines) is only shown for reference but is unrealistic according to the analysis in Section 6. We find that the 'comover' model with early pre-hadronic charm interactions (solid red line with stars, l.h.s.) is very close to the statistical hadronization model [101] (solid black line) at midrapidity except for very peripheral collisions. The 'threshold melting' scenario follows the trend in centrality but is down by about 30%. Thus at midrapidity there is no essential extra potential in differentiating the scenarios. Considering the full 4π acceptance (r.h.s.) we find a practically constant J/Ψ to pion ratio for $N_{coll} > 200$ from the HSD calculations as expected from the statistical model, however, the early model of Gorenstein and Gazdzicki [100] is down by about a factor of ~ 10 (and may be ruled out by present data).

Elliptic flow of charm

The elliptic flow of particles defined as

$$v_2(y, p_T) = \left\langle \frac{p_x^2 - p_y^2}{p_T^2} \right\rangle_{y,p_T} \tag{3.16}$$

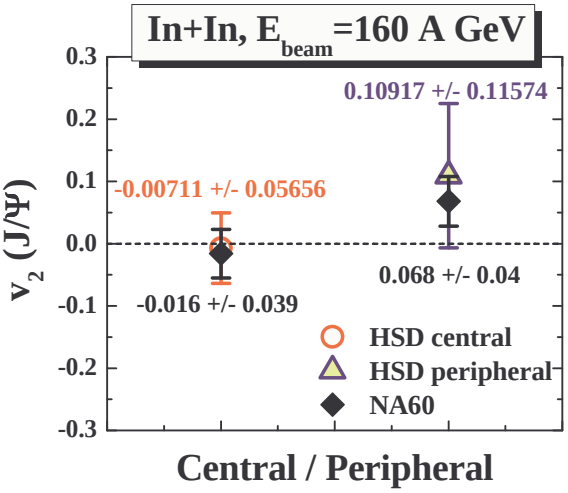

Figure 3.21: Elliptic flow v_2 of J/Ψ's produced in central and peripheral $In+In$ collisions at 158 A·GeV beam energy in the hadronic 'comover' mode of HSD (open circle and open triangle) compared to the NA60 data [159] represented by black diamonds.

(with $p_T^2 = p_x^2 + p_y^2$) provides additional information on the collective currents and pressure evolution in the early phase of the complex reaction [160] since it is driven by different pressure gradients in case of nonvanishing spatial anisotropy $\epsilon_2 =< \frac{y^2-x^2}{y^2+x^2} >$. Since ϵ_2 decreases fast during the expansion of a noncentral reaction the magnitude of v_2 gives information about the interaction strength or interaction rate of the early medium.

In Fig. 3.21 we test the HSD result for $v_2(J/\Psi)$ at SPS in the purely hadronic 'comover' scenario in comparison to the data for v_2 of the NA60 collaboration for In+In collisions [159]. In central collisions the elliptic flow is practically zero both in the calculation as well as in the experiment whereas in peripheral reactions a nonzero flow emerges. The agreement (within error bars) between the theory and the data indicates that in line with the reproduction of the J/Ψ suppression data [108] the low amount of v_2 does not point towards additional strong partonic interactions. Consequently, the present measurements of J/Ψ elliptic flow at SPS energies do not provide further constraints on the model assumptions.

The situation, however, is different for the collective flow of D-mesons at top RHIC energies. In Fig. 3.22 we show the elliptic flow of D-mesons produced in $Au + Au$ collisions at $\sqrt{s} = 200$ GeV as a function of the transverse momentum p_T in HSD (solid blue line with open circles) compared to the PHENIX data [161] on v_2 of non-photonic electrons. Here the elliptic flow of D-mesons is clearly underestimated in the standard HSD model (cf. Ref. [162]). Only when including pre-hadronic charm interactions - as described in Section 6 - the elliptic flow increases (red line with open stars) but still stays clearly below the PHENIX data for $p_T < 2$ GeV/c. We thus have to conclude that the modeling of charm interactions by pre-hadronic interactions - as described in Section 6 - does not provide enough interaction strength in the early phase of the collision. Quite remarkably this finding is again fully in line with the underestimation of high p_T hadron suppression [113] as well as far-side jet suppression [114] in the pre-hadronic interaction model. Independently, also the charm collective

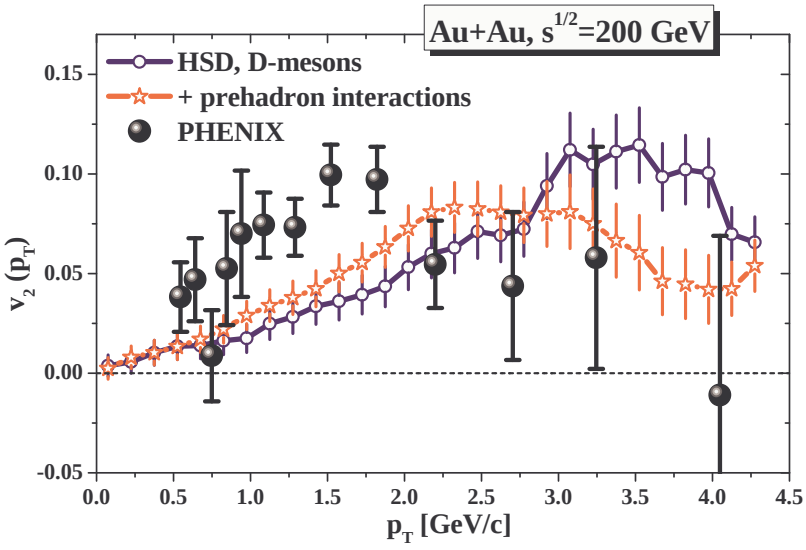

Figure 3.22: Elliptic flow of D-mesons produced in $Au+Au$ collisions at $\sqrt{s} = 200$ GeV as a function of p_T from HSD (solid blue line with open circles) in comparison to the PHENIX data [161] on v_2 of non-photonic electrons. The red line with open stars shows the HSD result for the v_2 of D-mesons when including additionally pre-hadronic charm interactions as described in Section 6.

flow points towards strong partonic interactions in the early reaction phase beyond the pre-hadronic scattering incorporated so far.

Since a large fraction of J/Ψ's in central Au+Au collisions at RHIC are created by $D - \bar{D}$ recombination, the elliptic flow of J/Ψ's obtained from HSD in the comover (purely hadronic) case is comparatively small, too, and should not be in accord with future experimental data. We consequently discard an explicit representation of the J/Ψ elliptic flow at RHIC energies since the calculations show the v_2 of charmonium to be very close to the D-meson flow within error bars.

The described here study essentially completed the investigations of charm production, propagation and chemical reactions within the HSD transport approach initiated more than a decade ago [163, 164]. The present systematic investigation extends earlier work to RHIC energies and clearly shows - as advocated before [109] - that the traditional concepts of 'charmonium melting' in a QGP state as well as the hadronic 'comover absorption and recreation model' are in severe conflict with the data from the PHENIX Collaboration at RHIC energies whereas both model assumptions work reasonably well at top SPS energies [108]. The essential result of this work was that (at top RHIC energies) we observed evidence for strong interactions of charm with the pre-hadronic medium from comparison to recent data from the PHENIX Collaboration [118]. In particular, pre-hadronic interactions (of unformed hadrons) with charm lead to dramatically different rapidity distributions for J/Ψ's and consequently to a substantially modified ratio $R_{AA}^{forward}(J/\Psi)$ to $R_{AA}^{mid}(J/\Psi)$ compared to earlier calculations/predictions.

Further results of the present microscopic transport study may be stated as follows:

- The J/Ψ suppression in $d+Au$ collisions at $\sqrt{s} = 200$ GeV is only roughly com-

patible with the charmonium absorption on nuclei as observed at SPS energies in $p + A$ reactions. We find a clear indication for shadowing effects at forward rapidity, but a conclusive answer about the size of this effect is not possible due to the statistical error bars in both the experimental data and the calculations. A proper answer can only be given by future high statistics data that allow to fix the scale of shadowing in a model independent way.

- The Ψ' to J/Ψ ratio is found to be crucial in disentangling the different charmonium absorption scenarios. This result essentially emerges from the early dissociation of Ψ' above the critical energy density $\epsilon_c \approx 1$ GeV/fm^3 in the 'QGP melting scenario' whereas the Ψ' in the 'comover model' survives to higher energy densities.

- A comparison of the transport calculations to the statistical model of Gorenstein and Gazdzicki [100] (in 4π acceptance) or the statistical hadronization model of Andronic *et al.* [101] (at midrapidity) shows differences in the energy as well as centrality dependence of the J/Ψ to pion ratio, which might be exploited experimentally to discriminate the different concepts.

- The collective flow of charm in the HSD transport appears compatible with the data at SPS energies, but the data are substantially underestimated at top RHIC energies (cf. Fig. 16). This not only holds for the standard hadronic comover scenario, but also when including interactions of charm with pre-hadronic states (unformed hadrons). Consequently the large elliptic flow v_2 of charm seen experimentally has to be attributed to early interactions of non-hadronic degrees of freedom.

The open problem - and future challenge - is to incorporate explicit partonic degrees of freedom in the description of relativistic nucleus-nucleus collisions and their transition to hadronic states in a microscopic transport approach. On the experimental side, further differential spectra of charmonia and open charm mesons then will constrain the transport properties of charm in the early non-hadronic phase of nucleus-nucleus collisions at RHIC (and possibly at SPS or even FAIR energies).

Chapter 4

Implementation of photon and dilepton production in the PHSD transport approach

4.1 Photon sources in heavy-ion collisions

The *inclusive* photon yield as produced in $p+p$, $p+A$ and $A+A$ collisions is divided into "*decay* photons" and "*direct* photons". The *decay photons* – which constitute the major part of the *inclusive* photon spectrum – stem from the photonic decays of hadrons (mesons and baryons) that are produced in the reaction. These decays occur predominantly at later times and outside of the active reaction zone and therefore carry limited information on the initial high-energy state. Consequently, it is attempted to separate the *decay* photons from the inclusive yield (preferably by experimental methods) and to study the remaining "*direct* photons". One usually uses the "cocktail" method to estimate the contribution of the photon decays to the spectra and to the elliptic flow v_2, which relies (among others) on the m_T-scaling assumption and on the photon emission only by the finally produced hadrons with momentum distributions of the final states. Depending on the particular experimental set-up, different definitions of the *decay* photons are applied by the various collaborations: all groups subtract the decays of π^0- and η-mesons, however, some groups also subtract the decays of the less abundant and short-living particles η', ω, ϕ, a_1 and the Δ-resonance. Indeed, the determination of the latter contributions (in particular from a_1 and Δ) by experimental methods is questionable, because of the photon emission during the multiple absorption and regeneration in the initial interaction phase. Therefore, a theoretical understanding of the *decay* photon contributions to the inclusive spectrum is important. Especially for analyzing simultaneously various measurements at different energies and within different experimental settings a theoretical analysis is mandatory which accounts for the different experimental acceptance cuts (from various collaborations) and allows for comparing spectra at different centralities and bombarding energies, ultimately bridging the gap from p-p to central heavy-ion collisions.

Within the PHSD we calculate the photon production from the following hadronic

decays:

$$\pi^0 \to \gamma+\gamma,\ \eta \to \gamma+\gamma,\ \eta' \to \rho+\gamma,\ \omega \to \pi^0+\gamma,\ \phi \to \eta+\gamma,\ a_1 \to \pi+\gamma, \quad \Delta \to \gamma+N,$$

where the parent hadrons may be produced in baryon-baryon (BB), meson-baryon (mB) or meson-meson (mm) collisions in the course of the heavy-ion collision or may stem from hadronization. The decay probabilities are calculated according to the corresponding branching ratios taken from the latest compilation by the Particle Data Group [165]. The broad resonances – including the a_1, ρ, ω mesons – in the initial or final state are treated in PHSD in line with their (in-medium) spectral functions and the differential photon or dilepton yield is integrated in time (see below).

Let us briefly describe the evaluation of the photon production in the decays of the Δ-resonance as an important example. The $\Delta \to N\gamma$ width depends on the resonance mass M_Δ, which is distributed according to the Δ spectral function. Starting from the pioneering work of Jones and Scadron [166], a series of models [167–169] provided the mass-dependent electromagnetic decay width of the Δ-resonance in relation to the total width of the baryon. We employ the model of Ref. [168] in the present calculations where the spectral function of the Δ-resonance is assumed to be of relativistic Breit-Wigner form. Furthermore, we adopt the "Moniz" parametrization [170] for the shape of the Δ-spectral function, i.e. the dependence of the width on the mass $\Gamma^{tot}(M_\Delta)$.

The *direct photons* are obtained by subtraction of the decay-photon contributions from the inclusive (total) spectra measured experimentally. So far, the following contributions to the *direct* photons have been identified:

- The photons at large transverse momentum p_T, so called *prompt* or *pQCD* photons, are produced in the initial hard $N+N$ collisions and stem from jet fragmentation; these contributions are well described by perturbative QCD (pQCD). The latter, however, might be modified in $A+A$ contrary to $p+p$ reactions due to a modification of the parton distributions (initial state effect) or the parton energy loss in the medium (final state effect). In $A+A$ collisions at large p_T there may also arise contributions from the induced jet-γ-conversion in the QGP and the jet-medium photons from the scattering of hard partons with thermalized partons $q_{hard} + q(g)_{QGP} \to \gamma + q(g)$; however, these contributions are negligible. As noted above the prompt photons are well modeled by perturbative QCD calculations.

- After the subtraction of the *prompt* photons from the *direct* photon spectra, there is a significant remaining photon yield for $p_T < 3$ GeV, which is denoted as *thermal* photons. These low-p_T photons can be emitted by various partonic and hadronic sources as listed below:

  1. Photons that are radiated by quarks in the interaction with antiquarks and gluons,

     $$q + \bar{q} \to g + \gamma, \qquad q/\bar{q} + g \to q/\bar{q} + \gamma.$$

     In addition, photon production in the bremsstrahlung reactions $q + q/g \to q + q/g + \gamma$ is possible [171]. The implementation of the photon production by the quark and gluon interactions in the PHSD is based on the off-shell

cross sections for the interaction of the massive dynamical quasi-particles as described in Ref. [20, 172]. The photon production rates in a thermal medium – calculated within the DQPM effective model for QCD – are within a factor of 2 similar to the rates obtained by the resummed pQCD approach from Ref. [173] (see Section 4.3.4). Since the quark-gluon-plasma produced in the heavy-ion collisions is strongly-interacting, the Landau-Migdal-Pomeranchuk (LPM) coherence effect can be important, too (cf. Section 4.3.5).

2. All colliding hadronic charges (meson, baryons) can also radiate photons by the bremsstrahlung processes:

$$m + m \to m + m + \gamma \qquad m + B \to m + B + \gamma.$$

These processes have been studied within the HSD/PHSD in Refs. [20–22, 174] in continuation of earlier work at lower energies [175, 176]. The implementation of photon bremsstrahlung from hadronic reactions in transport approaches has been based until recently in the 'soft photon' approximation (SPA). The soft-photon approximation [177–179] relies on the assumption that the radiation from internal lines is negligible and the strong interaction vertex is on-shell which is valid only at low energy (and p_T) of the produced photon. Since the relatively high transverse momenta of the *direct* photons ($p_T = 0.5 - 1.5$ GeV) are most important for a potential understanding of the "direct photon puzzle" we have departed from the SPA in the PHSD [22]. The PHSD results presented in this review have been obtained employing microscopic one-boson-exchange (OBE) calculations instead (cf. Section 4.4.1).

3. Additionally, the photons can be produced in binary meson+meson and meson+baryon collisions. We consider within the PHSD the *direct* photon production in the following $2 \to 2$ scattering processes:

$$\pi + \pi \to \rho + \gamma, \qquad \pi + \rho \to \pi + \gamma, \qquad V + N \to \gamma + N,$$

$$\text{where } V = \rho,\ \phi,\ \omega, \text{ and } N = n, p,$$

accounting for all possible charge combinations (cf. section 4.4.2).

4.2 Dilepton sources in relativistic heavy-ion collisions

Dileptons (e^+e^-, $\mu^+\mu^-$ pairs or virtual photons) can be emitted from all stages of the heavy-ion reactions as well as real photons. One of the advantages of dileptons – compared to photons – is an additional 'degree-of-freedom': the invariant mass M which allows to disentangle various sources. There are the following production sources of dileptons in $p + p, p + A$ and $A + A$ collisions:
1) Hadronic sources:
(i) at low invariant masses ($M < 1$ GeVc) – the Dalitz decays of mesons and

baryons ($\pi^0, \eta, \Delta, ...$) and the direct decay of vector mesons (ρ, ω, ϕ) as well as hadronic bremsstrahlung [174];
(ii) at intermediate masses (1 GeV$< M <$ 3 GeV) – leptons from correlated $D + \bar{D}$ pairs [180], radiation from multi-meson reactions ($\pi+\pi,\ \pi+\rho,\ \pi+\omega,\ \rho+\rho,\ \pi+a_1, ...$) denoted by "$4\pi$" contributions [181–184];
(iii) at high invariant masses ($M >$ 3 GeV) – the direct decay of vector mesons ($J/\Psi, \Psi'$) [185] and initial 'hard' Drell-Yan annihilation to dileptons ($q + \bar{q} \rightarrow l^+ + l^-$, where $l = e, \mu$) [186].
2) 'thermal' QGP dileptons radiated from the partonic interactions in heavy-ion collisions that contribute dominantly to the intermediate masses. The leading processes are the 'thermal' $q\bar{q}$ annihilation ($q + \bar{q} \rightarrow l^+ + l^-, \quad q + \bar{q} \rightarrow g + l^+ + l^-$) and Compton scattering ($q(\bar{q}) + g \rightarrow q(\bar{q}) + l^+ + l^-$) in the QGP [187].

The dilepton production by a (baryonic or mesonic) resonance R decay can be schematically presented in the following way:

$$BB \rightarrow RX \tag{4.1}$$
$$mB \rightarrow RX \tag{4.2}$$
$$R \rightarrow e^+e^-X, \tag{4.3}$$
$$R \rightarrow mX,\ m \rightarrow e^+e^-X, \tag{4.4}$$
$$R \rightarrow R'X,\ R' \rightarrow e^+e^-X, \tag{4.5}$$

i.e. in a first step a resonance R might be produced in baryon-baryon (BB) or meson-baryon (mB) collisions (4.1), (4.2). Then this resonance can couple to dileptons directly (4.3) (e.g., Dalitz decay of the Δ resonance: $\Delta \rightarrow e^+e^-N$) or decays to a meson m (+ baryon) or in (4.4) produce dileptons via direct decays (ρ, ω) or Dalitz decays (π^0, η, ω). The resonance R might also decay into another resonance R' (4.5) which later produces dileptons via Dalitz decay.

The electromagnetic part of all conventional dilepton sources – π^0, η, ω Dalitz decays, direct decay of vector mesons ρ, ω and ϕ – are described in detail in Ref. [188] – where dilepton production in pp and pd reactions has been studied. Actual modifications – relative to Ref. [188] – are related to the Dalitz decay of baryonic resonances and especially the strength of the pp and pn bremsstrahlung since calculations by Kaptari and Kämpfer in 2006 [189] indicated that the latter channels might have been severely underestimated in previous studies on dilepton production at SIS energies. For the results reported here we adopt the parametrizations from Ernst et al. [190] (Eqs. (9) to (13)) for the Dalitz decays of the baryonic resonances which are also incorporated in the PLUTO simulation program of the HADES Collaboration. For the bremsstrahlung channels in pp and pn reactions we adopt the results from the OBE model calculations by Kaptari and Kämpfer in Ref. [189].

4.3 Electromagnetic emission from the strongly interacting QGP

We address the dilepton production by the constituents of the strongly interacting quark-gluon plasma (sQGP). In order to make quantitative predictions for dilepton rates at experimentally relevant low dilepton mass (O(1 GeV)) and strong coupling ($\alpha_S \sim 0.5 \div 1$), we take into account non-perturbative spectral functions and self-energies of the quarks, anti-quarks and gluons. For this purpose, we use parametrizations of the quark and gluon propagators provided by the dynamical quasi-particle model (DQPM) matched to reproduce lattice QCD data. The DQPM describes QCD properties in terms of single-particle Green's functions and leads to the notion of the constituents of the sQGP being effective quasiparticles, which are massive and have broad spectral functions (due to large interaction rates). By "dressing" the quark and gluon lines with the effective propagators, we derive the off-shell cross sections for dilepton production in the reactions $q + \bar{q} \to l^+ l^-$ (Born mechanism), $q + \bar{q} \to g + l^+ l^-$ (quark annihilation with the gluon Bremsstrahlung in the final state), $q(\bar{q}) + g \to q(\bar{q}) + l^+ l^-$ (gluon Compton scattering), $g \to q + \bar{q} + l^+ l^-$ and $q(\bar{q}) \to q(\bar{q}) + g + l^+ l^-$ (virtual gluon decay, virtual quark decay). In contrast to previous calculations of these cross sections, we account for virtualities of all the quarks and gluons. We find that finite masses of the effective quasiparticles not only screen the singularities typical to the perturbative cross sections with massless quarks, but also modify the shape of the dilepton production cross sections, especially at low dilepton mass Q and at the edges of the phase space. Finally, we use the calculated mass-dependent cross sections to identify the dependence of the dilepton rates on the spectral function *widths* of the initial and final quarks and gluons, which has not been estimated so far. The results demonstrate that the multiple partonic scatterings encoded in the broad spectral functions of the dynamical quasiparticles have considerable effect on the dilepton rates.

Since many years the transition between the hadronic phase and the quark-gluon plasma (QGP) as well as the nonperturbative properties of the QGP motivate a large community and justify large-scale experiments, in which heavy nuclei are collided at relativistic energies in order to achieve the high energy densities necessary for the transition to the deconfined state of matter. Electromagnetic probes (i.e. dileptons and photons) are powerful tools to explore the early (hot and dense) stage of the heavy-ion collision, since, unaffected by the final state interaction, they carry to the detector information about the conditions and properties of the environment at the time of their production – encoded in their mass and momentum distributions, – thus providing a glimpse deep into the bulk of the strongly interacting matter [191, 192]. In 1978, E. Shuryak proposed to use dileptons as probes of QGP, after the suggestion was made that the dilepton and photon yields reflect the properties of the medium created in hadron-hadron collisions (see the pioneering works [193–197]).

Real and virtual photons, i.e. dileptons, are emitted over the entire space-time evolution of the heavy-ion collision, from the initial nucleon-nucleon collisions through the hot and dense phase and to the hadron decays after freeze-out. This is both a challenge and advantage of electromagnetic probes. Fortunately, lepton pairs possess an additional degree of freedom (the invariant mass Q^2), which allows to separate

different "physics" by observing the dilepton radiation in different mass ranges. The low mass ($Q < 1$ GeV) spectrum of dileptons – generated in heavy ion collisions – is dominated by the vector meson decays, the production of lepton pairs of high mass ($Q > 3$ GeV) is governed by the perturbative quantum chromodynamics (pQCD), while the dilepton yield in the intermediate mass range ($1 < Q < 3$ GeV) is sensitive to the possible formation of a QGP [198].

Dilepton measurements have possibly provided a signal of the deconfined matter at SPS energies. The NA60 Collaboration [199–201] has recently found that the effective temperature of the dileptons in the intermediate mass range is lower than the $T_{\rm eff}$ of dileptons at lower masses, which are of hadronic origin. This can be explained, if one assumes that the spectrum at the invariant masses above 1 GeV is dominated by the partonic channels in the QGP [185, 202, 203]. In this case, the softening of the transverse mass spectrum with growing invariant mass implies that the partonic channels occur dominantly before the collective radial flow has developed. The assumption that the dilepton spectrum at masses above 1 GeV could be dominated by QGP radiation was supported by the studies within the Hadron-String-Dynamics (HSD) transport approach [1]. While it was shown [204] that the measured dilepton yield at low masses ($Q \leq 1$ GeV) can be explained by the dilepton production in the hadron interaction and decay, there is a discrepancy between the HSD results and the data in the mass range above 1 GeV. This access seen at $Q > 1$ GeV is not accounted for by hadronic sources in HSD – in-medium or free – and might be seen as a signal of partonic matter, manifest already at 158 AGeV incident energy.

Recently, the PHENIX Collaboration has presented first dilepton data from pp and $Au + Au$ collisions at Relativistic Heavy Ion Collider (RHIC) energies of $\sqrt{s} =$ 200 GeV [205–208]. The data show a large enhancement over hadronic sources [209] in $Au + Au$ reactions in the invariant mass regime from 0.15 to 0.6 GeV and from 1 to 3 GeV, which could not be explained in the scope of the HSD approach neither by meson decays – in-medium or free – nor by hadronic Bremsstrahlung [204]. It is of interest, whether the excess at RHIC is due to the dominance of sources in the QGP.

First concepts of the QGP were guided by the idea of a system of partons which interact weakly, with pQCD cross sections. Consequently, early predictions of the dilepton emission from QGP relied on perturbative formulae for the cross sections of the virtual photon production in $q + \bar{q}$ and $q + g$ collisions [194, 210, 211]. Due to large running coupling, the next-to-leading order (NLO) gluon-quark interactions contribute considerably in addition to the leading order (Born) mechanism of quark-quark annihilation ($q\bar{q} \to l^+l^-$) to the QGP radiation spectrum [212]. While the effect of multiple scattering of the quark in the plasma (Landau-Pomeranchuk-Migdal effect [213–215]) on the rate of $q\bar{q} \to \gamma^*$ was stressed in [216].

Not long ago, a first attempt was made to calculate directly on the lattice the production of dileptons in the QGP [217]. The suppression at small Q^2 observed on the lattice has attracted a lot of interest, because it is not what one would expect from perturbation theory: The finite thermal masses would indeed produce a drop of the Born term $q + \bar{q} \to \gamma^*$ because of the threshold effect – as predicted [218] in relation to the cut-off in the momentum distribution of quarks and confirmed in effective perturbation theory in the works [33, 219, 220], – but there are higher order processes ($q\bar{q} \to \gamma^* g$, $qg \to \gamma^* q$) that have no threshold and would fill the spectrum at

small Q^2. Also, the rescattering effects can lead to the disappearance of the threshold behavior in the Born ($q\bar{q} \to \gamma^*$) rate [216].

Recent theoretical and experimental works have shown that the QGP as produced in heavy-ion collisions is a strongly interacting many-body system. Indeed, most theoretical estimates of the temperatures, which are reasonably expected to be currently achieved in heavy-ion collisions are not extremely large compared to the QCD scale Λ_{QCD} [221]. In agreement with this expectation, experimental observations at RHIC indicated that the new medium created in ultra-relativistic Au+Au collisions was interacting strongly – even stronger than hadronic matter. Moreover, in line with theoretical studies in Refs. [30, 222, 223] the medium showed phenomena of an almost perfect liquid of partons [224–227] as extracted from the strong radial expansion and elliptic flow of hadrons [224–227]. Studies performed in the framework of lattice QCD [228] have also shown that the high temperature plasma phase is a medium of interacting partons which are strongly screened and influenced by nonperturbative effects even at temperatures as high as $10\,T_c$. Consequently, the concept of perturbatively interacting quarks and gluons as constituents of the QGP had to be reconsidered. Thus one is forced to go beyond pQCD in calculating dilepton production in the strongly interacting QGP.

To some degree a solution can be found in reordering perturbation theory: by expanding correlation functions in terms of effective propagators and vertices instead of bare ones [187]. A powerful resummation technique was developed by Braaten, Pisarsky [229] and Wong [230]. The production of dileptons was calculated at leading order in the effective perturbation expansion in [229], using as the effective propagators the bare ones plus one loop corrections evaluated in the high-temperature limit [231–234]. In this approach the singularity of the production cross section – that dominates the dilepton rate – is regularized by the thermal masses of quarks m_{th} and gluons m_g, which are in turn determined by the one-loop leading order result in the thermal perturbation theory (HTL). The approach has been extended to the dilepton radiation from non-equilibrium plasmas in [235, 236].

On the other hand, the nonperturbative nature of the sQGP constituents manifests itself in their strong coupling, multiple scattering and modified spectral densities and self energies. In order to take *all* these phenomena into account in the calculation of dilepton production from the QGP, we refrain from a fixed order thermal loop calculation relying on perturbative self-energies (calculated in the limit of infinite temperature) to fix the in-medium masses of the quarks and gluons and pursue instead a phenomenological approach. Indeed, since virtual photon rates need to be evaluated at temperatures that are not very large compared to T_c, it is advisable to adopt values for m_{th}, m_g not from the HTL approximation. Possible alternative strategies are: (i) to treat the thermal masses in the calculation of the dilepton rates as phenomenological parameters as in [220] or (ii) to obtain them from fits of the lattice QCD entropy by an equation of state corresponding to a gas of quasiparticles (massive quarks and gluons) as in Refs. [237, 238] or (iii) *dynamical* quasi-particles (massive and *broad* quarks and gluons) as in Refs. [33, 219].

In the latter approach – followed here, – the (multiple) strong interactions of quarks and gluons in the sQGP are encoded in their effective broad spectral functions. The effective propagators, which are understood as resummed propagators in a hot QCD

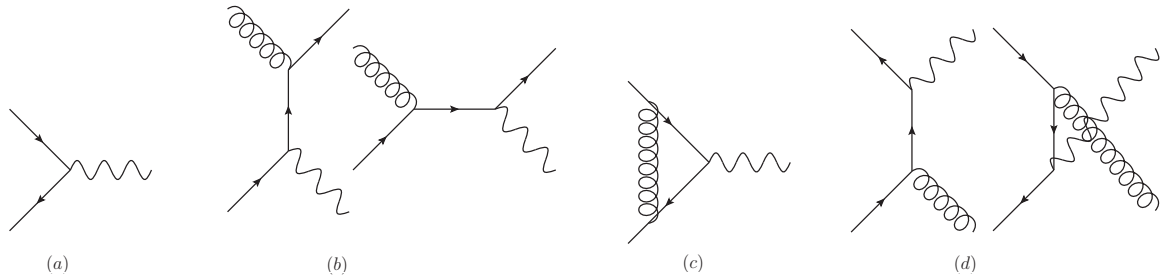

Figure 4.1: Perturbative QCD diagrams contributing to the dilepton production up to the order $O(\alpha_S)$: (a) Drell-Yan mechanism, (b) gluon Compton scattering (GCS), (c) vertex correction, (d) quark annihilation with gluon Bremsstrahlung. Virtual photons (wavy lines) split into lepton pairs, spiral lines denote gluons, arrows denote quarks. In each diagram, the time runs from left to right.

environment, have been extracted from lattice data in the scope of the Dynamical QuasiParticle Model (DQPM) in Ref. [32]. The DQPM describes QCD properties in terms of single-particle Green's functions (in the sense of a two-particle irreducible (2PI) approach) and leads to a quasi-particle equation of state, which reproduces the QCD equation of state extracted from Lattice QCD calculations. According to the DQPM, the constituents of the sQGP are strongly interacting massive partonic quasi-particles with broad spectral functions.

Let us note that we will study the dilepton production in the interaction of quarks and gluons in the sQGP, while explicitly taking into account their finite *widths*. The non-zero width of quark spectral functions reflects their strong interaction, which is manifest in the elastic scattering as well as in the virtual gluon emission. By dressing the external partonic lines in the dilepton production processes ($q+\bar{q} \to l^+l^-$, $q+\bar{q} \to g+l^+l^-$, $q+g \to q+l^+l^-$) with spectral functions we study the effect of the partonic interactions in the plasma on its dilepton radiation, especially in the interesting region of low Q^2. Certain aspects of the dilepton production by partons with finite masses have been studied in earlier works [186, 220, 239–241], but here we will extend these studies by assigning finite masses to *all* parton lines and, more importantly, by going beyond the zero width approximation for initial and finite partons. Thus we will be able to test to what extend the properties of the quark and gluon quasi-particles can be seen in the dilepton rates, e.g. due to large phase-space corrections, broad spectral function widths as well as a different dependance of the strong coupling on the temperature T of the medium.

For this purpose we first derive the off-shell cross sections of $q+\bar{q} \to l^+l^-$, $q+\bar{q} \to g+l^+l^-$, $q+g \to q+l^+l^-$ ($\bar{q}+g \to \bar{q}+l^+l^-$), $q \to q+g+l^+l^-$ ($\bar{q} \to \bar{q}+g+l^+l^-$) and $g \to q+\bar{q}+l^+l^-$ by calculating them for the arbitrary virtualities of external quarks and gluons, while dressing the internal lines with effective self energies. Consequently, we take into account the non-zero widths of initial and final state partons by convoluting the obtained cross sections with the effective spectral functions. Using the DQPM parametrizations for the quark(gluon) self-energies, spectral functions and interaction strength, we calculate the dilepton production from partonic interactions in the sQGP in the first order of electromagnetic coupling, i.e. incorporating only a single photon

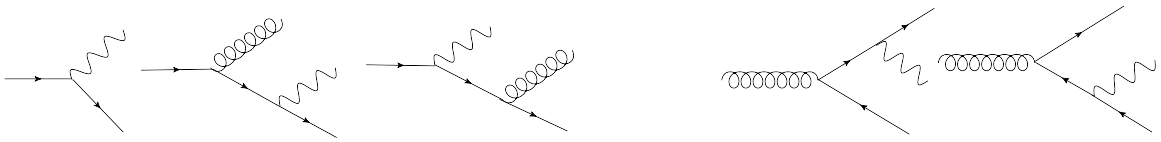

Figure 4.2: Diagrams contributing to the dilepton production by virtual quasi-particles in addition to the ones presented in Fig. 4.1. Lhs: the decay of a virtual quark; Rhs: the decay of a virtual gluon. Virtual photons (wavy lines) split into lepton pairs, spiral lines denote gluons, arrows denote quarks.

line. Verification of Ward identities in general for parton interaction within the DQPM model is beyond the scope of this publication and will be addressed elsewhere. For the current study, we check the gauge invariance of the final dilepton rates numerically, by varying the gauge parameter.

In the context of the hot QGP the perturbative diagrams for the dilepton production at order up to $O(\alpha_S)$ are illustrated in Fig. 4.1. Let us briefly summarize the differences of our phenomenological approach from the standard pQCD:

- (a) we take into account full off-shell kinematics, in particular the transverse motion and virtualities (masses) of the partons,

- (b) quark and gluon lines are dressed with nonperturbative spectral functions: the cross sections derived for arbitrary masses of all external parton lines are integrated over these virtualities weighted with spectral functions (see e.g. Refs [174, 186] for an introduction to the method); the internal lines are dressed with the real parts of the DQPM self energies,

- (c) vertices are modified compared to pQCD by replacing the perturbative coupling (that runs with the momentum transfer) with the full running coupling α_S that depends on the temperature T according to lattice data parametrization by [32], while the temperature is related to the local energy density ϵ by the lQCD equation of state. Note that close to T_c the full coupling increases with decreasing temperature much faster than the pQCD prediction.

- (d) Due to the broad width for quarks and gluons in the sQGP [33] – which is the consequence of their high interaction rate,– there are non-vanishing contributions also from the processes of the decays of virtual quarks ($q \to q + g + l^+l^-$) and gluons ($g \to q + \bar{q} + l^+l^-$), which are forbidden kinematically in pQCD (see Fig. 4.2).

This section is organized as follows. The analysis of the off-shell kinematics and the calculations of the off-shell cross sections (i.e. elementary cross sections for arbitrary values of quark and gluon off-shellness) are calculated in the subsection 4.3.2 for each of the gluon bremsstrahlung processes separately. On the other hand, in the limit of a high hard scale Q^2, the off-shell cross sections should approach the perturbative ones [242, 243]. In this spirit the off-shell cross sections will be compared to the

perturbative ones throughout the subsection 4.3.2. Accordingly, we first recapitulate the corresponding pQCD results first in the subsection 4.3.1.

In the Subsection 4.3.3 we will calculate the dilepton radiation rates in the (thermalized) sQGP to give a simple example for an application of the derived off-shell cross sections and to illustrate the relative importance of the different processes. We point out, however, that the considerations in the thermal medium will probably be not realistic enough to allow for a proper description of the hot and dense early phase of relativistic heavy-ion collisions, where the sQGP is formed. A quantitative comparison to the experimental data and reliable conclusions on the relative contribution of various sources to the experimentally observed thermal dilepton spectrum [199–201, 205–208] requires to account for the non-equilibrium dynamics of the heavy-ion collision in its full complexity by use of microscopic transport models, which will be done in the following chapters of this thesis. The main purpose of the current section is to present an effective approach for the off-shell photon and dilepton production in the interactions of dynamical quasi-particles as constituents of the sQGP. The qualitative analysis of the relative importance of different processes in section 4.3.3 should be understood as an illustration of the present results rather than a quantitative prediction for the dilepton yield from heavy-ion collisions.

Section 4.3.3 is devoted to analyzing the effect of finite quark and gluon widths on the dilepton rate explicitly. In the end of the Section, we summarize the results and their possible implications.

4.3.1 Dilepton and photon production by perturbative partons

In the present Section, we remind the cross sections and kinematics of the following partonic mechanisms for dilepton production in the standard pQCD:

1. Born mechanism of quark annihilation ($q + \bar{q} \to \gamma^*$),
2. quark + anti-quark annihilation with gluon Bremsstrahlung in the final state ($q + \bar{q} \to g + \gamma^*$),
3. Gluon Compton scattering ($q + g \to \gamma^* + q$ and $\bar{q} + g \to \gamma^* + \bar{q}$).

Born term

The leading order pQCD mechanism for the dilepton production in the partonic phase is the same as for the well known Drell-Yan (DY) process [244]: quark and antiquark annihilate into a lepton pair ($q\bar{q} \to l^+l^-$), as presented by the diagram (a) in Fig 4.1. The leading order leading twist pQCD result for the cross section of DY dilepton production is

$$\left(\frac{d^3\hat{\sigma}(q\bar{q} \to l^+l^-)}{dQ^2 dx_F dq_T^2}\right)^{\rm DY}_{\rm on\text{-}shell} = \frac{4\pi\alpha^2 e_q^2}{9Q^4}\frac{x_1x_2}{x_1+x_2}(1-x_1x_2) \times\delta(q_T^2)\delta\left(Q^2 - x_1x_2S_{NN}\right)\delta\left(x_F - \frac{x_2-x_1}{1-x_1x_2}\right), \quad (4.6)$$

where α is the electromagnetic fine structure constant, e_q the fractional quark charge, the lepton pair has invariant mass Q^2 and transverse momentum q_T. The formula (1) is written in the collinear approximation. Generalizations to the final intrinsic transverse momentum are possible (see [186] and references therein).

In collinear pQCD, the off-shellness, mass and transverse momentum of the annihilating quark and antiquark are neglected, and, therefore, the incoming parton momenta are simply related to the momenta of colliding nuclei as $p_{q(\bar{q})} = x_i P_A/A$. In this case, the parton momentum fractions x_1 and x_2 are related to the virtuality and x_F of the produced photon as (cf. delta-functions in (4.6)):

$$Q^2 = s = x_1 x_2 S_{NN}; \tag{4.7}$$

$$x_F = (x_2 - x_1)/(1 - x_1 x_2); \tag{4.8}$$

s denotes the invariant energy for the partonic process; S_{NN} – for the hadronic one; $x_F = q_z/(q_z)_{max}$; $q_z > 0$, if $x_2 > x_1$. The denominator of the x_F definition in (4.8) is omitted in some works, where an approximate definition $x_F \approx 2q_z/\sqrt{S_{NN}}$ is used.

The kinematical limits for this process are

$$S_{NN} \geq Q^2, \ |x_F| \leq 1, s = Q^2. \tag{4.9}$$

Note that in pQCD – both collinear and 'intrinsic k_T' approach – partons are bound by the on-shell condition

$$p_q^2 = E_q^2 - \vec{p}_q^2 = 0$$

(where the current quark mass is negligible). In Section 3 we will depart from the on-shellness and will consider quarks and gluons as dynamical quasi-particles that can assume arbitrary values of virtualities p^2, distributed according to phenomenological spectral functions.

Gluon Bremsstrahlung

The pQCD cross section of the *gluon Bremsstrahlung* process $\bar{q}q \to g + \mu^+\mu^-$ is [245, 246]

$$\left(\frac{d^2\hat{\sigma}(q\bar{q} \to gl^+l^-)}{dQ^2 d\cos\Theta}\right)^{\text{gBr}}_{\text{on-shell}} = \frac{8\alpha^2 e_q^2 \alpha_S}{27Q^2} \frac{s - Q^2}{s^2 \sin^2\Theta} \times \left(1 + \cos^2\Theta + 4\frac{Q^2 s}{(\hat{s} - Q^2)^2}\right), \tag{4.10}$$

where s is the total energy squared of the colliding partons, and Θ is the scattering angle of the outgoing lepton pair with respect to the incoming quark momentum in the quark center-of-mass system (CMS). Note that the cross section (4.10) can be written

in terms of the Mandelstam variables s, t and u as [210]

$$\left(\frac{d^2\hat{\sigma}(q\bar{q}\to gl^+l^-)}{dQ^2dt}\right)^{\rm gBr}_{\rm on\text{-}shell} = \frac{8\alpha^2e_q^2\alpha_S}{27Q^2}\frac{(t-Q^2)^2+(u-Q^2)^2}{s^2tu} \times\delta\left(s+t+u-Q^2\right) \tag{4.11}$$

$$= \frac{8\alpha^2e_q^2\alpha_S}{27Q^2s^2}\left(\frac{t}{u}+\frac{u}{t}+\frac{2sQ^2}{tu}\right) \times\delta\left(s+t+u-Q^2\right), \tag{4.12}$$

which coincides with the QED cross section for the virtual Compton scattering up to the color factor and the crossing transformation [247]. Here we denote the momenta of the incoming quark and antiquark as p_1 and p_2, the momenta of the outgoing gluon and virtual photon as k and q, $s=(p_1+p_2)^2$, $t=(p_1-q)^2$, $u=(p_2-q)^2$. The δ-function $\delta(s+u+t-Q^2)$ reflects the on-shell condition for the partons:

$$p_1^2+p_2^2+k^2=0. \tag{4.13}$$

The collinear divergence of the gluon Bremsstrahlung cross section for $t\to 0$ and $u\to 0$ (i.e. $\cos\Theta\to\pm1$) is obvious; a cut-off Λ^2 on $|\cos\Theta|$ can be used in order to regularize it. Another divergence in the perturbative expression (4.11) is the infrared (IR) divergence for the energy of the gluon $k^0\to 0$ due to the vanishing quark and gluon masses. Indeed, if all the partonic masses are neglected, we have in the CMS:

$$t=k^0(-\sqrt{s}+\sqrt{s}\cos\Theta_2)\to 0 \text{ at } k^0\to 0. \tag{4.14}$$

These divergences (the soft and collinear ones) can be remedied by introducing a small finite gluon mass μ_{cut} (cf. the plasmon mass in [221]). Indeed, the gluon thermal mass μ plays the role of a natural cut-off in the sQGP (cf. section 4.3.2).

At this point, a note on the soft gluon resummation is due. In standard pQCD calculations *real* gluon emission leads to large logarithms $\log Q^2/q_T^2$ when q_T is small. Therefore, fixed order perturbation theory breaks down and the logarithms must be resummed. In the approximation of collinear soft gluons with strongly ordered transverse momenta the resummation leads to the Sudakov factor. However, the strongly k_T-ordered phase space, which ignores overall transverse momentum conservation, is not the dominant configuration at small q_T. A correct resummation of logarithms can be achieved in b-space [248]. On the other hand, if the gluons have a finite thermal mass, as is realized in the DQPM model, the resummation is not necessary, since the divergence at $q_T\to 0$ is regularized.

Gluon Compton scattering

In QED, the Compton process refers to elastic scattering of a photon off a charged object, and has proven to be very important as it provided early evidence that the electromagnetic wave is quantized [249, 250]. In QCD, the corresponding process is the *gluon Compton scattering* $g+q(\bar{q})\to q(\bar{q})+\gamma^*$. The cross section in leading twist

of pQCD [245] is given by:

$$\left(\frac{d^2\hat{\sigma}(g+q)}{dQ^2 d\cos\Theta}\right)^{\rm GCS}_{\rm on\text{-}shell} = \frac{\alpha^2 e_q^2 \alpha_S}{18Q^2}\frac{s-Q^2}{s^2(1+\cos\Theta)} \times \left\{\frac{2s}{s-Q^2} + \frac{s-Q^2}{2s}(1+\cos\Theta)^2 - \frac{2Q^2}{s}(1-\cos\Theta)\right\}. \quad (4.15)$$

In terms of Mandelstam variables [210] it reads:

$$\left(\frac{d\hat{\sigma}(g+q)}{dQ^2 dt}\right)^{\rm GCS}_{\rm on\text{-}shell} = \frac{e_q^2\alpha^2\alpha_S}{9Q^2}\frac{s^2+t^2+2Q^2u}{-s^3t}\,\delta\left(s+t+u-Q^2\right), \quad (4.16)$$

which is obviously related by crossing transformation to (4.12).

4.3.2 Cross sections for dilepton production by off-shell quasiparticles.

Let us now proceed to the calculation of the dilepton production by effective strongly interacting partonic quasiparticles with broad spectral functions. Dilepton radiation by the dynamical quasiparticles proceeds via the elementary processes illustrated in Figs. 4.1 and 2: the basic Born $q+\bar{q}$ annihilation mechanism, Gluon Compton scattering ($q+g \to \gamma^* + q$ and $\bar{q}+g \to \gamma^* + \bar{q}$), quark + anti-quark annihilation with gluon bremsstrahlung in the final state ($q+\bar{q} \to g+\gamma^*$); virtual quark and virtual gluon decays. We recall that, in leading order the 'dressed propagators' and strong coupling lead to substantial phase-space corrections; furthermore, the relative contribution of different channels is expected to change significantly as a function of Q^2 due to different kinematical thresholds.

Ultimately, we are interested in the dilepton yield of the strongly coupled quark-gluon plasma. Due to the factorization property proven in Ref. [221], the dilepton emission from the QGP – created in a heavy-ion collision – is given by the convolution of the elementary sub-process cross sections (describing quark/gluon interactions with the emission of dileptons) with the structure functions that characterize the properties and evolution of the plasma (encoded in the distribution of the quarks and gluons with different momenta and virtualities):

$$\frac{d^3\sigma^{\rm QGP}}{dQ^2 dx_F dq_T^2} = \sum_{abc}\int d\hat{s}\int_0^\infty dm_1^i\int_0^\infty dm_2^i\int_0^\infty d\mu^f\, F_{ab}(\hat{s},m_1^i,m_2^i) \times {\rm A}_c(\mu^f)\frac{d^3\hat{\sigma}_{abc}(\hat{s},m_1^i,m_2^i,\mu^f)}{dQ^2 dx_F dq_T^2}, \quad (4.17)$$

where m_1^i and m_2^i are the off-shellnesses (i.e. virtualities) of the incoming partons, μ^f is the off-shellness of the outgoing parton, while the indices a,b,c denote quark, anti-quark or gluon so that all the considered mechanisms are covered. The cross sections $\hat{\sigma}_{abc}(\hat{s},m^{i1},m^{i2},\mu^f)$ for the different processes for arbitrary values of parton virtualities will be calculated in the current Section. Consequently – in Sections 4 and 5 – we will

integrate the elementary cross sections according to (4.17) over the motion of partons and over parton virtualities by employing phenomenological structure functions F_{ab} and spectral functions $\mathrm{A}_c(\mu^f)$.

Off-shell $q + \bar{q}$ in the Born mechanism

Let us first consider the general 'off-shell' kinematics, when the participating quarks are massive, with the masses distributed according to the spectral functions. We denote the masses of the quark and the anti-quark as m_1 and m_2. Just as in the 'on-shell' case, the mass of the produced dilepton pair is fixed to the invariant energy of the quark-antiquark collision: $s = Q^2$. However, the kinematical limit for the minimal dilepton mass is now higher than in the massless on-shell case:

$$Q_0^2 \equiv s_0 = (m_1 + m_2 + 2m_{lept})^2 > 4m_{lept}^2, \tag{4.18}$$

where m_{lept} is the mass of an electron or muon. Also, the incident current changes:

$$J = \frac{1}{2}\sqrt{(k_1 \cdot k_2)^2 - m_1^2 m_2^2} = \frac{1}{2}\sqrt{(s - m_1^2 - m_2^2)^2 - 4m_1^2 m_2^2},$$

compared to $J = s/2$ in the on-shell approximation.

In addition to the kinematics, the matrix element corresponding to the diagram (a) in Fig. 4.1 is modified in the general off-shell cases compared to the matrix element for the annihilation of massless quarks. The off-shell cross section was first addressed in [186] and reads:

$$\begin{aligned}\left(\frac{d^3\hat{\sigma}(m_1, m_2, \vec{p}_1, \vec{p}_2)}{dQ^2 dx_F dq_T^2}\right)^{DY}_{off-shell} = &\frac{\pi\alpha^2 e_q^2}{3Q^4 N_c \sqrt{(p_1 \cdot p_2)^2 - m_1^2 m_2^2}} \\ &\times \left[2Q^4 - Q^2\left(m_1^2 - 6m_1 m_2 + m_2^2\right) - \left(m_1^2 - m_2^2\right)^2\right] \\ &\times\delta\left(Q^2 - m_1^2 - m_2^2 - 2(p_1 \cdot p_2)\right) \\ &\times\delta\left(x_F - \frac{\sqrt{s_{NN}}}{s_{NN} - Q^2}\left(p_{2z} - p_{1z}\right)\right) \\ &\times\delta\left(q_T^2 - (\vec{p}_{1\perp} + \vec{p}_{2\perp})^2\right).\end{aligned} \tag{4.19}$$

In (4.19), N_c is the number of colors, $e_q(-e_q)$ is the fractional charge of the quark (antiquark), p_i are the 4-momenta of the annihilating quark and antiquark. For $Q^2 \gg m_1^2, m_2^2$ the expression (4.19) reduces to the leading twist pQCD formula (the 'on-shell' approximation).

The approximation $m_1 = m_2 \to 0$ in Eq. (4.19) is equivalent to restricting oneself to the leading term in the twist expansion, that is, in the case of the unpolarized Drell-Yan process, an expansion in powers of $1/Q$. One can see that in this limit (and additionally using the collinear kinematics $\vec{p}_{1\perp} = \vec{p}_{2\perp} = 0$) we recover the standard pQCD result (4.6).

The strong interaction of partons (reflected in the self-energies) leads to higher-twist corrections to the standard pQCD cross sections [186]. The higher twists by definition are vanishing in the limit of infinite invariant mass of the lepton pair [243]. However, the power-Q^2 suppressed contributions may be large at realistic energies. For

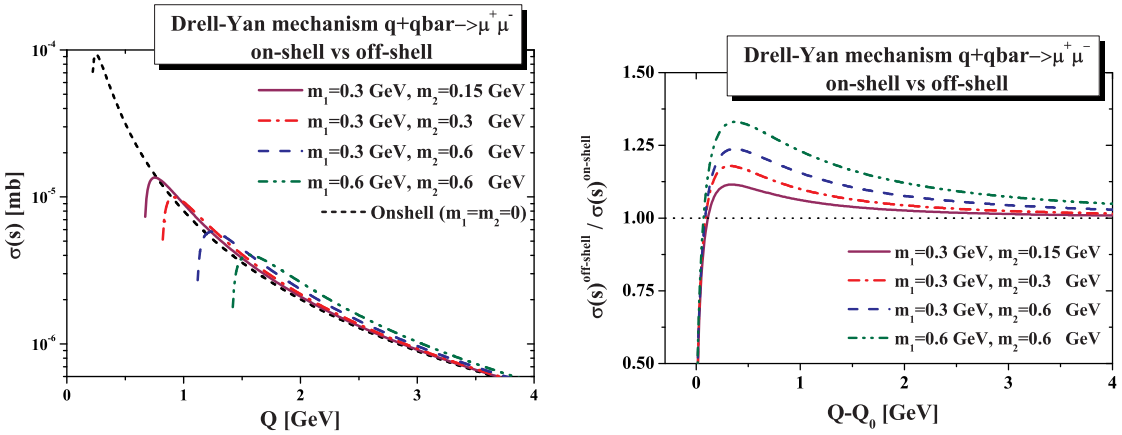

(a) Cross sections (b) Ratios of the cross sections

Figure 4.3: (color online) Dimuon production cross sections in the Drell-Yan channel ($q+\bar{q} \to \mu^+ + \mu^-$). **(a)** The cross section is presented versus the mass of the muon pair Q. The short dashes (black) line shows the on-shell, i.e. the standard perturbative result. The other lines show the off-shell cross section, in which the annihilating quark and antiquark have finite masses m_1 and m_2 with different values: $m_1 = 0.3$ GeV, $m_2 = 0.15$ GeV (solid magenta line), $m_1 = 0.3$ GeV, $m_2 = 0.3$ GeV (dash-dotted red line), $m_1 = 0.3$ GeV, $m_2 = 0.6$ GeV (dashed blue line), $m_1 = 0.6$ GeV, $m_2 = 0.6$ GeV (dash-dot-dot green line). **(b)** The ratio of the off-shell cross section to the on-shell result for the different values of quark and antiquark masses is plotted versus $Q - Q_0$, where Q_0 is the threshold value for the lepton pair mass. Line coding as in the figure (a).

instance, quark off-shellness – arising due to the non-perturbative interaction between the partons – have an effect on the transverse momentum distribution of Drell-Yan lepton pairs in $p + \bar{p}$ collisions [186, 241, 251].

The off-shell cross sections are quantitatively compared to the leading twist results in Fig. 4.3. The dimuon production cross sections in the Drell-Yan mechanism are plotted in Fig. 4.3 (a) versus the mass of the muon pair $Q = \sqrt{s}$. The short dashes (black) line shows the on-shell, i.e. the standard perturbative result. The other lines show the off-shell cross section, in which the annihilating quark and antiquark have finite masses m_1 and m_2 with different values: $m_1 = 0.3$ GeV, $m_2 = 0.15$ GeV (solid magenta line), $m_1 = 0.3$ GeV, $m_2 = 0.3$ GeV (dash-dotted red line), $m_1 = 0.3$ GeV, $m_2 = 0.6$ GeV (dashed blue line), $m_1 = 0.6$ GeV, $m_2 = 0.6$ GeV (dash-dot-dot green line).

The importance of finite mass corrections in the Drell-Yan process is illustrated by the ratio of the integrated cross section $\sigma(Q)$ in Fig. 4.3 (b). The ratio of the off-shell cross section to the on-shell result for the different values of quark and antiquark masses is plotted versus $Q - Q_0$, where Q_0 is the threshold value for the lepton pair mass. The line coding is the same as in the previous figure. With increasing Q^2, the off-shell cross sections approach the leading twist – on-shell – result.

The observed deviations of the derived cross sections from the massless limit at low Q^2 should be seen in the dilepton rates from the sQGP created in heavy-ion collisions

at relatively low dilepton masses. This question can be addressed by convoluting the off-shell cross section (4.19) with effective spectral functions $A(m_i)$ for quarks in plasma and with a model for the momentum distribution of quarks in plasma. We will return to this issue in Sections IV and V.

Off-shell gluon Bremsstrahlung $q\bar{q} \to gl^+l^-$

We start this section by stating the off-shell kinematics of the $q\bar{q} \to gl^+l^-$ process. The dilepton mass range is $4m_{lept}^2 < Q^2 < (\sqrt{s} - \mu)^2$, while the kinematical limits for the momentum transfer t are

$$t_{min}^{max} = -\frac{s}{2}(C_1 \pm C_2), \tag{4.20}$$

where

$$\begin{aligned} C_1 &= 1 - (\beta_1 + \beta_2 + \beta_3 + \beta_4) + (\beta_1 - \beta_2)(\beta_3 - \beta_4), \\ C_2 &= \sqrt{(1 - \beta_1 - \beta_2)^2 - 4\beta_1\beta_2} \\ &\quad \times \sqrt{(1 - \beta_3 - \beta_4)^2 - 4\beta_3\beta_4} \end{aligned} \tag{4.21}$$

with

$$\beta_1 = m_1^2/s,\ \beta_2 = m_2^2/s,\ \beta_3 = Q^2/s,\ \beta_4 = \mu^2/s. \tag{4.22}$$

Additionally, we note that there is a threshold in the CMS energy $\sqrt{s}$ for the $q + \bar{q}$ interaction:

$$s \geq \max\{(m_1 + m_2)^2, (\mu + Q)^2\}. \tag{4.23}$$

The off-shell cross section for the $q\bar{q}$ annihilation *with gluon Bremsstrahlung* in the final state has been calculated in Ref. [172]. We provide here a short description of its evaluation.

Starting from the formula for the unpolarized cross section

$$d\sigma = \frac{\Sigma|\bar{M_{i\to f}}|^2 \varepsilon_1 \varepsilon_2 \Pi \frac{d^3p_f}{(2\pi)^3}}{\sqrt{(p_1p_2)^2 - m_1^2m_2^2}}\ (2\pi)^4 \delta(p_1 + p_2 - \Sigma p_f), \tag{4.24}$$

where the incoming quark and antiquark momenta are p_1 and p_2 and their masses m_1 and m_2, respectively; p_f are the momenta of the outgoing particles, i.e. of the electron (muon) and positron (anti-muon) and gluon. We note that the dilepton production cross section can be easily obtained from the cross section for the production of virtual photons as

$$\frac{d\sigma(l^+l^-)}{dQ^2dt} = \frac{\alpha}{3\pi Q^2}\frac{d\sigma(\gamma^*)}{dt} FF(Q^2, Q_0^2) \tag{4.25}$$

with

$$FF(Q^2, Q_0^2) = \sqrt{1 - \frac{Q_0^2}{Q^2}}\left(1 + \frac{Q_0^2}{2Q^2}\right), \tag{4.26}$$

where $Q_0^2 = 4m_{lept}^2$ and m_{lept} is the lepton mass.

Furthermore, we define the momenta of the internal quark exchanged in the two relevant diagrams (see Fig. 1) as $p_3 \equiv p_1 - q$, $\bar{p_3} \equiv p_1 - p_2 - p_3$ and its mass as m_3.

The final gluon momentum is k and its mass is μ. Then the matrix element of the process $q + \bar{q} \to g + \gamma^*$ is

$$M = M_a + M_b, \tag{4.27}$$

where

$$M_a = -e_q e g_s T^l_{ij} \frac{\epsilon_\nu(q)\epsilon_{\sigma l}(k)}{p_3^2 - m_3^2} u_i(p_1, m_1) \left[\gamma^\nu(\hat{p}_3 + m_3)\gamma^\sigma\right] v_j(p_2, m_2) \tag{4.28}$$

and

$$M_b = -e_q e g_s T^l_{ij} \frac{\epsilon_{\sigma l}(k)\epsilon_\nu(q)}{\bar{p_3}^2 - m_3^2} u_i(p_1, m_1) \left[\gamma^\eta(\hat{\bar{p}}_3 + m_3)\gamma^\nu\right] v_j(p_2, m_2), \tag{4.29}$$

e is the electron charge while e_q is the quark fractional charge; T^l_{ij} is the generator of the SU(3) color group (that will yield the color factor in the cross section); $\epsilon_\nu(q)$ is the polarization vector for the virtual photon with momentum q; $\epsilon_{\sigma l}(k)$ is the polarization vector for the gluon of momentum k and color l; $u_i(p, m)$ is a Dirac spinor for the quark with momentum p, mass m and color i; and $v_i(p, m)$ is the spinor for the anti-quark.

The squared – and summed over spin polarizations as well as over color degrees of freedom – matrix element can be decomposed in the following summands:

$$\sum |M|^2 = \sum M_a^* M_a + \sum M_b^* M_b + \sum M_a^* M_b + \sum M_b^* M_b, \tag{4.30}$$

where the star denotes the complex conjugation.

The spinors for quark states with mass m_i contribute to the expression for the spin-averaged matrix element only in the combinations $\sum \bar{u}(p, m_i)u(p, m_i) = (\hat{p} + m_i)$ (cf [252]) and the correlation functions between the states with different masses does not enter $|M|^2$. Thus we find:

$$\begin{aligned}
\sum M_a^* M_b = &-\frac{e_q^2 e^2 g_s^2 \mathrm{Tr}\{T^2\}}{(p_3^2 - m_3^2)(\bar{p_3}^2 - m_3^2)} \\
&\times \Big[\mathrm{Tr}\left\{(\hat{p_2} - m_2)\gamma_\sigma(\hat{p_3} + m_3)\gamma_\nu(\hat{p_1} + m_1)\gamma^\sigma(\hat{\bar{p}_3} + m_3)\gamma^\nu\right\} \\
&-\frac{1}{Q^2}\mathrm{Tr}\left\{(\hat{p_2} - m_2)\gamma_\sigma(\hat{p_3} + m_3)\hat{q}(\hat{p_1} + m_1)\gamma^\sigma(\hat{\bar{p}_3} + m_3)\hat{q}\right\} \\
&-\frac{A}{k^2}\mathrm{Tr}\left\{(\hat{p_2} - m_2)\hat{k}(\hat{p_3} + m_3)\gamma_\nu(\hat{p_1} + m_1)\hat{k}(\hat{\bar{p}_3} + m_3)\gamma^\nu\right\} \\
&+\frac{A}{k^2 Q^2}\mathrm{Tr}\left\{(\hat{p_2} - m_2)\hat{k}(\hat{p_3} + m_3)\hat{q}(\hat{p_1} + m_1)\hat{k}(\hat{\bar{p}_3} + m_3)\hat{q}\right\}\Big],
\end{aligned} \tag{4.31}$$

$$\sum |M_a|^2 = -\frac{e_q^2 e^2 g_s^2 \mathrm{Tr}\{T^2\}}{(p_3^2 - m_3^2)^2} \times \Big[\mathrm{Tr}\left\{\gamma_\sigma(\hat{p_3} + m_3)\gamma_\nu(\hat{p_1} + m_1)\gamma^\nu(\hat{p_3} + m_3)\gamma^\sigma(\hat{p_2} - m_2)\right\} - \frac{1}{Q^2}\mathrm{Tr}\left\{\gamma_\sigma(\hat{p_3} + m_3)\hat{q}(\hat{p_1} + m_1)\hat{q}(\hat{p_3} + m_3)\gamma^\sigma(\hat{p_2} - m_2)\right\} - \frac{A}{k^2}\mathrm{Tr}\left\{\hat{k}(\hat{p_3} + m_3)\gamma_\nu(\hat{p_1} + m_1)\gamma^\nu(\hat{p_3} + m_3)\hat{k}(\hat{p_2} - m_2)\right\} + \frac{A}{k^2 Q^2}\mathrm{Tr}\left\{\hat{k}(\hat{p_3} + m_3)\hat{q}(\hat{p_1} + m_1)\hat{q}(\hat{p_3} + m_3)\hat{k}(\hat{p_2} - m_2)\right\}\Big]. \quad (4.32)$$

Note that we can readily obtain $\sum M_b^* M_a$ from $\sum M_a^* M_b$ and $\sum |M_b|^2$ from $\sum |M_a|^2$ by the transformation $\{p_3 \to \bar{p_3}, p_1 \to p_2, p_2 \to p_1, m_1 \to -m_2, m_2 \to -m_1\}$. In equations (4.31) and (4.32), A sets the gauge and we will discuss the dependance on A later on. We used the feynpar.m [253] package of the Mathematica program [254] to evaluate the traces of the products of the gamma matrices.

The resulting cross section has been shown explicitly in Ref. [172]. It is too bulky to present here. One can check that the expression for $m_i \to 0$ approaches the leading twist pQCD result, where $\mu_{cut} = \mu$. We illustrate this in Fig. 4.4 where the off-shell cross sections for the quark annihilation with gluon bremsstrahlung at various values of quark and gluon off-shellnesses (masses) are compared to the on-shell (pQCD) result. The dashed black line shows the on-shell cross section for $\mu_{cut} = 0.206$ GeV, the red solid line presents the off-shell cross section for the gluon mass fixed to $\mu = 0.8$ GeV and on-shell quark and anti-quark ($m_1 = m_2 = m_3 = 0$). The blue dash-dotted line gives the off-shell result for $\mu = 0.8$ GeV, $m_1 = m_2 = m_3 = m_q = 0.6$ GeV. One readily notices the shift of the maximum pair mass to a lower value (in order to produce a massive gluon in the final state). For the rest of the Q values, the effect of the quark and gluon off-shellness reaches at most 50% as seen in the ratios of the cross sections, plotted in Fig. 4.4 (b).

Next we compare the double differential off-shell and on-shell cross sections. The results for the transverse momentum distributions of the dileptons are presented in Fig. 4.5. The solid black line shows the differential on-shell cross section with $\mu_{cut} = 0.206$ GeV, the blue dashed line presents the off-shell cross section for the gluon mass fixed to $\mu = 0.8$ GeV and on-shell quark and anti-quark ($m_1 = m_2 = m_3 = 0$). The red dash-dotted line gives the off-shell result for $\mu = 0.8$ GeV, $m_1 = m_2 = m_3 = m_q = 0.6$ GeV. Again, we find the largest effect at the edge of the phase space, at the minimal q_T.

Off-shell gluon Compton scattering $gq \to ql^+l^-$

Kinematic limits for s, t, Q^2 in the off-shell GCS process are analogous to the $q+\bar{q}$ case. In the off-shell case, the dilepton mass range is $4m_{lept}^2 < Q^2 < (\sqrt{s} - m_2)^2$, while the kinematical limits on the momentum transfer t are given by the Eqs. (4.20)-(4.21) with

$$\beta_1 = m_1^2/s,\ \beta_2 = \mu^2/s,\ \beta_3 = Q^2/s,\ \beta_4 = m_2^2/s, \quad (4.33)$$

while

$$s \geq \max\{(m_1 + \mu)^2, (m_2 + Q)^2\},$$

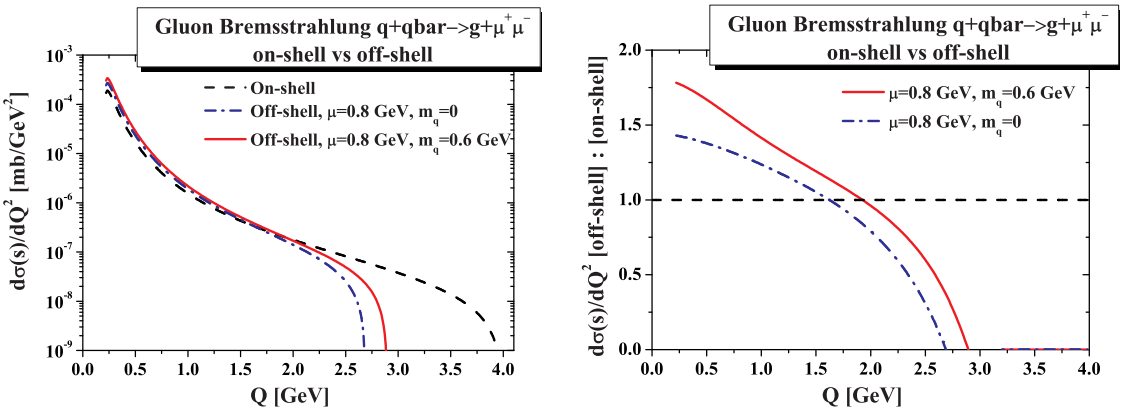

(a) Cross sections (b) Ratios of the cross sections

Figure 4.4: (color online) Comparison of off-shell and on-shell gluon Bremsstrahlung $q + \bar{q} \to g + \mu^+\mu^-$ cross sections at $\sqrt{s} = 4$ GeV. **(a)** The dashed black line shows the on-shell cross section with $\mu_{cut} = 0.206$ GeV, the blue dash-dotted line presents the off-shell cross section for the gluon mass fixed to $\mu = 0.8$ GeV and on-shell quark and anti-quark ($m_1 = m_2 = m_3 = 0$). The red solid line gives the off-shell result for $\mu = 0.8$ GeV, $m_1 = m_2 = m_3 = m_q = 0.6$ GeV. **(b)** The ratio of off-shell to on-shell cross sections using the same line coding is as in (a).

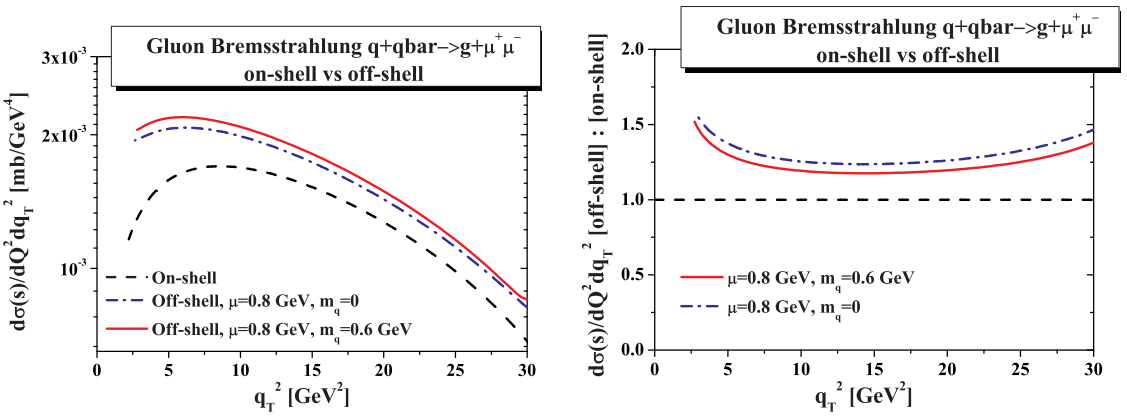

(a) Cross sections (b) Ratios of the cross sections

Figure 4.5: (color online) Comparison of the transverse momentum distributions of muon pairs produced in the gluon Bremsstrahlung $q+\bar{q} \to g+\mu^+\mu^-$ channel in the off-shell and on-shell cases. **(a)** The dashed black line shows the differential on-shell cross section with $\mu_{cut} = 0.206$ GeV, the blue dash-dotted line presents the off-shell cross section for the gluon mass fixed to $\mu = 0.8$ GeV and on-shell quark and anti-quark ($m_1 = m_2 = m_3 = 0$). The red solid line gives the off-shell result for $\mu = 0.8$ GeV, $m_1 = m_2 = m_3 = m_q = 0.6$ GeV. **(b)** The ratio of off-shell to on-shell cross sections using the same line coding.

where m_1 (m_2) is the mass of the incoming (outgoing) quark and μ is the mass of the gluon.

The cross sections for $g + q \to q + l^+ + l^-$ and $g + \bar{q} \to \bar{q} + l^+ + l^-$ are readily obtained from gluon bremsstrahlung cross section by the crossing transformation.

Virtual gluon decay $g \to q\bar{q}l^+l^-$ and virtual quark decay $q \to gql^+l^-$

Although the process of real gluon decay $g \to q + \bar{q} + l^+l^-$ is forbidden kinematically for perturbative particles, it has a finite region of phase space, if the gluon is off-shell due to its broad with and finite pole mass. Analogously, the virtual quark decay is also possible in the off-shell case. We present the Feynman diagrams for the corresponding processes in Fig. 4.2. The off-shell cross sections for these processes can straightforwardly be obtained from the gluon bremsstrahlung by the crossing relation. For example, the cross section for $q \to gql^+l^-$ is obtained from $q \bar{\to} gl^+l^-$ by changing $p_2 \to -p_2$.

Note that, in order to obtain the dilepton rates, the elementary cross sections have to be consequently convoluted with the effective spectral functions for quarks and gluons. The magnitude and shape of the contributions of the virtual decays to the dilepton rates is very sensitive to the final choice of the spectral function. In the DQPM the contribution from gluon decay is higher than that from virtual quark decay, since the gluonic quasi-particles are more massive and broader than the quarks [33], and thus the kinematically allowed region is larger for the virtual gluon than for the virtual quark decay.

On the other hand, within the DQPM parametrizations for the partonic spectral functions, both processes presented by the diagrams in Fig. 4.2 generate little dilepton yield anywhere except for extremely low masses: $Q \approx 2m_{muon}$. Therefore, we refrain from plotting here the contributions explicitly and also do not consider them in the next section dedicated to a comparison of the yields from different mechanisms.

4.3.3 Dilepton rates from the sQGP

In the following we are going to model the contributions of the different processes to the dilepton yield of the strongly coupled quark-gluon plasma. Using the factorization formula (4.17), we calculate the dilepton emission from the QGP by the convolution of the elementary sub-process cross sections with the distribution of the quarks and gluons with different momenta and virtualities. The elementary cross sections $\hat{\sigma}_{abc}(\hat{s}, m^{i1}, m^{i2}, \mu^f)$ for the different processes have been presented in the previous Section.

In Eq. (4.17) we integrate over the motion of partons, but also over their virtualities by employing phenomenological structure functions F_{ab} that depend on the invariant energy $\hat{s}$ of the partonic sub-process as well as on the virtualities of the incoming partons and the spectral function $\mathrm{A}(\mu^f)$ for the parton in the final state. Here, in principle, should be a two particle correlator, but we work in the 2PI approximation so that the parton in the sQGP can be characterized by a single-particle distribution.

We, therefore, we assume that the plasma structure function can be approximated by

$$F_{ab}(\hat{s}, m_1, m_2) = A_a(m_1) A_b(m_2) \frac{dN_{ab}}{ds}. \tag{4.34}$$

In this context, the quantity $dN_{q\bar{q}}/ds$ has the meaning of the number of $q+\bar{q}$ collisions in the plasma as a function of the invariant energy of these collisions $\sqrt{s}$. Analogously, dN_{gq}/ds denotes the number of $g+q$ collisions.

In order to address the relative importance of the different mechanisms for the dilepton production in the sQGP, we need a quantitative model for the number of $q+\bar{q}$ and $g+q$ ($g+\bar{q}$) collisions as functions of $\sqrt{s}$ of these collisions. On possibility is to use thermal distributions of quarks and gluons in order to estimate the number of parton collisions. We come back to this approach in the end of the present section.

Another possibility it to use dN/ds distributions from the PHSD calculations that occur in a realistic simulation of the heavy-ion collisions at the SPS energy. The maximum of $dN(q+\bar{q})/d\sqrt{s}$ is at $\sqrt{s}\approx 0.5$ GeV and the maximum of $dN(g+q)/d\sqrt{s}$ is at a higher value of $\sqrt{s}\approx 1.2$ GeV, reflecting the fact that the threshold $\sqrt{s_0} = m_a + m_b$ is higher for gq than for qq collisions. Indeed, the gluonic quasi-particles are expected to be more massive than the quark ones [33]. The functional form for $dN/d\sqrt{s}$ is taken as

$$\frac{dN_{ab}}{d\sqrt{s}} = K_{ab}\, s^{1/4}\, \left[(\sqrt{s} - P_{ab})^2 + W_{ab}\right]^{-3.5} \tag{4.35}$$

with ($P_{qq} = 0.5$, $W_{qq} = 1.2$) for $q\bar{q}$ collisions and ($P_{gq} = 1.2$, $W_{gq} = 0.6$) for gq collisions.

In Fig. 4.6 we plot the dilepton spectrum calculated using Eq. (4.17) and the cross sections given in Section 4.3.2 assuming $\alpha_S = 0.4$[1]. One observes that after the convolution with the distribution of possible $\sqrt{s}$ for the $q+\bar{q}$ annihilation in sQGP, the yield of lepton pairs produced in the Bremsstrahlung process is below the leading order Born contribution. Thus, the Born rate is higher in magnitude than that of the gluon Bremsstrahlung process despite the fact that the former one contributes only to lepton pairs with a mass equal to the $\sqrt{s}$.

On the other hand, one notices from Fig. 4.6 that the GCS mechanism is subleading, unless the gluonic content of the plasma is orders of magnitude above the quark content, which is achieved neither at SPS nor at RHIC energies. A very high gluon content might be found at LHC; in this case the GCS process would give a considerable contribution to the dilepton yield.

Let us remind that the running coupling α_S depends on the local energy density ε. The DQPM [32] provides a good parametrization of the QCD running coupling as a function of temperature in the non-perturbative regime for temperatures close to T_c (cf. Fig. 1 in Ref. [32]). Note that close to T_c the full coupling calculated on the lattice increases with the decreasing temperature much faster than the pQCD prediction.

The energy density as a function of temperature has also been calculated on the lattice [255] (cf. Fig. 4.7). A rather simple parametrization for the QCD energy density

[1]The absolute magnitudes of the dilepton rates presented in Figs.10,14,15 and 16 should not be directly compared to experimental data. The analysis of the relative yields serves as an illustration of an application of the off-shell cross sections.

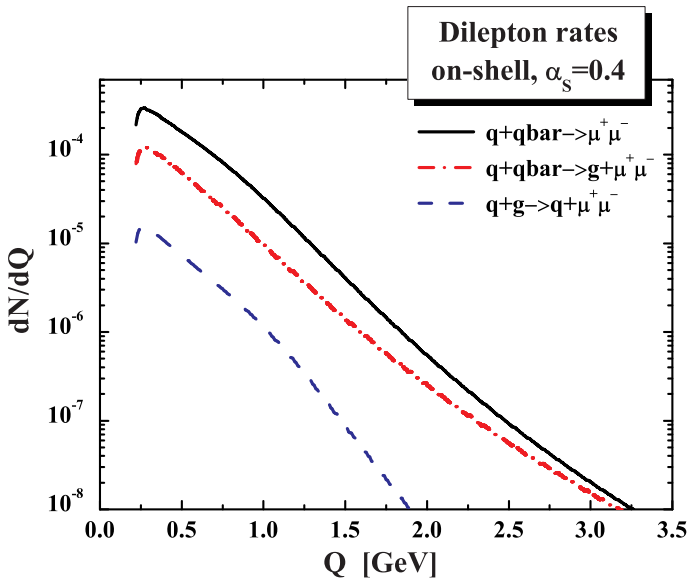

Figure 4.6: (color online) Dimuon rates dN/dQ from QGP calculated using the cross sections in the on-shell approximation, $\alpha_S = 0.4$. Black solid line shows the contribution of the Drell-Yan channel ($q + \bar{q} \to \mu^+\mu^-$), red dash-dotted line represents the contribution of the channel $q + \bar{q} \to g + \mu^-\mu^+$, blue dashed line shows the contribution of the channel $q + g \to q + \mu^+\mu^-$.

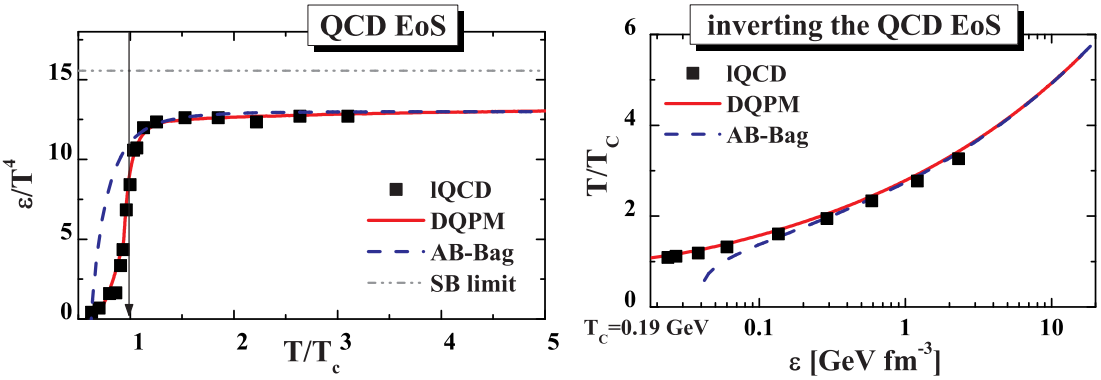

Figure 4.7: (color online) **L.h.s.** QCD energy density versus temperature from lattice QCD (square symbols) [255], the DQPM approach (red solid line) [33] and the 'A-Bag' model (blue dashed line) [256]. The grey dash-dotted line shows the Stefan-Boltzmann limit. The arrow indicates the critical temperature. **R.h.s.** Temperature as a function of the energy density from lattice QCD (square symbols) [255], the DQPM approach (red solid line) [33] and the 'A-Bag' model (blue dashed line) [256].

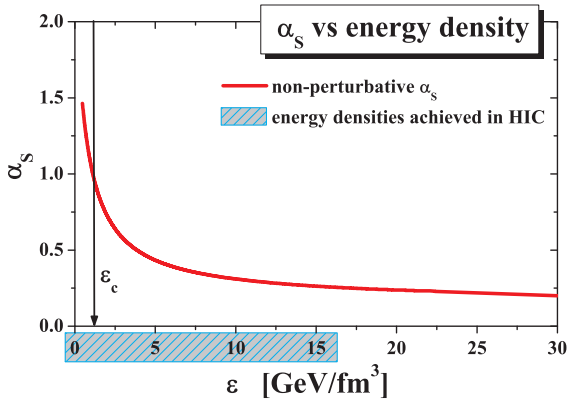

Figure 4.8: (color online) Non-perturbative running coupling as a function of the local energy density ε. The shadowed area indicates the energy densities reached in heavy ion collisions at SPS and RHIC. The arrow shows the critical energy-density.

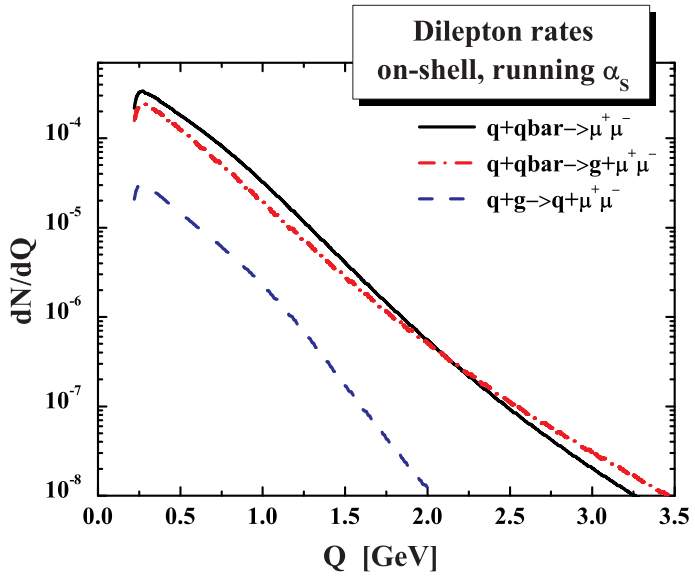

Figure 4.9: (color online) Dimuon rates dN/dQ from the QGP calculated using the cross sections in the on-shell approximation, $\alpha_S = 0.8$. Black solid line shows the contribution of the Drell-Yan channel ($q+\bar{q} \to \mu^+\mu^-$), the red dash-dotted line represents the contribution of the channel $q + \bar{q} \to g + \mu^-\mu^+$, the blue dashed line shows the contribution of the channel $q + g \to q + \mu^+\mu^-$.

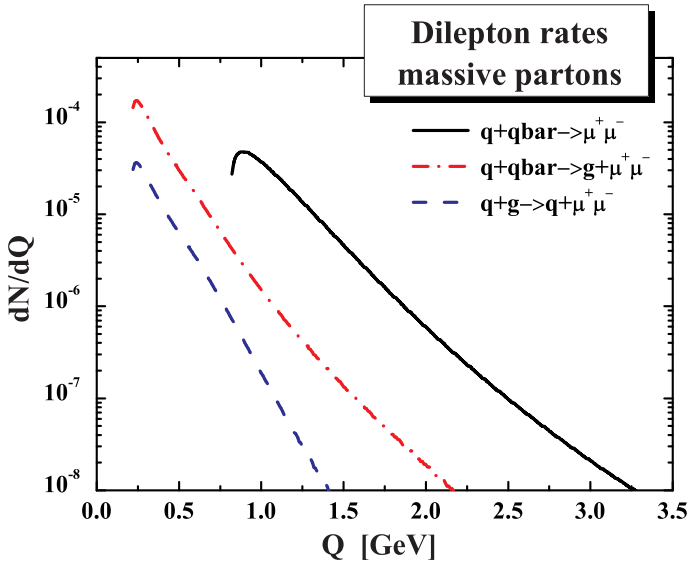

Figure 4.10: (color online) Dimuon rates from the QGP dN/dy beyond the on-shell approximation, $\alpha_S = 0.8$. dN/dQ calculated using the cross sections for quarks and gluons as massive quasi-particles, quark mass parameter being set to $m_q = 0.3$ GeV and gluon mass parameter to $\mu = 0.8$ GeV. The black solid line shows the contribution of the Drell-Yan channel ($q + \bar{q} \rightarrow \mu^+\mu^-$), the red dash-dotted line represents the contribution of the channel $q+\bar{q} \rightarrow g+\mu^-\mu^+$, blue dashed line shows the contribution of the channel $q + g \rightarrow q + \mu^+\mu^-$.

– the "A-Bag model" – is proposed in Ref. [256] and provides a good fit of the SU(3) lattice data above T_c; we extend this model to 3-flavors and also compare to lattice data from Ref. [255] in Fig 4.7. On the other hand, the DQPM model describes the QCD energy density at temperatures even as low as $T \sim T_c$ [33]. In Fig 4.7 we invert the relation and present the temperature as a function of the energy density.

Using this relation, we obtain the running coupling as a function of the energy density ε instead of T/T_c; we present α_S vs. ε in Fig. 4.8. On the other hand, simulations in transport theory [107] have shown that the local energy densities achieved in the course of heavy-ion collisions at SPS and RHIC energies reach at most 20 GeV/fm^3; this region is high-lighted in Fig. 4.8 by a shadowed area. One observes that α_S at the energy densities of interest is on average 0.8. Using this value for α_S, we compare the rates in Fig. 4.9. In this case, the contribution of the $O(\alpha_S)$ diagrams (gluon-Compton scattering $qg \rightarrow q\gamma^*$ and gluon Bremsstrahlung $q\bar{q} \rightarrow g\gamma^*$) is no more non-leading to the Born $q + \bar{q}$ annihilation mechanism!

Next, we plot the dilepton rates – within our approximation for the number of parton collisions in the plasma – for the case of *massive* quarks and gluons in Fig. 4.10. The rates are calculated by convoluting the off-shell cross sections obtained in the previous Section with our model $dN/d\sqrt{s}$. Quarks and gluons are massive quasi-particles, quark masses being set to $m_q = 0.3$ GeV and gluon mass $\mu = 0.8$ GeV. The black solid line shows the contribution of the channel $q + \bar{q} \rightarrow \mu^+\mu^-$, the red dash-dotted line represents the contribution of the channel $q + \bar{q} \rightarrow g + \mu^-\mu^+$, blue dashed line shows the contribution of the channel $q+g \rightarrow q+\mu^+\mu^-$. The rates in the

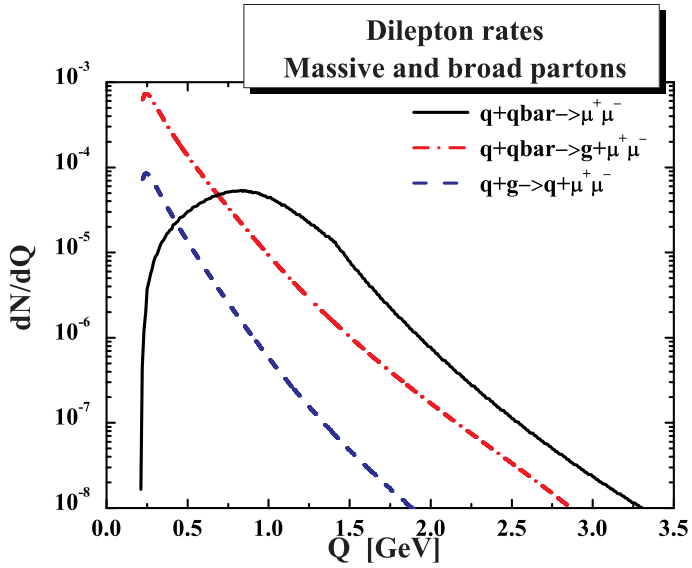

Figure 4.11: (color online) Dimuon rates from the QGP dN/dy beyond the on-shell approximation, $\alpha_S = 0.8$. The distribution dN/dQ calculated in the fully off-shell case of massive *and broad* dynamical quasi-particles. The rates are calculated using the off-shell cross sections convoluted with effective spectral functions of the Breit-Wigner type. The parameters of the spectral functions are: the peak of the quark spectral function is located at 0.3 GeV, the width is $\Gamma = 0.3$ GeV, the peak of the gluon spectral function is at 0.8 GeV, the width to $\Gamma = 0.3$ GeV.

three channels are modified compared to the massless case (cf. Fig. 4.9). In particular, we point the clear threshold behavior of the Born term as noted also by the authors of Refs. [33, 219, 220].

Effect of the finite quark and gluon widths on the QGP radiation

Finally, we calculate the QGP dilepton rate, taking into account not only the finite masses of the partons, but also their *broad spectral functions*, i.e. finite widths. For this purpose, we convolute the off-shell cross sections obtained in section 4.3.2 with $dN/d\sqrt{s}$ and with the spectral functions $A(m)$ in line with the equation (4.17).

The partonic spectral functions are related to the imaginary part of the trace of the effective propagator D^{μ}_{μ} and to the partonic self-energies Σ as follows:

$$A(p) = \frac{1}{\pi}\Im D^{\mu}_{\mu}(p) = -\frac{1}{\pi}\frac{\Im\Sigma(p)}{[p^2 - m^2_{current} - Re\Sigma(p)]^2 + [\Im\Sigma(p)]^2}. \tag{4.36}$$

For the current analysis, we use the approximation of constant real and imaginary parts of the self-energy, which corresponds to constant finite average masses for quarks ($< m_q >$) and gluons (μ) and a constant widths for given temperature T. Within these approximations the spectral function has a Breit-Wigner form. The DQPM fit to lattice data suggests that the partonic widths at temperatures around $1.5 - 2\ T_c$ are of the order of 300 MeV [33].

The results of the numeric convolution of the off-shell cross sections with the spec-

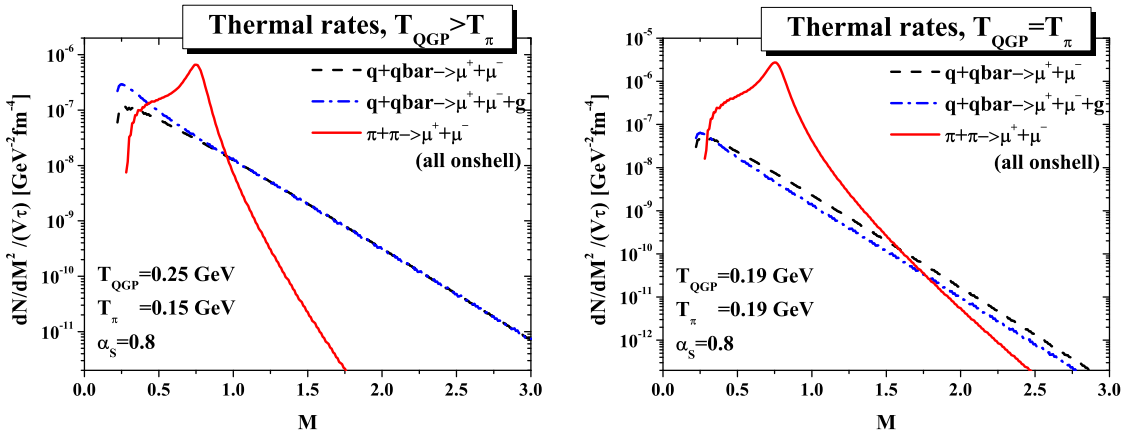

(a) (b)

Figure 4.12: (color online) Rates of dileptons created in $q + \bar{q}$ and $\pi + \pi$ annihilations within a thermalized gas of quarks with temperature T_{QGP} and pions with temperature T_π. (a) $T_{QGP} = 250$ MeV, $T_\pi = 150$ MeV; (b) $T_{QGP} = T_\pi = 190$ MeV.

tral functions and with the $dN/d\sqrt{s}$ distribution are shown in Fig. 4.11 for realistic values of the spectral function parameters: the peak of the quark spectral function is located at 0.3 GeV, the width is $\Gamma = 0.3$ GeV, the peak of the gluon spectral function is at 0.8 GeV, the width $\Gamma = 0.3$ GeV. The rate from the Drell-Yan mechanism is shown by the solid black line, while the $Q(\alpha_S)$ $2 \to 2$ processes are displayed by the dashed blue and dash-dotted red lines. We have checked numerically that the rates for different values of the gauge parameter lie on top of each other.

By dressing the quark and gluon lines with effective spectral functions we model the effect of the quasi-particle interaction, including their multiple scattering. One observes by direct comparison of the Fig. 4.10 and Fig. 4.11 that the effect of parton spectral function width on the dilepton rates is quite dramatic. In particular, the threshold of the Drell-Yan contribution is "washed-out". In this observation we confirm the results of [216]. On the other hand, the effect of the partonic width and/or of multiple scattering on the $2 \to 2$ processes has not been known so far. Wether the predicted shape of the dilepton spectrum in Fig. 4.11 is realized remains to be answered in a forthcoming comparison to experimental data [257].

The cross sections obtained in this study will form the basis of a consistent calculation of the dilepton production in heavy-ion collisions at SPS and RHIC energies by implementing the partonic processes into the transport approach PHSD.

Dilepton rates in thermal equilibrium

Before proceeding to the results of the transport calculations and the comparison to data, we dedicate this subsection to a study of the dilepton spectrum qualitatively in a thermal model. In Fig. 4.12, the dilepton production rates in thermal equilibrium are presented. We assume here that the system evolves through a thermalized system of quark in the hot initial stage of the heavy-ion collision and through the state of a high-density hadron gas in the later phase of the collision.

The main elementary process of dilepton production in a hadron gas is the pion annihilation into dileptons, mediated through vector meson dominance by the rho meson ($\pi + \pi \to \rho \to \gamma^* \to l^+ + l^-$) and controlled by the pole at the rho mass of the pion electromagnetic form factor. For the pion annihilation, we use the standard cross section as, e.g., in Ref. [181] and the Breit-Wigner form factor with the pole mass and width of the ρ meson.

In the partonic sector, the main sources of the dileptons are the reactions of quark-antiquark annihilation with the production of the virtual photon. Considering the temperatures and baryon densities relevant for the SPS energies, we expect in PHSD the contribution of the processes involving gluons to be small compared to the leading $q + \bar{q}$ mechanism of dilepton production (note, however, that at higher energies, such as those of RHIC and LHC, gluons can play an important role in the dilepton production [211]). For the calculation of the QGP yield in the qualitative analysis of this section, the most simple perturbative QCD cross sections are used for the processes $q + \bar{q} \to l^+ l^-$ and $q + \bar{q} \to g + l^+ l^-$, assuming $\alpha_S = 0.8$.

Thus we plot the dilepton yields from the reactions $\pi + \pi$ and $q + \bar{q}$, where the pions and quarks have in general different temperatures T_π and T_{QGP}. The space-time volumes of the two phases are assumed to be approximately equal. In Fig. 4.12(a), the gas of pions is assumed to have the temperature $T_\pi = 150$ MeV, while the gas of quarks the temperature $T_{QGP} = 250$ MeV. In Fig. 4.12(b), we have $T_{QGP} = T_\pi = 190$ MeV.

It has been originally suggested that a 'window' for observing dileptons from the plasma exists in the invariant mass region between the ϕ and J/Ψ peaks [194]. This is supported by the results shown in both Figs. 4.12(a) and 4.12(b). However, we see in Fig. 4.12(a) another region, i.e. $M < 0.5$ GeV, in which the $q + \bar{q}$ annihilation is compatible or even larger than the radiation from the $\pi + \pi$ annihilation; the contribution of the two-to-two process $q + \bar{q} \to g + l^+ l^-$ is especially important. The dominance of the thermal yield from quark interactions at masses below ≈ 0.5 GeV is in agreement with the conclusions of [258, 259]. The transport model results of the next section will clarify which of the equilibrium scenarios presented in Fig. 4.12 – (a) or (b) – gives a closer resemblance to the channel decomposition of the dilepton production within a microscopic simulation.

Of course, the observation of the QGP channels at low mass is possible only after the dilepton yield from the π-, η- and ω-Dalitz decays is removed. Another word of caution is in place here, because in Figs. 4.12 the vacuum properties of the ρ-meson have been used in plotting the $\pi + \pi$ contribution, whereas the ρ-meson properties are expected to be modified in medium. The modification of the ρ will change the size of the new, low mass window of the QGP observation.

4.3.4 Photon production by dynamical quasiparticles

We proceed to the description of *real* photon production in the interactions of quarks and gluons in the quark-gluon plasma, which dominantly proceeds through the quark-antiquark annihilation and the gluon Compton scattering processes:

$$q + \bar{q} \to g + \gamma \qquad q(\bar{q}) + g \to q(\bar{q}) + \gamma,$$

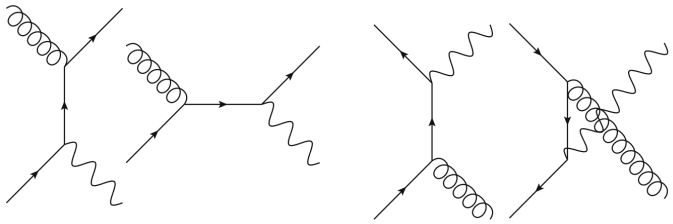

Figure 4.13: Feynman diagrams for the leading partonic sources of *thermal* photons ($q(\bar{q}) + g \to q(\bar{q}) + \gamma$ and $q + \bar{q} \to g + \gamma$) included in the PHSD calculations. The propagators and strong coupling are employed from the DQPM.

that are diagrammatically presented in Fig. 4.13. The evaluation of the cross sections for *dilepton* production by off-shell partons, taking into account finite masses for quarks, antiquarks (with generally $m_q \neq m_{\bar{q}}$) and gluons m_g as well as their finite spectral width (by integrating over the mass distributions) has been carried out in Refs. [172, 241] and presented in the previous section. In order to obtain the cross sections for the *real* photon production, we use the relation between the real photon production cross section and the cross section for dilepton production [260]:

$$\frac{d\sigma(\gamma)}{dt} = \lim_{M\to 0} \frac{3\pi}{\alpha} \frac{M^2}{L(M)} \frac{d^2\sigma(e^+e^-)}{dM^2 dt}, \tag{4.37}$$

where M^2 is the invariant mass squared of the lepton pair (virtual photon), while the kinematical factor $L(M)$ is given by

$$L(M) = \sqrt{1 - \frac{4m_e^2}{M^2}}\left(1 + \frac{2m_e^2}{M^2}\right) \tag{4.38}$$

with m_e denoting the lepton mass.

We take $d^2\sigma(e^+e^-)/dM^2dt$ from Ref. [172] and use relation (4.37) to implement the real photon production in the off-shell quark and gluon interactions into the PHSD transport approach. In each interaction of $q + \bar{q}$ or $q/\bar{q} + g$ the photon production probability and the elliptic flow of the produced photon are recorded differentially in transverse momentum p_T, rapidity y and interaction time t. Let us briefly summarize the differences of our 'effective' approach from the standard pQCD:

- We take into account full off-shell kinematics, i.e. the transverse motion and virtuality of the partons,
- quark and gluon lines in the diagrams in Fig. 4.13 and in the leading-order diagram $q + \bar{q} \to \gamma^*$ (which is relevant only for dilepton production) are dressed with non-perturbative spectral functions and self-energies: the cross sections are derived for arbitrary masses of all external parton lines and integrated over these virtualities weighted with spectral functions (see e.g. Refs [174, 241] for an introduction to the method); the internal lines are dressed with self energies.
- Strong vertices are modified compared to pQCD by replacing the perturbative coupling (that runs with the momentum transfer) with the running coupling

$\alpha_S(T)$ that depends on the temperature T of the medium according to the parametrization of lattice data in Ref. [32], while the temperature T is related to the local energy density $\epsilon(\mathbf{r};t)$ by the lQCD equation of state. Note that close to T_c the effective coupling $\alpha_S(T)$ increases with decreasing temperature much faster than the pQCD prediction.

- Due to the broad widths of quarks and gluons in the sQGP [33] – which is the consequence of their high interaction rate – there are non-vanishing contributions also from the decays of virtual quarks ($q \to q + g + l^+l^-$) and gluons ($g \to q+\bar{q}+l^+l^-$), which are forbidden kinematically in pQCD. However, we presently discard these processes in PHSD.

4.3.5 Thermal photon rates and the LPM effect

Using the cross sections for photon radiation by dressed quarks and gluons in the processes $q\bar{q} \to g\gamma$ and $qg \to q\gamma$ from Ref. [172] we can calculate the differential rate of photons from a thermalized strongly interacting QGP. Fig. 4.14 presents the invariant rate of photons produced from a QGP at the temperature $T = 200$ MeV (red solid line) in comparison to the leading-order Log-resummed perturbative QCD rate (blue solid line) from Arnold, Moore and Yaffe (AMY rate, taken from Ref. [173]). One observes a qualitative agreement between the results of both approaches although the degrees-of-freedom and their couplings are different. We mention that photon rates calculated recently at the NLO in perturbative QCD [261–263] also are approximately in line with those presented in Fig. 4.14 (l.h.s.).

The radiation of photons by charged particles is modified in the medium compared to the vacuum. One of such medium effects is caused by the absence of well-defined incoming and outgoing asymptotic states due to the multiple scattering of particles in a strongly interacting environment. If the subsequent scatterings occur within the time necessary for photon radiation $\tau_\gamma \sim 1/q_0$, then the amplitudes for the emission of photons before and after the charged particle scattering have to be summed coherently. The effect of this destructive interference on the photon spectrum by electrons transversing a dense medium was first studied by Landau and Pomeranchuk in Ref. [213, 214] and Migdal in Ref. [215]. Accordingly, the Landau-Pomeranchuk-Migdal (LPM) effect modifies the spectrum of photons produced in the medium in comparison to the incoherent sum of emissions in quasi-free scatterings, leading especially to a suppression of the low energy photons because the formation time of the photon τ_γ is proportional to the inverse photon energy $1/q_0$. In particular, the LPM effect regularizes the $1/q_0$ divergence of the quasi-free bremsstrahlung spectra. The LPM suppression and the induced thermal mass of the medium quanta (the dielectric effect) together ensure that the photon spectrum is finite in the limit $q_0 \to 0$.

The importance of the LPM effect for the case of dilepton and photon production from QCD systems was shown in Refs. [264–267] long ago. The magnitude of the LPM suppression is governed by the average time between the collisions τ, which in turn is given by the inverse scattering length a or by the inverse average spectral width of the particles γ:

$$\tau = \frac{1}{a} \sim \frac{1}{\gamma}. \tag{4.39}$$

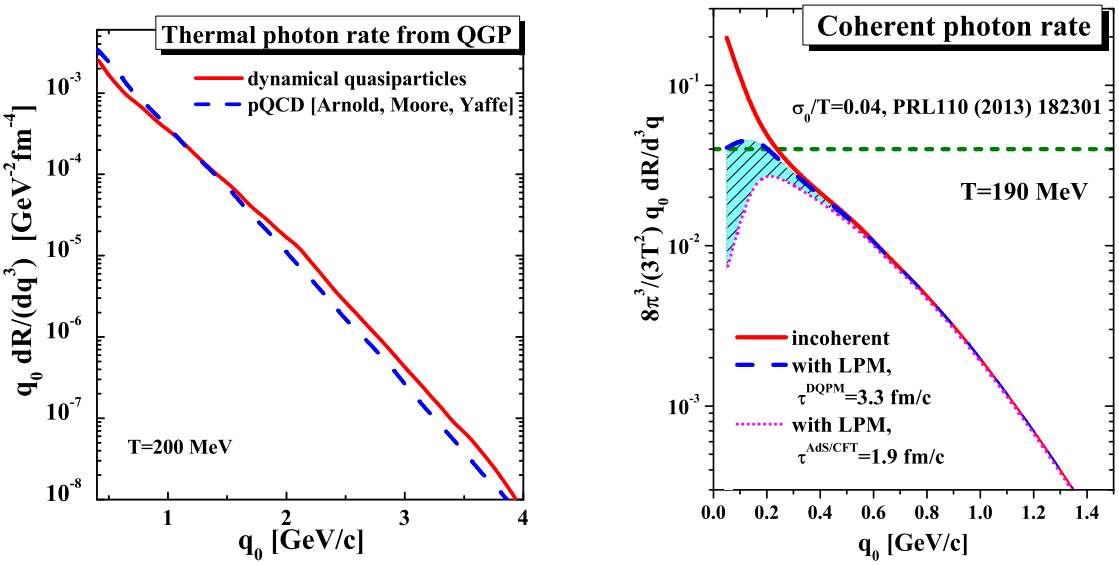

Figure 4.14: (l.h.s.) Invariant rate of photons produced from the strongly-interacting quark-gluon plasma (at temperature T= 200 MeV) consisting of massive broad quasi-particle quarks and gluons (red solid line). The leading-order pQCD rate (blue dashed line) from Ref. [173] (AMY-rate) is shown for comparison. (r.h.s.) Incoherent invariant photon production rate from the strongly-interacting quark-gluon plasma (at temperature T= 190 MeV) consisting of massive broad quasi-particle quarks and gluons (red solid line) scaled by $8\pi^3/(3T^2)$ in order to match the electric conductivity for $q_0 \to 0$ (cf. (4.43)). The blue dashed line and the magenta dotted line show the coherent rates for two assumptions on the average time between the collisions τ, i.e. from the DQPM model (upper, dashed line) and from the AdS/CFT correspondence as a lower limit (dotted line). The figures are taken from Ref. [22].

The LPM suppression is more pronounced in case of small τ, i.e. for high reaction rates γ. Thus we expect it to be important for the emission of photons from the strongly-interacting quark-gluon plasma (sQGP) as created in the early phase of the heavy-ion collision. Indeed, it was shown in Refs. [28, 64] in the scope of the DQPM that the average collision time of partons is as short as $\tau \approx 2-3$ fm/c for temperatures in the range $T = 1-2\ T_c$, where $T_c \approx 158$ MeV is the deconfinement transition temperature. In comparison, the average time between pion collisions in a thermalized pion gas at temperatures $T < T_c$ is above 10 fm/c [264, 265].

Let us now quantify the magnitude of the LPM effect on the spectrum of photons radiated from the QGP as calculated within the PHSD. The coherent photon production rate - taking into account the LPM effect - differs from the incoherent cross section by a suppression factor, which generally depends on the photon energy, temperature and the interaction strength of the constituents. The coherent photon emission rate has been derived in Ref. [264, 265] for an elastically interacting pion gas in the soft photon approximation for the photon radiation amplitudes. The authors of Ref. [264, 265] used the same method for the calculation of the photon emission over the whole trajectory of the charged particle as adopted in the original work by Migdal in Ref. [215]. After averaging over the times between collisions τ, assuming an

exponential distribution,

$$\frac{dW}{d\tau} = ae^{-\tau a}, \tag{4.40}$$

the coherent photon emission rate was found to be

$$\frac{dR}{dq^3} = N\frac{2\alpha_{EM}}{(2\pi)^2}\left\langle v^2 \frac{(1-\cos^2\Theta)}{a^2+q_0^2(1-v\cos\Theta)^2}\right\rangle, \tag{4.41}$$

where the brackets $< . >$ stand for an average over the velocities after the scattering (v, $\cos\Theta$), while N is the number of scatterings and $\alpha_{EM} \approx 1/137$. A realistic parametrization of the data was used for the pion elastic scattering cross section (cf. Section 4.4.1) but the scattering was assumed to be isotropic. We recall that the incoherent rate is obtained from Eq. (4.41) in the limit $a = 0$.

An analytical form of the coherence factor was obtained in Ref. [267] in the model of hard scattering centers, using a quantum mechanical approach to coherently sum the photon amplitudes from all the scatterings. In the thermal medium the spacial distribution of the scattering centers is assumed random. Consequently, the function (4.40) naturally arises in this model for the distribution of times between collisions by a direct calculation of the two-particle correlation function. The quenching factor in the dipole limit ($\vec{q} = 0$) was found to be

$$(G(q_0\tau))^2 = \left(\frac{(q_0\tau)^2}{1+(q_0\tau)^2}\right)^2. \tag{4.42}$$

Although formula (4.42) was obtained in a simple model, it is useful because it correctly captures the dependence of the LPM suppression on the average strength of the interaction given solely by the mean-free-time between collisions τ in the assumption of isotropic collisions.

We recall that the perturbative interaction of quarks and gluons is dominated by small angle scattering due to the massless particle exchange in the t-channel diagrams. In this case the coherence factor for the quark system in the limit of small scattering angles was obtained in Ref. [266]. However, the elastic scattering of dressed quarks in the PHSD is not dominated by the $t \to 0$ pole as in the perturbative case since the gluon mass (of order 1 GeV) acts as a regulator in the amplitude. Accordingly, the angular distribution for quark-quark scattering is closer to an isotropic distribution for low or moderate $\sqrt{s}$ in accordance with the model assumptions of Ref. [267] such that the expression (4.42) should apply as an estimate of the LPM suppression for the photon emission within the PHSD.

In Fig. 4.14 (r.h.s.) we show the photon emission rate in a QGP at the temperature T=190 MeV as calculated in the PHSD as an incoherent sum of the photon emission in quark and gluon scatterings (red solid line) which diverges for $q_0 \to 0$. The blue dashed line gives the same rate with the quenching factor (4.42) applied using $\tau(T) = 1/\Gamma(T) \approx 3.3$ fm/c from the DQPM (for T= 190 MeV). We observe that the suppression – in comparison to the incoherent rate – is visible only for photon energies $q_0 < 0.4$ GeV. For an estimate of the upper limit on the LPM suppression we employ the relaxation time approximation for the ratio of the shear viscosity over entropy

density η/s which gives $\eta/s \approx 0.14$ at T=190 MeV in the DQPM [15, 16]. The lowest bound as conjectured within the AdS/CFT correspondence is $\eta/s = 1/(4\pi) \approx 0.08$. In the relaxation time approximation this corresponds to a lower value of $\tau \approx 1.9$ fm/c. The coherent photon rate in this case is given by the (lowest) magenta dotted line and even shows a peak in the photon rate for $q_0 \approx 0.2$ GeV.

In order to further clarify the strength of the LPM suppression of the photon emission in the sQGP, we use the knowledge of the electric conductivity $\sigma_0(T)$ of the sQGP from the DQPM [64] which is roughly in line with more recent results from lattice QCD (cf. Fig. 6, r.h.s.). We recall that the photon emission rate from a thermal medium is controlled by σ_0 via the relation [268],

$$\frac{\sigma_0}{T} = \frac{8\pi^3}{3T^2} \lim_{q_0 \to 0} \left(q_0 \frac{dR}{d^3q} \right), \tag{4.43}$$

where T is the temperature of the system, q_0 is the photon energy and $\vec{q}$ is the photon momentum. Using the number for σ_0/T from the PHSD at the temperature of T = 190 MeV from Ref. [64] (or Fig. 6, r.h.s.), we obtain a limiting value for the scaled photon emission rate of 0.04 for $q_0 \to 0$ according to formula (4.43) (green short dashed line in Fig. 4.14, r.h.s.). The blue dashed line in Fig. 4.14 – the estimate of the rate based on formula (4.42) and the DQPM average spectral width of the quarks/antiquarks – indeed approaches the limiting value of 0.04 as given by the kinetic calculations of the electric conductivity.

Taking into account some uncertainty in the determination of τ and the expression (4.42), we conclude from Fig. 4.14 (r.h.s.) and analogous calculations at different temperatures that the LPM effect influences the photon production from the QGP for photon energies below $q_0 \approx 0.4$ GeV, but is negligible for higher photon energies. We note in passing that the suppression of the photon spectrum in the hadronic phase is much smaller due to the lower interaction rate, i.e. a longer interaction time τ and thus a lower LPM suppression factor at the same photon energy.

4.4 Cross sections and rates for electromagnetic emission from the hadronic phase

4.4.1 Bremsstrahlung $m + m \to m + m + \gamma$ beyond the soft-photon approximation

We briefly sketch the description of the photon bremsstrahlung in meson+meson scattering beyond the soft-photon approximation [269]. Since pions are the dominant meson species in the heavy-ion collisions [20], we concentrate here on the description of the bremsstrahlung photon production in pion+pion collisions. In order to calculate the differential cross sections for the photon production in the processes of the type $\pi + \pi \to \pi + \pi + \gamma$ we use the one-boson exchange (OBE) model as originally applied in Ref. [270] to the dilepton bremsstrahlung in pion+pion collisions, later on in Ref. [271] to the low-energy photon bremsstrahlung in pion+pion and kaon+kaon collisions. The calculations are based on a covariant microscopic effective theory with

the interaction Lagrangian,

$$L_{int} = g_\sigma \sigma \partial_\mu \vec{\pi} \partial^\mu \vec{\pi} + g_\rho \vec{\rho}^\mu \cdot (\vec{\pi} \times \partial_\mu \vec{\pi}) + g_f f_{\mu\nu} \partial^\mu \vec{\pi} \cdot \partial^\nu \vec{\pi}, \tag{4.44}$$

as suggested in Refs. [171, 270]. Within this model the interaction of pions is described by the exchange of scalar, vector and tensor resonances: σ, ρ and $f_2(1270)$, respectively. Additionally, form factors are incorporated in the vertices in the t- and u-channels to account for the composite structure of the mesons and thus to effectively suppress the high momentum transfers,

$$h_\alpha(k^2) = \frac{m_\alpha^2 - m_\pi^2}{m_\alpha^2 - k^2}, \tag{4.45}$$

where $m_\alpha = m_\sigma$ or m_ρ or m_f is the mass of the exchanged meson and k^2 is the momentum transfer squared.

The cross section for elastic $\pi + \pi \to \pi + \pi$ scattering is given by

$$\frac{d\sigma_{el}(s)}{dt} = \frac{|M_{el}|^2}{16\pi s(s - 4m_\pi^2)}, \tag{4.46}$$

where the matrix element $|M|^2$ is calculated by coherently summing up the Born diagrams of the σ-, ρ- and f_2-meson exchange in t, s and u channels (the u-channel diagrams are needed only in case of identical pions),

$$\begin{aligned} |M_{el}|^2 &= |M^s(\sigma) + M^t(\sigma) + M^u(\sigma) + M^s(\rho) \\ &\quad + M^t(\rho) + M^u(\rho) + M^s(f) + M^t(f) + M^u(f)|^2. \end{aligned} \tag{4.47}$$

Let us define the four-momenta of the incoming pions as $p_a = (E_a, \vec{p}_a)$ and $p_b = (E_b, \vec{p}_b)$, the momenta of the outgoing pions as $p_1 = (E_1, \vec{p}_1)$ and $p_2 = (E_2, \vec{p}_2)$ and the four-momentum of the exchanged resonance (σ, ρ or f_2) as k. The propagators of the massive and broad scalar and vector particles are used to describe the exchange of the σ and ρ mesons (see e.g. Ref. [270]). The resonance f_2 is a spin-2 particle, for which the full momentum-dependent propagator has been derived in Ref. [272]. The polarization sum is

$$\begin{aligned} P_{\mu\nu\alpha\beta} &= \frac{1}{2}(g_{\mu\alpha}g_{\nu\beta} + g_{\mu\beta}g_{\nu\alpha} - g_{\mu\nu}g_{\overline{\alpha\beta}})\frac{1}{2}(g_{\mu\alpha}\frac{k_\nu k_\beta}{m_f^2} + g_{\mu\beta}\frac{k_\nu k_\alpha}{m_f^2} + g_{\nu\alpha}\frac{k_\mu k_\beta}{m_f^2} + g_{\nu\beta}\frac{k_\mu k_\alpha}{m_f^2}) \\ &\quad + \frac{2}{3}(\frac{1}{2}g_{\mu\nu} + \frac{k_\mu k_\nu}{m_f^2})(\frac{1}{2}g_{\alpha\beta} + \frac{k_\alpha k_\beta}{m_f^2}). \end{aligned} \tag{4.48}$$

Following the example of the dilepton production study in Ref. [270], we use the same propagator for the f_2 resonance while additionally accounting for its finite width by adding an imaginary part to the self-energy in accordance with its lifetime.

As a result, the following expressions are obtained for the matrix elements in case of elastic $\pi + \pi$ scattering diagrams (we give here explicitly the t- and s-channel results,

the u-channels can be easily obtained by the crossing relations):

$$\begin{aligned}
M^t(\sigma) &= \frac{-g_\sigma^2 h_\sigma^2(t)\,(2m_\pi^2 - t)^2}{t - m_\sigma^2 + i m_\sigma \Gamma_\sigma}, \qquad M^s(\sigma) = \frac{-g_\sigma^2\,(s - 2m_\pi^2)^2}{s - m_\sigma^2 + i m_\sigma \Gamma_\sigma}, \\
M^t(\rho) &= \frac{-g_\rho^2 h_\rho^2(t)\,(s-u)^2}{t - m_\rho^2 + i m_\rho \Gamma_\rho}, \qquad M^s(\rho) = \frac{g_\rho^2\,(u-t)^2}{s - m_\rho^2 + i m_\rho \Gamma_\rho}, \qquad (4.49) \\
M^t(f) &= \frac{g_f^2 h_f^2(t)}{t - m_f^2 + i m_f \Gamma_f} \frac{1}{2} \left(\frac{2}{3}(2m_\pi^2 - t)^2 - (s - 2m_\pi^2)^2 - (2m\pi^2 - u)^2 \right), \\
M^s(f) &= \frac{g_f^2}{s - m_f^2 + i m_f \Gamma_f} \frac{1}{2} \left(\frac{2}{3}(s - 2m_\pi^2)^2 - (2m_\pi^2 - t)^2 - (2m\pi^2 - u)^2 \right),
\end{aligned}$$

where the Mandelstamm variables are defined as $s = (p_a + p_b)^2 = (p_1 + p_b)^2$, $t = (p_a - p_1)^2 = (p_b - p_2)^2$, $u = (p_a - p_2)^2 = (p_b - p_1)^2$. We point out that the formulae (4.49) are compact, because the masses of all pions were assumed to be equal to m_π and the energy-momentum conservation $p_a + p_b = p_1 + p_2$ has been used. These conditions are not satisfied for the off-shell $\pi + \pi \to \pi + \pi$ subprocess, which we encounter in the subsequent calculation of the bremsstrahlung photon production $\pi + \pi \to \pi + \pi + \gamma$. For the actual calculation we obtained the off-shell generalizations $M(p_a, p_b, p_1, p_2)$ of the formulae (4.49), which are too lengthy to be presented here explicitly.

A reduced version of the model with the exchange of only two resonances – the scalar σ and the vector ρ meson – was used by the authors of Ref. [271] to calculate the rate of the photon production from the $\pi + \pi \to \pi + \pi + \gamma$ process at low transverse momenta of the photons ($p_T < 0.4$ GeV). This approximation is suitable at low p_T because the photon rate in this kinematical region is dominated by pion collisions of low center-of-mass energy $\sqrt{s}$, for which the contribution of the f_2-exchange is small. However, relatively high transverse momenta of photons $p_T = 1 - 2$ GeV are of interest for our goal of clarifying the "puzzling" high elliptic flow of *direct* photons. Therefore, we use the OBE model with three mesons as interaction carriers (including the tensor particle $f_2(1270)$) in the PHSD calculations.

Phenomenological coupling constants, masses and widths of the three interaction-carriers – entering the Lagrangian (4.44) – have to be fixed to the integrated energy-dependent cross section for pion+pion elastic scattering $\sigma_{el}(\sqrt{s})$, which is known experimentally as a function of $\sqrt{s}$). We present in Fig. 4.15 (l.h.s.) the integrated cross section for $\pi + \pi$ elastic scattering in two versions of the OBE model described above: taking into account the 2 resonances σ, ρ (dashed blue line) and taking into account the 3 resonances σ, ρ and f_2 (solid red line). Fitting the parameters of both variants of the OBE model (with two- or three-resonance exchange) to the data from Refs. [273, 274] we find the best-fit parameters: $g_\sigma m_\sigma = 2.0$, $m_\sigma = 0.525$ GeV, $\Gamma_\sigma = 0.100$ GeV, $g_\rho = 6.15$, $m_\rho = 0.775$ GeV, $\Gamma_\rho = 0.15$ GeV, $g_f m_f = 8.0$, $m_f = 1.274$ GeV, $\Gamma_f = 0.18$ GeV. The values of the masses and widths suggest an identification of the ρ-resonance to the ρ-meson and of the particle f_2 to the $f_2(1270)$ in the particle data book [165]. One sees in Fig. 4.15 (l.h.s.) that the tensor particle f_2 is important for the description of the pion interaction at higher collision energies $\sqrt{s} > 1$ GeV.

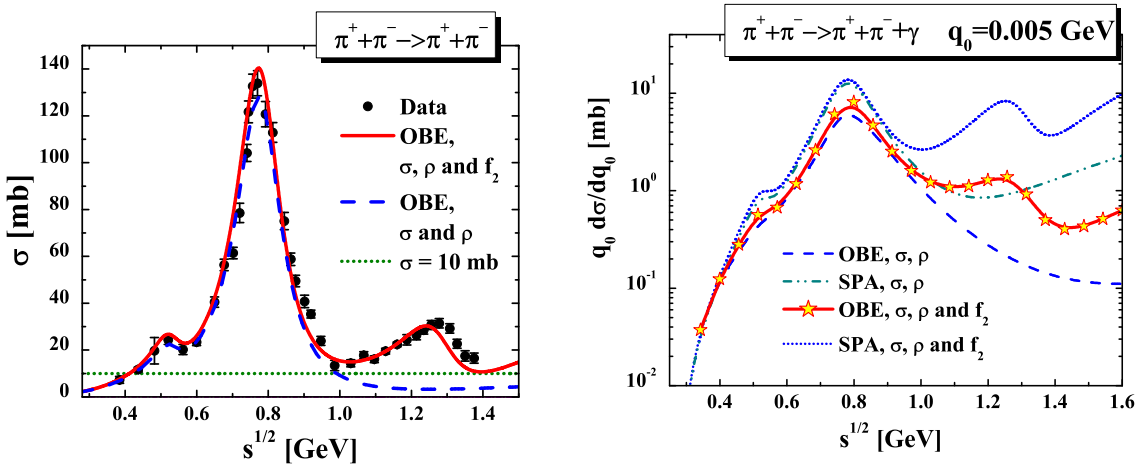

Figure 4.15: (l.h.s.) Cross section for pion+pion elastic scattering within the OBE effective models in comparison to the experimental data from Refs. [273, 274]: the exchange of two mesonic resonances, scalar σ and vector ρ (blue dashed line), and the exchange of three resonances σ, ρ and the tensor resonance $f_2(1270)$ of the particle data booklet [165] (red solid line). The green dashed line shows the constant and isotropic $\sigma_{el} = 10$ mb for orientation. (r.h.s.) Cross section for the production of a photon with energy $q_0 = 0.005$ GeV in the process $\pi + \pi - > \pi + \pi + \gamma$ within the following models: the exact OBE cross section within the effective model taking into account scalar, vector and tensor interactions via the exchange of σ, ρ and $f_2(1270)$-mesons (red line with star symbols), the soft photon approximation to this model (blue dotted line); the OBE result within the model taking into account only the scalar and vector interactions via the exchange of σ and ρ mesons (blue dashed line), and the soft photon approximation to this model (cyan dash-dot-dotted line). The figures are taken from Ref. [22].

Neglecting the contribution of the f_2 leads to an underestimation of the $\pi + \pi$ elastic scattering cross section by an order of magnitude around $\sqrt{s} = 1.2 - 1.3$ GeV. Later data on the $\pi + \pi$ interaction at $\sqrt{s}$ above 1 GeV – extracted in Ref. [275] from the measurement of the $K + p \to \Lambda + \pi + \pi$ reaction – also point to the importance of the tensor interaction in the resonance region of the $f_2(1270)$.

Within the OBE model for the covariant interactions of pions (described above), we can also calculate the emission of photons from the colliding pions by gauge coupling to the external hadron lines. The Feynman diagrams for the photon production in the process $\pi + \pi \to \pi + \pi + \gamma$ are shown in Fig. 4.16. For identical pions, e.g. $\pi^+ + \pi^+$, the u-channel diagrams have to be added, which are obtained from the t-channel diagrams by exchanging the outgoing pions. The applicability of this method is not limited to low photon energies but is restricted only by the applicability of the effective model to the description of the pion-pion (elastic) scattering.

Let us again denote the four-momenta of the incoming pions by p_a and p_b, the momenta of the outgoing pions by p_1 and p_2, and the photon momentum by $q = (q_0, \vec{q})$. The cross section for photon production in the process

$$\pi(p_a) + \pi(p_b) \to \pi(p_1) + \pi(p_2) + \gamma(q) \tag{4.50}$$

then is given by

$$d\sigma^{\gamma} = \frac{1}{2\sqrt{s(s-4m_{\pi}^2)}}|M(\gamma)|^2 dR_3, \tag{4.51}$$

where dR_3 is the three-particle phase space, which depends on the momenta of the outgoing pions and of the photon,

$$dR_3 = \frac{d^3p_1}{(2\pi)^3 2E_1}\frac{d^3p_2}{(2\pi)^3 2E_2}\frac{d^3q}{(2\pi)^3 2q_0}(2\pi)^4\delta^4\left(p_a+p_b-p_1-p_2-q\right). \tag{4.52}$$

The cross section (4.51) will be integrated over the final pion momenta to obtain the differential photon spectrum $d\sigma/d^3q$. The δ-function allows to perform four integrations analytically and the remaining two are done numerically.

The matrix element M in (4.51) is a coherent sum of the diagrams presented in Fig. 4.16 – i.e. of the photon attached to each pion line π_a, π_b, π_1 and π_2 – and of contact terms, which account for the emission from the vertices and the internal lines:

$$|M(\gamma)|^2 = M^*_{\mu}(\gamma)M^{\mu}(\gamma) = |M^{\mu}_a + M^{\mu}_b + M^{\mu}_1 + M^{\mu}_2 + M^{\mu}_c|^2 . \tag{4.53}$$

The complex matrix elements for the photon emission from each of the pion lines M^{μ}_i are calculated as sums of the three meson exchanges (σ, ρ, f_2). For instance:

$$M^{\mu}_1 = eJ^{\mu}_1\left[M^s_{el}(p_a,p_b,p_1+q,p_2) + M^t_{el}(p_a,p_b,p_1+q,p_2) + M^u_{el}(p_a,p_b,p_1+q,p_2)\right] \tag{4.54}$$

with

$$J^{\mu}_{a,b} = -Q_{a,b}\frac{(2p_{a,b}-q)^{\mu}}{2p_{a,b}\cdot q}, \qquad J^{\mu}_{1,2} = Q_{1,2}\frac{(2p_{1,2}-q)^{\mu}}{2p_{1,2}\cdot q}, \tag{4.55}$$

where Q_i are the charges of the pions in terms of the electron charge e. The matrix elements for the pion elastic subprocess $M_{el}(p_a,p_b,p_1+q,p_2)$ are the off-shell generalizations of the formulae (4.49).

The contact term M^{μ}_c is taken from Ref. [271], Eq. (14), where it was derived by demanding the gauge invariance of the resulting cross section. Indeed, the gauge invariance of the result has to be restored [276] in calculations within effective models. In the present work, we have used the contact terms in order to cancel the gauge-dependent parts in the matrix element as in Ref. [271]. Alternatively, one can take into account additional diagrams with the emission of photons from the internal lines (see Refs [270]) but this method does not always eliminate the need for contact terms (see Ref. [276]). We have verified that $q_{\mu}M^{\mu}(\gamma) = 0$ in our calculations and thus the resulting cross sections are gauge invariant.

The soft photon approximation is based on the first-order expansion in the Low theorem [269] and is valid at low photon energy and low $\sqrt{s_{mm}}$ of the meson+meson collision, as has been studied in detail for the production of dileptons in Ref. [270]. In this case the strong interaction part and the electromagnetic part can be separated, i.e. the soft-photon cross section for the reaction $m_1 + m_2 \to m_1 + m_2 + \gamma$ can be

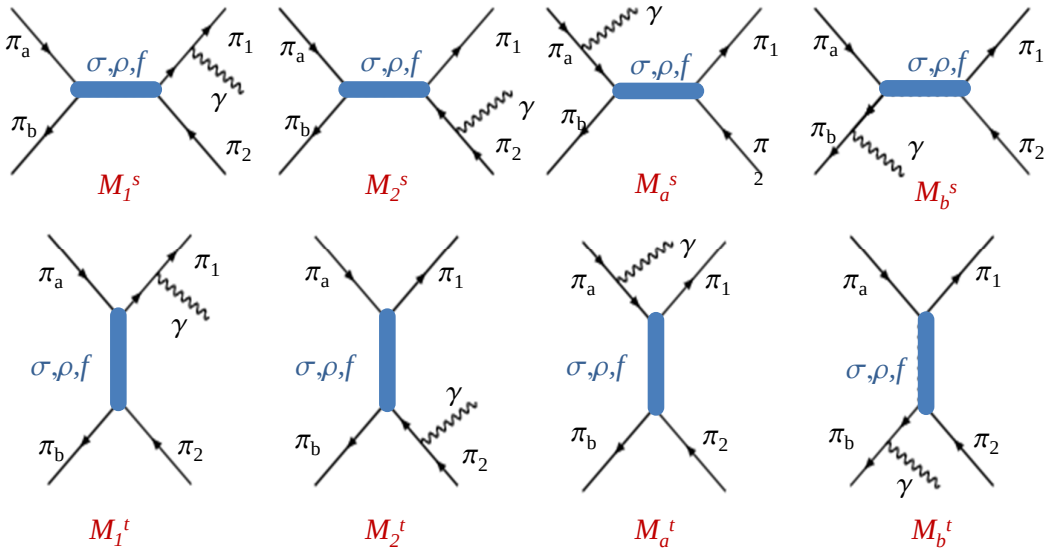

Figure 4.16: Feynman diagrams for photon production in the reaction $\pi+\pi \to \pi+\pi+\gamma$ in the one-boson exchange (OBE) model. The time goes from left to right. For identical pions, e.g. $\pi^+ + \pi^+$, the u-channel diagrams have to be added.

written as

$$q_0 \frac{d\sigma^\gamma(s)}{d^3q} = \frac{\alpha_{EM}}{4\pi^2} \int\limits_{-\lambda(s,m_a^2,m_b^2)/s}^{0} |\epsilon \cdot J(q,t)|^2 \frac{d\sigma_{el}(s)}{dt} dt, \tag{4.56}$$

where α_{EM} is the fine structure constant, t is the momentum transfer squared in the $\pi + \pi \to \pi + \pi$ subprocess and ϵ is the photon polarization. In (4.56) J^μ is the electromagnetic current

$$J^\mu = -Q_a \frac{p_a^\mu}{(p_a \cdot q)} - Q_b \frac{p_b^\mu}{(p_b \cdot q)} + Q_1 \frac{p_1^\mu}{(p_1 \cdot q)} + Q_2 \frac{p_2^\mu}{(p_2 \cdot q)}.$$

The polarization sum

$$|\epsilon \cdot J|^2 = \left\{ \sum_{pol\ \lambda} J \cdot \epsilon_\lambda J \cdot \epsilon_\lambda \right\} \tag{4.57}$$

depends on the photon momentum q, the charges of the pions Q_i as well as on the invariant kinematic variables, including t. For the case of equal-mass particle scattering

($m_a = m_b = m_1 = m_2 = m_\pi$) one obtains [171]:

$$
\begin{aligned}
|\epsilon \cdot J|^2 \;=\; & \frac{1}{q_0^2}\left\{ -(Q_a^2+Q_b^2+Q_1^2+Q_2^2) - 2(Q_aQ_b+Q_1Q_2)\frac{s-2m_\pi^2}{\sqrt{s(s-4m_\pi^2)}} \right. \\
& \qquad \left. \times \ln\left(\frac{\sqrt{s}+\sqrt{s-4m_\pi^2}}{\sqrt{s}-\sqrt{s-4m_\pi^2}}\right) \right. \\
& +2(Q_aQ_1+Q_bQ_2)\frac{2m_\pi^2-t}{\sqrt{t(t-4m_\pi^2)}} \ln\left(\frac{\sqrt{-t+4m_\pi^2}+\sqrt{-t}}{\sqrt{-t+4m_\pi^2}-\sqrt{-t}}\right) \\
& \left. +2(Q_aQ_2+Q_bQ_3)\frac{s-2m_\pi^2+t}{\sqrt{(s+t)(s+t-4m_\pi^2)}} \ln\left(\frac{\sqrt{s+t}+\sqrt{s+t-4m_\pi^2}}{\sqrt{s+t}-\sqrt{s+t-4m_\pi^2}}\right)\right\}. \quad (4.58)
\end{aligned}
$$

In Eq. (4.56), $d\sigma_{el}(s)/dt$ is the on-shell differential elastic $\pi+\pi$ cross section, which is a function of the invariant energy $\sqrt{s}$ and the pion scattering angle via the four-momentum transfer squared t.

The expression (4.56) is considerably simpler in comparison to the "full" OBE formula (4.51) due to the factorization of the diagrams from Fig. 4.16 into an electromagnetic part and an elastic $\pi+\pi \to \pi+\pi$ subprocess, for the cross section of which the photon q-dependence is omitted. This corresponds to neglecting the off-shellness of the pion emitting the photon, e.g. for the pion a:

$$p_a - q \approx p_a. \quad (4.59)$$

Consequently, the sub-process invariant energy $\sqrt{s_2}$ is also approximated by the total invariant energy $\sqrt{s}$ of the process $\pi+\pi \to \pi+\pi+\gamma$:

$$s_2 \equiv (p_a+p_b-q)^2 \approx (p_a+p_b)^2 = s, \quad (4.60)$$

and the limits of integration over t are also taken as for the on-shell case, i.e. from $-\lambda(s,m_a^2,m_b^2)/s$ to 0, while the actual integration over the full 3-particle phase space R_3 in the exact treatment (4.51) involves different limits for t.

In Fig. 4.15 (r.h.s.) we show the resulting cross sections for the photon production in the process $\pi+\pi \to \pi+\pi+\gamma$ within the following models: the "full" OBE taking into account scalar, vector and tensor interactions via the exchange of σ, ρ and $f_2(1270)$-mesons (red line with star symbols), the soft photon approximation (4.56) to this model (blue dotted line); the OBE result employing only the scalar and vector interactions via the exchange of σ and ρ mesons (blue dashed line), and the soft photon approximation to this model (cyan dash-dot-dotted line). For the very low energy of the photon of $q_0 = 5$ MeV the SPA agrees with the "exact" cross section very well in the region of $\sqrt{s} < 0.9$ GeV (see Fig. 4.15, r.h.s.). However, the discrepancy to the OBE result is increasing rapidly with growing $\sqrt{s}$; the calculations for the higher photon energy of $q_0 = 0.5$ GeV show an even larger discrepancy between the SPA and the exact OBE result (cf. Ref. [22]).

Using the cross section for the $\pi+\pi \to \pi+\pi+\gamma$ reaction according to Eq. (4.56) as a function of the photon energy q_0 and the collision energy $\sqrt{s}$, the yield dN/d^3q and the

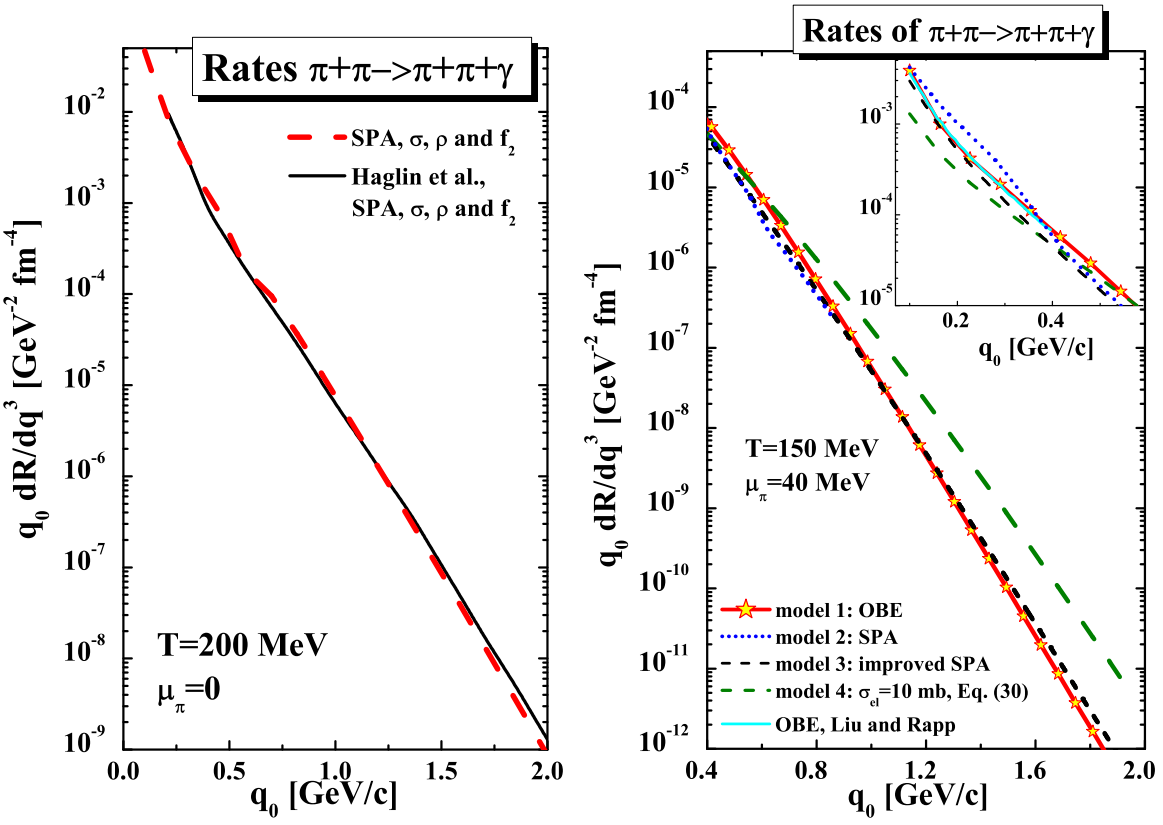

Figure 4.17: (l.h.s.) Invariant rate of the bremsstrahlung-photon production from an equilibrated pion gas at a temperature of $T = 200$ MeV and pion chemical potential $\mu_\pi = 0$ as calculated in the OBE model with three resonance exchange within the soft-photon approximation (red dashed line). The black solid line from Ref. [277] is shown for comparison and validation of our calculations. (r.h.s.) Invariant rate of bremsstrahlung photons produced from an equilibrated pion gas at $T = 150$ MeV and $\mu_\pi = 40$ MeV versus the photon energy q_0. The in-let shows the same quantity for the range of photon energies $q_0 = 0.1 - 0.4$ GeV. The calculations have been performed within the following models: (1) OBE model beyond the soft-photon approximation (red solid line with star symbols); (2) OBE model within the soft photon approximation (blue dotted line); (3) OBE model within the improved soft photon approximation (black short-dashed line) – the invariant energy $\sqrt{s_2}$ of the on-shell $\pi + \pi$ elastic process is not equal to the total invariant energy of the process $\sqrt{s}$: $s_2 = s - q_0\sqrt{s}$; (4) the soft photon approximation with the constant isotropic elastic cross section of $\sigma_{el} = 10$. The cyan solid line from Liu and Rapp [271] is shown for comparison. The figures are taken from Ref. [22].

invariant rate $q_0 dR/d^3q$ for bremsstrahlung photon production from an equilibrated pion gas can be evaluated in a straight forward manner. Within kinetic theory, the rate of photon production in the collisions of particles a and b in a thermalized medium (number of photons produced per unit space-time volume d^4x) is an integral over the three-momenta of the incoming particles (in the classical limit):

$$q_0 \frac{dN}{dx^4 d^3q} = g \int ds \int \frac{d^3p_a}{(2\pi)^3} \int \frac{d^3p_b}{(2\pi)^3} e^{-(E_a+E_b)/T} \; v_{rel} \; q_0 \frac{d\sigma^\gamma}{d^3q} \delta(s-(p_a+p_b)^2), \quad (4.61)$$

where T is the temperature, v_{rel} is the relative velocity given by

$$v_{rel} = \frac{\sqrt{(p_a \cdot p_b)^2 - m_a^2 m_b^2}}{E_a E_b}, \quad (4.62)$$

and $g = (2s_a+1)(2s_b+1)$ is the spin degeneracy factor. Integrating the expression (4.61) over the particle momenta one obtains [171]:

$$q_0 \frac{dN}{d^4x d^3q} = \frac{T^6 g}{16\pi^4} \int_{z_{min}}^{\infty} dz \frac{\lambda(z^2T^2, m_a^2, m_b^2)}{T^4} K_1(z) q_0 \frac{d\sigma^\gamma}{d^3q}, \quad (4.63)$$

where $z_{min} = (m_a + m_b)/T$, $z = \sqrt{s}/T$, and $K_1(z)$ is the modified Bessel function.

The expression (4.61) can be generalized to account for quantum effects such as Bose enhancement or Pauli blocking (depending on the particle type) by integrating additionally over the momenta of the final particles and changing the Boltzmann distributions to Fermi or Bose distribution functions $f_i(T)$:

$$q_0 \frac{dN}{dx^4 d^3q} = g \int ds \int \frac{d^3p_a}{(2\pi)^3} \int \frac{d^3p_b}{(2\pi)^3} \int \frac{d^3p_1}{(2\pi)^3} \int \frac{d^3p_1}{(2\pi)^3} f_a(T) f_b(T) (1 \pm f_1(T))(1 \pm f_2(T)) \times v_{rel} \; q_0 \frac{d\sigma^\gamma}{d^3q} \delta(s-(p_a+p_b)^2), \quad (4.64)$$

where the (-) sign has to be used in case of fermions. In the current section we calculate the thermal rates according to formula (4.61). However, within the PHSD transport approach for the heavy-ion collisions in Section 6 the effects of the quantum statistics will be taken into account (although of subleading importance).

In Fig. 4.17 (l.h.s.) the rates are presented for a temperature $T = 200$ MeV and pion chemical potential $\mu_\pi = 0$ for the OBE model with three resonance exchanges adopting the soft-photon approximation (red dashed line). We confirm the results from Haglin [277] (black solid line) calculated within the same assumptions (SPA, three resonances) but with a slightly different parameter set of the Lagrangian. It is, however, questionable that the SPA is applicable at high photon energies.

We note that the accuracy of the SPA approximation can be significantly improved and the region of its applicability can be extended by slightly modifying the formula (4.56) – i.e. by evaluating the on-shell elastic cross section at the invariant energy $\sqrt{s_2}$

of the sub-process. The latter is kinematically fixed to

$$s_2 = s - q_0\sqrt{s} \neq s. \tag{4.65}$$

Thus the modified SPA formula is

$$q_0\frac{d\sigma^\gamma(s)}{d^3q} = \frac{\alpha_{EM}}{4\pi}\int\limits_{-\lambda(s_2,m_a^2,m_b^2)/s_2}^{0} |\epsilon\cdot J(q,t)|^2\frac{d\sigma_{el}(s_2)}{dt}dt. \tag{4.66}$$

In the following, we will denote the approximation (4.66) as "improved SPA" and will show below that it provides a fairly good description of the exact photon production rates.

It is instructive to compare the photon production rates beyond the soft photon approximation for the $\pi+\pi\to\pi+\pi+\gamma$ reaction to the rates from the exact OBE expression (4.51). We present the calculated invariant rate $q_0 dR/dq^3$ of bremsstrahlung photons produced from an equilibrated pion gas at $T = 150$ MeV and $\mu_\pi = 40$ MeV in Fig. 4.17 (r.h.s.). The results of the following models are compared:

- model 1 (red solid line): exact rates within the one-boson exchange model (OBE) *beyond* the soft-photon approximation – i.e. using the formula (4.51) for the photon production cross section $q_0\ d\sigma^\gamma/d^3q$;

- model 2 (blue dotted line): result within the soft photon approximation – i.e. using the formula (4.56) – while using the elastic $\pi+\pi$ cross section calculated within the OBE model as given by equations (4.46)-(4.49);

- model 3 (black short-dashed line): results of the *improved* soft photon approximation – i.e. using the formula (4.66) in stead of (4.56) – and the same pion elastic scattering cross section as in the model 2;

- model 4 (upper green dashed line): soft photon approximation using a constant isotropic elastic cross section of $\sigma_{el} = 10$ mb and assuming for the pion charges $Q_a = Q_1 = 1$, $Q_b = Q_2 = 0$. In this case the elastic cross section does not depend on $\sqrt{s}$ and thus there is no difference between the SPA and improved SPA.

The rate of bremsstrahlung photons at low transverse momenta $p_T < 0.4$ GeV has been calculated before by Liu and Rapp in Ref. [271] within the one-boson exchange model with the exchange of two resonances for the same system. This previous result is shown for comparison by the cyan dashed line and is confirmed by our present calculations. The agreement is expected, since our calculations differ only in the inclusion of the f_2-meson exchange, which is important for larger $\sqrt{s}$ and does not play an important role for the production of low transverse momentum photons, which is dominated by low $\sqrt{s}$ of the $\pi+\pi$ collisions.

On the other hand, the SPA (model 2) deviates from the exact OBE result (model 1) even at low q_0 because the former directly follows the $\sqrt{s}$ dependence of the elastic $\pi-\pi$ cross section. Since the formula (4.56) does not account for the off-shellness of

the emitting pion, it overestimates the high-$\sqrt{s}$ regime of the elastic cross section in line with the findings of Refs. [171, 270]. We note that the OBE model presented here is constrained by the pion scattering data only up to $\sqrt{s_{\pi\pi}} = 1.4$ GeV and generally cannot be extended to larger $\sqrt{s}$. Thus the SPA scenario "model 2" is not reliable for large q_0 (approximately for $q_0 > 0.8$ GeV). This is not the case for the improved SPA (model 3).

One can see in Fig. 4.17 (r.h.s.) that the *improved* SPA (4.66) gives a very good approximation to the exact result at higher photon energies of up to $q_0 \approx 2$ GeV. This is because the $\sqrt{s_2}$ of the subprocess is always below $\sqrt{s}$, and the OBE model for the elastic cross section is sufficiently realistic in this region of $\sqrt{s_2}$. In comparison, the constant cross-section approximation overestimates the exact rates for $q_0 > 1$ GeV and underestimates for $q_0 < 0.4$ GeV. This model corresponds to the approximation used previously in the transport calculations in Refs. [20, 21, 174] for an estimate of the photon bremsstrahlung in meson+meson collisions. In the following we will report on results based on the exact OBE cross section $d\sigma^\gamma/d^3q$ for $\pi + \pi$ bremsstrahlung. The bremsstrahlung photon production in collisions of other meson types is treated in analogy to the $\pi + \pi$ collisions by means of mass-scaled cross sections.

We note that another important source of photons is the bremsstrahlung in *meson+ baryon* collisions. As we have shown above, the SPA gives a good approximation to the exact rates, if we use the correct invariant energy in the hadronic subprocess $s_2 = s - q_0\sqrt{s}$ and a realistic model for the differential cross section of the subprocess, i.e. for the elastic scattering of mesons on baryons. The cross sections for the meson+baryon elastic scatterings (implemented within the PHSD transport approach) have been previously adjusted to the data differentially in energy and angular distribution. Thus we evaluate the photon production in the processes $m + B \to m + B + \gamma$ in the PHSD by using realistic elastic scattering cross sections taken at the correct invariant energy $\sqrt{s_2}$ in the scope of the improved SPA.

4.4.2 Binary meson+meson and meson+nucleon reactions

We calculate the cross sections for the processes $\pi\pi \to \rho\gamma, \pi\rho \to \pi\gamma$ as in Ref. [174], i.e. the total cross section $\sigma_{\pi\pi\to\rho\gamma}(s, \rho_N)$ is obtained by folding the vacuum cross section $\sigma^0_{\pi\pi\to\rho\gamma}(s, M)$ with the (in-medium) spectral function of the ρ meson:

$$\sigma_{\pi\pi\to\rho\gamma}(s, \rho_N) = \int_{M_{min}}^{M_{max}} dM\ \sigma^0_{\pi\pi\to\rho\gamma}(s, M)\ A(M, \rho_N)\ P(s). \tag{4.67}$$

Here $A(M, \rho_N)$ denotes the meson spectral function for given total width Γ^*_V:

$$A_V(M, \rho_N) = C_1\ \frac{2}{\pi}\ \frac{M^2\ \Gamma^*_V(M, \rho_N)}{(M^2 - M_0^{*2}(\rho_N))^2 + (M\Gamma^*_V(M, \rho_N))^2}, \tag{4.68}$$

with the normalization condition for any ρ_N, $\int_{M_{min}}^{M_{lim}} A_V(M, \rho_N)\ dM = 1$, where $M_{lim} = 2$ GeV is chosen as an upper limit for the numerical integration while the lower limit of the vacuum ρ spectral function corresponds to the 2π decay threshold $M_{min} = 2m_\pi$

in vacuum and $2m_e$ in medium. M_0^* is the pole mass of the vector meson spectral function which is $M_0^*(\rho_N = 0) = M_0$ in vacuum, however, might be shifted in the medium (e.g. for the dropping mass scenario). Furthermore, the vector meson width is the sum of the vacuum total decay width and collisional width:

$$\Gamma_V^*(M, \rho_N) = \Gamma_V(M) + \Gamma_{coll}(M, \rho_N). \tag{4.69}$$

In Eq. (4.67) the function $P(S)$ accounts for the fraction of the available part of the full spectral function $A(M, \rho_N)$ at given energy $\sqrt{s}$, integrated over the mass M up to $M_{max} = \sqrt{s}$, with respect to the total phase space.

The cross section $\sigma^0_{\pi\pi\to\rho\gamma}(s, M)$ is taken in line with the model by Kapusta et al. [187] with the ρ-meson mass considered as a dynamical variable, i.e $m_\rho \to M$:

$$\begin{aligned}
&\frac{d\sigma}{dt}\left(\pi^\pm\pi^0 \to \rho^\pm\gamma\right) = \\
&-\frac{\alpha g_\rho^2}{16 s p_{CM}^2}\left[\frac{(s-2M^2)(t-m_\pi^2)^2}{M^2(s-M^2)^2} + \frac{m_\pi^2}{M^2} - \frac{9}{2} + \frac{(s-6M^2)(t-m_\pi^2)}{M^2(s-M^2)}\right. \\
&\left. + \frac{4(M^2-4m_\pi^2)s}{(s-M^2)^2} + \frac{4(M^2-4m_\pi^2)}{t-m_\pi^2}\left(\frac{s}{s-M^2} + \frac{m_\pi^2}{t-m_\pi^2}\right)\right].
\end{aligned} \tag{4.70}$$

The photon production in the $\pi+\rho$ interaction is calculated analogously (cf. Ref. [174] for details).

We recall that the PHSD and HSD are off-shell transport approaches and thus allow to study the effect of the modification of the vector-meson spectral functions in the medium. In particular the photon production in secondary meson interactions is sensitive to the properties of the vector mesons at finite density and temperature [174, 181, 278]. In this respect, we stress here that the yields and the in-medium spectral functions of vector mesons in PHSD have been independently constrained by the comparison to the data on dilepton mass-spectra (see Refs. [180, 204, 279] and Chapter 7, respectively).

We have incorporated into the PHSD approach additionally the $2 \to 2$ processes $V + N \to N + \gamma$, where V stands for a vector meson while N denotes a proton or neutron [22]. These processes are the baryonic counterparts to the mesonic $2 \to 2$ reactions $\pi + \rho/\pi \to \gamma + \pi/\rho$. We consider the interaction of nucleons with the mesons $V = \rho$, ϕ, ω, taking into account the various possible charge combinations, e.g. $\rho^0 + p \to \gamma + p$, $\rho^- + p \to \gamma + n$, $\rho^+ + n \to \gamma + p$, etc. In order to evaluate the probabilities for photon production in the collisions of vector mesons with nucleons, we use the inverse photoproduction processes $\gamma + N \to \rho + N$, $\gamma + N \to \phi + N$, $\gamma + N \to \omega + N$ (controlled by data) and employ detailed balance to obtain the differential cross sections for the processes $\rho + N \to \gamma + N$, $\phi + N \to \gamma + N$, $\omega + N \to \gamma + N$, i.e.

$$\sigma(NV \to \gamma N) \;=\; \frac{g_\gamma}{g_V}\frac{p_{N\gamma}^{*2}}{p_{NV}^{*2}}\,\sigma(\gamma N \to NV), \tag{4.71}$$

where $g_\gamma = 2$ and $g_V = 3$ are the spin degeneracy factors of the photon and the vector meson V. In Eq. (4.71) $p^*_{N\gamma}$ is the center-of-mass momentum in the $N+\gamma$ system and p^*_{NV} is the center-of-mass momentum in the $N + V$ system.

The cross sections for the exclusive photo-production of ρ, ϕ and ω vector mesons on the nucleon have been measured by the Aachen-Berlin-Bonn-Hamburg-Heidelberg-Munich (ABBHHM) Collaboration and published in Ref. [280]. In the same work also parametrizations for these cross section have been given that are based on the vector-meson-dominance model with a non-relativistic Breit-Wigner (BW) spectral function for the ρ-meson. Later, the fits have been updated in Ref. [281] using relativistic BW spectral functions for ρ, ω and ϕ mesons. The total cross sections – fitted in Ref. [281] to the data from Ref. [280] – are given by

$$\sigma(\gamma N \to VN) = \frac{1}{p^*_{N\gamma} s} \int d\mu |M_V|^2 p^*_{NV} A_V(\mu), \tag{4.72}$$

where the mass μ of the vector meson is distributed according to the spectral function $A_V(\mu)$:

$$A_V(\mu) = \frac{2}{\pi} \frac{\mu^2 \Gamma(\mu)}{(\mu^2 - M_i^2)^2 + \mu^2 \Gamma^2(\mu)}, \tag{4.73}$$

with M_i denoting the pole mass of the meson. The matrix elements for the reactions $\gamma + N \to V + N$ are parametrized as

$$\begin{aligned} |M_\rho|^2 &= 0.16 \text{ mb GeV}^2, \\ |M_\omega|^2 &= \frac{0.08\ p^{*2}_{VN}}{2(\sqrt{s} - 1.73\ \text{GeV})^2 + p^{*2}_{VN}} \text{ mb GeV}^2, \\ |M_\phi|^2 &= 0.004 \text{ mb GeV}^2. \end{aligned} \tag{4.74}$$

The cross sections (4.72) with the parameters (4.74) are consistent with the dynamics of vector mesons in the PHSD/HSD, where also relativistic BW spectral functions for vector mesons are used and propagated off-shell.

For the angular distribution of the ρ-meson production in the process $\gamma + N \to N + \rho$, we follow the suggestion of Ref. [281],

$$\frac{d\sigma}{dt} \sim \exp(Bt), \tag{4.75}$$

with the photon-energy dependent parameter B (fitted to the data): $B = 5.7$ for $q_0 \leq 1.8$ GeV, $B = 5.43$ for $1.8 < q_0 \leq 2.5$ GeV, $B = 6.92$ for $2.5 < q_0 \leq 3.5$ GeV, $B = 8.1$ for $3.5 < q_0 \leq 4.5$ GeV, $B = 7.9$ for $q_0 > 4.5$ GeV. The data in Ref. [281] have shown that the cross section is dominated by the $t \approx 0$ region in line with the vector dominance model (VDM) where the process $\gamma + N \to V + N$ is described by the incident photon coupling to the vector meson of helicity ± 1, which consequently is scattered elastically by the nucleon.

4.4.3 Vector-meson spectral functions

In order to explore the influence of in-medium effects on the vector-meson spectral functions we incorporate the effect of collisional broadening (as in Refs. [282–284]),

i.e. the vector meson width has been implemented as:

$$\Gamma_V^*(M, |\vec{p}|, \rho_N) = \Gamma_V(M) + \Gamma_{coll}(M, |\vec{p}|, \rho_N). \tag{4.76}$$

Here $\Gamma_V(M)$ is the total width of the vector mesons ($V = \rho, \omega$) in the vacuum. For the ρ meson we use

$$\begin{aligned} \Gamma_\rho(M) \;\simeq\; \Gamma_{\rho\to\pi\pi}(M) &= \Gamma_0 \left(\frac{M_0}{M}\right)^2 \left(\frac{q}{q_0}\right)^3 F(M), \\ q = \frac{(M^2 - 4m_\pi^2)^{1/2}}{2}, &\quad q_0 = \frac{(M_0^2 - 4m_\pi^2)^{1/2}}{2}. \end{aligned} \tag{4.77}$$

In Eqs. (4.77) M_0 is the vacuum pole mass of the vector meson spectral function, $F(M)$ is a formfactor taken from Ref. [285] as

$$F(M) = \left(\frac{2\Lambda^2 + M_0^2}{2\Lambda^2 + M^2}\right)^2 \tag{4.78}$$

with a cut-off parameter $\Lambda = 3.1$ GeV. This formfactor was introduced in Ref. [285] in order to describe the e^+e^- experimental data with better accuracy. For the ω meson a constant total vacuum width is used: $\Gamma_\omega \equiv \Gamma_\omega(M_0)$, since the ω is a narrow resonance in vacuum.

The collisional width in Eq. (4.76) is approximated as

$$\Gamma_{coll}(M, |\vec{p}|, \rho_N) = \gamma\ \rho_N < v\ \sigma_{VN}^{tot} > \approx\ \alpha_{coll}\ \frac{\rho_N}{\rho_0}.. \tag{4.79}$$

Here $v = |\vec{p}|/E$; $\vec{p}$, E are the velocity, 3-momentum and energy of the vector meson in the rest frame of the nucleon current and $\gamma^2 = 1/(1 - v^2)$. Furthermore, ρ_N is the nuclear density and σ_{VN}^{tot} the meson-nucleon total cross section. The parameter α_{coll} is determined dynamically within the transport calculation by recording the ρ collision rate as a function of the baryon density ρ_N.

In order to explore the observable consequences of vector-meson mass shifts at finite nuclear density – as suggested by the CBELSA-TAPS data [286] for the ω meson – the in-medium vector meson pole masses are modeled (optionally) according to the Hatsuda and Lee [287] or Brown/Rho scaling [288, 289] as

$$M_0^*(\rho_N) = \frac{M_0}{(1 + \alpha\rho_N/\rho_0)}, \tag{4.80}$$

where ρ_N is the nuclear density at the resonance decay position $\vec{r}$; $\rho_0 = 0.16$ fm^{-3} is the normal nuclear density and $\alpha \simeq 0.16$ for the ρ and $\alpha \simeq 0.12$ for the ω meson [290]. The parametrization (4.80) may be employed also at much higher collision energies (e.g. FAIR and SPS) and one does not have to introduce a cut-off density in order to avoid negative pole masses. Note that the effective mass (4.80) is uniquely fixed by the 'customary' expression $M_0^*(\rho_N) \approx M_0(1 - \alpha\rho_N/\rho_0)$ in the low density regime.

The resulting spectral functions for the ρ and ω meson are displayed in Fig. 4.18 for the case of 'collisional broadening' (upper part) as well as for the 'dropping mass

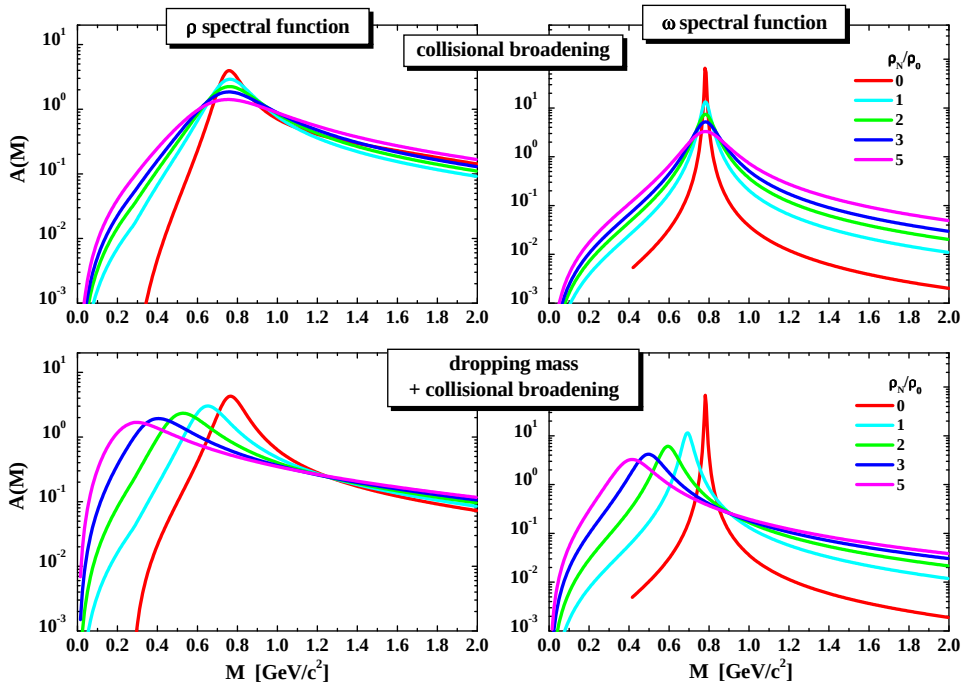

Figure 4.18: The spectral functions for the ρ and ω meson in the case of the 'collisional broadening' scenario (upper part) and the 'dropping mass + collisional broadening' scenario (lower part) for nuclear densities of 0,1,2,3,5$\times\rho_0$ as employed in the transport calculations (see text for details). The figures are taken from Ref. [291].

+ collisional broadening' scenario (lower part) for densities of 0,1,2,3,5 $\times\rho_0$. Note that in vacuum the hadronic widths vanish for the ρ below the two-pion mass and for the ω below the three-pion mass. With increasing nuclear density ρ_N elastic and inleastic interactions of the vector mesons shift strength to low invariant masses. In the 'collisional broadening' scenario we find a dominant enhancement of strength below the pole mass for the ρ meson while the ω meson spectral function is drastically enhanced in the low- and high-mass region with density (on expense of the pole-mass regime). In the 'dropping mass + collisional broadening' scenario both vector mesons dominantly show a shift of strength to low invariant masses with increasing ρ_N. Qualitatively similar pictures are obtained for the ϕ meson but quantitatively smaller effects are seen due to the lower effect of mass shifts and a substantially reduced ϕN cross section which is a consequence of the $s\bar{s}$ substructure of the ϕ meson. Since the ϕ dynamics turn out to be of minor importance for the dilepton spectra to be discussed below we discard an explicit representation. The 'family' of spectral functions shown in Fig. 4.18 allows for a sufficient flexibility with respect to the possible scenarios outlined above. A comparison to dilepton data is expected to provide further constraints on the possible realizations.

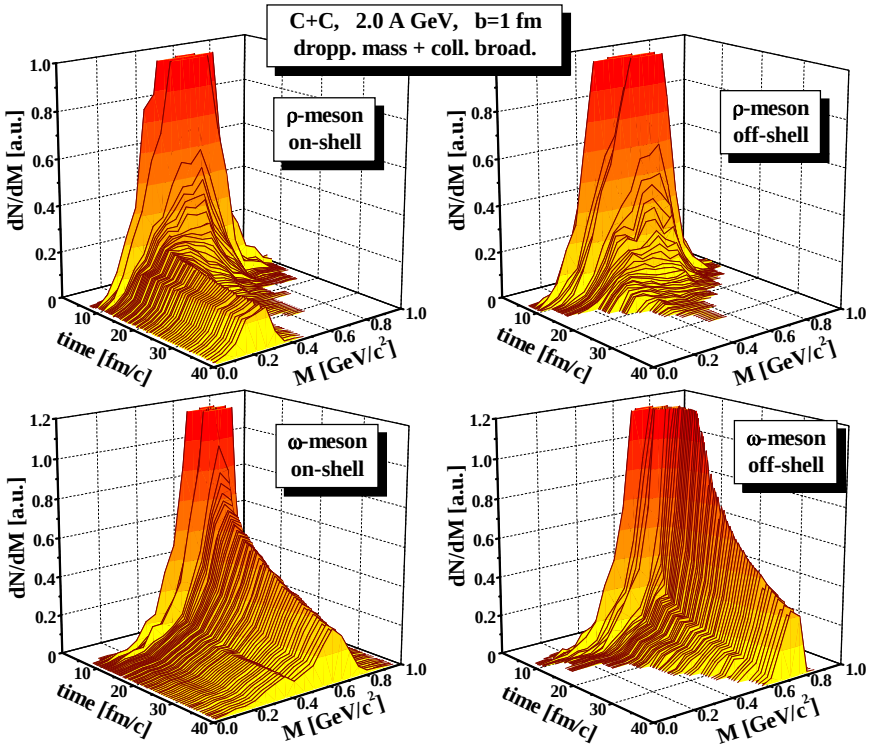

Figure 4.19: Time evolution of the mass distribution of ρ (upper part) and ω (lower part) mesons for central $C+C$ collisions (b=1 fm) at 2 A GeV for the dropping mass + collisional broadening scenario. The l.h.s. of Fig. 4.19 correspond to the calculations with on-shell dynamics whereas the r.h.s. show the off-shell results. The figures are taken from Ref. [291].

4.5 Off-shell propagation

The propagation of broad resonances in the off-shell transport approach has been described in Section 2.7 above. In order to demonstrate the importance of off-shell transport dynamics we present in Fig. 4.19 the time evolution of the mass distribution of ρ (upper part) and ω (lower part) mesons for central C+C collisions (b=1 fm) at 2 A GeV for the dropping mass + collisional broadening scenario (as an example). The l.h.s. of Fig. 4.19 corresponds to the calculations with on-shell propagation whereas the r.h.s. show the results for the off-shell dynamics. As seen from Fig. 4.19 the initial ρ and ω mass distributions are quite broad even for a small system such as $C+C$ where, however, the baryon density at 2 A GeV may reach (in some local cells) up to $2\rho_0$. The number of vector mesons decreases with time due to their decays and the absorption by baryons ($\rho N \to \pi N$ or $\rho N \to \pi\pi N$). Most of the ρ mesons decay/disappear already inside the "fireball" for density $\rho_N > 0$. Due to the "fireball" expansion the baryon density drops quite fast, so some amount of ρ (and ω) mesons reach the very low density zone or even the 'vacuum'. Since for the off-shell case (r.h.s. of Fig. 4.19) the ρ and ω spectral functions change dynamically by propagation in the dense medium according to Eqs. (2.85) and (2.86) they regain the vacuum shape for $\rho_N \to 0$. This does not happen for the on-shell treatment (l.h.s. of Fig. 4.19);

the ρ spectral function does not change its shape by propagation but only by explicit collisions with other particles. Indeed, there is a number of ρ's which survive the decay or absorption and leave the "fireball" with masses below $2m_\pi$.

Accordingly, the approximate on-shell propagation leads to the appearance of ρ mesons in the vacuum with $M \leq 2m_\pi$, which can not decay to two pions; thus they live practically 'forever' since the probability to decay to other channels is very small. Indeed, such ρ's will continuously shine low mass dileptons which leads to an apparent 'enhancement/divergence' of the dilepton yield at low masses (note, that the dilepton yield is additionally enhanced by a factor $\sim 1/M^3$). The same statements are valid for the ω mesons (cf. lower part of Fig. 4.19): since the ω meson is a long living resonance, a larger amount of ω's survives with an in-medium like spectral function in the vacuum (in case of on-shell dynamics). Such ω's with $M < 3m_\pi$ can decay only to $\pi\gamma$ or electromagnetically (if $M < m_\pi$). Since such phenomena appearing in on-shell transport descriptions (including an explicit vector-meson propagation) contradict basic physical principles, an off-shell treatment is mandatory.

4.6 Time integration method

Since the dilepton production is a very rare process (e.g. the branching ratio for the vector meson decay is $\sim 10^{-5}$), a perturbative method is used in the transport calculation in order to increase statistics. In the PHSD approach (in this report as well as in earlier investigations [180, 185, 204, 291–293]) we use the time integration (or 'shining') method first introduced by Li and Ko in Ref. [294]. The main idea of this method is that dileptons can be emitted during the full lifetime of the resonance R before its strong decay into hadrons or absorption by the surrounding medium. For example, the ρ^0 decay (with invariant mass M) to e^+e^- during the propagation through the medium from the production time $t = 0$ up to the final ("death") time t_F – which might correspond to an absorption by baryons or to reactions with other hadrons as well as the strong decay into two pions – is calculated as

$$\frac{dN^{\rho\to e^+e^-}}{dM} = \sum_{t=0}^{t_F} \Gamma^{\rho^0\to e^+e^-}(M) \cdot \frac{\Delta t}{\gamma(\hbar c)} \cdot \frac{1}{\Delta M} \tag{4.81}$$

in the mass bin ΔM and time step Δt (in fm/c). In (4.81) γ is the Lorentz factor of the ρ-meson with respect to the calculational frame. The electromagnetic decay width is defined as

$$\Gamma^{\rho^0\to e^+e^-}(M) = C_\rho \frac{M_0^{*4}}{M^3}, \tag{4.82}$$

where $C_\rho = \Gamma^{\rho\to e^+e^-}(M_0)/M_0$. Here M_0 is the vacuum pole mass, M_0^* is the in-medium pole mass which is equal to the vacuum pole mass for the collisional broadening scenario, however, is shifted for the dropping mass scenario according to Eq. (4.80). The time integration method allows to account for the full in-medium dynamics of vector mesons from production ("birth") up to their "death". In case of the ρ propagation in the vacuum only the 2 pion-decay channel contributes and the default results are regained after time integration.

Chapter 5

Comparison of our calculations to data on dilepton production in heavy-ion collisions

5.1 SPS energies

We compare calculation results with experimental data for dileptons from In+In collisions at 160 A GeV measured by the NA60 Collaboration. In Fig. 5.1 we present PHSD results for the dilepton excess over the known hadronic sources as produced in In+In reactions at 158 A GeV compared to the acceptance corrected data. We find here that the spectrum at invariant masses in the vicinity of the ρ-meson peak is well reproduced by the ρ meson yield, if a broadening of the meson spectral function in the medium is assumed, while the partonic sources account for the yield at high masses. Our analysis shows that the contributions of the "4π" processes (shown by the lines with symbols) – as first noted by the authors of Ref. [181] – are very much suppressed.

One concludes from Fig. 5.1 that the measured spectrum for $M > 1$ GeV is dominated by the *partonic* sources. Indeed, the dominance of the radiation from the QGP over the hadronic sources in PHSD is related to a rather long – of the order or 3 fm/c – evolution in the partonic phase (in co-existence with the space-time separated hadronic phase) on one hand (cf. Fig. 10 of Ref. [24]) and the rather high initial energy densities created in the collision on the other hand (cf. Fig. 6 of Ref. [107]). In addition, we find from Fig. 5.1 that in PHSD the partonic sources also have a considerable contribution to the dilepton yield for $M < 0.6$ GeV. The yield from the two-to-two process $q + \bar{q} \to g + l^+l^-$ is especially important close to the threshold (≈ 0.211 GeV). This conclusion from the microscopic calculation is in qualitative agreement with the findings of an early (more schematic) investigation in Ref. [299]. For related results from alternative models we refer the reader to the right panel of Fig. 5.1.

The comparison of the mass dependence of the slope parameter evolution in PHSD and the data from NA60 is shown explicitly in Fig. 5.2. Including the partonic dilepton sources allows to reproduce in PHSD the m_T-spectra as well as the finding of the NA60 Collaboration [117, 295–298] that the effective temperature of the dileptons (slope parameters) in the intermediate mass range is lower than that of the dileptons in the mass bin $0.6 < M < 1$ GeV, which is dominated by hadronic sources (cf.

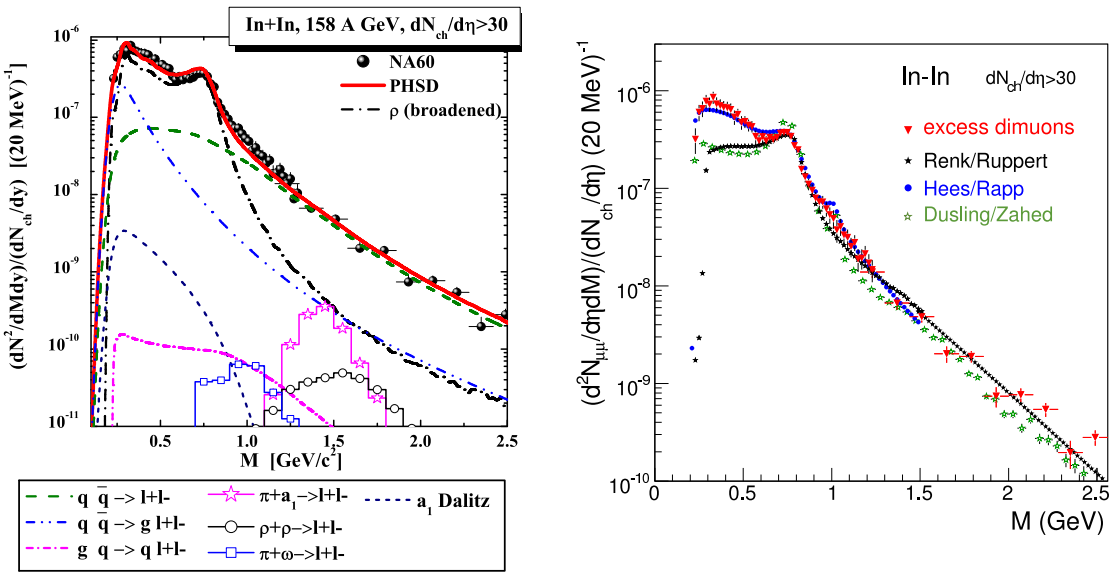

Figure 5.1: (l.h.s.) Acceptance corrected mass spectra of excess dimuons from In+In at 158 A GeV integrated over p_T in $0.2 < p_T < 2.4$ GeV from PHSD compared to the data of NA60 [295]. The dash-dotted line shows the dilepton yield from the in-medium ρ with a broadened spectral function, the dashed line presents the yield from the $q + \bar{q}$ annihilation, the dash-dot-dot line gives the contribution of the gluon Bremsstrahlung process ($q\bar{q} \rightarrow gl^+l^-$), while the solid line is the sum of all contributions. For the description of the other lines, which correspond to the non-dominant channels, we refer to the figure legend. The figure is taken from Ref. [180]. (r.h.s.) Acceptance-corrected invariant mass spectrum of excess dimuons in In+In collisions at 158 A GeV in comparison to model results from Renk and Ruppert, van Hees and Rapp as well as Dusling and Zahed. The figure is taken from Refs. [117, 295–298].

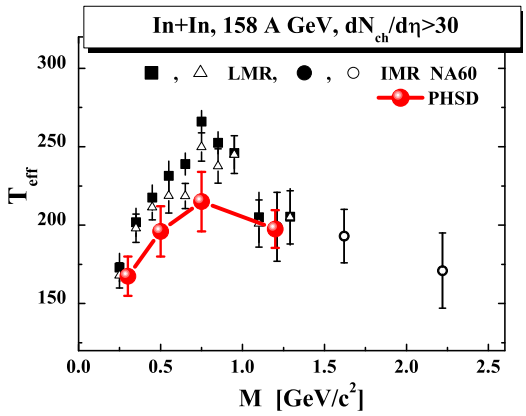

Figure 5.2: The inverse slope parameter T_{eff} of the dimuon yield from In+In at 158 A GeV as a function of the dimuon invariant mass M in PHSD (solid line with full dots) compared to the data of the NA60 Collaboration [117, 295–298]. The figure is taken from Ref. [180].

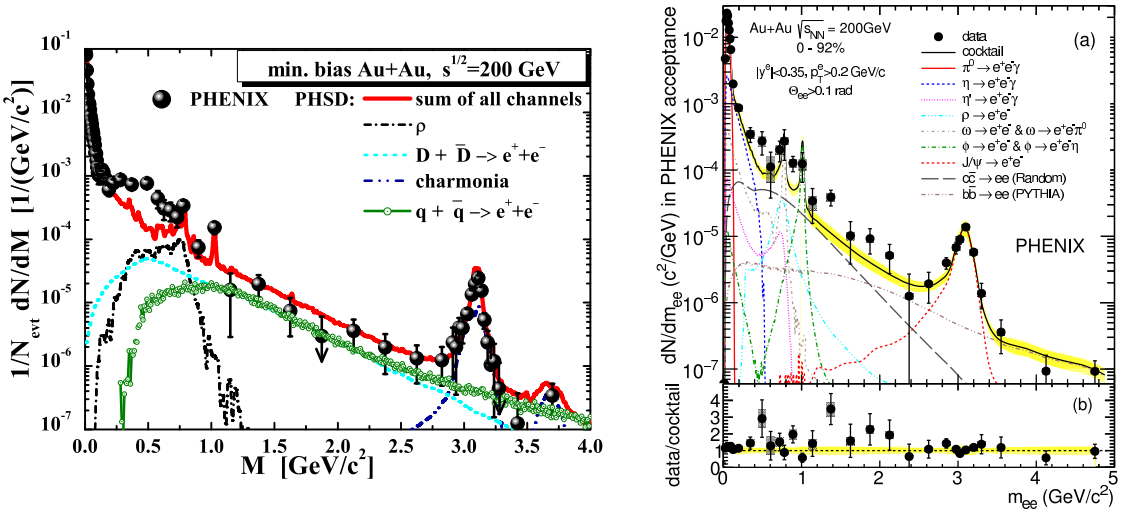

Figure 5.3: (l.h.s.) The PHSD results for the invariant mass spectra of inclusive dileptons in Au+Au collisions at $\sqrt{s_{NN}} = 200$ GeV within the PHENIX acceptance cuts in comparison to the data from the PHENIX Collaboration [205–207, 260] based on the data from 2004. The different lines indicate the contributions from different channels as specified in the figure, which is taken from Ref. [279]. (r.h.s.) New data of the PHENIX Collaboration measured in 2010 with the Hadron-Blind Detector compared to the cocktail of hadron decays. The figure is taken from Ref. [300].

Fig. 5.2). The softening of the transverse mass spectrum with growing invariant mass implies that the partonic channels occur dominantly before the collective radial flow has developed. Also, the fact that the slope in the lowest mass bin and the highest one are approximately similar – both in the data and in the PHSD – can be traced back to the two windows of the mass spectrum that in our picture are influenced by the radiation from the sQGP: $M = 2M_\mu - 0.6$ GeV and $M > 1$ GeV. For more details we refer the reader to Ref. [180].

5.2 RHIC energies

Now we are coming to the top RHIC energy of $\sqrt{s_{NN}} = 200$ GeV and present the most important findings from the PHSD study in Ref. [279]. In the left part of Fig. 5.3 we show the PHSD results for the invariant mass spectra of inclusive dileptons in Au+Au collisions for the acceptance cuts on single electron transverse momenta p_{eT}, pseudorapidities η_e, azimuthal angle ϕ_e, and dilepton pair rapidity y: $p_{eT} > 0.2$ GeV, $|\eta_e| < 0.35$, $-3\pi/16 < \phi_e < 5\pi/16$, $11\pi/16 < \phi_e < 19\pi/16$, $|y| < 0.35$.

In the low mass region $M = 0 - 1.2$ GeV, the dilepton yield in the PHSD is dominated by hadronic sources and roughly coincides with the earlier HSD result in Ref. [204]. Note that the collisional broadening scenario for the modification of the ρ-meson was used in the calculations presented in Fig. 5.3 that underestimates the PHENIX data from the run 2004 in the mass range from 0.2 to 0.7 GeV substantially. In contrast, the partonic radiation as well as the yield from correlated D-meson decays dominate and saturate the mass region $M = 1 - 3$ GeV as seen in Fig. 5.3 (left panel),

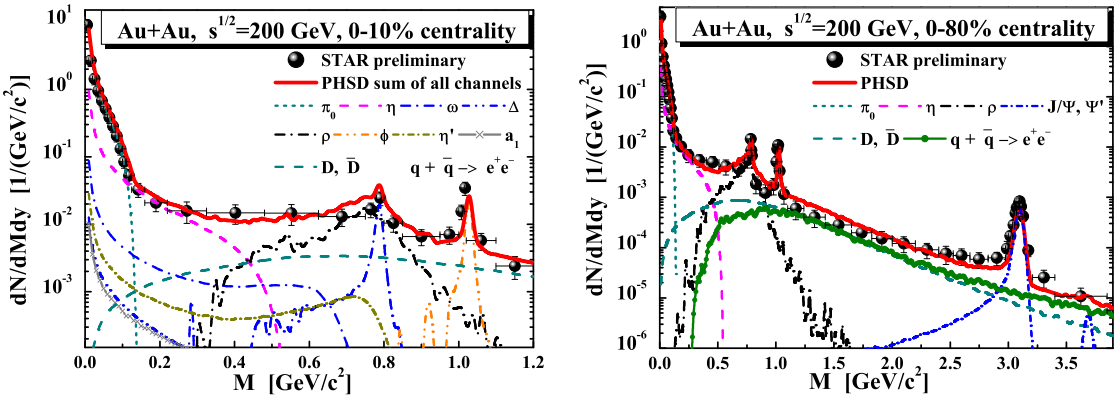

Figure 5.4: The PHSD results for the invariant mass spectra of dileptons in Au+Au collisions at $\sqrt{s_{NN}} = 200$ GeV for $M = 0-1.2$ GeV (left panel) and for $M = 0-4$ GeV (right panel) for 0 - 10 % or 0 - 80% centrality within the cuts of the STAR experiment. The data of the STAR Collaboration are adopted from Ref. [301]. The figures are taken from Ref. [279].

i.e. between the ϕ and J/Ψ peaks. The dileptons generated by the quark-antiquark annihilation in the sQGP from PHSD constitute about half of the observed yield in this intermediate-mass range. For $M > 2.5$ GeV the partonic yield is even higher than the D-meson contribution. Thus, the inclusion of the partonic radiation in the PHSD fills up the gap between the hadronic model results [204] and the data of the PHENIX Collaboration for $M > 1$ GeV. However, the early expectation of a strong partonic signal in the low mass dilepton spectrum is not substantiated by the microscopic PHSD calculations.

In order to investigate the "low-mass dilepton problem", the PHENIX Collaboration has performed a new measurement in 2010 with a different magnetic field setting, addition of the Hadron-Blind Detector, and modified analysis. The results of this experimental effort (very recently presented in Ref. [300]) are shown in the right hand side of Fig. 5.3. The new measurements suggest that the dilepton yield in the low-mass region from 0.2 to 0.7 GeV does no longer show such a strong enhancement over the cocktail of hadronic decay sources as assumed based on the earlier PHENIX analysis in Ref. [205–207, 260]. In fact, the new PHENIX data are in agreement with the theoretical expectations from the PHSD calculations.

In order to shed some further light on the "PHENIX puzzle", we compare the PHSD predictions with the data independently measured for Au+Au collisions at $\sqrt{s_{NN}} = 200$ GeV by the STAR Collaboration. The calculations are performed for the same model assumptions and parameters as those used for the comparison to the PHENIX data, only the different acceptance cuts on single electron transverse momenta p_{eT}, single electron pseudorapidities η_e and the dilepton pair rapidity y, i.e. $0.2 < p_{eT} < 5$ GeV, $|\eta_e| < 1$, $|y| < 1$. The PHSD predictions for the dilepton yield within these cuts are shown in Fig. 5.4 for 0-80%. One can observe generally a good agreement with the data from the STAR Collaboration [301] in the whole mass regime. Notably, our calculations are also roughly in line with the low mass dilepton spectrum from STAR in case of the most central collisions, whereas the PHSD results severely

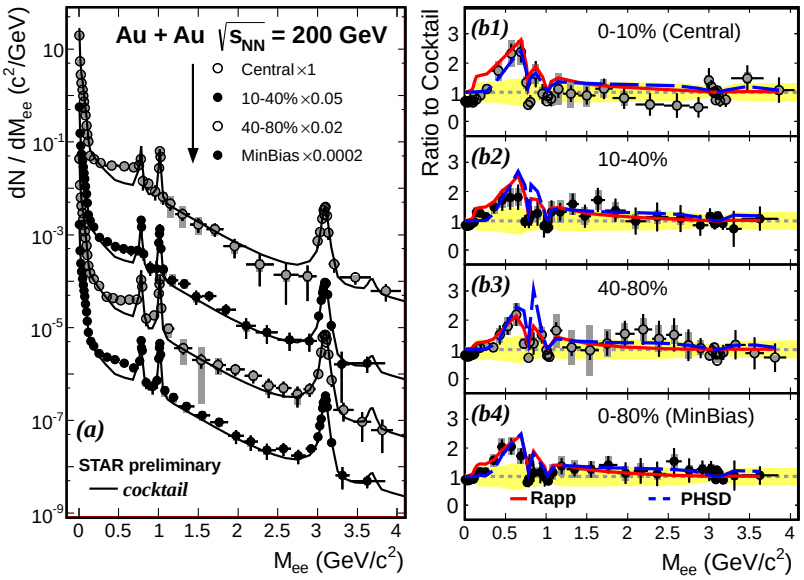

Figure 5.5: Centrality dependence of the midrapidity dilepton yields (left) and its ratios (right) to the 'cocktail' for 0-10%, 10-40%, 40-80%, 0-80% central Au+Au collisions at $\sqrt{s} = 200$ GeV: comparison of STAR data with theoretical predictions from the PHSD ('PHSD' - dashed lines) and the expanding fireball model ('Rapp' - solid lines). The figures are taken from Ref. [302].

underestimated the PHENIX data from the Run 2004 analysis for central collisions. The observed dilepton yield from STAR can be accounted for by the known hadronic sources, i.e. the decays of the π_0, η, η', ω, ρ, ϕ and a_1 mesons, of the Δ particle and the semi-leptonic decays of the D and $\bar{D}$ mesons, where the collisional broadening of the ρ-meson is taken into account.

More recently, the STAR Collaboration has released information on the explicit centrality dependence of the dilepton spectra. Fig. 5.5 shows the comparison of the STAR data of midrapidity dilepton yields (l.h.s.) and its ratios (r.h.s.) to the 'cocktail' for 0-10%, 10-40%, 40-80%, 0-80% central Au+Au collisions at $\sqrt{s_{NN}} = 200$ GeV in comparison to the predictions from the PHSD approach and the expanding fireball model of Rapp and collaborators. As seen from Fig. 5.5 the excess of the dilepton yield over the expected cocktail is larger for very central collisions and consistent with the model predictions including the collisional broadening of the ρ-meson spectral function at low invariant mass and QGP dominated radiations at intermediate masses. Accordingly, the tension between the PHENIX and STAR dilepton data (as well as PHSD predictions) no longer persists.

Moreover, the recent STAR dilepton data for Au+Au collisions from the Beam Energy Scan (BES) program for $\sqrt{s_{NN}} = 19.6, 27, 39$ and 62.4 GeV [302, 303] are also in line with the PHSD (as well as the expanding fireball model) predictions with a ρ-meson collisional broadening. According to the PHSD calculations the excess is increasing with decreasing energy due to a longer ρ-meson propagation in the high-baryon density phase (see Fig. 3 in Ref. [303]).

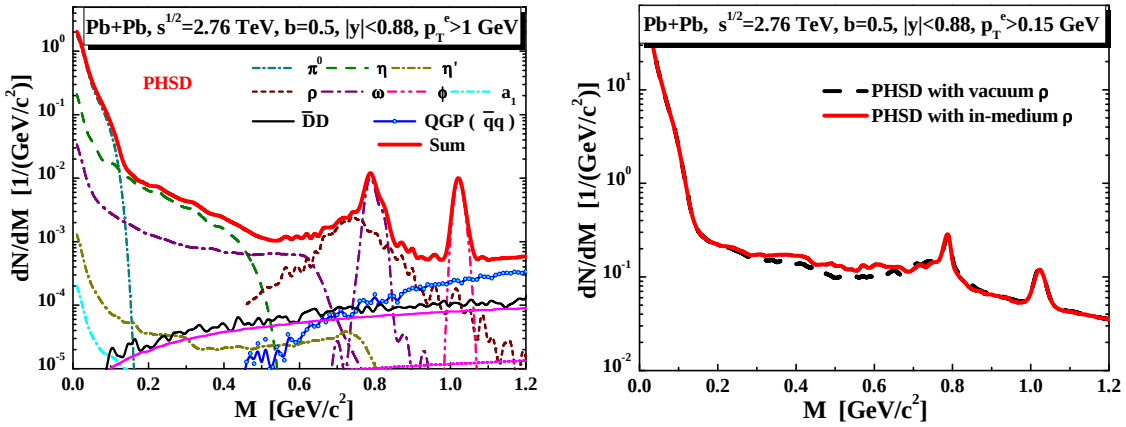

Figure 5.6: (l.h.s.) midrapidity dilepton yields for Pb+Pb at $\sqrt{s_{NN}} = 2.76$ TeV for a lepton p_T cut of 1 GeV/c. The channel decomposition is explained in the legend. (r.h.s.) Same as for the l.h.s. but for a lepton p_T cut of 0.15 GeV/c for a 'free' ρ spectral function (dashed line) and the collisional broadening scenario (solid line). The figures are taken from Ref. [304].

5.3 LHC energies

On the other hand, the upcoming ALICE data [305] for heavy-ion dileptons for Pb+Pb at $\sqrt{s} = 2.76$ TeV might give a further access to the dileptons emitted from the QGP [304, 306]. In Fig. 5.6 (l.h.s.) we present the PHSD predictions for central Pb+Pb collisions [304] in the low mass sector for a lepton p_T cut of 1 GeV/c. It is clearly seen that the QGP sources and the contribution from correlated $D\bar{D}$ pairs are non-leading in the low mass regime where we find the conventional hadronic sources. For a lepton p_T cut of 1 GeV/c (l.h.s.) one practically cannot identify an effect of the ρ-meson collisional broadening in the dilepton spectra in the PHSD calculations. Only when applying a low p_T cut of 0.15 GeV/c a small enhancement of the dilepton yield from 0.3 to 0.7 GeV becomes visible (r.h.s. of Fig. 5.6). This low sensitivity to hadronic in-medium effects at LHC energies from the PHSD is due to the fact that the hadrons appear late (after hadronization) in central Pb+Pb collisions and are boosted to high velocities due to the high pressure in the early partonic phase.

In the end, we mention that promising perspectives with dileptons have been suggested in Ref. [307] to measure the flow anisotropy coefficients v_n ($n = 2, 3$) similar to photons. The calculations with the viscous (3+1)d MUSIC hydro for central Au+Au collisions at RHIC energies show that the flow coefficients v_2, v_3 are sensitive to the dilepton sources and to the EoS and η/s ratio. The main advantage of measuring flow coefficients v_n with dileptons compared to photons is the fact that the extra degree-of-freedom M might allow to disentangle the sources additionally.

Chapter 6

Comparison of our calculations to the data on photon production in $A + A$ collisions

Direct photons are expected to provide a powerful probe of the quark-gluon plasma (QGP) as created in ultra-relativistic nuclear collisions. The photons interact only electromagnetically and thus escape to the detector almost undistorted through the dense and strongly interacting medium. Thus the photon transverse-momentum spectra and their azimuthal asymmetry carry information on the properties of the matter under extreme conditions, existing in the first few fm/c of the collisional evolution. On the other hand, the measured photons provide a time-integrated picture of the heavy-ion collision dynamics and are emitted from every moving electric charge – partons or hadrons. Therefore, a multitude of photon sources has to be differentiated in order to access the signal of interest. The dominant contributions to the *inclusive* photon production are the decays of mesons, dominantly pions, η- and ω-mesons. Experimental collaborations subtract the "*decay* photons" from the inclusive photon spectrum using a cocktail calculation [3, 4] and obtain the "direct" photons.

In particular the *direct* photons at transverse momenta $p_T < 3$ GeV/c are expected to be dominated by "thermal" sources, i.e. the radiation from the strongly interacting Quark-Gluon-Plasma (sQGP) [194, 310] and the secondary meson+meson and meson+baryon interactions in the hadronic phase [181, 182]. These partonic and hadronic channels have been studied within PHSD in detail in Refs. [20, 21] at Relativistic-Heavy-Ion-Collider energies and it was found that the partonic channels constitute up to half of the observed *direct* photon spectrum for central collisions. Other theoretical calculations also find a significant or even dominant contribution of the photons produced in the QGP to the *direct* photon spectrum [2, 6, 7, 25–27].

The low-p_T *direct* photons probe not only the temperature [2–4] of the produced QCD-matter, but also its (transport) properties, for instance, the shear viscosity η (cf. Section 4.4). Using the *direct* photon elliptic flow v_2 (a measure of the azimuthal asymmetry in the photon distribution) as a viscosimeter was first suggested by Dusling in Ref. [5]; this idea was later supported by the calculations in Refs. [2, 6–8]. It was also suggested that the photon spectra and v_2 are sensitive to the collective directed flow of the system [10, 311], to the equation of state [9, 10], to the possible production

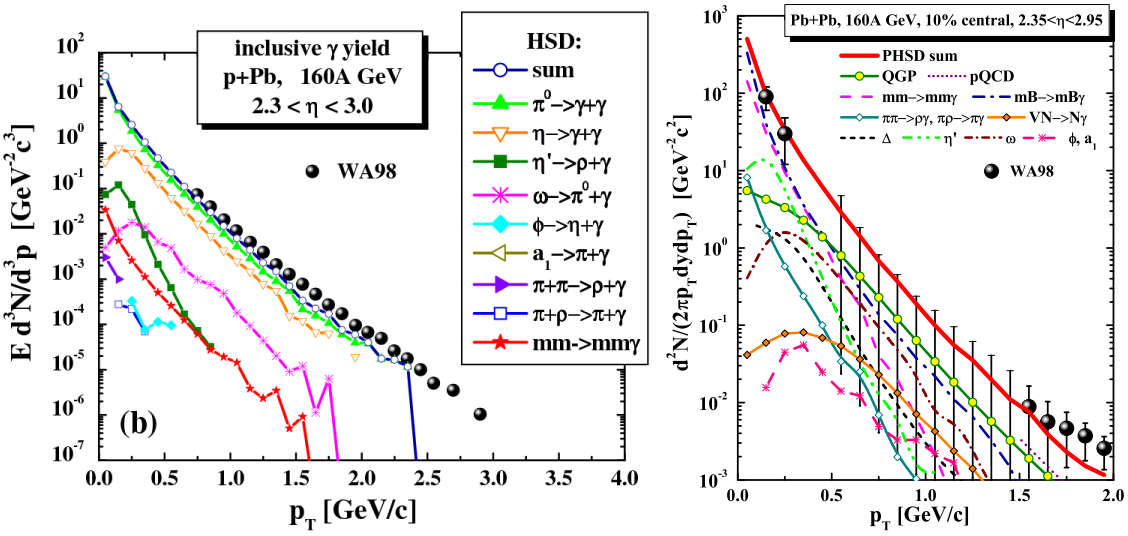

Figure 6.1: (l.h.s.) Comparison of the PHSD/HSD calculations for *inclusive* photons for p+Pb collisions at 160 GeV to the data of the WA98 Collaboration from Refs. [308, 309]. See legend for the contribution from the individual channels. (r.h.s.) Comparison of the PHSD calculations for *direct* photons from Pb+Pb at 158 A GeV collisions to the data of the WA98 Collaboration from Refs. [308, 309]. In comparison to the original HSD study [174]: (i) the meson+baryon bremsstrahlung (blue dash-dotted line), Δ decays (black short-dashed line) and the photons from QGP (green line with round symbols) are added (ii) and the meson+meson bremsstrahlung is now calculated beyond the SPA (magenta dashed line). The black line with diamond symbols labeled as "other" includes: ω, η', ϕ an d a_1-meson decays, binary channels $\pi + \rho/\pi \to \pi/\rho + \gamma$ and $N + V \to N + \gamma$. The figures are taken from Refs. [22, 174].

of a Glasma [11–13], to the rate of chemical equilibration in the QGP [14–16] and to the asymmetry induced by the strong magnetic field (flash) in the very early stage of the heavy-ion collision [17–19].

However, the observation by the PHENIX Collaboration [3] that the elliptic flow $v_2(p_T)$ of *direct* photons produced in minimum bias Au+Au collisions at $\sqrt{s_{NN}} = 200$ GeV is comparable to that of the produced pions was a surprise and in contrast to the theoretical expectations and predictions. Indeed, the photons produced by partonic interactions in the quark-gluon plasma phase have not been expected to show considerable flow because they are dominated by the emission in the initial phase before the elliptic flow fully develops. We here report about the studies within the PHSD approach on this issue and compare to other models in context of the available data from the different collaborations.

6.1 Direct photon spectra from SPS to LHC energies

We start with the system p+Pb at 160 GeV, i.e. at the top SPS energy. Fig. 6.1 (l.h.s.) shows the comparison of the HSD/PHSD calculations to the data of the WA98

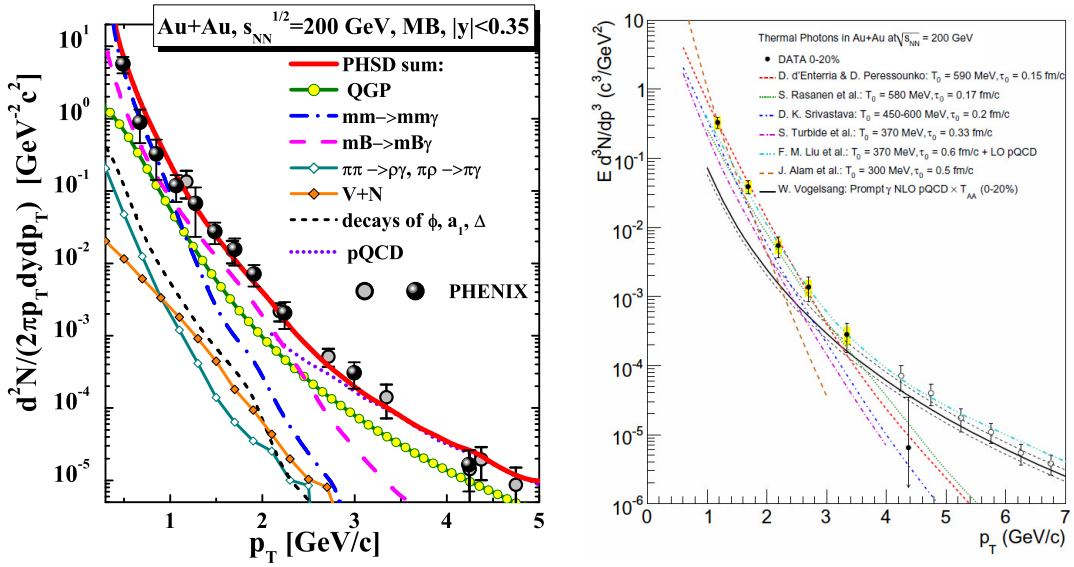

Figure 6.2: (l.h.s.) PHSD results for the spectrum of *direct* photons produced in 0-40% most central Au+Au collisions at $\sqrt{s_{NN}} = 200$ GeV as a function of the transverse momentum p_T at midrapidity $|y| < 0.35$. The data of the PHENIX Collaboration are adopted from Refs. [23, 312]. For the individual lines see the legend in the figure. The figure is taken from Ref. [22]. (r.h.s.) A compilation of various predictions for the *direct* photon yield in hydrodynamical models (see legend) in comparison to the data of the PHENIX collaboration. The figure is taken from Ref. [313].

Collaboration from Ref. [308, 309] in the pseudorapidity interval $2.3 < \eta < 3.0$. In this case almost the entire photon spectrum is described by the contribution from pion and η decays while the contribution from the heavier mesons is not leading. The successful description of these data by PHSD is dominantly due to the fact that the meson production itself is described very well in p+A reactions [174].

We continue with Pb+Pb collisions at $\sqrt{s_{NN}} = 17.3$ GeV. Fig. 6.1 (r.h.s.) shows the comparison of the PHSD calculations [22] for the *direct* photon p_T-spectrum to the data of the WA98 Collaboration from Ref. [308, 309] for 10% centrality in the pseudorapidity interval $2.35 < \eta < 2.95$. In addition to the sources, which had been incorporated in the original HSD study in 2008, the meson+baryon bremsstrahlung, $VN \to N\gamma$, $\Delta \to N\gamma$ decay and the QGP channels are added. Compared to the earlier results of Ref. [174], the description of the data is further improved and the conclusions remain unchanged: the bremsstrahlung contributions are essential for describing the data at low p_T. This interpretation is shared by the authors of Refs. [271, 277, 314], who also stressed the importance of the meson+meson bremsstrahlung in view of the WA98 data using hydrodynamical or fireball models. Note that the photon contribution from the QGP is practically negligible at this bombarding energy for low p_T and reaches at most 25% at $p_T > 0.5$ GeV.

We now step on to the top RHIC energy of $\sqrt{s_{NN}} = 200$ GeV and report on PHSD results for the differential photon spectra for the system Au+Au. The *direct* photon spectrum – as a sum of partonic as well as hadronic sources – in 0-40% central Au+Au collisions is presented in Fig. 6.2 (l.h.s.) as a function of the transverse momentum

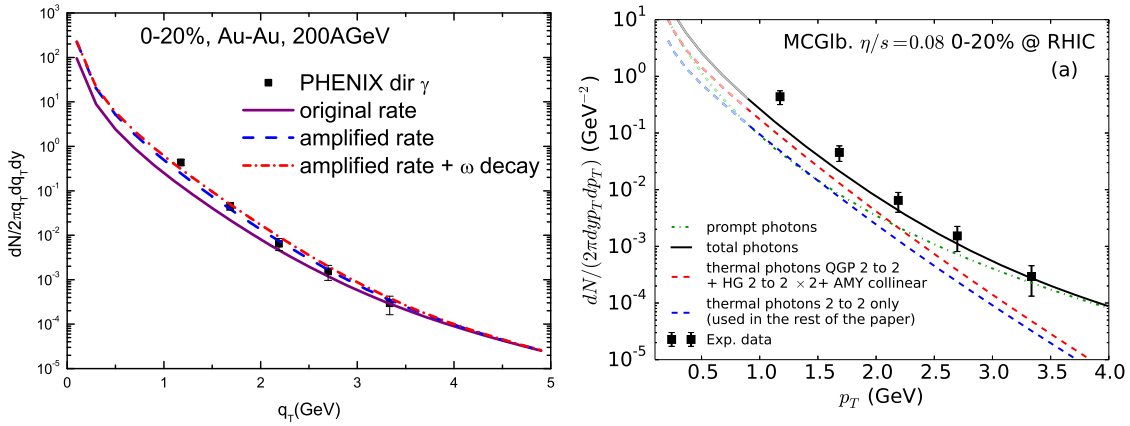

Figure 6.3: (l.h.s.) *Direct* photon spectra from the model of van Hees et al. [10] at RHIC when adding $\omega \to \pi^0 + \gamma$ decays at thermal freeze-out to a scenario with amplified rates at temperatures close to the pseudo-critical transition temperature T_c (dash-dotted line), compared to the amplified rate (dashed line) and default-rate (solid line) scenarios. The figure is taken from Ref.[10]. (r.h.s.) Calculated photon spectra in the viscous hydrodynamical model from Shen et al. [2] in comparison to the data from the PHENIX Collaboration [312].

p_T at midrapidity $|y| < 0.35$. While the 'hard' p_T spectra are dominated by the 'prompt' (pQCD) photons, the 'soft' spectra are filled by the 'thermal' sources: the QGP gives up to 50% of the *direct* photon yield below 2 GeV/c, a sizeable contribution stems from hadronic sources such as meson-meson (mm) and meson-Baryon (mB) bremsstrahlung while the contribution from binary mm reactions is of subleading order. Thus, according to the PHSD results the mm and mB bremsstrahlung turn out to be an important source of *direct* photons also at the top RHIC energy. We note, that the bremsstrahlung channels are not included in the mm binary 'HG' rate by Turbide et al. in Ref. [315] used in the hydro calculations addressed above. We stress that mm and mB bremsstrahlung can not be subtracted experimentally from the photon spectra and have to be included in theoretical models.

The right panel of Fig. 6.2 shows a compilation of various predictions for the *direct* photon yield in hydrodynamical models (see legend) in comparison to the data of the PHENIX collaboration from Ref. [313]. The NLO pQCD calculations for the prompt photon production from Vogelsang have been added to the *thermal* photon spectra. The actual results for the *direct* photon spectra depend on the initial temperature T_0 (varying by about a factor of 2) and the hydro starting time τ_0 which are fitted differently to final hadronic spectra, respectively. All these models only give a very low elliptic flow for the *direct* photons.

As an example for more recent calculations we show in Fig. 6.3 (l.h.s.) the results from the model of van Hees et al. [10] which is describing the PHENIX data [312] with a good accuracy. The calculations of Ref. [10] are based on a hydrodynamical model for the "fireball" evolution with the hypothesis that the rates of photon production are amplified for temperatures close to the hadronization transition and adding to the thermal spectra (calculated with the amplified rates) the photon contribution from

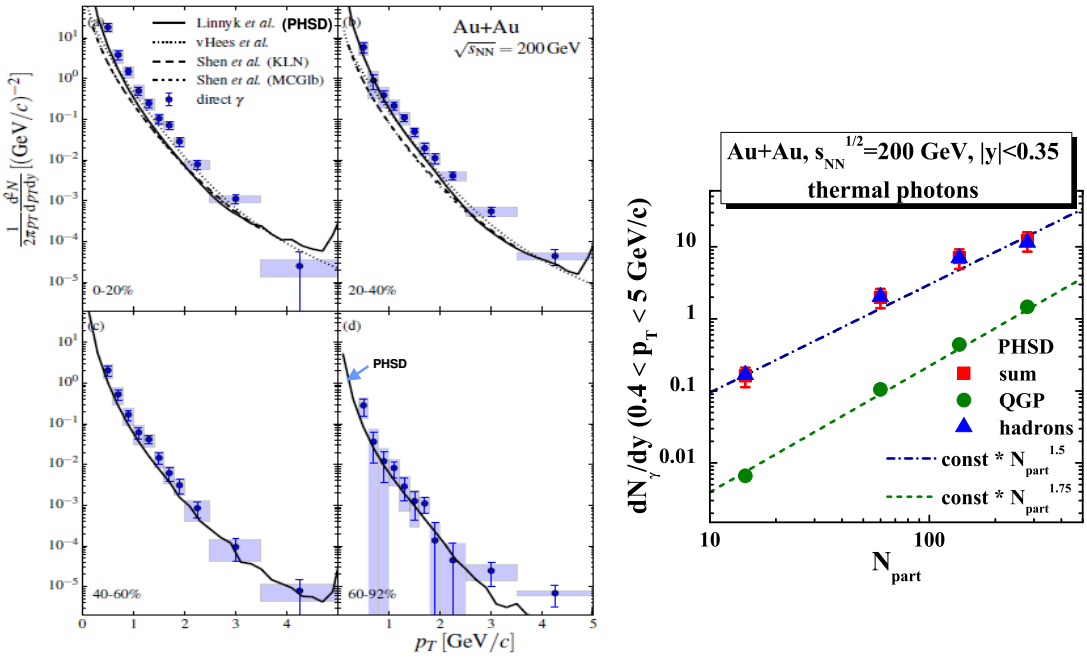

Figure 6.4: (*l.h.s*) Centrality dependence of the *direct* photon p_T-spectra for 0-20%, 20-40%, 40-60%, 60-92% central Au+Au collisions at $\sqrt{s} = 200$ GeV: model predictions vs. the PHENIX data [23]. The PHSD predictions are denoted by 'Linnyk et al.' (solid lines). The figure is taken from Ref. [316]. (*r.h.s*) The scaling of the integrated *thermal* photon yield from PHSD as a function of the number of participating nucleons in Au+Au collisions at $\sqrt{s_{NN}} = 200$ GeV for the hadronic channels (upper symbols) and partonic channels (lower symbols). The figure is taken from Ref. [21].

final-state ω-mesons at thermal freeze-out. The spectra presented on the right hand side of Fig. 6.3 have been calculated by Shen et al. [2] using a viscous hydrodynamical evolution and taking into account viscous effects in the photon rates. In this approach – that reproduces the final hadron spectra and hadron v_2 – the data are underestimated considerably. The discrepancy becomes enhanced when an alternative scenario of a gluon-dominated initial state is considered since the gluons do not carry electric charge.

Photon sources: QGP vs. HG

The question: "what dominates the photon spectra - *QGP radiation or hadronic contributions*" can be addressed experimentally by investigating the centrality dependence of the photon yield since the QGP contribution is expected to decrease when going from central to peripheral collisions where the hadronic channels are dominant. Fig. 6.4 (l.h.s.) shows the centrality dependence of the *direct* photon p_T-spectra for 0-20%, 20-40%, 40-60%, 60-92% central Au+Au collisions at $\sqrt{s} = 200$ GeV. The solid dots stand for the recent PHENIX data [23, 316] whereas the lines indicate the model predictions: solid line - PHSD (denoted as 'Linnyk et al.') [20–22], dashed and dashed-dotted lines ('Shen et al. (KLN)' and 'Shen et al.' (MCGib)') are the results from viscous (2+1)D VISH2+1 [311] and (3+1)D MUSIC [6, 7] hydro models whereas the

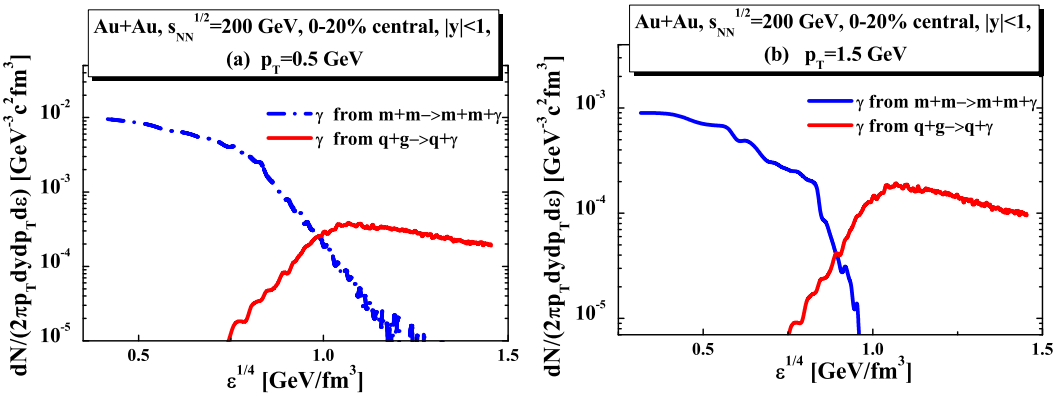

Figure 6.5: (l.h.s.) Photon yield with a transverse momentum $p_T = 0.5$ GeV/c at midrapidity produced in 0-20 % most central $Au + Au$ collisions as a function of the approximate local "temperature" (the fourth-root of the energy density) from the PHSD from meson-meson bremsstrahlung (dash-dotted lines) and gluon Compton scattering (solid lines). (r.h.s.) Same as in the left panel for photons with a transverse momentum $p_T = 1.5$ GeV/c. The figures are taken from Ref. [22].

dotted line ('vHees et al.') stands for the results of the expanding fireball model [317]. As seen from Fig. 6.4 (l.h.s.) for the central collisions the models deviate up to a factor of 2 from the data and each other due to the different dynamics and sources included (as discussed above); for the (semi-)peripheral collisions the PHSD results - dominated by mm and mB bremsstrahlung - are consistent with the data which favor these hadronic sources. Presently, no results from the other models for peripheral reactions are known.

The centrality dependence of the *direct* photon yield, integrated over different p_T ranges, has been measured by the PHENIX Collaboration, too [23, 316]. It has been found that the midrapidity 'thermal' photon yield scales with the number of participants as $dN/dy \sim N_{part}^{\alpha}$ with $\alpha = 1.48 \pm 0.08$ and only very slightly depends on the selected p_T range (which is still in the 'soft' sector, i.e. < 1.4 GeV/c). Note that the 'prompt' photon contribution (which scales as the pp 'prompt' yield times the number of binary collisions in A+A) has been subtracted from the data. The PHSD predictions [20–22] for the minimum bias Au+Au collisions give $\alpha(total) \approx 1.5$ (cf. Fig. 6.4, r.h.s.) which is dominated by hadronic contributions while the QGP channels scale with $\alpha(QGP) \sim 1.75$. A similar finding has been obtained by the viscous (2+1)D VISH2+1 and (3+1)D MUSIC hydro models [2]: $\alpha(HG) \sim 1.46$, $\alpha(QGP) \sim 2$, $\alpha(total) \sim 1.7$. Thus, the QGP photons show a centrality dependence significantly stronger than that of hadron gas (HG) photons.

Next, let us investigate the photon production across the phase transition in the heavy-ion collision to check whether the observed yield of *direct* photons is produced dominantly in some particular region of the energy-density or in some particular phase of matter. Fig. 6.5 shows the yield of photons produced at midrapidity in 0-20 % most central $Au + Au$ collisions at $\sqrt{s_{NN}} = 200$ GeV as functions of the approximate local "temperature" (i.e. the fourth-root of the energy density) from the PHSD. The left panel of Fig. 6.5 presents the calculations for photons with a transverse momentum

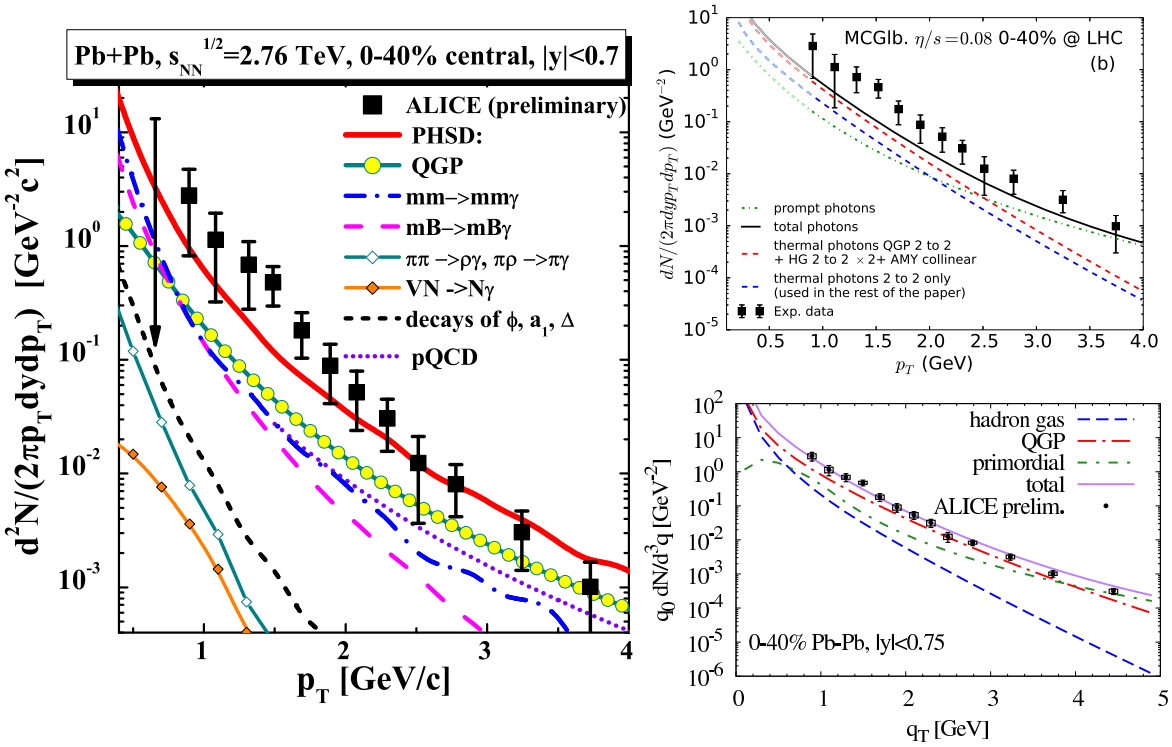

Figure 6.6: (l.h.s.) The yield of direct photons at midrapidity in Pb+Pb collisions at the invariant energy $\sqrt{s_{NN}}$ = 2.76 TeV for 0-40% centrality as predicted within the PHSD in comparison to the preliminary data from the ALICE Collaboration [4]. The figure is taken from Ref. [22]. (r.h.s., upper panel:) Photon spectra in 0−40% centrality Pb+Pb collisions at the LHC as calculated within the viscous hydrodynamics by Shen et al. [8]. The Pb+Pb data are from the ALICE Collaboration [4]. The figure is taken from Ref. [8]. (r.h.s., lower panel:) The same observable as calculated in the upper panel with an ideal hydrodynamical evolution and amplified photon rates around the transition temperature by van Hees et al. [10]. The figure is taken from Ref. [10].

p_T = 0.5 GeV/c, while the right panel corresponds to photons with a transverse momentum p_T = 1.5 GeV/c. We observe that the early, hot state does not dominate the photon production in the QGP contrary to expectations of the static thermal fireball model, where photon production is roughly proportional to a power of the temperature ($\sim T^4$). The integration over the dynamical evolution of the heavy-ion collision leads to roughly the same contribution of the different energy density regions since the rate decreases but the space-time volume increases. The photon production in the hadronic phase is dominated by the lower energies/temperatures because of the very long times over which the produced hadrons continue to interact elastically, which is accompanied by the photon bremsstrahlung in case of charged hadrons.

We now increase the invariant collision energy $\sqrt{s_{NN}}$ by a factor of 13.8. In Fig. 6.6 (l.h.s.) we show the *direct* photon yield from PHSD in Pb+Pb collisions at the invariant energy $\sqrt{s_{NN}}$ = 2.76 TeV for 0-40% centrality in comparison to the preliminary data of the ALICE Collaboration from Ref. [4]. We find a rather good overall agreement with

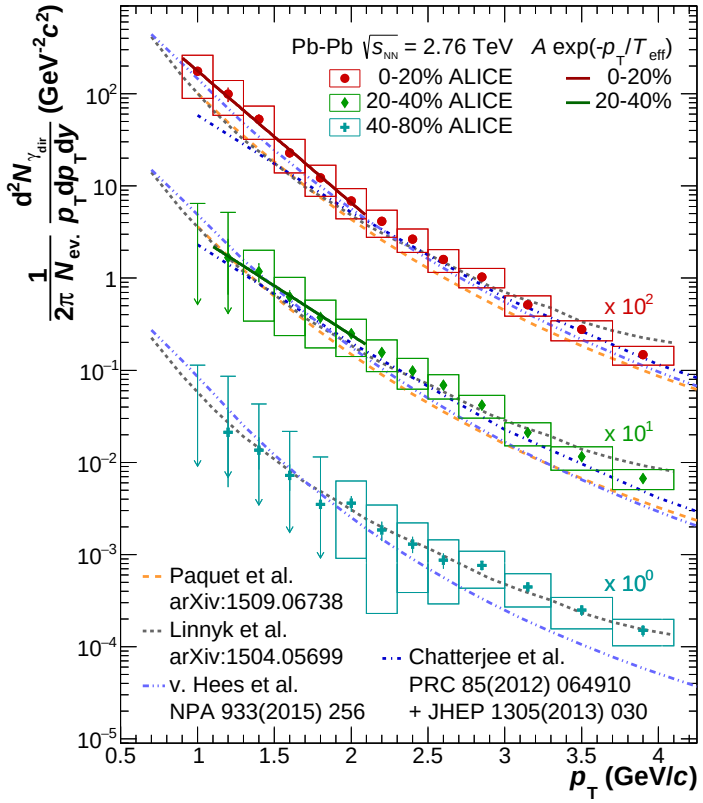

Figure 6.7: Centrality dependence of the *direct* photon p_T-spectra for 0-20%, 20-40%, 40-80% central Pb+Pb collisions at $\sqrt{s_{NN}}$=2.76 TeV: model predictions vs. the ALICE data [318]. The PHSD predictions are denoted by 'Linnyk et al.' (dotted lines). The figure is taken from Ref. [318].

the data within about a factor of 2 in the range of transverse momenta p_T from 1 to 4 GeV. On the other hand, the calculations tend to underestimate the preliminary data in the low-p_T region [319]. However, the significance of the comparison is not robust until the final data will be available. We, furthermore, present in Fig. 6.6 (r.h.s.) the photon spectra for 0−40% centrality Pb+Pb collisions at the LHC as calculated within the viscous hydrodynamics by Shen et al. [8] in comparison to the Pb+Pb data from the ALICE Collaboration [4] (upper right panel). In the right bottom panel we show the same observable as calculated in the ideal hydrodynamical model with amplified photon rates around the transition temperature by van Hees et al. [10]. Similar to RHIC energies the viscous hydro calculations [8] underestimate the measured photon yield for $p_T < 2$ GeV/c while the model of van Hees et al. [10] with amplified rates at T_c performs better.

An actual overview on the current situation with respect to the *direct* photon yields at different centralities has been provided by the ALICE Collaboration in Ref. [318] and is displayed in Fig. 6.7. The figure shows the centrality dependence of the *direct* photon p_T-spectra for 0-20%, 20-40%, 40-80% central Pb+Pb collisions at $\sqrt{s_{NN}}$=2.76 TeV in comparison to various model predictions. The PHSD predictions are denoted by 'Linnyk et al.' (dotted lines) and are compatible with the measurements within the error bars. This roughly holds also for the other models.

In conclusion, we have found that from SPS to LHC energies the radiation from the sQGP constitutes less than half of the observed number of *direct* photons for central reactions in the PHSD. The hydrodynamical and fireball models predict a larger fraction of the QGP photons to the total yield and are substantially lower in the hadronic contributions. The radiation from hadrons and their interaction – which are not measured separately so far – give a considerable contribution in the PHSD especially at low transverse momentum. The dominant hadronic sources are the meson decays, the meson-meson bremsstrahlung and the meson-baryon bremsstrahlung. While the first (e.g. the decays of ω, η', ϕ and a_1 mesons) can be subtracted from the photon spectra once the mesonic yields are determined independently by experiment, the reactions $\pi+\rho \to \pi+\gamma$, $\pi+\pi \to \rho+\gamma$, $V+N \to N+\gamma$, $\Delta \to N+\gamma$ as well as the meson-meson and meson-baryon bremsstrahlung can be 'separated' from the partonic sources only with the assistance of theoretical models (and corresponding uncertainties).

6.2 Elliptic flow of direct photons

We recall that the azimuthal momentum distribution of the photons is expressed in the form of a Fourier series as,

$$E\frac{d^3N}{d^3p} = \frac{d^2N}{2\pi p_T dp_T dy}\left(1+\sum_{n=1}^{\infty} 2v_n(p_T)\cos[n(\psi-\Psi_n)]\right), \tag{6.1}$$

where v_n is the magnitude of the n'th order harmonic term relative to the angle of the initial-state fluctuating spatial plane of symmetry Ψ_n and $p=(E,\vec{p})$ is the four-momentum of the photon. We here focus on the coefficients v_2 and v_3 which implies that we have to perform event by event calculations in order to catch the initial fluctuations in the shape of the interaction zone and the event plane Ψ_{EP}. We calculate the triangular flow v_3 with respect to Ψ_3 as $v_3\{\Psi_3\} = \langle\cos(3[\psi-\Psi_3])\rangle/\mathrm{Res}(\Psi_3)$. The event plane angle Ψ_3 and its resolution $\mathrm{Res}(\Psi_3)$ are evaluated as described in Ref. [86] via hadron-hadron correlations by the two-sub-events method [87, 88].

We note again that the second flow coefficient v_2 carries information on the interaction strength in the system – and thus on the state of matter and its properties – at the space-time point, from which the measured particles are emitted. The elliptic flow v_2 reflects the azimuthal asymmetry in the momentum distribution of the produced particles (p_x vs p_y), which is correlated with the geometrical azimuthal asymmetry of the initial reaction region. If the produced system is a weakly-interacting gas, then the initial spatial asymmetry is not effectively transferred into the final distribution of the momenta. On the other hand, if the produced matter has the properties of a liquid, then the initial geometrical configuration is reflected in the final particle momentum distribution.

More than a decade ago, the WA98 Collaboration has measured the elliptic flow v_2 of photons produced in $Pb+Pb$ collisions at the beam energy of $E_{beam}=$ 158 AGeV [320], and it was found that the $v_2(\gamma^{incl})$ of the low-transverse-momentum inclusive photons was about equal to the $v_2(\pi)$ of pions within the experimental uncertainties. This observation lead to the conclusion that either (Scenario a:) the contribu-

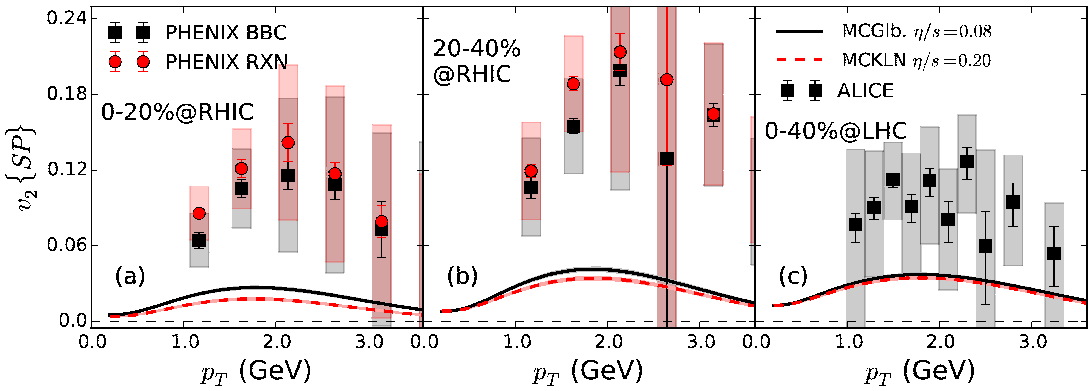

Figure 6.8: Comparison of *direct* photon (prompt + thermal (QGP+HG)) elliptic flow from event-by-event viscous hydrodynamics with recent experimental data from (a) 0-20% and (b) 20-40% central Au+Au collisions at RHIC [3] and (c) from 0-40% central Pb+Pb collisions at the LHC [321]. The solid black (dashed red) lines correspond to MCGlb (MCKLN) initial conditions evolved with a shear viscosity $\eta/s = 0.08$ (0.2), respectively. The figure is taken from Ref. [8].

tion of the *direct* photons to the inclusive ones is negligible in comparison to the *decay* photons, i.e. dominantly the π^0 decay products, or (Scenario 2:) the elliptic flow of the *direct* photons is comparable in magnitude to the $v_2(\gamma^{incl})$, $v_2(\gamma^{decay})$ and $v_2(\pi)$. However, in view of the *direct* photon spectrum from WA98, which we described in Section 6.1, there is a significant finite yield of *direct* photons at low transverse momentum. Thus the scenario 1 can be ruled out. Furthermore, the observed *direct* photons of low p_T must have a significant elliptic anisotropy v_2 of the same order of magnitude as the hadronic flow since they dominantly stem from hadronic sources. Thus the interpretation [174, 271] of the low-p_T *direct* photon yield measured by WA98 – as dominantly produced by the bremsstrahlung process in the mesonic collisions $\pi + \pi \to \pi + \pi + \gamma$ – is in accord also with the data on the photon elliptic flow $v_2(\gamma^{incl})$ at the top SPS energy.

Let us note that the same conclusions apply also to the most recent studies of the photon elliptic flow at RHIC and LHC. The PHENIX and ALICE Collaborations have measured the inclusive photon v_2 and found that at low transverse momenta it is comparable to the $v_2(p_T)$ of *decay* photons as calculated in cocktail simulations based on the known mesonic $v_2(p_T)$. Therefore, either (a) the yield of the *direct* photons to the inclusive ones is not statistically significant in comparison to the *decay* photons or (b) the elliptic flow of the *direct* photons must be as large as $v_2(\gamma^{decay})$ and $v_2(\gamma^{incl})$.

The direct photon v_2 "puzzle"

The recent observation by the PHENIX Collaboration [3] that the elliptic flow $v_2(p_T)$ of *direct* photons produced in minimum bias Au+Au collisions at $\sqrt{s_{NN}} = 200$ GeV is comparable to that of the produced pions was a surprise and in contrast to the theoretical expectations and predictions [6, 7, 25–27]. Indeed, the photons produced by partonic interactions in the quark-gluon plasma phase have not been expected to show a considerable flow because - in a hydrodynamical picture - they are dominated

by the emission at high temperatures, i.e. in the initial phase before the elliptic flow fully develops. Since the *direct* photon $v_2(\gamma^{dir})$ is a 'weighted average' (w_i) of the elliptic flow of individual contributions i,

$$v_2(\gamma^{dir}) = \sum_i v_2(\gamma^i) w_i(p_T) = \frac{\sum_i v_2(\gamma^i) N_i(p_T)}{\sum_i N_i(p_T)}, \tag{6.2}$$

a large QGP contribution gives a smaller $v_2(\gamma^{dir})$.

A sizable photon v_2 has been observed also by the ALICE Collaboration [4, 321] at the LHC. None of the theoretical models could describe simultaneously the photon spectra and v_2 which may be noted as a "puzzle" for theory (cf. Fig. 6.8 in case of viscuous hydro calculations by Shen et al. in Ref. [8]). Moreover, the PHENIX and ALICE Collaborations have reported recently the observation of non-zero triangular flow v_3 (see Refs. [303, 322]). Thus, the consistent description of the photon experimental data remains a challenge for theory and has stimulated a couple of new ideas and developments that are briefly outlined in the following.

Developments in hydrodynamical models

The following developments in the hydrodynamical modeling of the heavy-ion collision evolution and the photon rates were stimulated by the puzzling disagreement between the models and the photon data (cf. Fig. 6.8).

I.) The first hydrodynamical calculations on photon spectra were based on ideal hydrodynamics with smooth Glauber-type initial conditions (cf. Ref. [260]). The influence of *event-by-event (e-b-e) fluctuating initial conditions* on the photon observables was investigated within the (2+1)D Jyväskylä ideal hydro model [27] which includes the equilibrated QGP and Hadron Gas (HG) fluids. It has been shown that 'bumpy' initial conditions based on the Monte-Carlo Glauber model lead to a slight increase at high p_T (> 3 GeV/c) for the yield and v_2 which is, however, not sufficient to explain the experimental data – see the comparison of model calculations with the PHENIX data in Figs. 7,8 of Ref. [27] and with the ALICE data in Figs. 9,10 of Ref. [27].

II.) The influence of *viscous corrections* on photon spectra and anisotropic flow coefficients v_n has been investigated in two independent viscous hydro models: 1) (3+1)D MUSIC [6, 7] which is based on "bumpy" e-b-e fluctuating initial conditions from IP-Glasma and includes viscous QGP (with lQCD EoS) and HG fluids; 2) (2+1)D VISH2+1 [311] with 'bumpy' e-b-e fluctuating initial conditions from the Monte-Carlo Glauber model and viscous QGP (with lQCD EoS) and HG fluids. The photon rate has been modified in Refs. [6, 7, 311] in order to account for first order non-equilibrium (viscous) corrections to the standard equilibrium rates (i.e. the thermal QGP [173] and HG [315] rates). It has been found that the viscous corrections only slightly increase the high p_T spectra compared to the ideal hydro calculations while they have a large effect on the anisotropic flow coefficients v_n. Interesting to note that the viscous suppression of hydrodynamic flow for photons is much stronger than for hadrons. Also the photon v_n coefficients are more sensitive to the QGP shear viscosity which might serve the photon flow observables as a *QGP viscometer* as suggested in Ref. [311].

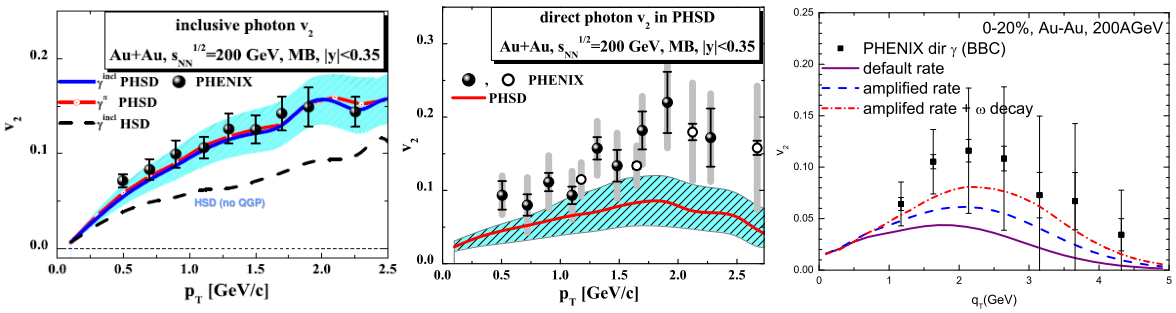

Figure 6.9: *Inclusive* (left) and *direct* (middle) photon elliptic flow coefficient $v_2(p_T)$ from the PHSD approach in comparison to the PHENIX data [3] for midrapidity minimum bias Au+Au collisions at $\sqrt{s} = 200$ GeV. The figures are taken from Ref. [20–22]. (r.h.s.) *Direct* photon spectra v_2 from the fireball model at RHIC when adding $\omega \to \pi^0 + \gamma$ decays at thermal freeze-out to the scenario with amplified rates (dash-dotted line), compared to the amplified-rate (dashed line) and default-rate (solid line) scenarios. The figure is taken from Ref.[10].

It is important to stress that the state-of-art hydro models discussed above reproduce well the hadronic 'bulk' observables (e.g. rapidity distributions, p_T spectra and v_2, v_3 of hadrons). However, in spite of definite improvements of the general dynamics by including the fluctuating initial conditions (IP-Glasma or MC-Glauber type) and viscous effects, the hydro models underestimate the spectra and v_2 of photons at RHIC and LHC energies.

III.) Another idea, which has been checked recently within the (2+1)D VISH2+1 viscous hydro model by Shen et al. [311], corresponds to the generation of *'pre-equilibrium' flow* (see Ref. [323]). The idea of 'initial' flow has been suggested in Ref. [317] and modeled as a rapid increase of bulk v_2 in the expanding fireball model which leads to a substantial enhancement of photon v_2. In a viscous hydro model [323] the generation of pre-equilibrium flow has been realized using a free-streaming model to evolve the partons to 0.6 fm/c where the Landau matching takes over to switch to viscous hydro. Such a scenario leads to a quick development of momentum anisotropy with saturation near the critical temperature T_c. Although the pre-equilibrium flow effect increases the photon v_2 slightly this is not sufficient to reproduce the ALICE data (the same holds for the PHENIX data at RHIC energies). Note, that the actual strength of such an effect depends on the way of its modeling (cf. Ref. [317]). Moreover, the physical origin of such 'initial' (pre-equilibrium) flow has to be justified/found first before robust conclusions can be drown.

One may speculate about the possible effects on photon observables from further improvements of hydro models such as an inclusion of the finite bulk viscosity as well as other transport coefficients and their temperature dependence etc. However, the failure of the state-of-art viscous hydro models to describe the photon observables is striking although the hadronic 'bulk' dynamics is well reproduced.

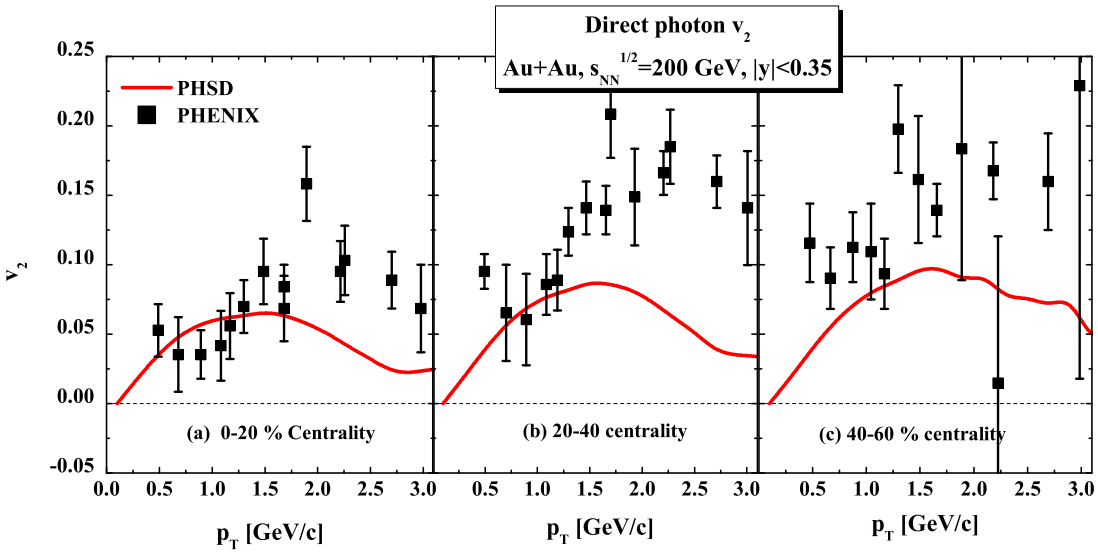

Figure 6.10: Centrality dependence of the *direct* photon v_2 for Au+Au collisions at $\sqrt{s_{NN}}$ = 200 GeV for different centralities (see legend); the data from the PHENIX Collaboration [23, 324] are compared to the earlier PHSD predictions from Ref. [21].

Photons from non-equilibrium transport

In order to shed some light on the photon v_2 puzzle outlined above, we consider the influence of *non-equilibrium dynamics* on the photon production in the following. As a 'laboratory' for that we will employ the microscopic PHSD transport approach that has been derived and described in Sections 2-4, while the implementation of photon production by the various partonic and hadronic channels has been explained in Chapter 5. Since the elliptic flow of pions (or charged hadrons) is under control in PHSD in comparison to the data from the PHENIX, STAR and ALICE Collaborations (cf. Refs. [3, 20, 68, 325, 326]); also the spectrum of their *decay* photons is predicted reliably by the approach. This allows for a solid computation of the *direct* photon yield at all energies from SPS to LHC.

In the PHSD the *direct* photon $v_2(\gamma^{dir})$ is calculating by building the weighted sum of the channels, which are not subtracted by the data-driven methods, as follows: the photons from the quark-gluon plasma, from the initial hard parton collisions (pQCD photons), from the decays of short-living resonances (a_1-meson, ϕ-meson, Δ-baryon), from the binary meson+meson and meson+baryon channels ($\pi + \rho \to \pi + \gamma$, $\pi + \pi \to \rho + \gamma$, $V + p/n \to n/p + \gamma$), and from the bremsstrahlung in the elastic meson+meson and meson+baryon collisions ($m + m \to m + m + \gamma$, $m + B \to m + B + \gamma$). The *direct* photon v_2 is extracted by summing up the elliptic flow of the individual channels contributing to the *direct* photons, using their contributions to the spectrum as the relative p_T-dependent weights, $w_i(p_T)$, cf. Eq. 6.2.

The results for the elliptic flow $v_2(p_T)$ of *direct photons* produced in $Au + Au$ collisions at the top RHIC energy are shown in the middle panel of Fig. 6.9 while the elliptic flow in the left panel in comparison to the PHENIX data [3]. Since the inclusive photons dominantly stem from π^0 decay the left panel of Fig. 6.9 demonstrates again that the pion v_2 is under control in PHSD while HSD calculations (dashed line) fail

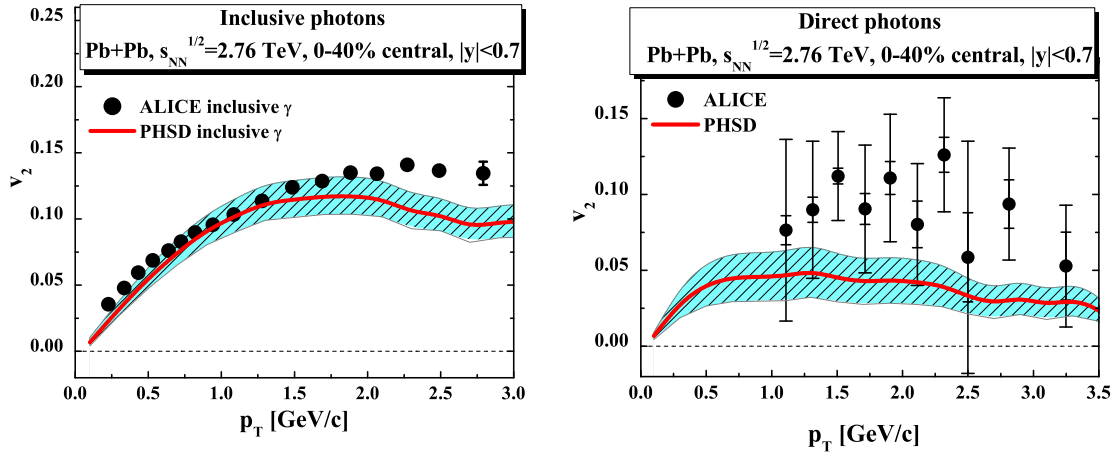

Figure 6.11: (l.h.s.) Elliptic flow v_2 versus transverse momentum p_T for the *inclusive* photons produced in 0-40% central Pb+Pb collisions at $\sqrt{s_{NN}} = 2.76$ TeV as calculated by the PHSD (solid red line); the blue error band reflects the finite statistics and the uncertainty in the modeling of the cross sections for the individual channels. (r.h.s.) Elliptic flow v_2 versus transverse momentum p_T for the *direct* photons produced in 0-40% central Pb+Pb collisions at $\sqrt{s_{NN}} = 2.76$ TeV as predicted by the PHSD (solid red line); the blue error band is dominated by the uncertainty in the modeling of the cross sections for the individual channels. The data from the ALICE Collaboration are taken from Ref. [327].

substantially. According to the PHSD calculations for the *direct* photon spectra almost half of the *direct* photons measured by PHENIX (in central collisions) stems from the collisions of quarks and gluons in the deconfined medium created in the initial phase of the collision. The photons produced in the QGP carry a very small v_2 and lead to an overall *direct* photon v_2 about a factor of 2 below the pion $v_2(\pi)$ even though the other channels in the sum (6.2) have large elliptic flow coefficients v_2 of the order of $v_2(\pi)$ (cf. Fig. 7 of Ref. [20]). This leads to a final elliptic flow for *direct* photons which is about half of the measured v_2 in PHSD. The right panel of Fig. 6.9 shows the photon v_2 from the fireball model of van Hees et al. [10] for different scenarios: the solid line corresponds to the 'default scenario', which is comparable to the PHSD results for v_2 (middle panel). The dashed line is obtained when amplifying the production rate close to T_c while the dash-dotted line additionally includes the photons from ω-decay at freeze-out. We note that in PHSD we do not find an enhanced photon rate close to T_c (cf. Fig. 27) and the ω-decay contributions are included by default. In summary, we conclude that the PHSD results lead to a *direct* photon v_2 at RHIC which is substantially larger that that from hydro calculations (cf. Fig. 29) but still underestimates the PHENIX data at RHIC.

The PHSD results are readily understood as follows: the partonic collisions – producing photons in the QGP – take place throughout the evolution of the collision but the collision rate falls rapidly with time in PHSD and thus the production of photons from the QGP is dominated by the early times. As a consequence, the elliptic flow 'picked up' by the photons from the parent parton collisions saturates after about

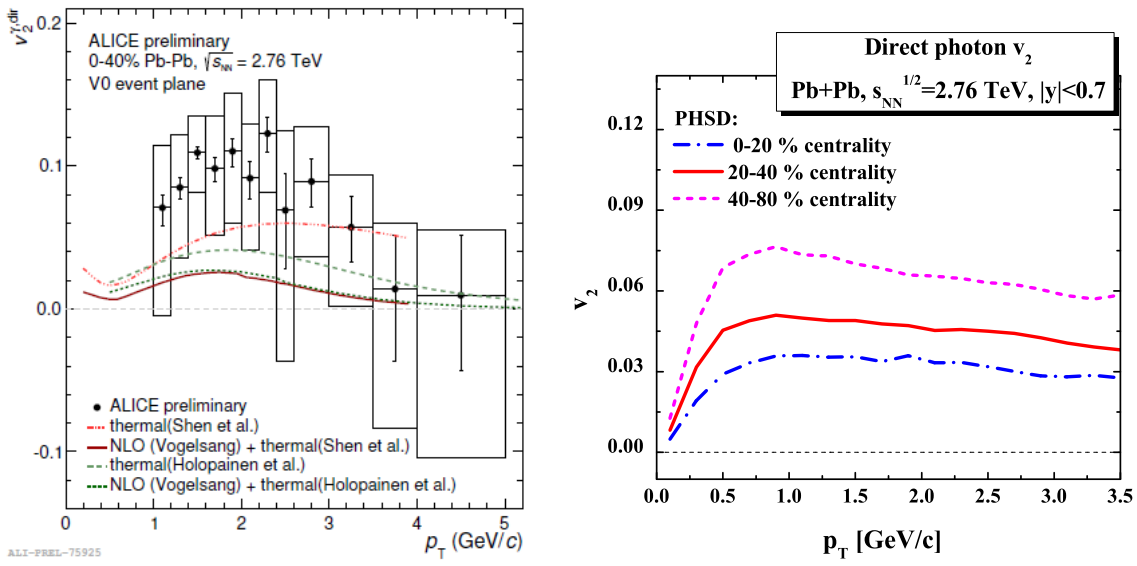

Figure 6.12: (l.h.s.) Preliminary data of the ALICE Collaboration for the *direct* photon elliptic flow v_2 in comparison to theoretical calculations from Refs. [8, 328, 329]. The figure is taken from Ref. [327]. (r.h.s.) Predictions for the elliptic flow v_2 of *direct* photons from PHSD versus transverse momentum p_T produced in Pb+Pb collisions at $\sqrt{s_{NN}} = 2.76$ TeV for different centrality classes (see legend).

5 fm/c and reaches a relatively low value of about 0.02, only. We note that a delayed production of charges from the strong gluon fields ('glasma' [330–333]) might shift the QGP photon production to somewhat later times when the elliptic flow is built up more but this also decreases the amount of QGP photons! However, we cannot quantitatively answer whether the additional evolution in the pre-plasma state could generate considerable additional v_2 while reproducing the photon spectra.

A preliminary summary of the current situation is displayed in Fig. 6.10 where the photon elliptic flow from PHENIX is compared to the PHSD predictions for different centrality classes 0-20% (a), 20-40% (b) and 40-60% (c). Whereas the elliptic flow is roughly described in the most central class there is an increasing tendency to underestimate in the PHSD the strong elliptic flow especially for peripheral collisions where some additional source might be present. Thus the observed centrality dependence of the elliptic flow is roughly in agreement with the interpretation that a large fraction of the *direct* photons is of hadronic origin (in particular from the bremsstrahlung in meson+meson and meson+baryon collisions); the latter contribution becomes stronger or even dominant in more peripheral collisions. But more precise data will be mandatory for a robust conclusion.

We finally present the PHSD predictions/calculations for the elliptic flow of inclusive and *direct* photons produced in $Pb + Pb$ collisions at the energy of $\sqrt{s_{NN}} = 2.76$ TeV at the LHC within the acceptance of the ALICE detector. Since the pion v_2 is described well within the PHSD at $\sqrt{s_{NN}} = 2.76$ TeV this is expected also for the inclusive photon v_2 due to the dominance of photons from π^0 decay. The left panel of Fig. 6.11 presents predictions/calculations for the elliptic flow v_2 versus transverse momentum p_T for the *inclusive* photons produced in 0-40% central Pb+Pb collisions

at $\sqrt{s_{NN}}$ = 2.76 TeV (solid red line) with the blue error band reflecting the finite statistics and the theoretical uncertainty in the modeling of the cross sections for the individual channels. The elliptic flow $v_2(p_T)$ of *direct* photons produced in 0-40% central Pb+Pb collisions at $\sqrt{s_{NN}} = 2.76$ TeV as predicted by the PHSD (solid red line) is shown in the right panel of Fig. 6.11, the blue error band is dominated by the uncertainty in the modeling of the cross sections for the individual channels. As in case of the PHENIX data at RHIC the preliminary data of the ALICE Collaboration for the *direct* photon elliptic flow v_2 for the same centrality are slightly higher than the PHSD predictions (although compatible within error bars). The different lines in Fig. 6.12 (l.h.s.) show the *direct* photon $v_2(p_T)$ from the theoretical calculations in Refs. [8, 328, 329] (see legend) which are similar to the PHSD predictions or even below. The situation at the LHC energy of $\sqrt{s_{NN}} = 2.76$ TeV is thus comparable to the one at the top RHIC energy and the v_2 puzzle remains.

We, furthermore, provide predictions for the centrality dependence of the *direct* photon $v_2(p_T)$ in Pb+Pb collisions at $\sqrt{s_{NN}} = 2.76$ TeV in the centrality classes 0-20%, 20-40% and 40-80% which are of relevance for the upcoming measurements by the ALICE Collaboration at the LHC. The actual results from PHSD are displayed in Fig. 6.12 (r.h.s.) and show a very similar centrality dependence as in case of Au+Au collisions at the top RHIC energy.

We note that there are other scenarios towards the solution of the *direct* photon v_2 puzzle proposed during the 'Quark Matter-2014 Conference': early-time magnetic field effects [334, 335], Glasma effects [11], or non-perturbative effects of a 'semi-QGP' [336]. We discard an explicit discussion of these suggestions.

6.3 Triangular flow of direct photons

We have seen in the previous Chapters that the measured spectra of *direct* photons could be reproduced by the PHSD calculations at least within a factor of 2 (which is comparable with the current accuracy of the measurements). Also, the *inclusive* photon v_2 was well described and the elliptic flow of *direct* photons was qualitatively in line with the data and attributed essentially to hadronic sources although still underestimating the data.

On the other hand, there exists an alternative interpretation of the strong elliptic flow of *direct* photons, in which the azimuthal asymmetry of the photons is due to the initial strong magnetic field essentially produced by spectator charges (protons). Indeed, the magnetic field strength in the very early reaction stage reaches up to $eB_y \approx 5m_\pi^2$ in semi-peripheral $Au + Au$ collisions at $\sqrt{s_{NN}} = 200$ GeV (see the calculations within the PHSD in Ref. [338]; comparable estimates have been obtained also in Refs. [18, 19, 339]). These strong magnetic fields might influence the photon production via the polarization of the medium, e.g. by influencing the motion of charged quarks in the QGP, or by directly inducing a real photon radiation via the virtual photon ($\vec{B}$-field) coupling to a quark loop and (multiple) gluons; the photons are then produced azimuthal asymmetrically with positive v_2.

The photon production under the influence of magnetic fields has been calculated in Refs. [11, 17–19, 334, 340]. The observed spectra and elliptic flow of *direct* photons

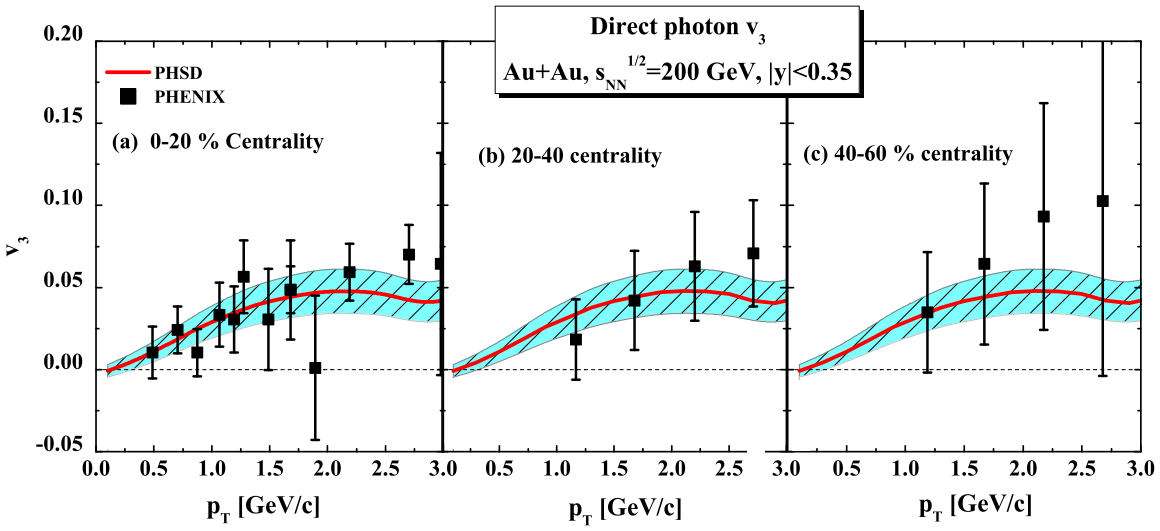

Figure 6.13: (Color on-line) Triangular flow v_3 versus transverse momentum p_T for the *direct* photons produced in Au+Au collisions at $\sqrt{s_{NN}} = 200$ GeV in three centrality classes (see legends). The PHSD results are shown by the solid red lines in comparison to the data of the PHENIX Collaboration (black symbols) taken from Ref. [324, 337].

could be explained using suitable assumptions on the conductivity, bulk viscosity or degree of chemical equilibration in the early produced matter. The common feature of these calculations was that the *triangular* flow coefficient v_3 of the *direct* photons was expected to be very small. Indeed, the magnetic field may lead to an azimuthal asymmetry v_2 but not to a triangular mode v_3.

Consequently, it is of interest to measure experimentally the third flow coefficient $v_3(p_T)$ and to compare it to the calculations in the different classes of models: (a) those attributing the large elliptic flow and strong yield of *direct* photons dominantly to hadronic sources, e.g. the PHSD transport approach; (b) the models suggesting the large azimuthal asymmetry and additional yield of *direct* photons to be caused by the early magnetic fields; (c) the models assuming that the yield of *direct* photons at low p_T is dominated by partonic channels.

In Fig. 6.13 we present our results for the triangular flow v_3 versus transverse momentum p_T for the *direct* photons produced in Au+Au collisions at $\sqrt{s_{NN}} = 200$ GeV from the PHSD (solid red lines) for 0-20% (a), 20-40% (b) and 40-60% (c) centrality. The PHSD gives a positive non-zero triangular flow of *direct* photons up to 6% with very little centrality dependence on the level of the present accuracy ($\sim 25\%$). The PHSD results are in agreement with the data of the PHENIX Collaboration from Refs. [303, 316, 337] which suggests that the scenario (a) is at least compatible with the measurements.

The preliminary data of the ALICE Collaboration for the v_3 of inclusive photons in Fig. 6.14 (l.h.s.) do not seem to point towards an interpretation of the *direct* photons being dominantly produced in the early stage under the influence of the magnetic field (b), because the v_3 of these photons is expected to be close to zero. Of course, the photon production in the magnetic fields occurs on top of other channels, which may carry finite triangular flow v_3. But the weighted sum of all the channels including the

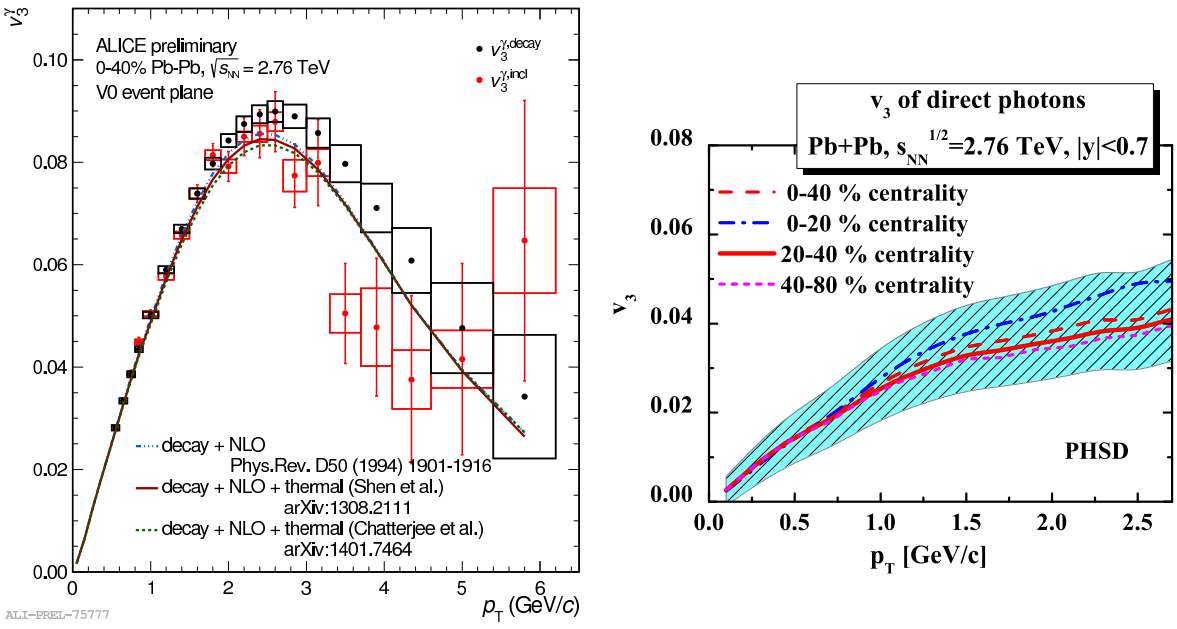

Figure 6.14: (l.h.s.) Preliminary data of the ALICE Collaboration for the inclusive photon $v_3(p_T)$. The lines represent contributions of *decay* photons with added theoretical calculations from Refs. [8, 328, 329]. The figure is taken from Ref. [341]. (r.h.s.) Predictions for the triangular flow v_3 versus transverse momentum p_T for the *direct* photons produced in different centrality classes for Pb+Pb collisions at $\sqrt{s_{NN}} = 2.76$ TeV from the PHSD (see legend); the blue band reflects the uncertainty in the modeling of the cross sections for the individual channels and give a measure of the present level of accuracy. The figure is taken from Ref. [22].

magnetic-field-induced photons will give a smaller $v_3 \neq 0$ than the sum without this channel. The scenario (c) has been studied by other groups within a hydrodynamic modeling of the collision in Refs. [8, 342]. The triangular flow $v_3(p_T)$ of *direct* photons from Refs. [8, 342] is about a factor of 2 smaller than that obtained in the PHSD approach.

In Fig. 6.14 (r.h.s.) we present predictions for the triangular flow v_3 versus transverse momentum p_T for the *direct* photons produced in different centrality classes for Pb+Pb collisions at $\sqrt{s_{NN}} = 2.76$ TeV from the PHSD (see legend); the blue band reflects the uncertainty in the modeling of the cross sections for the individual channels and give a measure of the present level of accuracy. The centrality dependence of $v_3(p_T)$ turns out to be low and is practically constant within the accuracy of the present PHSD calculations. An experimental confirmation of this expectation could further affirm the notion of large hadronic contributions to the *direct* photons and in particular the photon production via the bremsstrahlung in meson and baryon collisions. It should be possible to differentiate between the scenarios in the future, when data of higher accuracy and information on the centrality dependence of *direct* photons (especially on v_2 and v_3) will become available.

Chapter 7

Summary

In this thesis we have addressed the dynamics of relativistic heavy-ion reactions and in particular the information obtained from electromagnetic probes that stem from the partonic and hadronic phases. While the out-of-equilibrium description of strongly interacting relativistic fields has been based on the theory of Kadanoff and Baym, the description of QCD in equilibrium has been performed within an effective dynamical quasiparticle model (DQPM). The width of the dynamical quasiparticles is controlled by transport coefficients in equilibrium that can be compared to the same quantities from lattice QCD. The resulting off-shell transport approach is denoted by Parton-Hadron-String Dynamics (PHSD) and reproduces the equation of state, the sound velocity squared $c_s^2(T)$ as well as the relevant transport coefficients such as the shear viscosity η, the bulk viscosity ζ and the electrical conductivity σ_0 in the partonic phase from lattice QCD. Furthermore, it includes dynamical transition rates for hadronization, i.e. for the change of colored partonic to colo-neutral hadronic degrees-of-freedom, that satisfy all conservation laws and do not violate the second law of thermodynamics. It has been shown that the PHSD captures the bulk dynamics of heavy-ion collisions from lower SPS to LHC energies and thus provides a solid ground for the evaluation of the electromagnetic emissivity on the basis of the same dynamical propagators in the partonic phase that are employed for the dynamical evolution of the partonic system. The PHSD 'tests' indicate that the 'soft' physics at LHC in central A-A reactions is very similar to the top RHIC energy regime although the invariant energy is higher by more than an order of magnitude.

The main messages from the *photon* studies can be summarize briefly as:

- the photons provide a critical test for the theoretical models: the standard dynamical models - constructed to reproduce the 'hadronic world' - fail to explain the photon experimental data;

- the details of the hydro models (fluctuating initial conditions, viscosity, pre-equilibrium flow) have a small impact on the photon observables;

- as suggested by the PHSD transport model calculations, the role of such background sources as mm and mB bremsstrahlung has been underestimated in the past and was found to be dominant at low photon p_T;

- the dynamics of the initial phases of the reaction might turn out to be important (pre-equilibrium /'initial' flow, Glasma effect etc.).

Finally, one must conclude that the photons are one of the most sensitive probes for the dynamics of heavy-ion collisions and for the role of the partonic phase. We also mention that in an initial 'Glasma' phase the photon/dilepton production is suppressed by about an order of magnitude since the gluon fields do not carry electric charge. In this case the *direct* photons would practically stem for the hadronic stages and carry the full hadronic elliptic flow v_2.

The main messages from the dilepton studies in are:

- at low masses ($M = 0.2 - 0.6$ GeV/c^2) the dilepton spectra show sizable changes due to hadronic in-medium effects, i.e. multiple hadronic resonance formation or a modification of the properties of vector mesons (such as collisional broadening) in the hot and dense hadronic medium (partially related to chiral symmetry restoration); these effects can be observed at all energies from SIS to LHC but are most pronounced in the FAIR/NICA energy regime;

- at intermediate masses the QGP ($q\bar{q}$ thermal radiation) dominates for $M > 1.2$ GeV/c^2. The fraction of QGP sources grows with increasing energy and becomes dominant at the LHC energies.

- The tension between the PHENIX and STAR dilepton data at the top RHIC energy (as well as PHSD predictions) no longer persists.

Finally, the dilepton measurements within the future experimental energy and system scan (pp, pA, AA) from low to top RHIC energies as well as new ALICE data at LHC energies will extend our knowledge on the properties of hadronic and partonic matter via its electromagnetic radiation and show if the very initial degrees-of-freedom in relativistic heavy-ion collisions are electrically charged (quarks and antiquarks) or not (gluons).

Bibliography

[1] W. Cassing, E. L. Bratkovskaya, Phys. Rept. 308 (1999) 65.

[2] C. Shen, U. W. Heinz, J.-F. Paquet, C. Gale, Phys. Rev. C89 (2014) 044910.

[3] A. Adare, et al., Phys. Rev. Lett. 109 (2012) 122302.

[4] M. Wilde, Nucl. Phys. A904 (2013) 573c.

[5] K. Dusling, Nucl. Phys. A839 (2010) 70.

[6] M. Dion, et al., J. Phys. G38 (2011) 124138.

[7] M. Dion, et al., Phys. Rev. C84 (2011) 064901.

[8] C. Shen, U. W. Heinz, J.-F. Paquet, I. Kozlov, C. Gale, Phys. Rev. C91 (2015) 024908.

[9] V. Goloviznin, A. Snigirev, G. Zinovjev, JETP Lett. 61 (2013) 054906.

[10] H. van Hees, M. He, R. Rapp, Nucl. Phys. A933 (2014) 256.

[11] L. McLerran, B. Schenke, Nucl. Phys. A929 (2014) 71.

[12] A. Monnai, Phys. Rev. C90 (2014) 021901.

[13] F.-M. Liu, S.-X. Liu, Phys. Rev. C89 (2014) 034906.

[14] G. A. Almasi, G. Wolf, arXiv:1407.2047 (2014).

[15] V. Ozvenchuk, O. Linnyk, M. Gorenstein, E. Bratkovskaya, W. Cassing, Phys. Rev. C87 (2013) 024901.

[16] V. Ozvenchuk, O. Linnyk, M. Gorenstein, E. Bratkovskaya, W. Cassing, Phys. Rev. C87 (2013) 064903.

[17] A. Bzdak, V. Skokov, Phys. Rev. Lett. 110 (2013) 192301.

[18] K. Tuchin, Phys. Rev. C91 (2015) 014902.

[19] K. Tuchin, Phys. Rev. C87 (2013) 024912.

[20] O. Linnyk, et al., Phys. Rev. C88 (2013) 034904.

[21] O. Linnyk, W. Cassing, E. Bratkovskaya, Phys. Rev. C89 (2014) 034908.

[22] O. Linnyk, V. Konchakovski, T. Steinert, W. Cassing, E. Bratkovskaya (2015) arXiv:1504.05699.

[23] A. Adare, et al., Phys. Rev. C91 (2015) 064904.

[24] W. Cassing, E. L. Bratkovskaya, Nucl. Phys. A 831 (2009) 215.

[25] R. Chatterjee, et al., Phys. Rev. Lett. 96 (2006) 202302.

[26] F.-M. Liu, T. Hirano, K. Werner, Y. Zhu, Nucl. Phys. A830 (2009) 587C.

[27] R. Chatterjee, et al., Phys. Rev. C 88 (2013) 034901.

[28] E. L. Bratkovskaya, W. Cassing, V. P. Konchakovski, O. Linnyk, Nucl. Phys. A856 (2011) 162.

[29] W. Ehehalt, W. Cassing, Nucl. Phys. A 602 (1996) 449.

[30] A. Peshier, W. Cassing, Phys. Rev. Lett. 94 (2005) 172301.

[31] A. Peshier, Phys. Rev. D 70 (2004) 034016.

[32] W. Cassing, Nucl. Phys. A791 (2007) 365.

[33] W. Cassing, Nucl. Phys. A795 (2007) 70.

[34] W. Cassing, Eur. Phys. J. ST 168 (2009) 3.

[35] H.-U. Bengtsson, T. Sjostrand, Comput. Phys. Commun. 46 (1987) 43.

[36] Y. Aoki, S. Borsanyi, S. Durr, Z. Fodor, S. D. Katz, S. Krieg, K. K. Szabo, JHEP 06 (2009) 088.

[37] B. Vanderheyden, G. Baym, J. Stat. Phys. 93 (1998) 843.

[38] L. Rauber, W. Cassing, Phys. Rev. D89 (2014) 065008.

[39] W. Cassing, E. L. Bratkovskaya, Phys. Rev. C 78 (2008) 034919.

[40] C. B. Dover, U. W. Heinz, E. Schnedermann, J. Zimanyi, Phys. Rev. C44 (1991) 1636–1654.

[41] S. A. Bass, et al., Prog. Part. Nucl. Phys. 41 (1998) 255.

[42] M. Bleicher, et al., J. Phys. G25 (1999) 1859–1896.

[43] T. Sjostrand, et al., Comput. Phys. Commun. 135 (2001) 238.

[44] Z.-W. Lin, C. M. Ko, B.-A. Li, B. Zhang, S. Pal, Phys. Rev. C72 (2005) 064901.

[45] S. Juchem, W. Cassing, C. Greiner, Phys. Rev. D69 (2004) 025006.

[46] S. Wang, W. Cassing, Annals Phys. 159 (1985) 328.

[47] M. Bonitz, Quantum kinetic theory, B.G. Teubner, Stuttgart, 1998.

[48] L. P. Kadanoff, G. Baym, Quantum statistical mechanics, Benjamin, New York, 1962.

[49] K. Morawetz, H. Köhler, Eur. Phys. J. A4 (1999) 291.

[50] H. Köhler, K. Morawetz, Phys. Rev. C64 (2001) 024613.

[51] S. Juchem, W. Cassing, C. Greiner, Nucl. Phys. A743 (2004) 92.

[52] W. Botermans, R. Malfliet, Phys. Rept. 198 (1990) 115.

[53] Y. Ivanov, J. Knoll, D. Voskresensky, Nucl. Phys. A657 (1999) 413.

[54] J. Knoll, Y. Ivanov, D. Voskresensky, Annals Phys. 293 (2001) 126.

[55] A. Lang, et al., J. of Comp. Phys. 106 (1993) 391.

[56] W. Cassing, Nucl. Phys. A700 (2002) 618.

[57] Z. Xu, C. Greiner, Phys. Rev. C79 (2009) 014904.

[58] Z. Xu, C. Greiner, Nucl. Phys. A774 (2006) 787–790.

[59] Z. Xu, C. Greiner, Phys. Rev. C71 (2005) 064901.

[60] R. Kubo, J. Phys. Soc. Jap. 12 (1957) 570.

[61] R. Kubo, Rep. Prog. Phys. 29 (1966) 255.

[62] P. Chakraborty, J. I. Kapusta, Phys. Rev. C83 (2011) 014906.

[63] S. Mattiello, W. Cassing, Eur. Phys. J. C70 (2010) 243.

[64] W. Cassing, O. Linnyk, T. Steinert, V. Ozvenchuk, Phys. Rev. Lett. 110 (2013) 182301.

[65] T. Steinert, W. Cassing, Phys. Rev. C89 (2014) 035203.

[66] L. McLerran, Nucl. Phys. A 787 (2007) 1.

[67] L. McLerran, Int. J. Mod. Phys. A 21 (2006) 694.

[68] V. Konchakovski, W. Cassing, V. Toneev, J. Phys. G 42 (2015) 055106.

[69] C. Blume, et al., J. Phys. G 35 (2008) 044004.

[70] H. Ströbele, et al., Proceedings of the CPOD-2009: Workshop on 'Critical Point and Onset of Deconfinemet', Brookhaven, June 8-12 (2009).

[71] C. Alt, et al., Phys. Rev. C 66 (2002) 054902.

[72] C. Alt, et al., Phys. Rev. C 77 (2008) 024903.

[73] S. S. Adler, et al., Phys. Rev. C 69 (2004) 034909.

[74] J. Adams, et al., Phys. Rev. Lett. 92 (2004) 112301.

[75] E. L. Bratkovskaya, S. Soff, H. Stöcker, M. van Leeuwen, W. Cassing, Phys. Rev. Lett. 92 (2004) 032302.

[76] E. L. Bratkovskaya, et al., Phys. Rev. C69 (2004) 054907.

[77] B. B. Abelev, et al., Phys. Lett. B727 (2013) 371.

[78] K. Aamodt, et al., Phys. Rev. Lett. 107 (2011) 032301.

[79] V. Konchakovski, W. Cassing, V. Toneev, J. Phys. G41 (2014) 105004.

[80] B. Abelev, et al., Phys. Lett. B720 (2013) 52.

[81] B. B. Abelev, et al., Eur. Phys. J. C73 (2013) 2662.

[82] B. B. Abelev, et al., Phys. Lett. B736 (2014) 196.

[83] J. Adams, et al., Phys. Rev. Lett. 92 (2004) 052302.

[84] J. Adams, et al., Phys. Rev. Lett. 95 (2005) 122301.

[85] A. Adare, et al., Phys. Rev. Lett. 98 (2007) 162301.

[86] A. Adare, et al., Phys. Rev. Lett. 107 (2011) 252301.

[87] A. M. Poskanzer, S. Voloshin, Phys. Rev. C58 (1998) 1671–1678.

[88] A. Bilandzic, R. Snellings, S. Voloshin, Phys. Rev. C83 (2011) 044913.

[89] B. B. Back, et al., Phys. Rev. C72 (2005) 051901.

[90] E. L. Bratkovskaya, W. Cassing, H. Stöcker, Phys. Rev. C67 (2003) 054905.

[91] W. Cassing, E. L. Bratkovskaya, S. Juchem, Nucl. Phys. A674 (2000) 249.

[92] J. Geiss, W. Cassing, C. Greiner, Nucl. Phys. A644 (1998) 107.

[93] H. Weber, E. Bratkovskaya, W. Cassing, H. Stöcker, Phys. Rev. C67 (2003) 014904.

[94] E. L. Bratkovskaya, et al., Phys. Rev. C69 (2004) 054907.

[95] O. Linnyk, E. L. Bratkovskaya, W. Cassing, H. Stöcker, Nucl. Phys. A786 (2007) 183–200.

[96] O. Linnyk, E. L. Bratkovskaya, W. Cassing, Nucl. Phys. A807 (2008) 79.

[97] O. Linnyk, E. L. Bratkovskaya, W. Cassing, H. Stöcker, Phys. Rev. C76 (2007) 041901.

[98] S. S. Adler, et al., Phys. Rev. C71 (2005) 034908.

[99] P. Braun-Munzinger, D. Miskowiec, A. Drees, C. Lourenco, Eur. Phys. J. C1 (1998) 123.

[100] M. Gazdzicki, M. I. Gorenstein, Phys. Rev. Lett. 83 (1999) 4009–4012.

[101] A. Andronic, P. Braun-Munzinger, K. Redlich, J. Stachel, Phys. Lett. B652 (2007) 259–261.

[102] P. Braun-Munzinger, J. Stachel, Phys. Lett. B490 (2000) 196.

[103] P. Braun-Munzinger, J. Stachel, Nucl. Phys. A690 (2001) 119–126.

[104] R. L. Thews, M. Schroedter, J. Rafelski, Phys. Rev. C63 (2001) 054905.

[105] C. Lourenco, H. Wohri, Phys. Rept. 433 (2006) 127.

[106] B. Brambilla, et al., CERN Yellow Report, CERN-2005-005 (2005).

[107] O. Linnyk, E. L. Bratkovskaya, W. Cassing, Int. J. Mod. Phys. E17 (2008) 1367.

[108] O. Linnyk, E. L. Bratkovskaya, W. Cassing, H. Stöcker, Nucl. Phys. A786 (2007) 183–200.

[109] O. Linnyk, E. L. Bratkovskaya, W. Cassing, H. Stöcker, Phys. Rev. C76 (2007) 041901.

[110] W. Cassing, E. L. Bratkovskaya, A. Sibirtsev, Nucl. Phys. A691 (2001) 753.

[111] T. Falter, K. Gallmeister, W. Cassing, U. Mosel, Phys. Rev. C70 (2004) 054609.

[112] T. Falter, K. Gallmeister, W. Cassing, U. Mosel, Phys. Lett. B594 (2004) 61.

[113] W. Cassing, K. Gallmeister, C. Greiner, Nucl. Phys. A735 (2004) 277.

[114] K. Gallmeister, W. Cassing, Nucl. Phys. A748 (2005) 241.

[115] A. Andronic, P. Braun-Munzinger, K. Redlich, J. Stachel, Nucl. Phys. A789 (2007) 334.

[116] A. Adare, et al., Phys. Rev. C77 (2008) 024912.

[117] R. Arnaldi, Phys. Rev. Lett. 96 (2006) 162302.

[118] A. Adare, et al. (2006).

[119] D. Kharzeev, R. L. Thews, Phys. Rev. C60 (1999) 041901.

[120] B. Alessandro, et al. (2006).

[121] G. Borges, et al., J. Phys. G32 (2006) S381–S390.

[122] K. Martins, D. Blaschke, E. Quack, Phys. Rev. C51 (1995) 2723.

[123] C. Gerschel, J. Hufner, Z. Phys. C56 (1992) 171–174.

[124] S. S. Adler, et al., Phys. Rev. Lett. 96 (2006) 012304.

[125] I. C. Arsene, et al. (2007).

[126] A. Capella, E. G. Ferreiro, A. Capella, E. G. Ferreiro, Phys. Rev. C76 (2007) 064906.

[127] R. Vogt, Phys. Rev. C71 (2005) 054902.

[128] B. Kopeliovich, A. Tarasov, J. Hufner, Nucl. Phys. A696 (2001) 669–714.

[129] A. Capella, et al. (2007).

[130] R. Granier de Cassagnac, J. Phys. G34 (2007) S 955.

[131] B. Müller, Nucl. Phys. A661 (1999) 272c.

[132] P. Braun-Munzinger, K. Redlich, Eur. Phys. J. C16 (2000) 519.

[133] K. Martins, D. Blaschke, E. Quack, Phys. Rev. C51 (1995) 2723.

[134] C. Y. Wong, E. S. Swanson, T. Barnes, Phys. Rev. C62 (2000) 045201.

[135] C. M. Ko, X. N. Wang, X. F. Zhang, Phys. Lett. B444 (1998) 237.

[136] F. O. Duraes, et al., Phys. Rev. C68 (2003) 035208.

[137] W. Cassing, L. A. Kondratyuk, G. I. Lykasov, M. V. Rzjanin, Phys. Lett. B513 (2001) 1.

[138] Z. Lin, C. M. Ko, Phys. Rev. C62 (2000) 034903.

[139] Z. Lin, C. M. Ko, J. Phys. G27 (2001) 617.

[140] N. Armesto, A. Capella, Phys. Lett. B430 (1998) 23.

[141] P. Braun-Munzinger, K. Redlich, Nucl. Phys. A661 (1999) 546.

[142] L. Grandchamp, R. Rapp, Phys. Lett. B523 (2001) 60–66.

[143] L. Grandchamp, R. Rapp, Nucl. Phys. A709 (2002) 415–439.

[144] Z.-w. Lin, C. M. Ko, J. Phys. G27 (2001) 617–624.

[145] Z.-W. Lin, C. M. Ko, Phys. Rev. C65 (2002) 034904.

[146] T. Matsui, H. Satz, Phys. Lett. B178 (1986) 416.

[147] H. Satz, Rep. Progr. Phys. 63 (2000) 1511.

[148] H. Satz, J. Phys. G32 (2006) R25.

[149] F. Karsch, D. Kharzeev, H. Satz, Phys. Lett. B637 (2006) 75.

[150] G. Aarts, et al. (2007).

[151] S. Datta, F. Karsch, P. Petreczky, I. Wetzorke, Phys. Rev. D69 (2004) 094507.

[152] P. Petreczky, K. Petrov, Phys. Rev. D70 (2004) 054503.

[153] K. Petrov, PoS LAT2006 (2006) 144.

[154] O. Kaczmarek, PoS CPOD07 (2007) 043.

[155] A. Mocsy, P. Petreczky (2007).

[156] H. van Hees, R. Rapp, Phys. Rev. C71 (2005) 034907.

[157] K. Gallmeister, T. Falter, Phys. Lett. B630 (2005) 40.

[158] A. Andronic (2008). Private communication.

[159] R. Arnaldi, et al., Nucl. Phys. A783 (2007) 261–268.

[160] H. Stöcker, Nucl. Phys. A750 (2005) 121–147.

[161] A. Adare, et al., Phys. Rev. Lett. 98 (2007) 172301.

[162] E. L. Bratkovskaya, W. Cassing, H. Stöcker, N. Xu, Phys. Rev. C71 (2005) 044901.

[163] W. Cassing, E. L. Bratkovskaya, Nucl. Phys. A623 (1997) 570.

[164] W. Cassing, W. Ehehalt, C. M. Ko, Phys. Lett. B363 (1995) 35.

[165] J. Beringer, et al., Phys. Rev. D86 (2012) 010001.

[166] H. Jones, M. Scadron, Annals Phys. 81 (1973) 1.

[167] G. Wolf, G. Batko, W. Cassing, U. Mosel, K. Niita, et al., Nucl. Phys. A517 (1990) 615.

[168] M. Krivoruchenko, A. Faessler, Phys. Rev. D65 (2002) 017502.

[169] M. Zetenyi, G. Wolf, Heavy Ion Phys. 17 (2003) 27.

[170] J. Koch, N. Ohtsuka, E. Moniz, Annals Phys. 154 (1984) 99.

[171] K. Haglin, C. Gale, V. Emel'yamnov, Phys. Rev. D47 (1993) 973.

[172] O. Linnyk, J. Phys. G38 (2011) 025105.

[173] P. B. Arnold, G. D. Moore, L. G. Yaffe, JHEP 0112 (2001) 009.

[174] E. L. Bratkovskaya, S. M. Kiselev, G. B. Sharkov, Phys. Rev. C78 (2008) 034905.

[175] W. Bauer, G. F. Bertsch, W. Cassing, U. Mosel, Phys. Rev. C34 (1986) 2127.

[176] W. Cassing, V. Metag, U. Mosel, K. Niita, Phys. Rept. 188 (1990) 363–449.

[177] C. Gale, J. Kapusta, Phys. Rev. C 35 (1987) 2107.

[178] C. Gale, J. Kapusta, Phys. Rev. C 38 (1988) 2659.

[179] C. Gale, J. Kapusta, Nucl. Phys. A 495 (1989) 423c.

[180] O. Linnyk, et al., Phys. Rev. C84 (2011) 054917.

[181] C. Song, C. M. Ko, C. Gale, Phys. Rev. D50 (1994) 1827.

[182] G.-Q. Li, C. Gale, Phys. Rev. C58 (1998) 2914–2927.

[183] H. van Hees, R. Rapp, Phys. Rev. Lett. 97 (2006) 102301.

[184] H. van Hees, R. Rapp, Nucl. Phys. A806 (2008) 339–387.

[185] O. Linnyk, E. L. Bratkovskaya, W. Cassing, Nucl. Phys. A830 (2009) 491c–494c.

[186] O. Linnyk, S. Leupold, U. Mosel, Phys. Rev. D75 (2007) 014016.

[187] J. I. Kapusta, P. Lichard, D. Seibert, Phys. Rev. D44 (1991) 2774.

[188] E. L. Bratkovskaya, W. Cassing, U. Mosel, Nucl. Phys. A686 (2001) 568.

[189] L. Kaptari, B. Kämpfer, Nucl. Phys. A764 (2006) 338.

[190] C. Ernst, S. Bass, M. Belkacem, H. Stöcker, W. Greiner, Phys. Rev. C58 (1998) 447.

[191] I. Tserruya, in "Relativistic Heavy-Ion Physics", edited by R. Stock, Landolt-Boernstein, Volume 1-23A (2010).

[192] R. J. Fries, B. Müller, D. K. Srivastava, Phys. Rev. Lett. 90 (2003) 132301.

[193] E. V. Shuryak, Sov. Phys. JETP 47 (1978) 212.

[194] E. V. Shuryak, Phys. Lett. B78 (1978) 150.

[195] E. L. Feinberg, Izv. Akad. Nauk Ser. Fiz. 34 (1970) 1987.

[196] E. L. Feinberg, Nuovo Cim. A34 (1976) 391.

[197] J. D. Bjorken, H. Weisberg, Phys. Rev. D13 (1976) 1405.

[198] J. Cleymans, J. Fingberg, K. Redlich, Phys. Rev. D35 (1987) 2153.

[199] R. Arnaldi, et al., Phys. Rev. Lett. 96 (2006) 162302.

[200] J. Seixas, et al., J. Phys. G34 (2007) S1023–1028.

[201] S. Damjanovic, et al., Nucl. Phys. A783 (2007) 327c.

[202] R. Rapp, J. Wambach, H. van Hees (2009). In "Relativistic Heavy-Ion Physics", edited by R. Stock, Landolt-Boernstein, Volume I/23, 4-1 (2010).

[203] O. Linnyk, E. L. Bratkovskaya, W. Cassing, AIP Conf. Proc. 1257 (2010) 700.

[204] E. L. Bratkovskaya, W. Cassing, O. Linnyk, Phys. Lett. B670 (2009) 428.

[205] A. Toia, Nucl. Phys. A774 (2006) 743.

[206] A. Toia, Eur. Phys. J. C49 (2007) 243.

[207] S. Afanasiev, et al. (2007) arXiv:0706.3034.

[208] A. Adare, et al. (2009).

[209] J. Manninen, E. L. Bratkovskaya, W. Cassing, O. Linnyk, Eur. Phys. J. C71 (2011) 1615.

[210] F. Halzen, D. M. Scott, Phys. Rev. D18 (1978) 3378.

[211] Z.-W. Lin, C. M. Ko, Nucl. Phys. A671 (2000) 567.

[212] F. Halzen, D. M. Scott, Phys. Rev. Lett. 40 (1978) 1117.

[213] L. Landau, I. Pomeranchuk, Dokl. Akad. Nauk Ser. Fiz. 92 (1953) 535.

[214] L. Landau, I. Pomeranchuk, Dokl. Akad. Nauk Ser. Fiz. 92 (1953) 735.

[215] A. B. Migdal, Phys. Rev. 103 (1956) 1811.

[216] P. Aurenche, F. Gelis, G. D. Moore, H. Zaraket, JHEP 12 (2002) 006.

[217] F. Karsch, E. Laermann, P. Petreczky, S. Stickan, I. Wetzorke, Phys. Lett. B530 (2002) 147.

[218] M. I. Gorenstein, O. A. Mogilevsky, Phys. Lett. B228 (1989) 121.

[219] A. Peshier, B. Kämpfer, O. P. Pavlenko, G. Soff, Phys. Lett. B337 (1994) 235–239.

[220] M. H. Thoma, S. Leupold, U. Mosel, Eur. Phys. J. A7 (2000) 219–223.

[221] L. D. McLerran, T. Toimela, Phys. Rev. D31 (1985) 545.

[222] E. Shuryak, Prog. Part. Nucl. Phys. 53 (2004) 273.

[223] M. H. Thoma, J. Phys. G31 (2005) L7.

[224] K. Adcox, et al., Nucl. Phys. A757 (2005) 184.

[225] J. Adams, et al., Nucl. Phys. A757 (2005) 102–183.

[226] I. Arsene, et al., Nucl. Phys. A757 (2005) 1–27.

[227] B. B. Back, et al., Nucl. Phys. A757 (2005) 28.

[228] F. Karsch, Nucl. Phys. A698 (2002) 199–208.

[229] E. Braaten, R. D. Pisarski, T.-C. Yuan, Phys. Rev. Lett. 64 (1990) 2242.

[230] S. M. H. Wong, Z. Phys. C58 (1993) 159.

[231] R. D. Pisarski, Phys. Rev. Lett. 63 (1989) 1129.

[232] V. P. Silin, Sov. Phys. J.E.T.P. 11 (1960) 1136.

[233] V. V. Klimov, Sov. Phys. J.E.T.P. 55 (1982) 199.

[234] H. A. Weldon, Phys. Rev. D26 (1982) 1394.

[235] R. Baier, M. Dirks, K. Redlich, Acta Phys. Polon. B28 (1997) 2873–2895.

[236] M. Strickland, Phys. Lett. B331 (1994) 245–250.

[237] J.-P. Blaizot, F. Gelis, Eur. Phys. J. C43 (2005) 375–380.

[238] F. Gelis, Nucl. Phys. A715 (2003) 329–338.

[239] R. Baier, B. Pire, D. Schiff, Phys. Rev. D38 (1988) 2814.

[240] T. Altherr, P. Aurenche, T. Becherrawy, Nucl. Phys. B315 (1988) 436.

[241] O. Linnyk, S. Leupold, U. Mosel, Phys. Rev. D71 (2005) 034009.

[242] R. L. Jaffe (1985). Lectures presented at the Los Alamos School on Quark Nuclear Physics, Los Alamos, N.Mex., Jun 10-14, 1985.

[243] E. V. Shuryak, A. I. Vainshtein, Nucl. Phys. B199 (1982) 451.

[244] S. D. Drell, T.-M. Yan, Phys. Rev. Lett. 24 (1970) 181.

[245] G. Altarelli, G. Parisi, R. Petronzio, Phys. Lett. B76 (1978) 351.

[246] A. I. Vainshtein, V. I. Zakharov, V. A. Novikov, M. A. Shifman, JETP Lett. 24 (1976) 341. [Pisma Zh. Eksp. Teor. Fiz. 24, 376 (1976)].

[247] M. E. Peskin, D. V. Schroeder, An Introduction to quantum field theory, Reading, USA: Addison-Wesley, 1995.

[248] V. V. Sudakov, Sov. Phys. JETP 3 (1956) 65–71. [Zh. Eksp. Teor. Fiz.30,87(1956)].

[249] A. H. Compton, Phys. Rev. 21 (1923) 483–502.

[250] A. H. Compton, Phys. Rev. 22 (1923) 409–413.

[251] J. Collins, H. Jung (2005).

[252] A. I. Akhiezer, V. B. Berestetsky, Quantum electrodynamics (in Russian), Moscow: Nauka, 1981.

[253] T. H. West, Comp. Phys. Comm. 77 (1993) 286.

[254] S. Wolfram, The Mathematica Book, Fifth Edition, Champaign, USA: Wolfram Media, 2003.

[255] F. Karsch, E. Laermann, A. Peikert, Phys. Lett. B478 (2000) 447–455.

[256] V. V. Begun, M. I. Gorenstein, O. A. Mogilevsky (2010).

[257] O. Linnyk, et al. (2015). work in progress.

[258] K. Gallmeister, B. Kämpfer, O. P. Pavlenko, Phys. Lett. B473 (2000) 20.

[259] K. Gallmeister, B. Kämpfer, O. P. Pavlenko, C. Gale, Nucl. Phys. A688 (2001) 939.

[260] A. Adare, et al., Phys. Rev. C 81 (2010) 034911.

[261] J. Ghiglieri, J. Hong, A. Kurkela, E. Lu, G. D. Moore, D. Teaney, JHEP 05 (2013) 010.

[262] G. Vujanovic, et al., Nucl. Phys. A 932 (2014) 230.

[263] J. Ghiglieri, Nucl. Phys. A 932 (2014) 326.

[264] J. Cleymans, V. Goloviznin, K. Redlich, Phys. Rev. D47 (1993) 173.

[265] J. Cleymans, V. Goloviznin, K. Redlich, Phys. Lett. B319 (1993) 520.

[266] J. Cleymans, V. Goloviznin, K. Redlich, Phys. Rev. D47 (1993) 989.

[267] J. Knoll, R. Lenk, Nucl. Phys. A561 (1993) 501.

[268] Y. Yin, Phys. Rev. C90 (2014) 044903.

[269] F. Low, Phys. Rev. 110 (1958) 974.

[270] H. Eggers, R. Tabti, C. Gale, K. Haglin, Phys. Rev. D53 (1996) 4822.

[271] W. Liu, R. Rapp, Nucl. Phys. A796 (2007) 101.

[272] H. van Dam, M. Veltman, Nucl. Phys. B22 (1970) 397.

[273] V. Srinivasan, et al., Phys. Rev. D12 (1975) 681.

[274] S. Protopopescu, et al., Phys. Rev. D7 (1973) 1279.

[275] D. Aston, et al., Nucl. Phys. Proc. Suppl. 21 (1991) 105.

[276] K. Haglin, J. I. Kapusta, C. Gale, Phys. Lett. B224 (1989) 433.

[277] K. L. Haglin, J. Phys. G30 (2004) L27.

[278] C. Song, Phys. Rev. C 47 (1993) 2861.

[279] O. Linnyk, W. Cassing, J. Manninen, E. Bratkovskaya, C. Ko, Phys. Rev. C85 (2012) 024910.

[280] ABBHHM, Phys. Rev. 175 (1968) 1669.

[281] M. Effenberger, E. Bratkovskaya, U. Mosel, Phys. Rev. C60 (1999) 044614.

[282] E. L. Bratkovskaya, C. M. Ko, Phys. Lett. B 445 (1999) 265.

[283] W. Cassing, Y. S. Golubeva, A. S. Iljinov, L. A. Kondratyuk, Phys. Lett. B 396 (1997) 26.

[284] Y. S. Golubeva, L. A. Kondratyuk, W. Cassing, Nucl. Phys. a 625 (1997) 832.

[285] R. Rapp (2002). arXiv:nucl-th/0204003.

[286] D. Trnka, et al., Phys. Rev. Lett. 94 (2005) 192303.

[287] T. Hatsuda, S. Lee, Phys. Rev. C 46 (1992) R34.

[288] G. E. Brown, M. Rho, Phys. Rev. Lett. 66 (1991) 2720.

[289] G. E. Brown, M. Rho, Phys. Rept.. 363 (2002) 85.

[290] V. Metag, Prog. Part. Nucl. Phys. 61 (2008) 245.

[291] E. Bratkovskaya, W. Cassing, Nucl. Phys. A807 (2008) 214.

[292] E. L. Bratkovskaya, W. Cassing, Nucl. Phys. A 619 (1997) 413.

[293] W. Cassing, E. L. Bratkovskaya, R. Rapp, J. Wambach, Phys. Rev. C 57 (1998) 916.

[294] G.-Q. Li, C. M. Ko, Nucl. Phys. A582 (1995) 731–748.

[295] R. Arnaldi, et al., Eur. Phys. C 59 (2009) 607.

[296] J. Seixas, et al., J. Phys. G34 (2007) S1023.

[297] S. Damjanovic, Nucl. Phys. A 783 (2007) 327c.

[298] R. Arnaldi, Eur. Phys. J C61 (2009) 711.

[299] J. K. Nayak, J.-e. Alam, T. Hirano, S. Sarkar, B. Sinha, Phys. Rev. C85 (2012) 064906.

[300] A. Adare, et al. (2015) arXiv:1509.04667.

[301] J. Zhao, J. Phys. G38 (2011) 124134.

[302] P. Huck, Nucl. Phys. A931 (2014) c659.

[303] L. Ruan, Nucl. Phys. A931 (2014) 185.

[304] O. Linnyk, et al., Phys. Rev. C87 (2013) 014905.

[305] M. K. Köhler, Nucl. Phys. A931 (2014) c665.

[306] R. Rapp, Adv. High Energy Phys. 2013 (2013) 148253.

[307] G. Vujanovic, S. Young, B. Schenke, R. Rapp, S. Jeon, C. Gale, Phys. Rev. C89 (2014) 034904.

[308] M. Aggarwal, et al., Phys. Rev. Lett. 85 (2000) 3595.

[309] M. Aggarwal, et al. (2000) arXiv:nucl–ex/0006007.

[310] E. V. Shuryak, Sov. J. Nucl. Phys. 28 (1978) 408. Yad. Fiz. 28 (1978) 796.

[311] C. Shen, U. Heinz, J.-F. Paquet, C. Gale, Nucl. Phys. A 932 (2014) 184.

[312] A. Adare, et al., Phys. Rev. Lett. 104 (2010) 132301.

[313] A. Drees, Nucl. Phys. A910 (2013) 179.

[314] K. Dusling, I. Zahed, Phys. Rev. C82 (2010) 054909.

[315] S. Turbide, R. Rapp, C. Gale, Phys. Rev. C69 (2004) 014903.

[316] S. Mizuno, Nucl. Phys. A931 (2014) 686.

[317] H. van Hees, C. Gale, R. Rapp, Phys. Rev. C84 (2011) 054906.

[318] J. Adam, et al. (2015) arXiv:1509.07324.

[319] O. Linnyk, E. Bratkovskaya, W. Cassing, PoS (Baldin ISHEPP XXII), 084 (2015).

[320] M. Aggarwal, et al., Eur. Phys. J. C41 (2005) 287.

[321] D. Lohner, J. Phys. Conf. Ser. 446 (2013) 012028.

[322] F. Bock (2014). Direct-photon spectra and flow in PbPb collisions at the LHC measured with the ALICE experiment, contributed talk at the Quark Matter 2014, https://indico.cern.ch/event/219436/session/16/contribution/152.

[323] C. Shen, J.-F. Paquet, J. Liu, G. Denicol, U. Heinz, C. Gale, Nucl. Phys. A931 (2014) 675–680.

[324] A. Adare, et al. (2015) arXiv:1509.07758.

[325] J. Adams, et al., Phys. Rev. C 72 (2005) 014904.

[326] S. Adler, et al., Phys. Rev. Lett. 91 (2003) 182301.

[327] A. Morreale (2014) arXiv:1409.4456.

[328] L. E. Gordon, W. Vogelsang, Phys. Rev. D50 (1994) 1901–1916.

[329] H. Holopainen, S. Rasanen, K. J. Eskola, Phys. Rev. C84 (2011) 064903.

[330] L. McLerran, Phys. Part. Nucl. Lett. 8 (2011) 673.

[331] M. Chiu, et al., Nucl. Phys. A 900 (2013) 16.

[332] J.-P. Blaizot, et al., Nucl. Phys. A 904-905 (2013) 829c.

[333] C. Gale, et al., Phys. Rev. Lett. 110 (2013) 012302.

[334] G. Basar, D. Kharzeev, V. Skokov, Phys. Rev. Lett. 109 (2012) 202303.

[335] G. Basar, D. E. Kharzeev, E. V. Shuryak, Phys. Rev. C90 (2014) 014905.

[336] Y. Hidaka, S. Lin, R. D. Pisarski, D. Satow, V. V. Skokov, Nucl. Phys. A931 (2014) 681–685.

[337] B. Bannier, Nucl. Phys. A931 (2014) 1189.

[338] V. Voronyuk, et al., Phys. Rev. C83 (2011) 054911.

[339] V. Skokov, A. Y. Illarionov, V. Toneev, Int. J. Mod. Phys. A24 (2009) 5925.

[340] V. Skokov, J. Phys. Conf. Ser. 432 (2013) 012021.

[341] D. Peressounko, in: Proceedings, 30th International Workshop on High Energy Physics: Particle and Astroparticle Physics, Gravitation and Cosmology: Predictions, Observations and New Projects (IHEP 2014), pp. 181–188.

[342] R. Chatterjee, D. K. Srivastava, T. Renk, Nucl. Phys. A 931 (2014) 670.

Acknowledgements

My special thanks go in the first place to W. Cassing for giving me honest advice, generous support, personal inspiration and opportunities to grow. He motivates me in my research, and at the same time allows me the creative freedom for own development.

I deeply value the long-lasting cooperation with E. Bratkovskaya, who introduced me to the fascinating world of heavy-ion collisions. Throughout the years, her suggestions, ideas, and wide knowledge have enriched my work.

Many thanks go to J. Aichelin, P.-B. Gossiaux, M. Gorenstein, C.-M. Ko, V. Konchakovski, J. Manninen, V. Ozvenchuk, A. Palmese, T. Song, T. Steinert, H. Stöcker and V. Toneev for the important contributions to our common papers.

Besides the close collaborators, I thank U. Heinz, L. McLerran, T. Biro and R. Pisarski for enlightening conversations. I am very grateful to C. Gale for his valuable academic advice and for the inspiring discussions, which left a lasting impression. I especially thank L. Csernai and T. Kodama for the encouragement and support and H. Stöcker for always finding time to answer my questions. I am very grateful to G. David, X. Dong, F. Geurts, B. Jacak, K. Reygers, L. Ruan, J. Stachel, A. Toia, I. Tserruya and N. Xu for helpful explanations of their experimental work.

I would like to thank my colleagues at the University of Gießen and in the Frankfurt Institute for Advanced Studies, in particular, K. Brinkmann, C. Fischer, S. Kraft-Bermuth, H. Lenske, B.J. Schaefer, L. von Smekal, M. Thoma and N. Tsoneva for the productive and friendly atmosphere in Gießen, and M. Bleicher, V. Begun, C. Greiner, I. Mishustin, J. Schaffner-Bielich, G. Torrieri and M. Strikland for the lively discussions in Frankfurt, which have influenced my thinking and my following research. I appreciate the hard administrative work of E. Jung, I. Sporates, M. Weingärtner.

Let me express my gratitude to V.K. Tartakovskyi, P.A. Molchanov, U. Mosel and S. Leupold for encouraging my early scientific experiences and to K. Becker, an insightful mentor, for inspiring me to follow my passion. I cordially thank families Farina, Kirchhübel-Gilardi, Skipa and R. Schmidt for their friendship.

Finally, a heartfelt thank you to my husband Z. Gagyi Palffy and my mother N. Linnyk, who spent long evenings advising me on layout, science, life and everything. Talking to them often gave me new fruitful impulses. My thanks also go to my mother-in-law T. Gagyi Palffy, who is ready to help us at all times, my sister O. Shostak for her unconditional support and my son Almos for being a source of motivation and love. My father A. Linnyk will always be present in my life.

This work was possible due to the vast computing powers of Loewe-CSC, Skylla Cluster and the support of DAAD, DFG and the HIC for FAIR program.